High magnetic field neutron stars: Cyclotron lines and Polarization

A Thesis

Submitted For the Degree of

Doctor of Philosophy

in the Faculty of Science

by

Chandreyee Maitra

Under the Supervision of

Prof. Biswajit Paul

Raman Research Institute

Astronomy And Astrophysics

Indian Institute of Science

BANGALORE – 560 012

November 2013

TO

My parents

DECLARATION

I hereby declare that the work presented in this thesis is entirely original and has been carried out by me at the Raman Research Institute under the auspices of the Joint Astronomy Programme of the Department of Physics, Indian Institute of Science. I further declare that this has not formed the basis for the award of any degree, diploma, membership, associateship or similar title of any University or Institution.

Department of Physics
Indian Institute of Science
Bangalore -560012
India

Chandreyee Maitra
Date:

Acknowledgements

My journey through the Ph.D tenure has been a pleasent one thanks to the numerous people around me who have supported me by all means possible.
Firstly I am greatly indebted to my supervisor Prof. Biswajit Paul for the very smooth and peaceful years that I spent in RRI even amidst many many deadlines and pressures. He allowed me to grow and explore on my own, while providing the very valuable suggestions and help wherever required. Without him I could not have progressed whatever I have today. He has also extended full support and understanding in many difficult times of my life due to which I could work peacefully and complete my thesis in time.
I deeply thank Prof Dipankar Bhattacharya for the innumerable things I learnt from him, specially during my visit to IUCAA. Discussing and working freely with him gave much more clarity to my thoughts, and most of the understanding developed on CRSFs is due to him. I also thank him and Sunita for introducing me to the cats of IUCAA.
I am thankful to Dr Sachindra Naik for teaching me *Suzaku* analysis for the first time.
I thank prof Avinash Deshpande for the many stimulating discussions that we had during my PhD years, due to which I explored many newer things. Desh is really nice and very approchable at times of need.
I thank all the faculties on the astro floor and all the people who have taught me during my course work for the many things I picked up from them in all these years.
I thank Rishin, Gopalkrishna and all the people in the X-ray lab who have taught me various things on instrumentation and the X-ray polarimeter. I especially thank Rishin for bearing me with my innumerable doubts and questions, which he happily answered and solved immediately whenever I asked. I have bugged him many times specially during presentations or examinations.
I thank Prof Andrzej Zdziarski for hosting me twice in Poland. It was a great experience

working and collaborating with him and I hope to continue with it.
I also thank prof Rajaram Nityananda for providing a patient ear to my queries and providing very valuable suggestions regarding my work. I am also thankul to Dr Sushan Konar, who also provided many valuable inputs during my discussions with her.
I thank Harsha who has solved my numerous doubts on various occasions and have critically examined my results whenever I needed helping me to learn a lot. I also thank Jincy and Marykutty for being great friends as well as colleagues with whom I could discuss my work critically.
Vidya is one of the kindest people I have ever met, and she has taken care of every possible things ensuring a smooth stay in RRI, as she does for everyone else. I thank her for bearing with me many times when I have been careless or unreasonable.
I thank Ram, Narayanswamy and Ganesh for providing such a musical atmosphere in RRI and ever encouraging me to pursue this interest of mine. Krishnamurthy has also provided great support in this respect and has always cheered me up by sharing his rich collection of music.
I thank all the stuff of Computer section, Library, canteen and security providing support in various ways and ensuring a pleasent stay at RRI. Jacob and Krishnamurthy from the computer section have especially immediately hepled during the scary hours of machine breakdown or hard disk damage.
I thank all the staff in the hostel especially the cooks Umaji, Shardaji and Padmaji for providing great food and also making the hostel a home away from home. I thank Lasmamma for providing the ever refreshing and energizing tea and coffee.
I thank my friends in the hostel especially Tripta, Amrita, Chaitra, Anjan, Jyoti, Mriaganko for many enjoyable years spend there.
I thank Kaalu, Whisky, Fluffy, Bluffy and Kesto for being great canine companions.
I thank Mayuri, Lijo, Yogesh, Kanhaiya, Jagdish, Nishant for being very good friends as well as colleagues with whom I have spent many enjoyable moments in RRI and who have hepled me many times in various ways.
I thank Wasim for the brotherly care and warmth that he always gave me, and despite our various disagreements he has been one of the most supportive person here. Mamta and I have shared our joys and sorrows and I thank here being there for me always. Nazma has been the most adorable and loving junior and friend that I could have ever hoped for and our bond has seen me though many frustrating times. Nipanjana, Kshitij and myself have share a very deep bond which is not enough to describe in words. They

are one of the best things that happened to me here, and I pray we remain together forever.

I thank all my school and college buddies especially Anubhav, Anwesha, Ashmita, Ankur and Sweta for supporting me in everything and making my stay in Bangalore extremely enjoyable. The numerous weekend siestas and trips that we had together charged me up always.

I thank Deepak for being with me though thick and thin. He is the best gift that RRI has given me for life, and I will be ever greatful for that.

My parents have been the strongest pillars of my life and whatever I am today is solely due to them. They have always encouraged me in all my decisions and it is they who gave me the courage to pursue a Ph.D in astrophysics after completing my engineering degree. While trying to live up to their expectations I have progressed a lot. Love you Ma and Baba.

PUBLICATIONS

PUBLICATIONS INCLUDED IN THE THESIS

1. Pulse phase resolved spectroscopy of A 0535+26, XTE J1946+274 and 4U 1907+09 with Suzaku, **Maitra, C.**; & Paul, B., 2013, ApJ, 771, 96.

2. Timing and Spectral Properties of Be/X-ray Pulsar EXO 2030+375 during a Type I Outburst., Naik, S.; **Maitra, C.**; Paul, B. & Jaisawal, G. K, 2013, ApJ, 764, 158.

3. Pulse phase resolved spectroscopy of Vela X-1 with Suzaku, **Maitra, C.**; & Paul, B., 2013, ApJ, 763, 79.

4. Timing and broad-band spectroscopy of 1A 1118-61 with Suzaku., **Maitra, C.**; Paul, B. & Naik, S., 2012, MNRAS, 420, 2307.

5. Prospect of polarization measurements from black hole binaries in their thermal state with a scattering polarimeter, **Maitra, C.**; & Paul, B., 2011, MNRAS, 414, 2618.

OTHER PUBLICATIONS

1. Revisiting SWJ2000.6+3210 : A persistent Be X-ray pulsar ?, Pradhan, P.; **Maitra, C.**; Paul, B.; Paul, B. C.; 2013, MNRAS accepted,(arXiv:1308.2739) .

2. Energy-dependent orbital modulation of X-rays and constraints on emission of the jet in Cyg X-3, Zdziarski A. A., **Maitra C.**, Frankowski A., Skinner G. K., Misra R., 2012, MNRAS, 426, 1031

ASTRONOMICAL CIRCULARS & BULLETINS

1. Detection of periodic X-ray modulation of SFXT IGR J16207-5129 in the Swift-BAT light curve., Jain C., Paul B., **Maitra C.**, 2011, ATel, 3785, 1

CONFERENCE PROCEEDINGS

1. Latest results of pulse phase resolved spectroscopy of cyclotron lines in accretion powered pulsars; Maitra,C & Paul,B; Contribution to the proceedings of the conference "Physics at the Magnetospheric Boundary", Geneva, 25th-28th June, 2013, (arXiv:1309.5790)

2. A Thomson X-ray polarimeter for a small satellite mission and its scientific prospects; Paul, B., Gopala Krishna, M. R., Rishin, P. V., Duraichelvan, R.; **Maitra, C** ; 39th COSPAR Scientific Assembly. Held 14-22 July 2012, in Mysore, India. Abstract C1.1-35-12, p.1467

3. Pulse Phase resolved spectroscopy of HMXB accretion powered pulsars- a powerful tool to probe the dips in the pulse profiles; **Maitra, C** , Paul, B., Devasia, J.; 39th COSPAR Scientific Assembly. Held 14-22 July 2012, in Mysore, India. Abstract A1.1-67-12, p.1148

4. Thomson X-ray Polarimeter for a Small Satellite Mission., Rishin, P. V., Paul, B., Gopalkrishna, M. R., Duraichelvan, R., Ateequlla, C.M., **Maitra C.**, & 7 coauthors, Proceedings of the 29th Meeting of the Astronomical Society of India, held 23-25 February, 2011. ASI Conference Series, Vol. 3, Edited by P. Khare and C.H. Ishwara-Chandra, 2011, p. 165

5. Thomson X-ray Polarimeter for a Small Satellite Mission., Paul. B., Rishin, P. V., **Maitra C.**, Gopalkrishna, M. R., Duraichelvan, R., Ateequlla, C.M., Cowsik, R., Devasia, J., James, M., "The First Year of MAXI: Monitoring Variable X-ray Sources", Poster Presentations, 4th International MAXI Workshop held November 30 - December 2, 2010 in Tokyo, Japan.

6. Intensity and energy dependent profiles of transient HMXB pulsars GRO J1008-57, 1A 1118-61 and GX 304-1., Paul, B., Devasia, J., **Maitra C.**, James, M., Naik, S., Indulekha, K., "The First Year of MAXI: Monitoring Variable X-ray Sources", Poster Presentations, 4th International MAXI Workshop held November 30 - December 2, 2010 in Tokyo, Japan.

Abstract

Thousands of X-ray sources are known today which includes the X-ray binaries, Active Galactic Nuclei (AGNs), cataclysmic variables, supernova remnants, protostellar objects and even weak emission from the planets including our earth. In addition, it has also been discovered that the space between galaxies in galaxy clusters are filled with very hot and optically thin gas which shine in X-rays at a temperature between 10^7 *to and* 10^8 *K. X-ray astronomy has thus taken many giant leaps after the discovery of the first X-ray source Sco X-1 in 1962. With the advent of the latest technologies and the new age satellite missions allowing us high sensitivity and good spatial, temporal and energy resolution, detailed studies have been made to study the hot and energetic phenomena of the universe which reveals itself through their study in the X-ray regime.*

This thesis concerns with the study of X-ray binaries which are gravitationally bound systems consisting of a compact object (either a neutron star or a black hole) and usually a non degenerate companion star, both rotating around the common centre of mass. The compact star shines brightly in the X-ray regime ($L_x \simeq 10^{33} - 10^{38}\, erg\, s^{-1}$*). They can be further divided into High mass X-ray binaries (HMXBs) and Low mass X-ray binaries (LMXBs) depending on the mass of the companion. Emission from these systems are powered by accretion which is the most radiatively efficient mechanism known in the universe by the release of gravitational potential energy when matter from the companion star falls on the compact object. The mass transfer from the donor to the compact object can also take place via different mechanisms, namely by stellar wind accretion (common in HMXBs), Roche lobe overflow (prevalent in systems where accretion discs are formed mainly LMXBs) and mass loss from the equatorial discs in HMXBs with Be companions. Accretion onto high magnetic field neutron stars (*$B \sim 10^{12}$ *G) are special as the magnetic field plays a crucial role in governing the dynamics of gas flow and the flow of the matter*

close to the compact object. At the point where the magnetic pressure wins over the ram pressure of the infalling matter, matter is channeled along the magnetic field lines to the poles of the neutron star. The matter decelerates rapidly near the surface of the neutron star either by radiative shock or Coulomb interactions depending on the mass accretion rate. The accumulation of matter on the neutron star poles leads to the formation of accretion column which radiates in X-rays. This radiation is anisotropic and for a distant observer, the intensity is modulated at the spin period of the neutron star, hence the object are called accretion powered pulsars . The angular pattern of the emitted radiation is highly anisotropic and depends on the accretion rate and hence the luminosity.

The beaming pattern commonly known as the pulse profiles exhibit a wide variety in the pulse shape and pulse fraction and vary with energy as well as intensity. Although the pattern is mainly governed by the intrinsic beaming pattern, they are affected by strong gravitational effects like light bending, gravitational redshift etc. The energy spectra of these systems are a result of various physical processes involved in the interactions of the thermal X-rays produced from the mounds on the neutron star poles with the hot plasma in the accretion column. Most of the soft photons are Comptonized and upscattered by this processes forming a powerlaw form of spectra with an exponential decay in the range of 20–50 keV. Other processes which produce clear observable signature are fluorescence emission of different elements (mainly iron) and soft excess formed by reprocessing, and most importantly for this thesis, the formation of the Cyclotron Absorption Scattering Features (CRSF) by the interactions of the photons with the electrons quantized into Landau levels in strong magnetic fields. The CRSFs further provide a direct probe to the magnetic field and emission geometry in these systems.

The thesis is mainly dedicated to the study of the magnetic field and emission geometry of accretion powered pulsars through the pulse phase resolved studies of the cyclotron absorption features which are a direct probe to the magnetized plasma. In order to study these features in detail broadband continuum modeling of the energy spectrum is done, taking care of all other factors which may smear the pulse phase dependence. Another prerequisite for detailed continuum modeling is accounting for the low absorption dips in the pulse profiles of many these sources. The dips are presumable formed by phase locked accretion stream causing partial covering absorption when the stream is along our line of sight towards the emission region. Studying the pulse phase dependence of this partial covering absorber also provides us with important clues on the local environment

of the neutron star and the structure of the accretion stream. All of these studies are performed with data from the broadband and most sensitive instruments onboard the Japanese satellite Suzaku . Lastly we provide estimates of the polarization expected to be detected from these sources by a Thomson scattering polarimeter being developed to observe the polarization of X-rays in the energy range of 5–30 keV. Along with the X-ray pulsars, we also make an estimate of the likelihood of detection of X-ray polarization from black hole X-ray binaries in different spectral states. polarization being the holy grail in X-ray astronomy will provide the crucial clues to the magnetic and accretion geometry and break many degeneracies in future. Given below is the brief outline of the thesis.

- ***Chapter 1*** *gives a brief introduction of the X-ray sky, the binary systems and the different mechanisms of accretion onto the compact objects from the binary companion with a special emphasis on accretion onto highly magnetized compact objects (vis neutron stars). It then describes the instruments onboard the satellites whose data have been used in this thesis and techniques of X-ray timing and spectral measurement. Finally a brief description of the sources studied in detail in this thesis are provided.*

- *In* ***Chapter 2*** *the evolution of the pulse profiles with energy are presented for many accretion powered pulsars , and a systematic study is performed of the sources in two categories: which show complex energy dependent pulse profiles, and the ones which show variations in the relative strength of the different emission components with energy. Implications of these energy dependencies are discussed.*

- *In* ***Chapter 3****, the results of broadband spectroscopy of many bright accretion powered pulsars are presented and the results are compared with different broadband continuum and line models. Sources which show narrow low energy dips in their pulse profiles require an additional partial covering absorber in their energy spectra. The high energy broad absorption dips or the cyclotron features are accounted by Gaussian or Lorentzian profiles. The broadband spectral properties of different sources are summarized and certain observed trends in continuum modeling are discussed.*

- *In the next* ***Chapter 4****, the results of Chapter 3 are further utilized to perform a pulse phase resolved spectroscopy of many sources which exhibit complex energy*

dependent low energy dips as discussed in Chapter 2. The role of these results in constraining the structure of the accretion stream is also presented.

- *In* ***Chapter 5****, the results of Chapter 3 are further utilized to perform a pulse phase resolved spectroscopy of the Cyclotron parameters of many sources. The results obtained are discussed in the light of its role in constraining the magnetic field geometry and beaming pattern of the sources. In the next section of the chapter, the results of the energy dependence of the pulse profiles near their corresponding cyclotron energy is also presented and discussed.*

- ***Chapter 6*** *describes the Thomson X-ray polarimeter being developed to observe the polarization of X-rays in the energy range of 5–30 keV, and discusses its prospect of observing compact objects. This is a particularly interesting topic as it will play a crucial role in providing additional handles on the magnetic field geometry in accretion powered pulsars as well as constrain the fundamental parameters of a black hole in black hole binaries.*

- ***Chapter 7*** *summarizes the results and discusses the future prospects.*

Contents

1 Introduction **1**

1.1 Introduction . . . 1
1.2 The X-ray sky . . . 2
1.2.1 Origin of X-ray emission . . . 2
1.2.2 X-ray missions . . . 3
1.3 X-ray Binaries . . . 4
1.4 Accretion . . . 6
1.5 Accretion mechanisms . . . 9
1.5.1 Accretion mechanism of wind accretors . . . 9
1.5.2 Roche Lobe overflow . . . 11
1.5.3 Accretion from Be stars . . . 11
1.5.4 Formation of Accretion Disks . . . 12
1.5.5 Accretion onto Magnetized objects: Accreting X-ray pulsars and Polars . . . 15
1.6 Outline . . . 17
1.7 *Suzaku* & *RXTE* . . . 21
1.7.1 *Suzaku* : Satellite overview . . . 21
1.7.2 Hard X-ray Detector (HXD) . . . 23
1.7.3 Observation modes: . . . 24
1.7.4 *RXTE* :Satellite overview . . . 25
1.7.5 Proportional Counter Array (PCA) . . . 25
1.7.6 High Energy X-ray Timing Instrument (HEXTE) . . . 26
1.8 Analysis . . . 27
1.9 Sources . . . 28
1.9.1 1A 1118-61 . . . 28
1.9.2 Vela X-1 . . . 29
1.9.3 A0535+26 . . . 30
1.9.4 XTE J1946+274 . . . 31
1.9.5 4U 1907+09 . . . 31
1.9.6 GX 301-2 . . . 32
1.9.7 4U 1626-67 . . . 32

1.9.8 Cen X-3 . . . 33
1.9.9 Her X-1 . . . 33
1.9.10 EXO 2030+375 . . . 34
1.9.11 GX 1+4 . . . 35

2 Energy Dependence of the Pulse profiles in accretion powered pulsars 37
2.1 Complex nature of the pulse profile: Dips in the pulse profiles of accretion powered pulsars . . . 39
2.2 Observations . . . 40
2.3 Analysis & Results . . . 41
2.3.1 Timing Analysis . . . 41
2.4 Energy dependence pulse profiles showing dips at low energies: evolution of the dips . . . 42
2.4.1 1A 1118-61 . . . 43
2.4.2 VELA X-1 . . . 43
2.4.3 A0535+26 . . . 45
2.4.4 XTE J1946+274 . . . 46
2.4.5 4U 1626-67 . . . 49
2.4.6 EXO 2030+375 . . . 50
2.4.7 GX 1+4 . . . 52
2.5 Energy dependence of pulse profiles with no low energy dips . . . 52
2.5.1 GX 301-2 . . . 53
2.5.2 4U 1907+09 . . . 55
2.5.3 Discussion & Summary . . . 56

3 Broadband X-ray spectroscopy of accretion powered X-ray pulsars 57
3.1 Spectral formation in accretion powered pulsars: Its broadband nature . 57
3.2 Theoretical models of spectral formation: . . . 58
3.3 Phenomenological spectral models: The need for multicomponent modeling 59
3.4 Requirements for broadband spectroscopy . . . 63
3.5 Observations . . . 63
3.6 Reduction & Analysis . . . 64
3.7 1A 1118-61 . . . 65
3.7.1 Broadband Continuum modeling . . . 65
3.8 Vela X-1 . . . 68
3.8.1 Light curves & hardness ratio . . . 68
3.8.2 Intensity dependence of the pulse profiles . . . 69
3.8.3 Broadband Continuum modeling . . . 71
3.9 A0535+26 . . . 72
3.9.1 Broadband Continuum modeling . . . 73
3.10 XTE J1946+274 . . . 75
3.10.1 Broadband Continuum modeling . . . 76
3.11 4U 1907+09 . . . 79
3.11.1 Light curves and hardness ratio . . . 80

3.11.2 Broadband Continuum modeling . . . 80
3.12 GX 301-2 . . . 81
3.12.1 Broadband Continuum modeling . . . 83
3.13 4U 1626-67 . . . 85
3.13.1 Broadband Continuum modeling . . . 87
3.14 Cen X-3 . . . 88
3.14.1 Broadband Continuum modeling . . . 90
3.15 Her X-1 . . . 91
3.15.1 Broadband Continuum modeling . . . 92
3.16 EXO 2030+375 . . . 93
3.16.1 Broadband Continuum modeling . . . 94
3.17 GX 1+4 . . . 95
3.17.1 Broadband Continuum modeling . . . 96
3.18 Discussion & Summary . . . 96

4 phase resolved spectroscopy 104
4.1 Dips in pulse profiles . . . 104
4.2 Results . . . 104
4.2.1 1A 1118-61 . . . 105
4.2.2 VELA X-1 . . . 106
4.2.3 A0535+26 . . . 109
4.2.4 XTE J1946+274 . . . 111
4.2.5 EXO 2030+375 . . . 113
4.2.6 GX 1+4 . . . 118
4.3 Discussion & Summary . . . 118

5 Pulse phase resolved spectroscopy of CRSF 122
5.1 Formation of cyclotron resonance scattering feature . . . 122
5.2 Significant observational results of cyclotron resonance scattering feature 125
5.3 Pulse phase resolved spectroscopy of cyclotron resonance scattering feature and its importance . . . 128
5.4 Requirements for phase resolved spectroscopy . . . 128
5.5 Results . . . 129
5.5.1 1A 1118-61 . . . 130
5.5.2 VELA X-1 . . . 130
5.5.3 A0535+26 . . . 132
5.5.4 XTE J1946+274 . . . 134
5.5.5 4U 1907+09 . . . 136
5.5.6 GX 301-2 . . . 137
5.5.7 4U 1626-67 . . . 140
5.6 Model independent verification of the pulse phase dependence of CRSF . 140
5.7 Variation of the pulse profiles around the cyclotron line . . . 142
5.7.1 Timing Analysis . . . 145

5.7.2 Results: Energy Dependence of the high energy pulse profiles near the CRSF . . . 145
5.8 Discussion & Summary . . . 146
5.8.1 1A 1118-61 . . . 153
5.8.2 Vela X-1 . . . 153
5.8.3 A 0535+26 . . . 154
5.8.4 XTE J1946+274 . . . 154
5.8.5 4U 1907+09 . . . 155
5.8.6 GX 301-2 . . . 155
5.8.7 4U 1626-67 . . . 156

6 Thomson X-ray polarimeter, prospects for compact objects 158
6.1 Introduction . . . 158
6.2 . . . 160
6.2.1 Objective . . . 160
6.2.2 Design and polarization measurement technique . . . 161
6.3 Polarization from BHBs . . . 165
6.3.1 Analysis and Results . . . 166
6.3.2 GRO J1655-40 . . . 168
6.3.3 GX 339-4 . . . 171
6.3.4 CYGNUS X-1 . . . 173
6.3.5 H 1743-322 . . . 176
6.3.6 XTE J1817-330 . . . 176
6.3.7 Discussion & Conclusions . . . 181
6.4 polarization from BHBs . . . 182
6.4.1 Analysis and Results . . . 183
6.5 results . . . 184
6.5.1 Discussion & Conclusions . . . 184
6.6 polarization from pulsars . . . 185
6.6.1 Analysis & Results . . . 187
6.6.2 Discussion & Conclusions . . . 189
6.7 Angle of polarization . . . 190

7 Summary 193

List of Tables

1.1 Comparison of HMXBs and LMXBs 6
1.2 Accretion efficiency 8
1.3 Summary of observation modes in *Suzaku* XIS 24

2.1 Table of accretion powered pulsars showing dips in their profile. 40
2.2 Observation details 41
2.3 Determined pulse periods 42

3.1 Observation details 64
3.2 Best fitting phase averaged spectral parameters of 1A 1118-61. Errors quoted are for 99 per cent confidence range. 67
3.3 Best fitting spectral parameters of Vela X-1 with a partial covering high-energy cutoff model. Errors quoted are for 99 per cent confidence range. . 73
3.4 Best fitting phase averaged spectral parameters of A 0535+26. Errors quoted are for 99 per cent confidence range. 75
3.5 Best fitting phase averaged spectral parameters of XTE J1946+274. Errors quoted are for 99 per cent confidence range. 79
3.6 Best fitting phase averaged spectral parameters of 4U 1907+09. Errors quoted are for 99 per cent confidence range. 82
3.7 Best fitting phase averaged spectral parameters of GX 301-2. Errors quoted are for 99 per cent confidence range. 86
3.8 Best fitting phase averaged spectral parameters of 4U 1626-67. Errors quoted are for 99 per cent confidence range. 89
3.9 Best fitting phase averaged spectral parameters of Cen X-3. Errors quoted are for 99 per cent confidence range. 99
3.10 Best fitting phase averaged spectral parameters of Her X-1. Errors quoted are for 99 per cent confidence range. 100
3.11 Best fitting phase averaged spectral parameters of EXO 2030+375. Errors quoted are for 99 per cent confidence range. 101
3.12 Best fitting phase averaged spectral parameters of GX 1+4. Errors quoted are for 99 per cent confidence range. 102

3.13 Summary of broadband spectroscopy of accretion powered pulsars 103

5.1 cyclotron resonance scattering feature Table 127
5.2 Determined pulse periods 145

6.1 Instrument specifications of the Thomson X-ray Polarimeter 161
6.2 Energy dependent efficiency for Li & Be scatterer 167
6.3 Net Minimum detectable polarization calculated for all the sources during the specified **thermal emission dominated** stretches. The values are given in percentages 179
6.4 Energy dependent efficiency for Li & Be scatterer 184
6.5 Net Minimum detectable polarization calculated for 5 σ detection of the sources in a single day (integration time T = 43 200 secs). The values are given in percentages. 185
6.6 Energy dependent efficiency for Li & Be scatterer 188
6.7 Exposure times per phase bin required at 9 keV. Time in secs 189
6.8 Exposure times required at 18 keV. Time in secs 189

List of Figures

1.1 X-ray binary zoo 4
1.2 X-ray binary zoo 7
1.3 Roche lobe 13
1.4 Accretion in supergiant and Be X-ray binary 14
1.5 Accretion powered pulsars 18
1.6 *Suzaku* satellite 22
1.7 *RXTE* satellite 26

2.1 Energy dependent pulse profiles of 1A 1118-61 near the CRSF band . . . 44
2.2 Energy dependent pulse profiles of Vela X-1 45
2.3 Energy dependent pulse profiles of A 0535+26 47
2.4 Energy dependent pulse profiles of XTE J1946+274 48
2.5 Energy dependent pulse profiles of 4U 1626-67 49
2.6 Energy dependent pulse profiles of EXO 2030+375 51
2.7 Energy dependent pulse profiles of GX 1+4 53
2.8 Energy dependent pulse profiles of GX 301-2 54
2.9 Energy dependent pulse profiles of 4U 1907+09 55

3.1 Spectrum of 1A 1118-61 with *Suzaku* observation 68
3.2 Spectrum of Vela X-1 with *Suzaku* observation 69
3.3 Intensity dependent pulse profiles of Vela X-1 70
3.4 Spectrum of Vela X-1 with *Suzaku* observation 72
3.5 Spectrum of A 0535+26 with *Suzaku* observation 74
3.6 Spectrum of XTE J1946+274 with *Suzaku* observation 77
3.7 Ratio of counts in different phases to show the detection of the CRSF in XTE J1946+274 78
3.8 light curves and hardness ratio of 4U 1907+09 83
3.9 Spectrum of 4U 1907+09 with *Suzaku* observation 83
3.10 Same as Figure 3.9 for Obs. 2 of 4U 1907+09 84
3.11 Light curve of GX 301-2 folded with the orbital period. 84
3.12 Spectrum of GX 301-2 with *Suzaku* observation 87

3.13 Spectrum of 4U 1626-67 with *Suzaku* observation 88
3.14 Light curve and hardness ratio of Cen X-3 for the entire observation duration. 90
3.15 Spectrum of Cen X-3 with *Suzaku* observation 91
3.16 Spectrum of Her X-1 with *Suzaku* observation 93
3.17 Spectrum of EXO 2030+375 with *Suzaku* observation 95
3.18 Spectrum of GX 1+4 with *Suzaku* observation 97

4.1 Comparison of low and high energy pulse profiles in 1A 1118-61 107
4.2 phase resolved spectroscopy of the continuum parameters of 1A 1118-61 . 108
4.3 Same as in Figure 4.1 for Vela X-1 110
4.4 Same as in Figure 4.2 for Vela X-1 111
4.5 Same as in Figure 4.1 for A 0535+26 112
4.6 Same as in Figure 4.2 for A 0535+26 113
4.7 Same as in Figure 4.1 for XTE J1946+274 114
4.8 Same as in Figure 4.2 for A 0535+26 115
4.9 Same as in Figure 4.1 for EXO 2030+375 116
4.10 Same as in Figure 4.2 for EXO 2030+375 117
4.11 Same as in Figure 4.1 for XTE J1946+274 119
4.12 Same as in Figure 4.2 for GX 1+4 120

5.1 Cross sections for Compton scattering in presence of strong magnetic fields 124
5.2 First detection of CRSF 125
5.3 CRSF variation with pulse phase in 1A 1118-61 131
5.4 Same as in Figure 5.3 in Vela X-1 133
5.5 Variation of the ratio of the two cyclotron lines E2/E1 for Vela X-1 . . . 134
5.6 Same as in Figure 5.3 in A 0535+26 135
5.7 Same as in Figure 5.3 in XTE J1946+274 136
5.8 Same as in Figure 5.3 for the two observation in 4U 1907+09 138
5.9 Same as in Figure 5.3 in GX 301-2 139
5.10 Same as in Figure 5.3 in 4U 1626-67 141
5.11 Plots for ratio of the PIN spectra for sources at phases corresponding to the lowest CRSF energy to the highest CRSF energy. 143
5.12 Same as in Figure 5.11 at phases corresponding to the deepest to the shallowest CRSF (widest to narrowest for GX 301-2). 144
5.13 Pulse profile of 1A 1118-61 near the CRSF band 147
5.14 Pulse profile of GX 301-2 near the CRSF band 147
5.15 Pulse profile of Her X-1 near the CRSF band 148
5.16 Pulse profile of A 0535+26 near the CRSF band 148
5.17 Pulse profile of XTE J1946+274 near the CRSF band 149
5.18 Pulse profile of Cen X-3 near the CRSF band 149
5.19 Pulse profile of 4U 1626-67 near the CRSF band 150
5.20 Pulse profile of 4U 1907+09 near the CRSF band 150
5.21 Pulse profile of Vela X-1 near the CRSF band 151
5.22 Pulse profile of GX 304-1 near the CRSF band 151

6.1 Intensity distribution of polarized photons 162
6.2 X ray polarimeter configuration 163
6.3 One day averaged long term ASM light curve of GRO J1655 − 40 showing the 2005 outburst of GRO J1655 − 40. 169
6.4 spectrum of GRO J1655-40 170
6.5 Figures showing the blackbody and powerlaw fluxes in different energy bands and the corresponding MDP for GRO J1655-40 171
6.6 Same as Figure 6.5 for the second stretch of its outburst of GRO J1655-40 in the year 2005 172
6.7 One day averaged long term ASM light curve of GX 339 − 4 showing the 2002 outburst of GX 339 − 4. 173
6.8 Same as Figure 6.5, for the source GX339-4 for the outburst in the year 2002 174
6.9 One day averaged long term ASM light curve of Cygnus X-1 showing the 1996 soft state transition of Cygnus X-1 175
6.10 Figure showing the fluxes and MDP in different energy bands for Cygnus X-1 177
6.11 One day averaged long term ASM light curve of H 1743 − 322 showing the 2003 outburst of H 1743 − 322 178
6.12 Same as Figure 6.5 for the source H1743-322 for the outburst in the year 2003 178
6.13 One day averaged long term ASM light curve of XTE J1817 − 330 showing the 2006 outburst of XTE J1817 − 330 179
6.14 Same as Figure 6.5 for the source XTE J1817-330 for the outburst in the year 2006 180
6.15 Intensity distribution of polarized photons 183
6.16 Meszaros et al 1988 Figure 191
6.17 The 1σ deviation in position angle versus the number of sigma statistical detection 192

Keywords

X-ray binaries, accretion powered pulsars, black hole binaries, spectroscopy, Cyclotron lines, polarization

Chapter 1

Introduction

"Man must rise above the Earth to the top of the atmosphere and beyond – for only thus will he fully understand the world in which he lives."

..... **Socrates**

1.1 Introduction

Astronomical records can be traced back to early work of the Babylonians ($\sim$ 1600 B.C.) of recording the positions of planets, and determining the times of eclipses as well as in the memoirs of ancient Chinese and North Europeans cultures. Although it was at first introduced for more practical purposes like navigation and prediction of seasons, the seed of curiosity which was sown in human minds soon lead mankind to the world of new and exciting discoveries of the cosmos. The first calalog of stars and the stellar constellations was constructed by Hipparchus in 100 B.C. while the first solar system model was proposed by Heraclides in 330 B.C. For the next centuries a number of significant discoveries shaped the study of astronomy and astrophysics as we know today. Out of them, few significant were the observation of the first Supernova explosion (Crab) by the Chinese in 1024, the observation of the Cassieopia Supernova by Tycho Brahe in 1572 and to name a few discoveries of the last century, the discovery of the expansion of the universe by Edwin Hubble in 1929, the Cosmic Microwave Background Radiation (CMBR) in 1965 by Arno Penzias and Robert Wilson, the pulsars in 1967 by Jocelyn Bell and Antony Hewish would top the many others in the illustrious list. Astronomical data of increased statistical quality and with higher temporal, spatial and

spectral resolution have been obtained over the last few decades from a huge variety of astrophysical objects and over different parts of the electromagnetic waveband. The radio waveband has opened our senses to the most distant cosmological signals, the infrared waveband has revealed the cool and dusty universe, while the ultraviolet, X-ray and Gamma rays have revealed the hot, energetic and violent universe to us. Moreover observing the same object over different wavelengths have unfolded many unknown and unexpected facets of it. This thesis deals with the study of the Galactic astrophysical objects visible mainly at the X-ray wavelengths, and the next few sections are therefore dedicated to a more detailed description of the X-ray sky and the objects and phenomena it reveals to us.

1.2 The X-ray sky

1.2.1 Origin of X-ray emission

As the X-rays are absorbed by the earth's atmosphere, the X-ray sky revealed itself only with the advent of technologies equipped to cross over the high altitudes and outer space in the form of balloons, sounding rockets and satellite missions. The first instruments sent to space to detect X-ray radiation were simple detectors carried aloft rockets. They detected X-ray emission from the Sun in 1949. X-rays are expected from astronomical objects that contain extremely hot gases at temperatures of $\sim 10^7$ K to 10^8 K. The sun being relatively cooler (5800 K) is not very bright in X-rays and is a million times less than its emission at the visible waveband. Following this, not much X-ray emission was expected from similar stars and the early space missions were mainly devoted to detect gamma rays from nuclear weapons tests. It was only after the serendipitous discovery in 1962 of the first extra solar X-ray source, Sco X-1 was X-ray astronomy born. Sco X-1 was a point like source in the constellation Scorpius. An estimate of its distance revealed that its X-ray luminosity was about ten thousand times the total luminosity of the Sun at all wavelengths. Moreover the optical counterpart of Sco X-1 was found to be only a 13th magnitude star, insignificant compared to the bright X-ray object. This startling revelation indicated that the emission was a result of phenomena energetic enough to be visible only in the X-ray wavelengths. Today it is known that matter can be excited to such high temperatures only by the gigantic cosmic explosions, or in the presence of intense gravitational or magnetic fields, and such conditions are observed from the

vast spaces between the galaxies to the collapsed environment around compact objects. Many thousands of X-ray sources are known which includes the X-ray binaries, Active Galactic Nuclei (AGNs), cataclysmic variables, extended objects, protostellar objects and even weak emission from the planets including our earth. In addition, it has also been discovered that the space between galaxies in galaxy clusters are filled with a very hot and optically thin gas at a temperature of about $\sim 10^8$ K. The total mass of this gas is five to ten times the total mass in the visible galaxies.
The same mission which discovered Sco X-1 also discovered the X-ray background, a hard X-ray sky-glow which peaks at the galactic poles. This comes from the "Local Bubble" which surrounds the Solar System. Recent deep surveys have revealed that the X-ray background stems from mostly resolved extragalactic X-ray sources, bulk of which are AGNs (Active Galactic Nuclei).

1.2.2 Past X-ray missions and all sky surveys

In 1972 the first orbiting X-ray astronomy mission *Uhuru* was launched, dedicated entirely to celestial X-ray astronomy, a feat credited to Dr Richard Giacconi for which he won the Noble prize in Physics in 2002. *Uhuru*, discovered $\sim$ 400 X-ray sources of various types, and among them was a peculiar X-ray variation of Cen X-3. Apart from measuring a periodic intensity variation at 4.8 s, it also revealed the binary nature of the system from the periodic Doppler shift of the pulse frequency. After *Uhuru* followed the *Einstein* observatory (HEAO 2) which was the first fully imaging X-ray telescope sent to space. It was a key mission and its scientific outcome completely changed our views of the X-ray sky. The *EXOSAT* launched in 1983 carried onboard an X-ray telescope, a medium energy proportional counter, and a gas scintillation proportional counter, enabling observations in the range 0.05–50 keV. During its lifetime of three years, it made observations on a wide variety of objects like X-ray binaries and clusters of galaxies. Another important mission launched in 1987 was the Japanese satellite *Ginga* which was equipped with the Large Area Proportional Counter (LAC) operational from 1.5–37 keV. The *Ginga* too made numerous observations of all classes of X-ray sources then known. The next mission worth mentioning was the *ROSAT*, launched in 1990, as it obtained the first X-ray and XUV all sky survey. The ROSAT All Sky Survey (RASS) was carried out over 6 months between 1990 and 1991. It detected more than 60,000 X-ray sources

over the whole sky. The image shown in Figure 1.1 shows the counts detected in the ROSAT survey at 0.25 keV. The map is in Galactic coordinates. Apart from this, during its lifetime it made deep observations of a wide variety of objects.

The *ASCA* (The Advanced Satellite for Cosmology and Astrophysics) launched in 1993 was the first X-ray mission to use CCD detectors and it too revolutionized our view of the sky, mainly through X-ray spectroscopy. *RXTE* launched in 1995, was dedicated to study the variability in the X-ray emissions. *BeppoSAX* launched in 1996 was the first X-ray mission with a set of scientific payloads covering more than three decades of energy (0.1–300 keV). Several present day X-ray missions like the *Chandra* X-ray observatory (CXO), *XMM-Newton*, *Suzaku*, *Integral* , *Swift* and more recently *NuStar* are still presenting us with many surprises and new exciting results everyday.

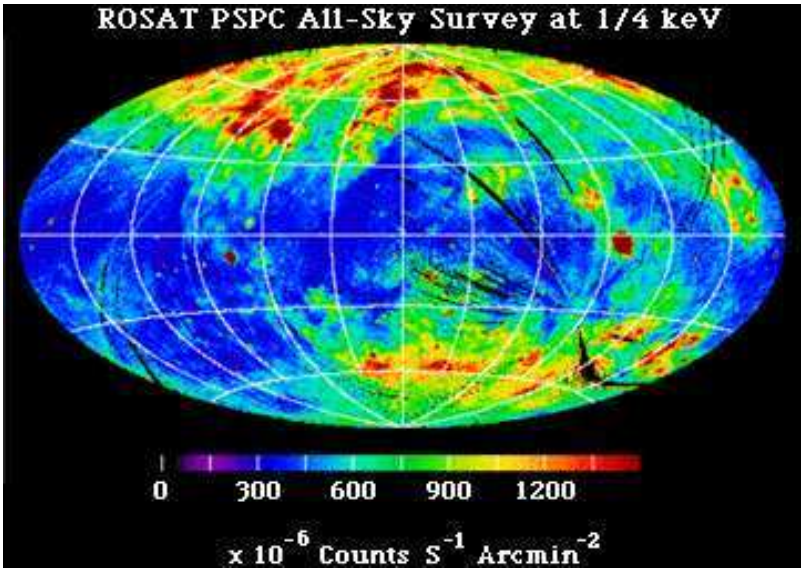

Figure 1.1: Figure showing the *ROSAT* All Sky Survey. Figure courtesy:NASA/GSFC

1.3 X-ray Binaries

As the name suggests, X-ray binaries are gravitationally bound systems consisting of two stars which rotate around a common centre of mass and shine brightly in the X-ray regime ($L_x \simeq 10^{33} - 10^{38}\, erg\, s^{-1}$). One of them is a compact object namely a black hole or a neutron star, and the other is a normal star or a white dwarf. They are powered by the accretion of matter from the companion to the compact object in a close binary

orbit.

X-ray binaries are conventionally classified as Low Mass X-ray Binaries (LMXBs) and High Mass X-ray Binaries (HMXBs) depending on the mass of the donor star. Although this does not allow a distinction between the nature of the compact objects (which may either be a neutron star or a black hole in both cases), it does allow to a large degree, a phenomenological classification of the properties of the two classes of sources and pinpoint the nature of their optical counterpart. The formation and properties of the above two classes of sources are summarized below:

HMXB: One third of the ~ 300 X-ray binaries known are HMXBs, which contain an early type (O-B) companion with its mass, $M > 5M\odot$. The compact object is mostly a neutron star although a few of them are also known to host black holes. They are young stars (population I) and are distributed on the Galactic disk.

HMXBs are formed out of a system of two stars having different masses, when the more massive star evolves faster and reaches the end of its life first, after a few million years or so. It becomes a giant and the outer layers are lost, partly to its companion. Then it explodes in a supernova leaving behind either a neutron star or a black hole. This can disrupt the binary system, but if the star that exploded was less massive than its companion when it exploded then the systems will remain intact, although the orbits may become more eccentric.

LMXB: These X-ray binaries typically contain a late type (K, M) low mass donor star (or, in the case of very short orbital period binaries, a white dwarf). About ten LMXBs are close to the core of globular clusters and many of the others are concentrated in the vicinity of the Galactic bulge, therefore indicating a distribution characteristic of old stars (population II).

Their origin is not very clear. The most likely explanation is that they form by capture mechanism. The lone compact object, the remnant of a massive star, has a close interaction in a cluster and picks up a companion thus forming LMXB systems. Figure 1.2 shows a pictorial representation of the different types of X-ray binaries found till date and Table 1.3 lists the main properties of these classes of sources.

Table 1.1: Comparison of HMXBs and LMXBs

Properties	HMXBs	LMXBs
Donor star	O–B ($M > 5M_{\odot}$)	K–M or WD($M < 1M_{\odot}$)
Optical spectrum	Stellar like	disk dominated
Compact object	NS (only a few BHs)	BHs & NSs
Population	I (10^7 yr)	II ($5 - 1510^9$ yr)
$\frac{L_x}{L_{opt}}$	0.001–10	100-1000
Rapid variability	Less	More
Orbital period	1–100 d	10 mins–10 d
X-ray eclipses	Common	Rare
X-ray spectra	Hard ($KT > 15$ keV)	Soft ($KT < 10$ keV)
Magnetic field (for NS)	$\sim 10^{12}$ G	$10^7 - 10^9$ G
X-ray pulsations (for NS)	Common	Rare
Type I bursts (for NS)	Absent	Common

1.4 Accretion: One of the most powerful sources of energy generation

The most energetic sources known in the astronomical zoo are powered by the process of accretion, the infall of matter to the compact objects (white dwarfs, neutron stars, black holes or supermassive black holes) by the influence of their strong gravitational field. This is the mechanism by which the X-ray binaries are powered. That the process of accretion is the most efficient one to liberate energy can be seen from the simple calculation given below.

If a particle falls to a compact object with mass M and radius R from an infinite distance, the velocity at 'r' equals its free fall velocity given by

$$veff_r = \sqrt{\frac{2GM}{R}}$$

where $veff_r$ is the free fall velocity of the object. Assuming that all the kinetic energy liberated is converted to energy at the surface of the star, the total liberated gravitational

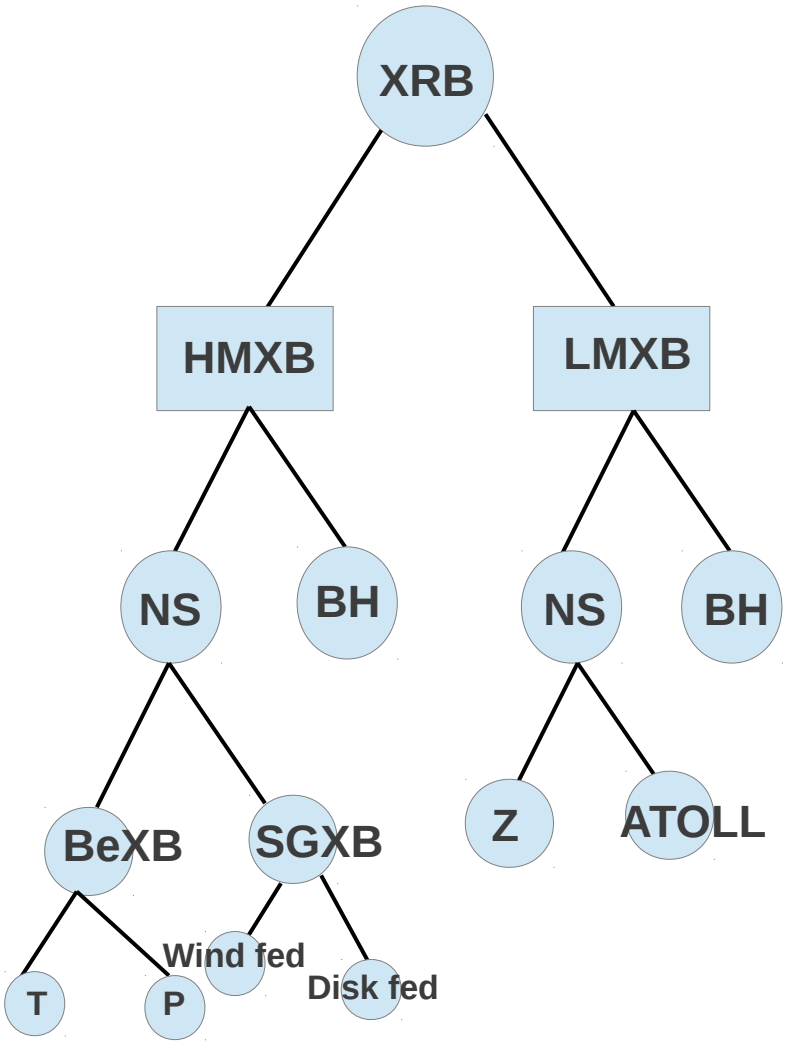

Figure 1.2: X-ray binary zoo: The following abbreviations are used. XRB: X-ray binary; NS: neutron star; BH: black hole; BeXB: Be X-ray binary; SGXB: supergiant X-ray binary;T: transient; P: persistent.

potential energy, hence the luminosity can be given by

$$L_{acc} = \frac{1}{2}\dot{M}veff^2_{(R)} = \frac{GM\dot{M}}{R}$$

$$L_{acc} = \frac{1}{2}\dot{M}veff^2_{(R)} = \frac{GM\dot{M}}{R}$$

where L_{acc} is the liberated accreted energy and $\dot{M}$ is the accreted mass. The corresponding accreted efficiency η_{acc} is

$$\eta_{acc} = \frac{L_{acc}}{\dot{M}c^2} = \frac{GM}{Rc^2} \simeq \frac{R_s}{2R}$$

where R_s is the Schwarzchild radius $= \frac{2GM}{c^2}$. Assuming appropriate values of M, R and R_s for white dwarfs, neutron stars and black holes the typical accreting efficiency of accreting objects are given in Table 1.4 as follows: From the above table it can be seen

Table 1.2: Accretion Efficiency for different Compact Objects

Object	M	R	η_{acc}
–	$M\odot$	cm	$\frac{R_s}{2R}$
White Dwarf	≤ 1.4	10^9	1.5×10^{-4}
Neutron Stars	~ 1.4	10^6	~ 0.15
Black holes	> 3	$3 \times 10^{-5}\frac{M}{M\odot}$	0.1–0.4

that the accretion efficiency can be upto even 40% under some conditions for black holes. The efficiency of nuclear burning inside a star by (P–P) chain is however only 0.7%. The liberated accreted energy L_{acc} can also be expressed in terms of its Eddington luminosity L_{edd}. Assuming spherical symmetry, fully ionized accreted matter consisting of only hydrogen, and a steady accretion, this represents the maximum accretion luminosity that can be reached above which a star of given mass M starts blowing away its outer layers by radiation pressure. Thus L_{edd} can be derived by equating the gravitational force exerted by a star to the radiation force by fully ionized hydrogen plasma, and is given by

$$\frac{GMm_p}{r^2} = \frac{L_{edd}\sigma_T}{4\pi r^2 c} \Rightarrow L_{edd} = \frac{4\pi GMm_p c}{\sigma_T} \simeq 1.3 \times 10^{38}(\frac{M}{M\odot})ergs^{-1}$$

where r is the distance to the stellar center, m_p is the proton mass, and σ_T is the Thomson scattering cross section ($\sigma_T = 6.6 \times 10^{-25}\, cm^{-2}$).

This standard model of X-ray sources consisting of accreting neutron stars or black

holes were first suggested by Salpeter (1964); Zel'dovich & Novikov (1964); Zeldovich & Guseynov (1966). The first suggestion that X-ray binaries were powered by accretion onto a compact object was made by Shklovsky in 1967. As also mentioned in the section on formation of HMXBs and LMXBs, mass transfer from the donor to the compact object takes place by different mechanisms as follows:

- **Stellar wind accretion** where as much as $10^{-5} M_{\odot} yr^{-1}$ of the stellar mass of the companion may be ejected and a fraction of the wind be captured gravitationally by the compact object. This mass transfer mechanism is applicable to the HMXBs with Supergiant companions.

- **Mass loss from the equatorial disk (deccretion disk)** where an eruptive mass loss occurs from the equatorial region of the rapidly spinning B-emission stars (Be). The compact object, often in a highly eccentric (e $\geq$ 0.3) orbit accretes from this outflowing disk during its periastron passage. This is the mechanism of mass transfer for HMXBs with Be companions.

- **Roche Lobe Overflow** where one of the stars in the binary system may increase in radius, or the binary separation may shrink to the point where the gravitational pull of the companion can gradually remove material from the companion star to the compact star. This mass transfer mechanism is applicable to systems where accretion disk are formed specially in LMXBs and in a few HMXBs.

1.5 Accretion mechanisms

This section describes the different accretion mechanisms and accreting systems.

1.5.1 Accretion mechanism of wind accretors

The majority of wind accretors are usually accretion powered X-ray pulsars (neutron stars) which have companions of early spectral type (O–B). They are very luminous in nature and hence most of the first sources to be discovered like Cen X-3, SMC X-1 and Vela X-1 fall in this category. Mass loss from these early type companions are very high upto $\sim 10^{-6} - 10^{-5}\, M_{\odot}\, yr^{-1}$ and are in the form of intense, supersonic stellar winds. This wind velocity greatly exceeds the sound velocity (v_{sound}) the local medium given by $v_{sound} \sim 10(\frac{T}{10^4 K})\, km\, s^{-1}$. The accreting gas as a result is not in the form of hydrostatic

equilibrium. A compact object (usually a neutron star) with mass M_x and moving with relative velocity v_{rel} through a medium with sound speed c_s will gravitationally capture matter along a roughly cylindrical region with its axis along the relative wind direction (Davidson & Ostriker, 1973; Lamb et al., 1973). The radius r_{acc} of the cylinder also called the accretion radius or gravitational capture radius is given by

$$r_{acc} = \frac{2GM_x}{v_{rel}^2 + c_s^2} \, where \; v_{rel}^2 = v_{orb}^2 + v_{wind}^2$$

v_{orb} being the orbital velocity of the compact object, and $v_s \ll v_{rel}$ in most cases the former term can be neglected. Assuming spherical symmetry and a steady state accretion, the amount of mass accreted by the compact object can be calculated by combining the above relationship with Kepler's third law and the Continuity equation. Assuming a to be the orbital separation and ρ to be the wind density near r_{acc} one obtains

$$v_{orb}^2 = \frac{G(M_x + M_p)}{a}$$

$$\dot{M}_p = 4\pi a^2 \rho v_{rel}$$

where M_p is the mass of the companion.

$$\frac{r_{acc}}{a} = \frac{2}{1 + (\frac{M_p}{M_x})} \frac{1}{1 + (\frac{v_{wind}}{v_{orb}})^2} \; \ll 1$$

Thus the mass $\dot{M}$ accreted on the compact object is

$$\dot{M} = 4\pi r_{acc}^2 \rho v_{rel}$$

Substituting the values of r_{acc}, v_{rel} and ρ we obtain the expression for mass accreted ($\dot{M}$) on the compact object given by

$$\dot{M} = \frac{(GM_x)^2}{a^2 (v_{orb}^2 + v_{wind}^2)^2} \dot{M}_p$$

Thus

$$\frac{\dot{M}}{\dot{M}_p} = \frac{1}{1 + (\frac{M_p}{M_x})^2} (\frac{v_{orb}}{v_{wind}})^4 \frac{1}{(1 + (\frac{v_{orb}}{v_{wind}})^2)^{\frac{3}{2}}} \simeq 10^{-5} - 10^{-4}$$

Therefore assuming a mass loss rate of $\sim 10^{-6} - 10^{-5}\, M_{\odot}\, yr^{-1}$ from the companion star as stated above, the accretion luminosity lies within the range of $10^{35} - 10^{37}\, ergs\, s^{-1}$ as observed in wind accreting binary systems.

1.5.2 Roche Lobe overflow

This is the dominant mechanism of accretion for LMXBs or late type stars where the stellar wind is not very intense in nature. Considering two stars of masses M_x and M_p, in the Roche Lobe approximation, they are assumed to be point masses revolving around their centre of mass in a circular orbit. For this system it is possible to derive its net potential and map its corresponding equipotential surfaces as shown in Figure 1.3. In a frame corotating with the binary revolution, the net potential (ϕ) can be written as:

$$\phi = -\frac{GM_x}{r_x} - \frac{GM_p}{r_p} - \frac{\Omega^2 r_3^2}{2}$$

where r_x and r_p are the distances to the centres of the stars with masses M_x and M_p respectively, Ω is the orbital velocity and r_3 is the distance from the axis of rotation of the binary (Frank et al., 2002). Close to each object, the potential is dominated by the gravitational potential of the star making the surfaces almost spherical. As one moves farther from a stellar centre, two effects start to became important: (a) the tidal effect, which causes an elongation in the direction of the companion and (b) flattening due to the centrifugal force. Consequently the surfaces are distorted in a way that their largest dimension is along the line of centers. Most relevant to the mass transfer mechanism is the the critical surface with a figure-of-eight cross section which passes through the inner Lagrangian point L1. The two cusped volumes which are enclosed by this critical surface are called the Roche lobes of the respective stars. Mass transfer through L1 can either be triggered by the expansion of the star to fill its Roche Lobe during its evolution or the decrease in the size of the Roche Lobe due to the loss of angular momentum from the system.

1.5.3 Accretion from Be stars

These represent a large fraction of the HMXBs. In these binary systems, the companion is a rapidly rotating B-star, so-called B-emission stars. Such B-type stars show, at irregular time intervals, outbursts of equatorial mass ejection which produce a rotating

ring of gas around the star, giving rise to hydrogen emission lines in the optical spectrum. The star can appear as a normal main-sequence B-star for many years and suddenly go through a B-emission phase, becoming a Be star for periods ranging from a few weeks to many years (Slettebak & Snow 1987), while others are Be-stars almost permanently. The binary optical companion lies well within the Roche lobe. The objects in these binary systems are typically in a wide orbit with moderate eccentricity. The abrupt accretion of matter onto the neutron star while passing through the circumstellar disk of the Be companion or during the periastron passage results in strong X-ray outbursts (Okazaki & Negueruela, 2001). The ejected matter from the equatorial disk is captured at a distance r_{acc} from the neutron star as in the case of wind fed HMXBs and the same description can be assumed to the first approximation. During such outbursts, the X-ray emission can be transiently enhanced by a large factor. Be/X-ray binary systems generally show periodic normal (type I) X-ray outbursts that coincide with the periastron passage of the neutron star, and giant (type II) X-ray outbursts which do not show any clear orbital dependence. It also shows a persistent low luminosity X-ray emission during quiescence (Negueruela et al., 1998). Most Be/X-ray binary systems are known to host accretion powered X-ray pulsars except a very few cases such as LS I+61303 (Massi et al., 2004). Figure 1.4 show cartoons of accretion onto supergiant HMXBs and Be X-ray binaries.

1.5.4 Formation of Accretion Disks

If the matter falling on the compact object has sufficient specific angular momentum J, it will form a rotationally flattened disk around the compact object referred as the accretion disk. Thus the accreting matter forms a disk when its J is too large to hit the compact object directly. The radius where matter orbits by loosing its energy but not the angular momentum is its circularization radius. The formation of disk requires the condition that the circularization radius (R_{circ}) is greater than the size of the accretor.

$$R_{circ} = \frac{J^2}{GM_x}$$

R_{circ} gives the radius at which the disk begins to form and the size of the accretion disks in different kinds of accretors.

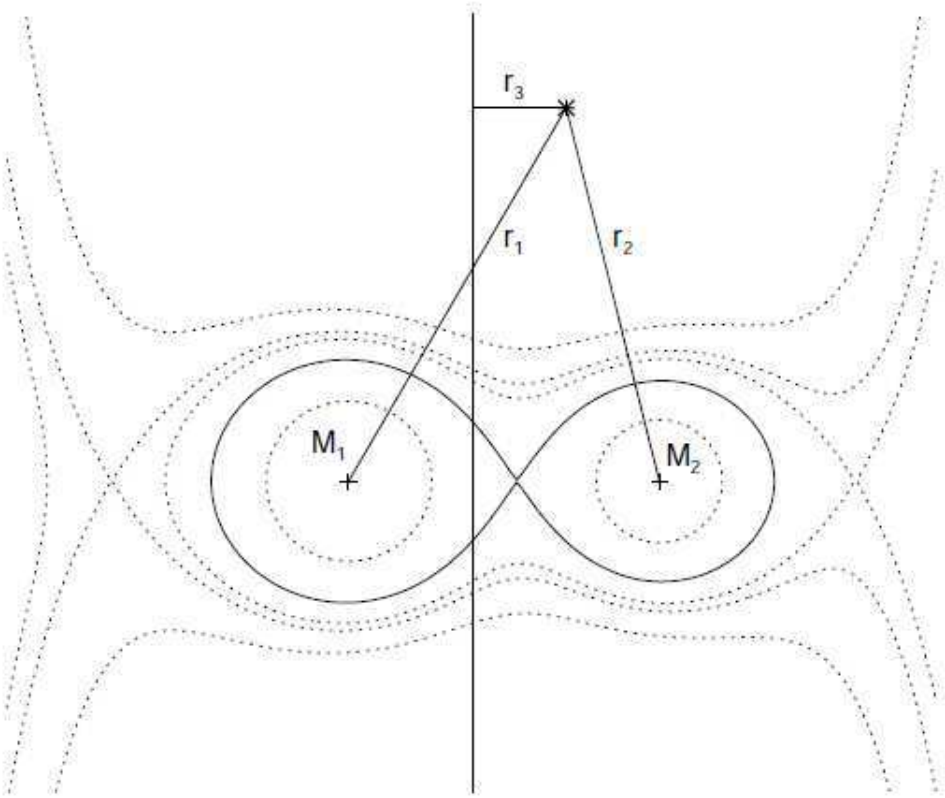

Figure 1.3: Equipotential lines of the Roche potential. Image taken from Dmitry Klochkov PhD thesis.

Stellar wind accretion The specific angular momentum J is given by

$$J = \frac{1}{2}\Omega_{orb} r_{acc}^2$$

where Ω_{orb} is the orbital angular momentum. R_{circ} can be derived to be

$$R_{circ}^{wind} = \frac{r_{acc}^4}{8}\frac{\Omega_{orb}^2}{GM_x} \simeq 1.3 \times 10^6 (\frac{M_p}{M_\odot})^{\frac{1}{3}} (\frac{P_{orb}}{10d})^{\frac{2}{3}} \ cm$$

For $M_p = 10M_\odot$ this is greater than the size of the accretors in case of neutron star or white dwarf binaries (10^6 and 10^9 cm respectively.) So in case of wind accretors, accretion disks may form but are small in size.

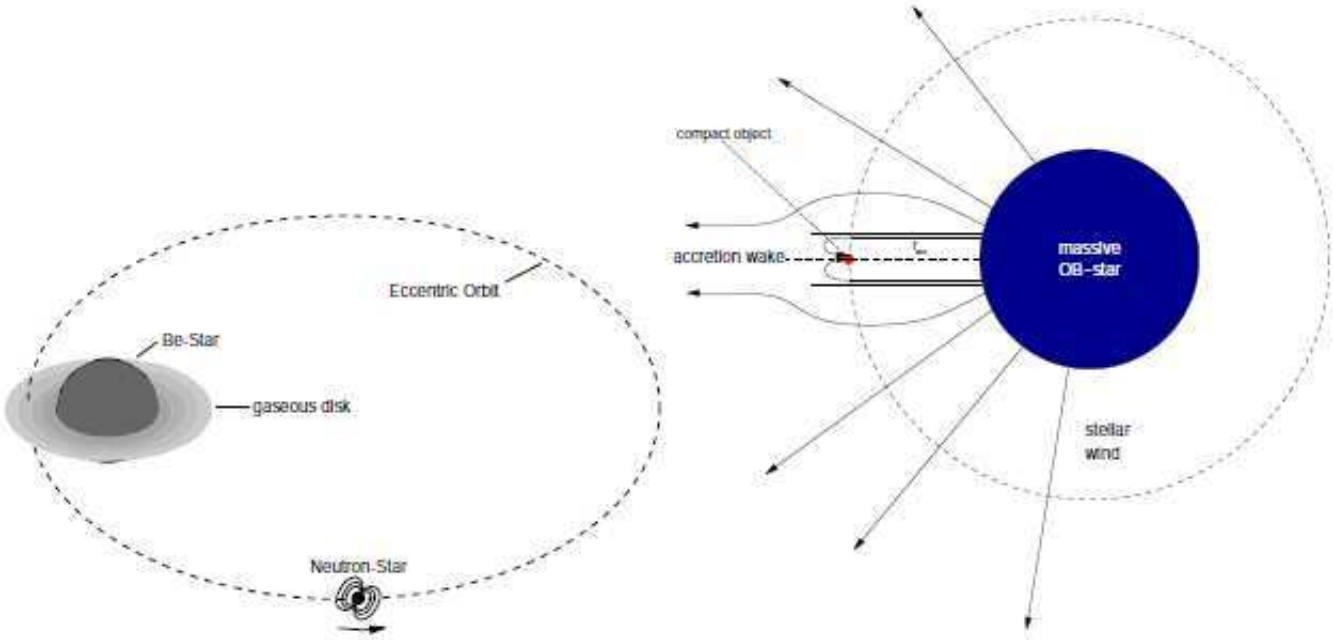

Figure 1.4: Accretion from supergiant X-ray binaries and Be X-ray binaries. Image credit Kretschmar 2004 and Kreykenbohm 2004.

Accretion by Roche Lobe overflow Similarly,

$$J \simeq \Omega_{orb}(a - r_L)^2$$

where r_L is the Roche Lobe radius assuming all matter leaves the companion through the critical point Lagrangian point L1.

$$R_{circ}^{roche} \simeq r_L^4 \frac{\Omega_{orb}^2}{GM_x} \simeq 3.5 \times 10^9 (\frac{M_p}{M_\odot})^{\frac{1}{3}} (\frac{P_{orb}}{1hr})^{\frac{2}{3}} \ cm$$

As it can be clearly seen, in case of accretion via Roche Lobe Overflow, $R_{circ} \gg$ the size of the accretors for both neutron stars and white dwarfs. Therefore accretion disks are always formed in these cases. An accretion disk which spreads out enough within the Roche lobe of the compact object will also be subject to tidal torques from the secondary star. This effect limits the size of the disk. Tidal torques can take angular momentum from matter at the outer disk edge, and return it to the binary orbit. A steady state is reached when the tidal torques remove the angular momentum at the

rate it is transported outwards in the disk by viscosity.
Although the outer radius and the size of the accretion disk is fixed by the nature of the accretion, the inner radius of the accretion disk is fixed by the nature of the compact object residing in the binary system. In case of neutron star LMXBs it can reach upto the surface of the star, where as in neutron star HMXBs it can only reach upto the corresponding Alfven radius (r_A) of the system. The mechanism of accretion in these type of sources is discussed in detail in the next section. In case of black hole accretors, the inner radius can only extend upto the ISCO (Innermost Stable Circular Orbit).
Matter in the accretion disk looses its angular momentum through viscosity thereby allowing it to slowly fall towards the compact object and be accreted. In many cases the accretion disk may be described using the thin disk approximation which is the definition for a geometrically thin, Keplerian and efficiently cooled accretion disk. This provides a rough description of the systems where the mass transfer occurs via Roche Lobe Overflow.

1.5.5 Accretion onto Magnetized objects: Accreting X-ray pulsars and Polars

Accretion in binary systems consisting of white dwarfs or neutron stars are special because of the presence of highly magnetized compact objects ($\sim 10^8$ G for white dwarfs and $\sim 10^{12}$ G for neutron stars) in these systems. The strong magnetic fields play a crucial role in governing the dynamics of gas flow and the flow of the matter close to the compact object (Pringle & Rees, 1972). The observed X-ray flux is also modulated with the spin period of the accretor provided the magnetic axis is not aligned with the rotation axis of the magnetized object (Lamb et al., 1973). In case of magnetized neutron stars, the systems are called accretion powered pulsars , and in case of white dwarfs, they are called polars. Figure 1.5 shows the diagram of accretion in magnetized neutron stars or accretion powered pulsars .
Assuming partially ionized matter falling towards the magnetized star, there will be a point when the motion of the matter will be channeled along the magnetic field lines. Magnetosphere is the volume within which the dynamical properties of the infalling flow are strongly affected by the magnetic field. Assuming spherically symmetric infall of matter, the magnetospheric or Alfven radius, (r_A) can be determined from the balance

between the magnetic pressure and the ram pressure of the infalling matter as given by:

$$\frac{B(r)^2}{8\pi} = \rho v_{in}(r)^2$$

where $B(r)$ and $v_{in}(r)$ are the magnetic field of the magnetized star and the velocity of infalling matter at a distance r from the surface of the magnetized star. Assuming a dipole magnetic field of $B(r) = \frac{\mu}{r^3}$ where μ is the magnetic dipole moment and *vin* equal to the free fall velocity $v_{free} = \sqrt{\frac{2GM}{R}}$; r_A can be derived to be

$$r_A = 2.7 \times 10^8 \mu_{30}^{\frac{4}{7}} M_{\odot}^{\frac{-1}{7}} \dot{M}_{17}^{\frac{2}{7}} \ cm \ for \ NS$$

&

$$r_A = 5.1 \times 10^{10} \mu_{34}^{\frac{4}{7}} M_{\odot}^{\frac{-1}{7}} \dot{M}_{17}^{\frac{2}{7}} \ cm \ for \ WD$$

where $\mu_{30} = \frac{\mu}{10^{30}} \, G\, cm^3$, $\mu_{34} = \frac{\mu}{10^{34}} \, G\, cm^3$ and $\dot{M}_{17} = \frac{\dot{M}}{10^{17}} \, g/s$.
The minimum condition for the binary X-ray source to show prominent magnetic behavior is $r_A \geq R_x$, where R_x is the size of the magnetized compact object. To determine the flow of matter in these magnetized compact objects, besides the two characteristic radius r_{acc} (already discussed) and r_A, there is a third radius called the Corotation radius (r_{cor}) which is the distance at which the neutron star spin velocity (Ω_x) matches to the Keplerian one. This can be determined from the balance between the Centrifugal force and the local gravity given by:

$$r_{cor} = (\frac{GM_x}{\Omega_x^2})^{\frac{1}{3}} = 1.5 \times 10^8 M_{\odot}^{\frac{1}{3}} P^{\frac{2}{3}} \ cm$$

where M_x is the mass of the magnetized object and P is the spin period in secs. The relative size of r_A, r_{acc} and r_{cor} determines the different accretion regimes possible in these systems as discussed below.
Regime I: $r_{acc} > r_A$ **&** $r_{cor} > r_A$ The captured matter flows from r_{acc} to r_A where it is stopped by a collisionless shock. It then penetrates the magnetosphere after which matter is channeled along the magnetic field lines towards the magnetized object. For magnetic fields $> 10^{10}$ G (in the case of accretion powered pulsars), matters falls on the poles of the compact object (neutron star in this case) where it is stopped either by a radiative shock or Coulomb interactions depending on $\dot{M}$. The accumulation of matter on the neutron star poles leads to the formation of accretion column which radiates in

X-rays. This radiation is modulated with the spin period to emit pulsations in accretion powered pulsars . The angular pattern of the emitted radiation depends on $\dot{M}$ and hence the luminosity. In high luminosity sources ($10^{37} - 10^{38}$erg s^{-1}), the radiation primarily escapes through the column walls, forming a Fan beam pattern (Davidson & Ostriker, 1973). For lower luminosity sources ($\sim 10^{35}$ erg s^{-1}), radiation escapes from the top of the column forming a Pencil beam pattern (Burnard et al., 1991). At intermediate luminosities, the emission pattern may be a hybrid combination (Blum & Kraus, 2000).

This thesis concentrates largely on the radiation mechanisms in these sources and this topic is described and discussed in detail in the later chapters.

Regime II: $r_{acc} > r_A > r_{cor}$ Centrifugal inhibition of accretion occurs as the inflowing matter is stopped at r_A, since $r_A > r_{cor}$, and the drag exerted by the magnetic field is super Keplerian. Some or all of the matter may be ejected beyond r_{acc} via propeller mechanism (Pringle & Rees, 1972; Lamb et al., 1973).

Regime III $r_{acc} > r_A$ **&** $r_{cor} > r_{acc}$ Magnetic inhibition of accretion may occur in this case and formation of accretion disk may be affected. The infalling gas will flow around the obstacle presented by the magnetosphere and very little matter will be able to penetrate it to be accreted onto the compact object. Such accretion mechanism requires that the light cylinder radius ($r_c = \frac{cP}{2\pi}$) , beyond which the magnetic field lines cannot propagate, is larger than r_{acc} (See section 1.5.1) , so that the spin period must be

$$P > 9 \times 10^3 m (\frac{v_{wind}}{10^8\, cm\, s^{-1}})^{-2}\ s$$

This implies that for slowly rotating and strongly magnetized neutron stars, magnetic inhibition of accretion may occur before the centrifugal inhibition. Supergiant Fast X-ray Transients (SFXTs), a special class of HMXBs recently discovered are speculated to belong to this category (Bozzo et al., 2008).

1.6 Motivation of the thesis & outline of the thesis

This thesis aims at studying the high magnetic field neutron stars through the absorption features found in their high energy spectra, i.e. the cyclotron lines and their polarization properties. Accretion onto these magnetized neutron stars (accretion powered pulsars) are much more complex than assumed theoretically. The complexities include :

- The process of magnetically channeled mass transfer to the neutron star from the

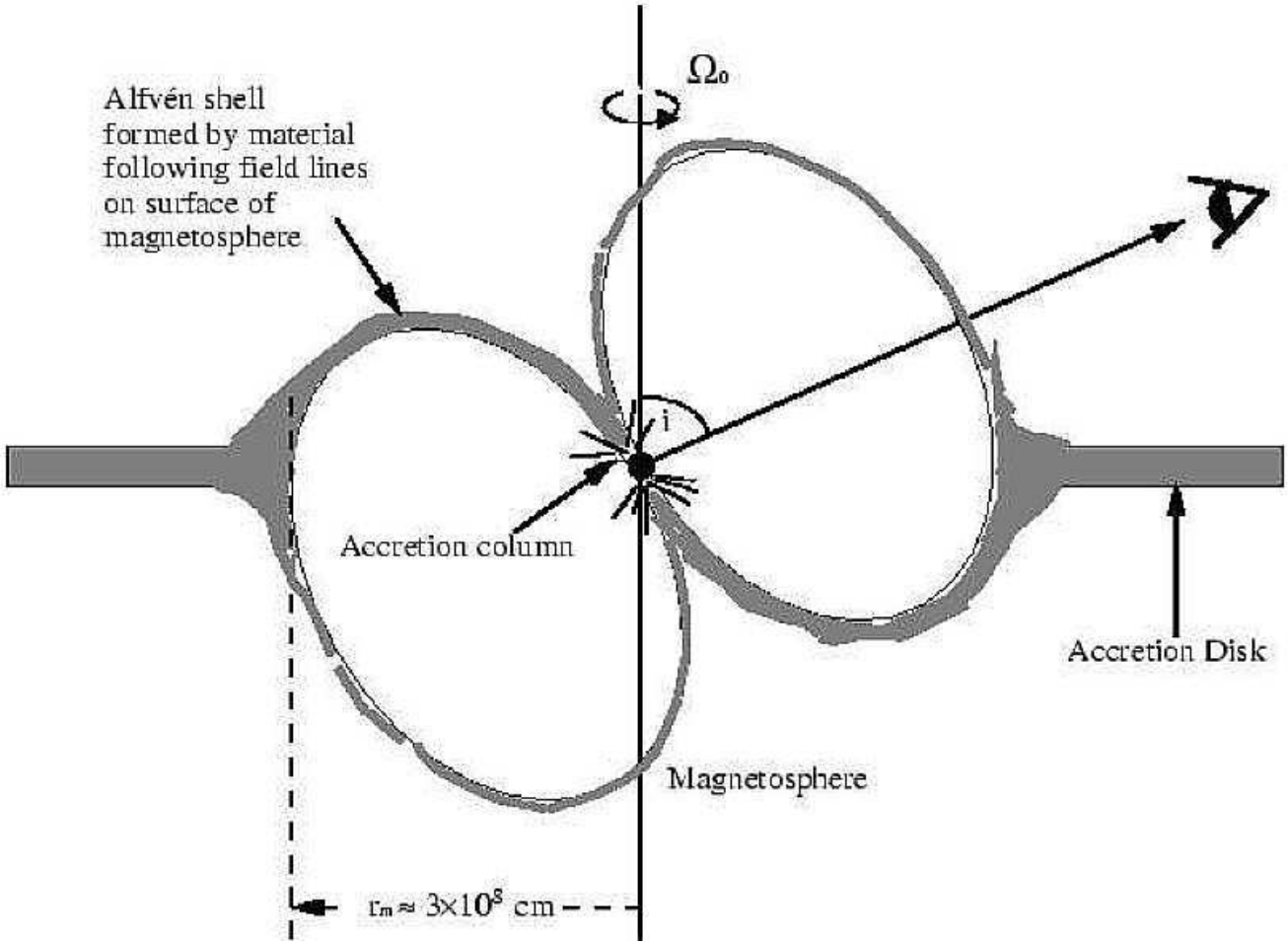

Figure 1.5: Accretion in strongly magnetized neutron stars (accretion powered pulsars) showing the Alfven surface and channeling of matter by the magnetic field lines. Image credit:http://lheawww.gsfc.nasa.gov/users/audley/diss/img203.gif

companion.

- Complex interactions between the matter at the magnetospheric boundary.
- Formation and structure of the accretion stream channeling the matter to the poles.
- Geometry of the accretion column near the poles of the neutron star.
- Nature of the emitted radiation.

All these are further dependent on the environment of the binary system and the rate of the mass accreted on the neutron star. Another key question is the magnetic field

geometry of the neutron stars which is ideally assumed to be a magnetic dipole. Although the dipole approximation is realistic at distances far away from the neutron star, the neutron star is expected to have a more complicated magnetic field geometry near its surface, specially due to the effect of the accretion introducing a possibility of distorting the field lines (Mukherjee & Bhattacharya, 2012a,b). It is important to look for clues in the observables of these systems, like the pulse profiles and energy spectra to have a better handle of the theory of accreting onto magnetized compact objects, and solve many degeneracies in this area of research. With the space missions providing very high quality X-ray data, it is necessary to exploit the capability of the data in full and make a detailed study of the accretion mechanism and magnetic field geometry in these sources. The main aim of this thesis is to study the magnetic field and emission geometry of accretion powered pulsars through the pulse phase resolved studies of the cyclotron absorption features which are a direct probe to the above mentioned. Cyclotron lines are broad absorption like features found in the energy spectrum of accretion powered pulsars due to resonant scattering in the presence of high magnetic fields. In order to study these features in detail, broadband continuum modeling is done, taking care of all other factors which may smear the pulse phase dependence. Another prerequisite for detailed continuum modeling are accounting for the low absorption dips in the pulse profiles of many sources by a phase locked partial covering absorber along our line of sight. Studying the pulse phase dependence of this partial covering absorber also provides us with important clues on the local environment of the neutron star and the structure of the accretion stream. Lastly we provide estimates of the polarization expected to be detected from these sources by a Thomson scattering polarimeter. Along with the X-ray pulsars, we also make an estimate of the likelihood of detection of X-ray polarization from black hole X-ray binaries in different spectral states. Polarization being the holy grail in X-ray astronomy will provide the crucial clues to the magnetic and accretion stream geometry and break many degeneracies in future. Given below is the brief outline of the thesis.

- The first chapter gives a brief introduction of the X-ray sky, the binary systems and the different mechanisms of accretion onto the compact object from the binary companion. It then describes the instruments onboard the satellites whose data have been used in this thesis and techniques of X-ray timing and spectral measurement. Finally a brief description of the sources studied in detail in this thesis are

described.

- In Chapter 2 the evolution of the pulse profiles with energy are presented for many accretion powered pulsars , and a systematic study is performed of the sources which show complex energy dependent pulse profiles as well as show variations in the relative strength of the different emission components with energy. Implications of these energy dependencies are discussed.

- In Chapter 3, the results of broadband spectroscopy of many bright accretion powered pulsars are presented and the results are compared with different broadband continuum and line models. Sources which show narrow low energy dips in their pulse profiles require an additional partial covering absorber in their energy spectra. The high energy broad absorption dips or the cyclotron features are accounted by Gaussian or Lorentzian profiles.

- In the next Chapter 4, the results of Chapter 3 are further utilized to perform a pulse phase resolved spectroscopy of many sources which exhibit complex energy dependent low energy dips as discussed in Chapter 2. The role of these results in constraining the structure of the accretion stream is also presented.

- In Chapter 5, the results of Chapter 3 are further utilized to perform a pulse phase resolved spectroscopy of the Cyclotron parameters of many sources. The results obtained are discussed in the light of its role in constraining the magnetic field geometry and beaming pattern of the sources. In the next section of the chapter, the results of the energy dependence of the pulse profiles near their corresponding cyclotron energy is also presented and discussed.

- Chapter 6 describes the Thomson X-ray polarimeter being developed to observe the polarization of X-rays in the energy range of 5–30 keV, and discusses its prospect of observing compact objects. This is a particularly interesting topic as it will play a crucial role in providing additional handles on the magnetic field geometry in accretion powered pulsars as well as constrain the fundamental parameters of a black hole in black hole binaries.

- Chapter 7 summarizes the results and discusses the future prospects.

1.7 Brief description of the Instruments onboard the satellites used in the thesis

The problems described in the previous section are studied with the archival data from mainly two satellites, namely the *Suzaku* and *RXTE* . In chapters 2, 3, 4 and 5, we have analyzed the data from the *Suzaku* observations, and in chapter 6, we have used both *RXTE* and *Suzaku* observations. The subsections below provide a brief overview of the above mentioned satellites.

1.7.1 *Suzaku* : Satellite overview

Suzaku (former ASTRO-E2) was launched in July 10, 2005 as a joint collaborative effort between Japan and USA. It is the best broadband high sensitive mission available till date and is continuing to provide exciting scientific inputs to the global astrophysics community. It was developed by the Institute of Space and Astronautical Science of JAXA and National Aeronautics and Space Administration's Goddard Space Flight Center (NASA/GSFC). It is a reflight of the ASTRO-E which was lost during its flight in 2000. The satellite payloads consists of five telescopes, one telescope with a calorimeter as the focal plane instrument, and four with X-ray CCDs and co-aligned with the telescopes. It also has a non-imaging hard X-ray instrument with two components, PIN and GSO. This allows the scientists to simultaneously study cosmic X-ray sources using the different capabilities of the various onboard instruments. Figure 1.6 is a schematic view of *Suzaku* showing all the instruments on board. The X-ray spectrometer (XRS) especially, was a new-generation micro-calorimeter detector designed to provide better spectral resolution compared to the gratings used in XMM-Newton and Chandra. Unfortunately the detector was only operational for 2 weeks when it was lost due to a failure in the cooling system. The performance of the instrument could, however, be verified and most likely another incarnation of the instrument will fly on one of the next-generation missions (ASTRO-H). Below are given the main characteristics of the XIS and HXD detectors and its observation modes.

X-ray Imaging Spectrometer (XIS)

The XIS (0.2–12 keV) (Koyama et al., 2007), consists of four X-ray Imaging Spectrometers (XIS), each with a 1024×1024-pixel X-ray-sensitive Charge Coupled Device similar

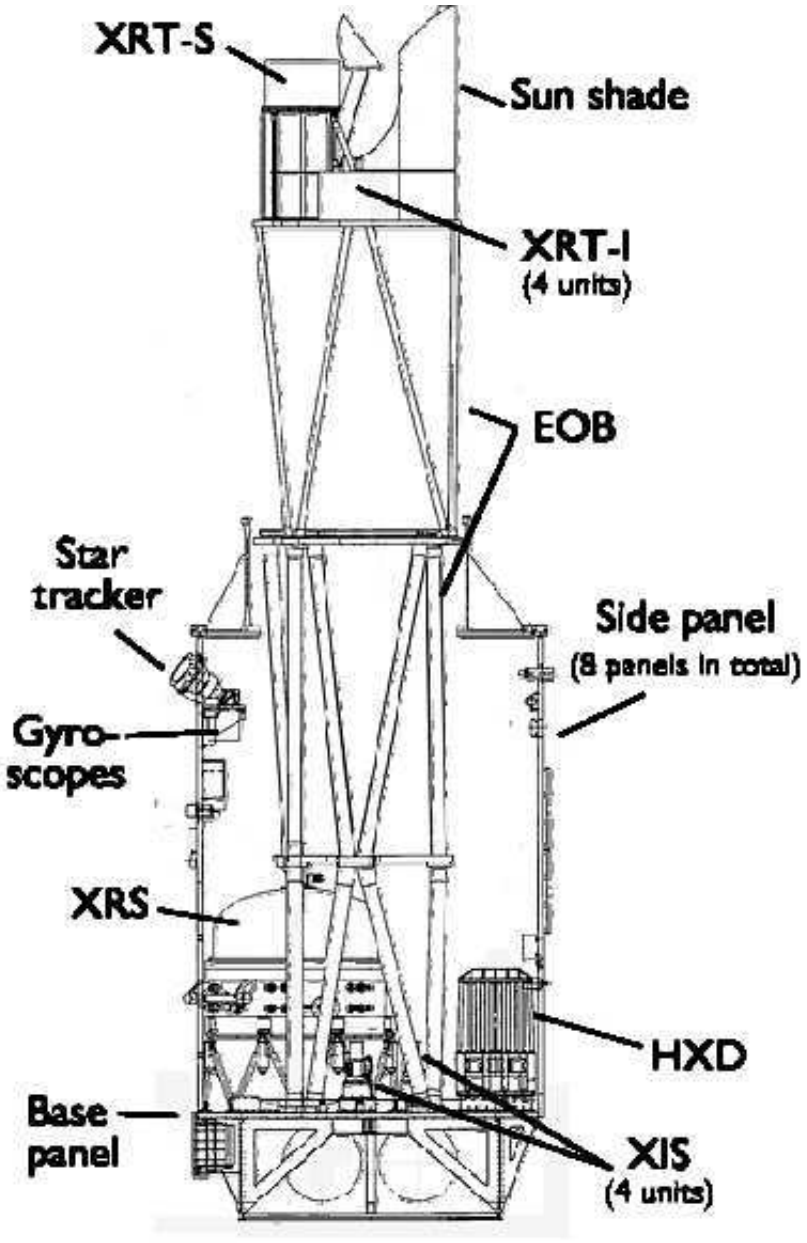

Figure 1.6: *Suzaku* spacecraft and its instruments on board. Image credit JAXA.

to the CCD detectors in the previous generation Japanese satellite *ASCA*. This corresponds to 17.80 arcmin ×17.80 arcmin area on the sky (each pixel has 24 μm^2, so the physical size of the CCD is $\sim 25 \times 25mm$). One of the XIS (XIS1) CCD is back illuminated for improved low-energy (< 1 keV) sensitivity, while the others use front-illuminated CCDs. Note that even for front-illuminated CCDs, the pulse-height distribution to monochromatic X-rays has a much smaller low energy wing compared to the

CCDs on previous missions. This makes it possible to clearly recognize low energy lines, a strength of these detectors. The CCD devices are located at the focus of four X-ray telescopes (XRTs) which are gold coated grazing-incidence reflective optics consisting of tightly nested, thin-foil conical mirror shells and high density nesting thus providing large aperture efficiency in the operational energy range of the XISs i.e. 0.2–12 keV. The effective area (including the detector efficiency) at launch was about 330 and 370 cm^2 on the FI and BI at 1.5 keV, and the angular resolution is $\sim 2'$.

1.7.2 Hard X-ray Detector (HXD)

The HXD (10–600 keV) (Takahashi et al., 2007) is a non-imaging collimated instrument consisting of 16 identical veto shielded detector modules arranged in 4×4 array. Each unit is composed of two detector layers at the bottom of a passive collimator (i.e. well): a GSO/BGO phoswich counter (scintillator), sensitive above $\sim$ 30 keV; and, on top of it, a 2- mm thick PIN silicon diode, sensitive below $\sim$ 60 keV. The scintillator signals from GSO/BGO are read out by photomultiplier tubes located below the crystals. The field of view of HXD is energy dependent and is significantly less than it's contemporary missions at the same energy range, the *RXTE* HEXTE and *BeppoSAX* PDS, at least below $\sim$ 100 keV. This makes the background rate of *Suzaku* the lowest among the existing missions in most of the energy range. Another important point is that the background is stable and can be confidently modeled with a better precision than other collimated instruments (currently the uncertainty in background approaches a target value of 1%). This clearly brings out the advantage of probing in detail the higher energy phenomena upto $\sim$ 50 keV with HXD better than the other contemporary instruments, a technique utilized to its maximum in this thesis. Above 100 keV the fine collimators become transparent and the active shielding defines a wide ($4.5 \times 4.5^\circ$) field of view. The HXD features an effective area of $\sim$ 160 cm^2 at 20 keV, and $\sim$ 260 cm^2 at 100 keV. The energy resolution is $\sim$ 3 keV (FWHM) for the PIN diodes, and $\frac{7.6}{\sqrt{E_{MeV}}}$% (FWHM) for the scintillators, where E_{MeV} is energy in MeV. The HXD time resolution is 61 μs.

The above section clearly highlights the fact that *Suzaku* with its broadband instruments combined with high sensitivity is most suited to perform detailed spectroscopic studies, particularly constrain broadband spectral changes associated with different pulse phases and the line properties against the continuum spectra like the Cyclotron lines. The above reasons have also motivated me to use *Suzaku* for most of the work presented in this

thesis in similar lines.

1.7.3 Observation modes:

The observation modes for the *Suzaku* satellite are mainly determined by two factors:

- The clock modes describe how the XIS CCD clocks are driven, and determine the exposure time, exposure region, and time resolution. Usually the normal and parallel sum clock modes are available.

  - Normal mode: All the pixels from the CCD are read out at every 8 seconds unless the window option is specified. Time resolution can be 8, 4 and 1 s depending on the window option.
  - Parallel sum mode: Pixel data from plural rows are summed in the Y-direction, and the sum is put in the Pixel RAM as a single row. The number of rows to add is commendable.

  Further, Normal window mode can be used in combination of various "window" and "burst" options. Table 1.3 summarizes the characteristics of the XIS in various "window" and "burst" options.

Table 1.3: Properties of XIS in normal mode observation

Mode	Effective Area	Exposure (s)
Normal window	25 × 25 square mm	8
$\frac{1}{4}$ window	lower	2 × 4
$\frac{1}{8}$ window	lower	1 × 8
Burst option	25 × 25 square mm	lower

- The instrument can be set to either **XIS nominal pointing** where the target is at the centre of the XIS field of view, or **HXD nominal pointing** where the target about 5 arcmin off-axis relative to the XIS, but at a point of maximum throughput of the HXD/PIN.

1.7.4 *RXTE* :Satellite overview

The Rossi X-ray Timing Explorer (*RXTE*) is one of the most versatile X-ray satellites flown till date dedicated to the study of Galactic X-ray sources. Launched on December 30 1996, it remained operational till the end of 2011 although the expected mission lifetime was only five years initially. The mission was specially tailored to explore the variability of X-ray sources starting from microseconds to years along with moderate spectral resolution from 3–250 keV provided by the collimated and coaligned instruments having sufficient spectral overlap. The two coaligned instruments on board were the following: The Proportional Counter Array (Zhang et al., 1993; Jahoda et al., 1996) which covered the energy range from 3 to 60 keV (although the sensitivity and reliability of the calibration dropped above 30 keV), and the High Energy X-ray Timing Experiment (Rothschild et al., 1998) covering the higher energy range of 18–250 keV. The collimators limited the field of view of both the instruments to $\sim 1^{\circ}$, and provided a low background level of ~ 0.2 mCrab. In addition to the pointed instruments, RXTE was equipped with a small 1D coded mask All Sky Monitor (ASM) (Levine et al., 1996). The ASM scanned about 70 % of the sky in every revolution. The main purpose of this instrument was to regularly monitor the complete sky in order to detect numerous transient sources and to trigger the follow-up pointed observations with the main instruments on board RXTE along with other X-ray missions. The advantage of sampling of most of the sources in the sky was a sensitivity of 20 mCrab per day, which also made it a one of the most prominent instruments for monitoring the activity of known persistent sources in its lifetime. Figure 1.7 shows a schematic view of *RXTE* with all the instruments onboard.

1.7.5 Proportional Counter Array (PCA)

The PCA on board Rossi XTE consisted of five identical Xenon proportional counter units (PCUs) with a geometrical collecting area of 1600 cm^2 each. The PCUs consisted of several layers to increase the sensitivity of the instrument. The propane layer at the top acted as a veto Layer. An additional veto layer was situated at the bottom of the detector. The peak effective area was 6000 cm^2 in the 3-6 keV range after which it fell rapidly above 15 keV. The energy resolution was about 18 % at 6 keV.

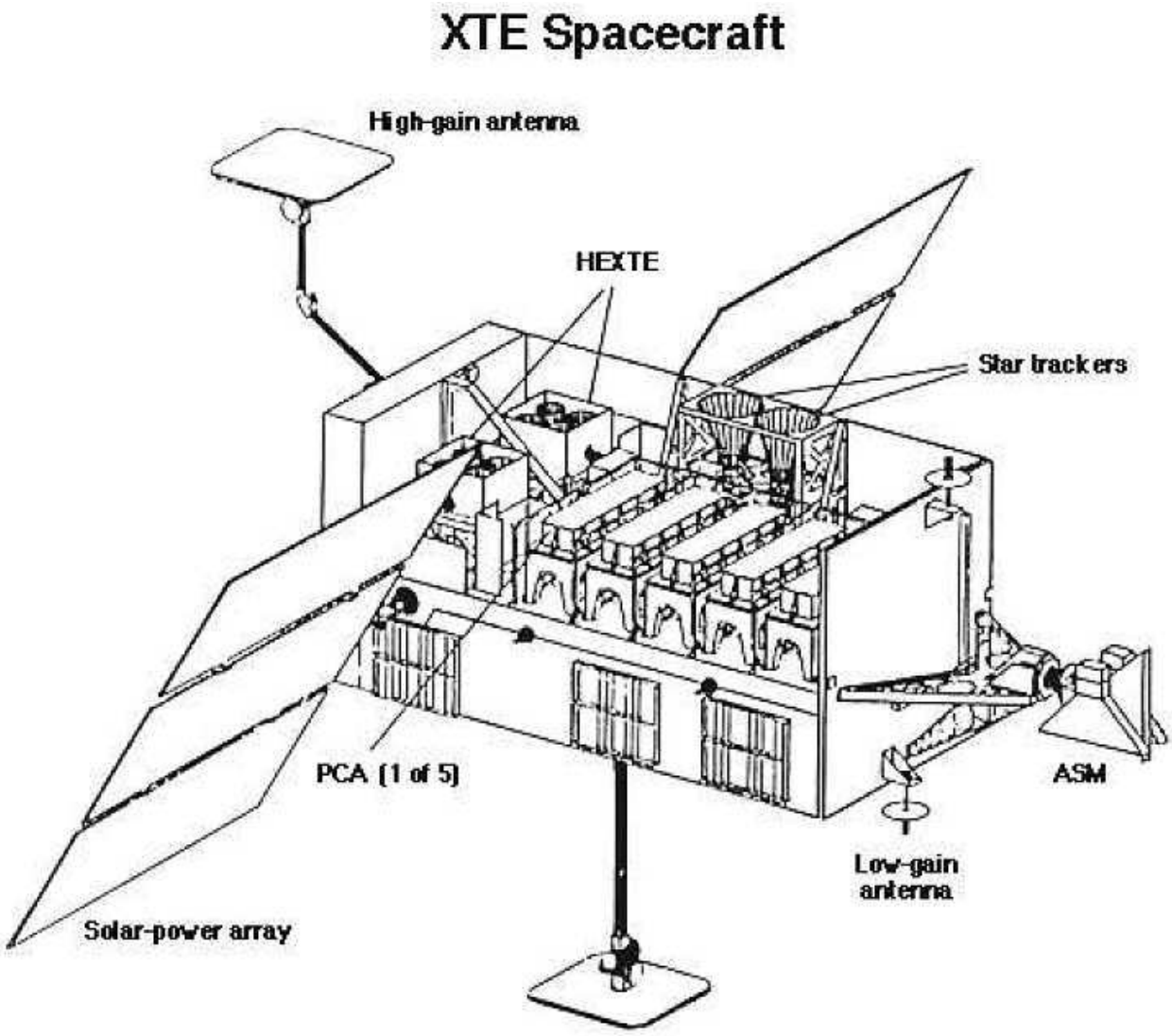

Figure 1.7: *RXTE* spacecraft and its instruments on board. Image credit NASA/GSFC.

1.7.6 High Energy X-ray Timing Instrument (HEXTE)

The High Energy X-ray Timing Experiment was the successor of the A4 detector onboard the High Energy Astrophysics Observatory (HEAO). It consisted of two clusters (A and B) of four NAI(TI)/CsI(Na)-Phoswich scintillation detectors each (Rothschild et al. 1998) with a total effective area of about 1600 cm^2 at 50 keV.
The ability of *RXTE* for monitoring of sources with many short observations carried out, allowed the determination of the spectral states and evolution of the fluxes of different spectral components. With this we investigated the polarization of black hole binary in

Chapter 6.

1.8 Techniques of X-ray timing and spectral measurements

Timing analysis of the data available from *Suzaku* and *RXTE* observations are performed with a general purpose timing analysis package 'XRONOS' (available as a part of FTOOLS). Although it is detector and wavelength independent, it is designed mainly for its use in X-ray astronomy. It includes programs for generating light curves, power spectrum, epoch folding, auto and cross correlation and various other statistical techniques. Given below are a brief description of the timing analysis tools used in this thesis.

- lcurve: This program produces binned lightcurves from input file and plots up to four simultaneous energy time series. For multi-time series, hardness ratio and their sum are also calculated.

- efsearch: This tool is used for searching for periodicities in the data from the input light curve. It searches for periodicities in a time series by folding data over a period range, determines the chi-square when plotted with a constant, plots the chi-square values versus the trial periods and the result is plotted and saved.

- efold: This tool is used for folding light curves with a periodicity w.r.t to an epoch, and has been used extensively to produce pulse profiles and orbital modulation patterns in this thesis. It calculates folded lightcurves, plots and outputs the results. The error bars are calculated after averaging folded lightcurves from different intervals in a frame, either using the standard deviation of the mean values of each phase bin or propagating the error in each phase.

Spectral analysis of the data are performed with XSPEC or the "X-ray Spectral Fitting Package". The basic principle of spectral fitting is as follows: The counts 'C' per channel 'I' : Count(I), which are actually measured by a spectrometer are related to the intrinsic spectrum F(E) by $Count(I) = \int_0^\infty f(E)\, F(I,E) dE$. where F(I,E) is the instrumental response for the particular detector and is proportional to the probability that an incoming photon of energy E will be detected in channel I. Spectral fitting is performed by

choosing a model spectrum, f(E) in terms of model parameters f(E,p1,p2,p3...) and fit it to the data measured by the spectrometer. For each f(E), a predicted count spectrum is calculated and compared to the observed data Cobs(I). A fit statistic is then computed to obtain the goodness of the fit. The fit statistic used in this thesis is the χ^2 which is defined as :
$\chi^2 = \frac{\sum(Count(I)-Cobs(I))^2}{(\sigma(I))^2}$ where $\sigma(I)$ is the error associated with each count Count(I). The χ^2 is estimated for a certain number of degrees of freedom ν given by number of channels minus the number of model parameters. In general a fit is said to be satisfactory is the reduced χ^2_{red} ($\frac{\chi^2}{\nu}$) is ~ 1. A χ^2_{red} that is much greater than one indicates a poor fit, while a χ^2_{red} that is much less than one indicates that the errors on the data have been over estimated or the model has been over specified, like too many parameters than what can be measured with the given data. The confidence interval or the error associated with a given parameter is computed by varying the parameter value until the χ^2 increases by a particular number above the best-fit value.
In Chapter 3, 4 and 5 of this thesis, confidence contours have been plotted to check the inter dependence between the parameters for the different models used for spectral fitting. For a particular model with a set of parameters, a grid of χ^2 values in a given region of two dimensional parameter space are computed and the difference with respect to the minimum χ^2 is plotted as contour plots at different confidence levels.

1.9 Sources studied in the thesis

A large part of the thesis is dedicated to the study of timing and spectral properties of accretion powered pulsars (Chapter 2, 3, 4 and 5) and to study their magnetic field structure and emission geometry. For studying all these aspects a particular set of bright accretion powered pulsars were used which had relatively long observations with *Suzaku* . The sources are referred to frequently throughout the thesis and therefore their basic properties are listed here comprehensively in the order they appear in the subsequent chapters.

1.9.1 1A 1118-61

1A 1118-615 is a hard X-ray transient pulsar that was discovered with *Ariel V* in an outburst in 1974. The same series of observations revealed X-ray pulsations with a period

of 405.6 s (Ives et al., 1975). The optical counterpart (He 3-640="WRA 793") is a highly reddened Be star classified as an O9.5IV-Ve star (Chevalier & Ilovaisky, 1975). It shows strong Balmer emission lines indicating the presence of an extended envelope (Motch et al., 1988). The distance to the source is estimated to be 5 ± 2 kpc from photometric and spectroscopic observations (Janot-Pacheco et al., 1981). *UV* observations (Coe & Payne, 1985) reveal a P-Cygni profile in the C IV line which indicates a stellar outflow with a velocity of the order of 1600±300 km s^{-1}. Coe & Payne (1985) also confirmed the magnitude of the companion and from the extinction value, the distance was suggested to be about 4 kpc. An orbital period of 24±0.4 days was reported by Staubert et al. (2011). Three giant outbursts have so far been detected from this source. The first was in 1974 (Maraschi et al., 1976). The second was detected in January 1992, and was observed by the Burst and Transient Source Experiment (*BATSE*) covering an energy range of $15 - 50$ keV (Coe et al., 1994; Maraschi et al., 1976). The outburst lasted for ∼30 days and pulsations with a period ∼406.5 s were detected up to 100 keV (Coe et al., 1994). The same work also reported a spin change rate of -0.016 s/day at the decay of the outburst. The source remained in quiescence for 17 years until 4 January 2009 when a third outburst was detected by *Swift* (Mangano, 2009). *RXTE* observations of the source was analyzed by Doroshenko et al. (2011) who presented the broad-band spectrum, and reported the presence of a broad prominent absorption feature at ∼55 keV which they interpreted as a CRSF. Detailed timing and spectral analysis of the same set of observations was reported by Devasia et al. (2011a) which included the energy dependence of the pulse profiles and pulse phase-resolved spectroscopy of the continuum spectra. They also detected quasi-periodic oscillations (QPO) at 0.07-0.09 Hz which showed a significant energy dependence. Analysis of the same *Suzaku* observations was reported by Suchy et al. (2011) which confirmed the presence of the cyclotron resonance scattering feature at ∼55 keV.

1.9.2 Vela X-1

Vela X-1 (4U 0900-40) is a an eclipsing and persistently active high mass X-ray binary (HMXB) system consisting of a massive ($23M_{\odot}$; $34R_{\odot}$) B0.5 1b supergiant HD 77581 (Brucato & Kristian, 1972; Nagase, 1989); and a $\sim 1.77M_{\odot}$ neutron star (Rawls et al., 2011). It has an orbital period of 8.964 days (van Kerkwijk et al., 1995) with a slightly eccentric orbit ($e \sim 0.1$). Being a closely spaced binary system (Quaintrell et al., 2003),

the neutron star is deeply embedded in the strong stellar wind of the companion which has a mass loss rate in excess of 10^{-7} $M_{\odot}yr^{-1}$ (Nagase et al., 1986; Sako et al., 1999). It is a prototype candidate for accretion via stellar wind, and the typical X-ray luminosity is of the order of $\sim 4 * 10^{36}$ ergs s^{-1}. It exhibits pulsations with a period $\sim$ 283 s. The source is extremely variable undergoing giant flares (where flux increases by a factor of 20), and abrupt off-states, where the source is almost undetectable for several pulse periods (Inoue et al., 1984; Kreykenbohm et al., 2008; Doroshenko et al., 2011).

The structure of the wind and hence the flaring behavior of Vela X-1 was investigated by Fürst et al. (2010) who also found a systematic trend in the change of column density of absorbing matter along the line of sight in different phase of the the orbit. The pulse profiles of Vela X-1 show a complex structure with multiple energy dependent dips. An cyclotron resonance scattering feature at $\sim$ 55 keV was first reported by Kendziorra et al. (1992) using data from *HEXE*. Makishima & Mihara (1992) and Choi et al. (1996) reported an absorption feature at $\sim$ 32 keV from the Ginga data. Mihara (1995) performed a detailed analysis of the Ginga observations and found that the CRSFs vary in strength over the pulse phase. Kretschmar et al. (1997) also confirmed the existence of two absorption features at $\sim$ 23 keV and $\sim$ 45 keV using the broadband data from the HEXE and TTM, and found similar variations with pulse phase as from the Ginga data. Subsequently more detailed pulse phase resolved analysis was performed by Kreykenbohm et al. (1999, 2002) using RXTE data who confirmed the existence of the two lines at $\sim$ 25 & 55 keV and also reported it's variation with the pulse phase. Orlandini et al. (1998b) and La Barbera et al. (2003) performed phase resolved analysis of Vela X-1 using *BeppoSAX* data, but this observation only showed an absorption line at $\sim$ 55 keV.

1.9.3 A0535+26

A0535+26 is a Be/X-ray binary pulsar which was discovered during a giant outburst in 1975 by *Ariel V* (Rosenberg et al., 1975). It consists of a 103 s pulsating neutron star with a O9.7IIIe optical companion HDE245770 (Bartolini et al., 1978) in an eccentric orbit of e=0.47, with orbital period of 111 days (Finger et al., 2006). The distance to the source is $\sim$ 2 kpc (Giangrande et al., 1980; Steele et al., 1998). Six giant outbursts have been detected in this source so far, the latest ones during 2009/2010 (Caballero

et al., 2011b,a). The last giant outburst was followed by two smaller outbursts with a periodicity of 115 days which is longer than its orbital period. Precursors to the giant outburst was also observed with the same periodicity (Mihara et al., 2010). CRSFs at $\sim$ 45 keV and $\sim$ 100 keV were discovered in this source during the 1989 giant outburst with *HEXE* (Kendziorra et al., 1994). The second harmonic at $\sim$ 110 keV was confirmed with *OSSE* during the 1994 outburst (Grove et al., 1995), although the presence of the fundamental at $\sim$ 45 keV was dubious. It was later confirmed during the 2005 outburst with *Integral*, *RXTE* (Caballero et al., 2007) and *Suzaku* observations (Terada et al., 2006). The source shows X-ray pulsations at very low X-ray intensity level (Mukherjee & Paul, 2005). Same *BeppoSAX* observation also showed a thermal emission from the neutron star poles.

1.9.4 XTE J1946+274

XTE J1946+274 is a transient Be/X-ray binary pulsar discovered by ASM onboard *RXTE* (Smith et al., 1998), and CGRO onboard *BATSE* (Wilson et al., 1998) during a giant outburst in 1998, revealing 15.8 s pulsations. The optical counterpart was identified as an optically faint B $\sim$ 18.6 mag, bright infrared (H $\sim$ 12.1) Be star (Verrecchia et al., 2002). The source has a moderately eccentric orbit of 0.33 with an orbital period of 169.2 days (Paul et al., 2001; Wilson et al., 2003). After the initial giant outburst and several short outbursts at periodic intervals, the source went into quiescence for a long time until the recent outburst in 2010 (Caballero et al., 2010). A CRSF was discovered at $\sim$ 35 keV from the *RXTE* data of the 1998 outburst observations (Heindl et al., 2001).

1.9.5 4U 1907+09

4U 1907+09 is a persistent wind accreting high mass X-ray binary discovered in the *Uhuru* survey (Giacconi et al., 1971; Schwartz et al., 1972), having a highly redenned companion star (O8-O9 Ia) of magnitude 16.37 mag and a mass loss rate of $\dot{M} = 7 * 10^{-6} M_{\odot} yr^{-1}$ (Cox et al., 2005). It has a moderately eccentric (e=0.28) orbit of 8.3753 days (in 't Zand et al., 1998). It is a slowly rotating neutron star with period of $\sim$ 440 s, and has showed several episodes of torque reversals with a steady spin-down from 1983 to 1998 (in 't Zand et al., 1998; Mukerjee et al., 2001), a much slower spin-down from 1998 to 2003 (Baykal et al., 2006), a torque reversal between 2004 and 2005 (Fritz et al., 2006) and a second torque reversal between 2007 and 2008 (Inam et al., 2009), which restored

the source to the same spin-down rate before 1998. A CRSF at $\sim$ 19 keV was reported using data from the *Ginga* /observations (Makishima & Mihara, 1992; Makishima et al., 1999) and was later confirmed from the *BeppoSaX* observations with the discovery of a harmonic at $\sim$ 36 keV (Cusumano et al., 1998). Rivers et al. (2010) performed a time and phase resolved analysis of the *Suzaku* observations of the source made during 2006 and 2007.

1.9.6 GX 301-2

GX 301-2 is a HMXB system consisting of a neutron star orbiting a B2 Iae star (WRA 977). The distance to the source is $\sim$ 3 kpc as derived from the recent luminosity estimates using atmosphere models Kaper et al. (2006). It has undergone several episodes of spin up phases and the current pulse period is $\sim$ 681 s. The neutron star is in an eccentric orbit (e=0.462) with an orbital period of 41.498 $\pm$0.002 days Koh et al. (1997). The underlying orbital variability follows a consistent pattern: shortly ($\sim$ 1.4 d) before the periastron passage the neutron star encounters a gas stream from the companion resulting in an extended X-ray flare, the activity decreases during the periastron passage and reaches a minimum shortly after that. The X-ray luminosity slowly increases over the orbit again until a second minimum is encountered near the apastron where the spiral shaped gas stream is intercepted a second time. The overall change in luminosity through the orbit is about a factor of ten. GX 301-2 exhibits a CRSF at $\sim$ 35 keV (discovered by Mihara (1995)) which is ideally suited for investigation with the PIN as the whole cyclotron line and the continuum are covered. Proper continuum modeling which is also necessary to correctly detect the CRSF is also provided ideally by Suzaku given its broad energy range and good spectral resolution. For the same reason it is also best suited to perform phase resolved spectroscopy of these features. Earlier *BeppoSAX* observations of the source at four different orbital phases had indicated a dependence of the CRSF on the orbital phase and hence luminosity (La Barbera et al., 2005). However, *BeppoSAX* could detect the line only at the two brightest orbital phases.

1.9.7 4U 1626-67

4U 1626-67 is an LMXB discovered by the *Uhuru* satellite (Giacconi et al., 1972). It consists of a 7.66 s X-ray pulsar accreting from a very low mass companion ($0.04\,M_{\odot}$ for $i = 18°$; Levine et al. (1988)). The faint secondary companion (Kz TrA, V $\sim$ 17.5)

has a strong UV excess and a strong optical pulsed fraction (McClintock et al., 1980). Orbital motion has never been detected in the X-ray data. However, the reprocessed emission from the surface of the secondary star (detected in optical) shows strong pulsed emission and indicates an orbital period of 42 mins (Middleditch et al., 1981). It was also confirmed later by Chakrabarty (1998). Orlandini et al. (1998a) discovered a cyclotron resonance scattering feature in the spectrum of this source at $\sim$ 37 keV. It was studied in detail by Iwakiri et al. (2012). 4U 1626-67 has shown two episodes of torque reversals, *BATSE* detected the first torque reversal in the form of spin down in 1991 (Bildsten et al., 1994). *Fermi*/GBM detected the second torque reversal in the form of spin up in 2008. This was studied in detail in a comparative manner by Camero-Arranz et al. (2012).

1.9.8 Cen X-3

Cen X-3 was the first binary X-ray pulsar to be discovered (Giacconi et al., 1971). It is an HMXB consisting of a 4.8 s pulsar and an orbital period of 2.1 days (Schreier et al., 1972). It has a neutron star of mass $1.21 \pm 0.21\, M_{\odot}$ accompanied by an O 6-8 III supergiant star (V779 Cen) with a mass and radius of $20.5 \pm 0.7\, M_{\odot}$ and 12 $R\odot$, respectively (Hutchings et al., 1979; Ash et al., 1999). The distance to the source is $5.7 \pm$ 1.5 kpc (Thompson & Rothschild, 2009). Although the source is a wind fed supergiant HMXB, the average luminosity of $\sim 5 \times 10^{37}\, erg\, s^{-1}$ (Suchy et al., 2008) suggests that the predominant mode of accretion is via a disc, and the neutron star is accreting via Roche lobe overflow. A cyclotron resonance scattering feature at $\sim$ 28 keV was discovered in the *BeppoSAX*spectra (Santangelo et al., 1998). A comprehensive study of the energy spectrum over the binary orbit of the source was presented in Naik et al. (2011a).

1.9.9 Her X-1

Her X-1 is an intermediate mass binary discovered by the *Uhuru* satellite (Giacconi et al., 1972). It a compact binary system consisting of a 1.24 s pulsar and an orbital period of 1.7 days (Liller, 1972). It is an eclipsing binary having an almost circular orbit and inclination of $\sim$ 85–88° (Gerend & Boynton, 1976). Like Cen X-3, the average luminosity of the source is high $\sim 2 \times 10^{37}\, erg\, s^{-1}$ assuming a distance of 7 kpc (Reynolds et al., 1997). The secondary companion is Hz Her - a main sequence star of spectral type A/F (Crampton, 1974). The first *Uhuru* observations of the source also revealed an

underlying 35 days periodicity in the source. This also manifests as a bimodal flux distribution having the "on" and "off" states of high and low flux in this source. The pattern follows a 10 days "main" on followed by a 5 days "short on", separated by two 10 days "off states". It is also the first source where a cyclotron resonance scattering feature was discovered in its energy spectrum ($\sim$ 40 keV, (Truemper et al., 1978)). This feature and its variability with different parameters was later studied extensively by dal Fiume et al. (1998); Gruber et al. (2001); Vasco et al. (2013); Postnov et al. (2013).

1.9.10 EXO 2030+375

The transient X-ray pulsar EXO 2030+375 was discovered during a giant outburst in 1985 with *EXOSAT* observatory (Parmar et al. 1989a). Optical and near-infrared observations of the *EXOSAT* error circle identified a B0 Ve star as the counterpart of EXO 2030+375 (Motch & Janot-Pacheco 1987; Coe et al. 1988). Using the *EXOSAT* observations in 1985, the spin and orbital periods of the pulsar were estimated to be 42 s and 44.3-48.6 days, respectively. Analyzing *BATSE* monitoring data of several consecutive outbursts of the pulsar EXO 2030+375 in 1992, Stollberg et al. (1997) derived following orbital parameters of the binary system : orbital period P_{orb} = 46.02$\pm$0.01 days, e = 0.36$\pm$0.02, $a_x \sin i$ = 261$\pm$14 lt-sec, $\omega = 223^\circ.5 \pm 1^\circ.8$, and time of periastron passage τ = 2448936.8 $\pm$ 0.3 days. During the giant outburst in 1985, the pulsar was observed with *EXOSAT* observatory. A dramatic change in pulse period was seen during the luminosity decline with spin-up timescale of $-P/\dot{P} \sim$ 30 yr (Parmar et al. 1989a). During the outburst, the pulse profile of the pulsar was found to be strongly luminosity dependent. At high luminosity, the pulse profile consisted of one main pulse and a small inter-pulse, separated by $\sim$180° phase. The strength of the two pulses was reversed when the luminosity was decreased by a factor of $\sim$100 (Parmar et al. 1989b). By using a geometric model, Parmar et al. (1989b) explained that the dominant beam of emission changed from a fan-beam to a pencil-beam during the decrease in luminosity and that resulted in the strength reversal of the main and inter-pulse. An extensive monitoring campaign of EXO 2030+375 with *BATSE* and Rossi X-ray Timing Explorer (*RXTE*) showed that a normal outburst has been detected for nearly every periastron passage for $\sim$13.5 years (Wilson, Fabregat & Coburn 2005). The spectral analysis of EXO 2030+375 had been carried out by using *EXOSAT* data during outburst (Reynolds, Parmar & White (1993); Sun et al. (1994)). A spectral feature at $\sim$36 keV in the *RXTE* composite

spectrum (in 17-65 keV range) was ascribed to a possible cyclotron absorption line in the spectra of the source (Reig & Coe, 1999a). However, using regular monitoring data of EXO 2030+375 with the *RXTE* from 2006 June to 2007 May, covering the first giant outburst since its discovery in 1985, Wilson et al. (2008) reported a cyclotron feature at ∼11 keV. This feature was consistently detected in the pulsar spectrum for about 90 days when the 2-100 keV luminosity was above 5×10^{37} erg s^{-1}. Again, pulse-phase resolved spectroscopy of *INTEGRAL* observation of the pulsar during the giant outburst showed significant spectral variability of the continuum parameters (Klochkov et al. 2008). In the process, evidence of the presence of an absorption line at ∼63 keV was found at a narrow pulse phase interval when the source was at the peak of its giant outburst. This feature was interpreted as the harmonic of the previously reported ∼36 keV cyclotron resonance scattering feature . Therefore there is no clear agreement on the presence of a cyclotron absorption feature in this source.

1.9.11 GX 1+4

GX 1+4 is a bright persistent source, and is a prototype of the rare class of Symbiotic X-ray binaries in which a compact object accretes from the wind of a M type giant companion (Corbet et al. (2008) and references therein). It was discovered in 1970 by a balloon borne experiment exhibiting pulsations above 15 keV at a periodicity of ∼ 2 minutes (Lewin et al., 1971). Its optical counterpart was identified as the infrared source V2116 Oph (Glass & Feast, 1973). The observed optical spectrum indicated that the object was almost certainly a binary system, consisting of a symbiotic red giant and a much hotter source. Later, infrared observations indicated a mass of $1.2M_{\odot}$ indicating that the system is an LMXB with a M6III companion (Hinkle et al., 2006). The same observations also indicated a 1161 day binary period for the system. After an extended low state in the 1980s, the source has exhibited a strong spinning down trend (González-Galán et al., 2012). The stellar wind has a velocity of ∼ 250 km s^{-1} (Chakrabarty & Roche, 1997), which is low compared to that in HMXBs and a low orbital velocity result in a large wind accretion radius around the neutron star.

The X-ray spectrum of the source shows strong intrinsic absorption and a strong Fe fluorescent line whose equivalent width is correlated with the column density (Kotani et al., 1999). It also exhibits one of the hardest spectra among accretion powered pulsars , and correlation between magnetic field strength and spectral hardness observed in

various sources (Coburn et al., 2002), would indicate a magnetic field in excess of 10^{13} G. On the other hand, evidence of weak CRSF at $\sim$ 34 keV in the spectra have been hinted in Ferrigno et al. (2007), which indicates a magnetic field strength of $\sim 10^{12}$ G.

Chapter 2

Energy Dependence of the Pulse profiles in accretion powered pulsars

With the total number of accretion powered pulsars detected nearing ~ 200 today , there have been a lot of effort to study their pulsation characteristics and beaming patterns at different intensity and energy levels and associated variability with time. The beaming patterns commonly known as the "pulse profiles" are obtained by folding the light curves with the accurate pulse period of the pulsar in question with respect to a reference epoch of folding. In this chapter we concentrate mainly on the energy dependence of the pulse profiles at both soft and hard X-ray ranges. Below are summarized the main characteristics that have been observed and modeled from the huge database of the pulse profiles obtained from the data of various X-ray observations:

- There **is a wide variety** in the pulse shape and pulse fraction between one pulsar to another (White et al., 1983, 1995). The pulse profiles can appear single or double peaked depending on the visibility of the **emission region** , likely the polar caps which mainly depends on the **intrinsic beaming pattern** and viewing angles of the neutron star (Bulik et al., 2003). If α and β are the angles between the rotation axis and the magnetic axis and the line of sight respectively, the pulse profiles appear single or double peaked depending whether $\alpha + \beta < \frac{\pi}{2}$ or $> \frac{\pi}{2}$. Other factors can further add to the complexity of the pulse shapes like the offset of the magnetic dipole from the center of the neutron star (Leahy, 1991; Riffert

et al., 1993), difference in the size and radiating properties of the emitting regions, etc. The effect of light bending in the region close to the neutron star also plays a crucial role in modifying the inherent shape of the pulse profiles (Beloborodov, 2002).

- In general, the hard X-ray or high energy pulses (> 10 keV) have simpler shapes and the pulse fraction ($\frac{F_{max}-F_{min}}{F_{max}+F_{min}}$) increase with energies (White et al., 1983; Bildsten et al., 1997).

- Variability is also found on pulse to pulse timescales (Klochkov et al., 2011)

- Multi peaked profile at lower energies and and a single asymmetric peak at higher energies ($>$ 10 keV) have been found in many pulsars: Her X-1 (Nagase, 1989), 4U 0115+63 (Tsygankov et al., 2007), and more recently in GRO J1008-57 (Naik et al., 2011b), GX 304-1 (Devasia et al., 2011b) and 1A 1118-61 (Doroshenko et al., 2011; Devasia et al., 2011a; Nespoli & Reig, 2011).

Many aspects of the pulse shape formation have also been investigated theoretically. The mechanism of the deceleration of the accreted matter on the surface of the neutron star determines the geometry and characteristics of the emission region : In the low luminosity regime ($\sim 10^{35}$ ergs s^{-1}), the matter is decelerated by coulomb interactions and slowly settles on the neutron star surface forming a slab type of emission geometry. On the other hand in the high luminosity regime ($\sim 10^{37}$ ergs s^{-1}) matter is abruptly stopped by the radiative shock at some distance from the neutron star surface and forms a column of plasma on the pole, from the sides of which the radiation is emitted. At intermediate luminosities it can be thought to be a combination of both the geometries. A detailed discussion on this can be found in Becker et al. (2012) and references therein. Radiative transfer calculations have been performed to determine the local emission pattern of these slab and column geometries. In the presence of the strong magnetic field of the neutron stars, the cross sections are highly anisotropic and energy dependent (Nagel, 1981; Meszaros & Nagel, 1985b; Kii, 1987; Burnard et al., 1991). The radiation may also be **initially** beamed towards the neutron star due to the plasma bulk motion (Brainerd & Meszaros, 1991). Furthermore, scattering of this emitted radiation in the upper accretion streams can also modify the angular dependence of the emitted radiation (Brainerd & Meszaros, 1991). Several attempts have also been made to fit the observed pulse profiles by assuming different emission regions and geometries like filled or hollow

columns, accretion halo etc (Riffert et al., 1993; Leahy & Li, 1995; Kraus, 2001). Using the pulse profile decomposition method, pulse profiles of several accretion powered pulsars have been analyzed which has shed light on their beaming patterns and geometries (Kraus et al., 1996; Blum & Kraus, 2000; Sasaki et al., 2010; Caballero et al., 2011b).

In the next section we study the complex nature of the pulse profiles **which are multipeaked in the low energies turning to a simpler profile at higher energies.**

2.1 Complex nature of the pulse profile: Dips in the pulse profiles of accretion powered pulsars

An interesting feature found in the pulse profiles of many sources are the sharp drops in intensity over a narrow phase range. There may be more than one such features (referred to as dips) present in the pulse profiles of a particular source, and they are more predominant at lower energies, and often disappear at higher energies. It was first proposed by Cemeljic & Bulik (1998) that these could be attributed to the accretion flow (which is phase locked to the neutron star) passing through our line of sight as the star rotates. They further pointed out that this reprocessing of the emitted radiation in the accretion flow/column could explain the dips in the pulse profile in A 0535+26 observed by *BATSE*. Indeed at certain viewing angle configurations of the system allowing passage of the accretion column through our line of sight, reprocessing of the emitted radiation from the column may occur, where the softer low energy photons can get preferably absorbed or scattered out of our line of sight. This was further confirmed by Galloway et al. (2001) who performed pulse phase resolved spectroscopy from the *RXTE* observation of GX 1+4 and RX J0812.423114 to show that the dip phase corresponds to the closest approach of the column axis to the line of sight, and the additional optical depth of photons escaping from the column in this direction gives rise to both the decrease in flux and increase in the fitted optical depth measured at that phase. Giles et al. (2000) further showed that the dip like features in GX 1+4 shows change in its characteristic and position with the orbital phase and the wander in the position of the dips can be interpreted as wander in the position of accretion column. Table 2.1 lists the accretion powered pulsars showing dips in their pulse profiles.For more details refer to Devasia (2012). Here we make a comprehensive study of the energy dependent pulse

profiles of some bright accretion powered pulsars observed with the *Suzaku* observatory. We have categorically mentioned the sources as "dip" and "non dip" sources. For the "dip" sources, we have made a systematic study of the evolution of the pulse profiles with energy, tracing the morphology of the "dips" in the process. *Suzaku* with its broadband energy range and good sensitivity is very suitable for this purpose.

Table 2.1: Table of accretion powered pulsars showing dips in their profile.

Source name	Companion	Source Type(P/T)[1]
Her X-1	A9-B	P
4U 1626-67	WD?	P
OAO 1657-415	OB	P
GX 1+4	V2116Oph	P
4U 0115+63	BO.5 Ve	T
Vela X-1	B0.5Ib	P
Cep X-4	B1.5 Ve	T
XTE J1946+274	B0-1 V-IVe	T
1A 0535+26	O9.7 IIe	T
1A 1118-61	O9.5IV-Ve	T
2S 1417-624	OB	T
KS 1947+300	B0Ve	T
RX J0812.4-3114	B0-1III-V	T
GRO J1008-57	OB	T
GS 1843-02	Be ?	T

[P] Persistent , [T] Transient

2.2 Observations

For probing the energy dependent pulse profiles in accretion powered pulsars , we have analyzed *Suzaku* observations of several sources which had ≥ 50 **Ks** exposures with *Suzaku* .For sources with more than one observation, we have analyzed the brighter/longer observation. The log of the observations along with their exposure time and observation mode is given in table 2.2. Each source is categorized to "dip" and "non dip" sources from the **investigation of their pulse profiles in different energy bands as given**

from Figures 2.1 to 2.9.

Table 2.2: Observation details

Source name	Time	Observation Id	Exposure (Ks)	Pointing position	XIS mode	Type
1A 1118-61	2009-01-15	403049010	49.7	'HXD nominal'	Normal clock,$\frac{1}{4}$ window	Dip
Vela X-1	2008-06–17-18	403045010	103	'HXD nominal'	Normal clock,$\frac{1}{4}$ window	Dip
A0535+26	2009-08-24	404054010	52	'HXD nominal'	Burst clock,$\frac{1}{4}$ window	Dip
XTE J1946+274	2010-10-11	405041010	51	'HXD nominal'	Normal clock,$\frac{1}{4}$ window	Dip
4U 1907+09	2006-05-02	401057010	123	'XIS nominal'	Normal clock , $\frac{1}{4}$ window	Non dip
GX 301-2	2009-01-05–07	403044020	62	'HXD nominal'	Normal clock,$\frac{1}{4}$ window	Non dip
4U 1626-67	2006-03-09–11	400015010	72	'XIS nominal'	Normal clock,$\frac{1}{8}$ window	Dip
EXO 2030+375	2007-07-29	402068010	57	'HXD nominal'	Burst clock,$\frac{1}{4}$ window	Dip
GX 1+4	2010-10-02	405077010	99	'HXD nominal'	Normal clock,$\frac{1}{4}$ window	Dip

2.3 Analysis & Results

The XIS data was reduced and extracted from the unfiltered XIS events, which were reprocessed with the CALDB version 20120428. For the extraction of XIS light curves from the reprocessed XIS data, a $4^{'}$ diameter circular region was selected around the source centroid. The HXD/PIN light curves were extracted after reprocessing the unfiltered event files [2].

2.3.1 Timing Analysis

For the timing analysis, we applied barycentric corrections to the event data files using the FTOOLS task 'aebarycen'. Light curves **were extracted** with the minimum time resolution available (8 s for no window, 2 s for $\frac{1}{4}$ window, and 1 s for $\frac{1}{8}$ window) for the XISs (0.2–12 keV) and **1 s time resolution for the HXD/PIN (10–70 keV)**, respectively . For 4U 1626-67, which has a short pulse period, HXD/PIN light curves were extracted with a time resolution of 80 ms. Pulsations were searched in the XIS data by applying pulse folding and χ^2 maximization technique, except for 4U 1626-67 for which pulsations were searched in the PIN data. The best estimate of the period for each source is tabulated in Table 2.3. For Vela X-1 and 4U 1907+09 having short orbital periods of 8.96 and 8.37 days respectively, correction of the pulse arrival times are required to accurately determine the pulse periods. For Vela X-1, check for the correction

[2]http://heasarc.nasa.gov/docs/suzaku/analysis/hxd_repro.html

of the pulse arrival times due to the orbital motion of the neutron star showed that the filtered events corresponded to an orbital phase $\sim$ 0.17 to 0.36. The orbital motion curve however fitted well to a straight line in this phase range. This implied only a linear correction in the pulse arrival times which would not alter our results significantly for this observation of the source and hence orbital correction of the pulse arrival times was not performed. For 4U 1907+09 on the other hand, the source has an eccentric orbit and the the orbital ephemeris of this source is not known with high accuracy (in 't Zand et al., 1998). Thus to account for the orbital motion of the binary, we included a $\frac{dp}{dt}$ term in the fitting, starting with an initial guess consistant with the parameters of the binary, and iterating for different values of $\frac{dp}{dt}$ to get the maximum χ^2.

Table 2.3: Determined pulse periods

Source name	Period (s)
1A 1118-61	407.49 ± 0.73
Vela X-1	283.24 ± 0.16
A0535+26	103.47 ± 0.09
XTE J1946+274	15.75 ± 0.11
4U 1907+09	441.113 ± 0.035 (MJD 54209.43189 with $\frac{dp}{dt} = 3.1 \times 10^{-6}$)
GX 301-2	685.48 ± 0.21
4U 1626-67	7.67794 ± 0.00001
EXO 2030+375	$41.410(2) \pm 0.003$
GX 1+4	159.94 ± 0.02

2.4 Energy dependence pulse profiles showing dips at low energies: evolution of the dips

Energy resolved pulse profiles were created for all the sources classified as "dip" sources in Table 2.2) by folding the light curves in different energy bands with the obtained pulse periods of the respective sources. The pulse profiles in the energy range of 0.3-12 keV were created using all the three XISs (0, 1 & 3), and in the 10-70 keV range were created from the PIN data. **The pulse profiles shown in this chapter are normalized to the average intensity of each source.** The pulse profiles are complex in structure with narrow dips (in the low energy ranges $\leq$ 12 keV except for EXO 2030+375) which morphed to become a simpler profile at higher energies. The following characteristics are observed with a careful examination of the profiles of each source.

2.4.1 1A 1118-61

The energy dependent pulse profiles of the source are shown in Figure 2.1. The pulse profiles are found to have complex energy dependent structures, with more than one peak in the XIS energy band, and a single peaked but asymmetric structure in the PIN energy band. With a careful examination of the pulse profiles, the following characteristics can be observed:

1. The profiles show a double peaked structure at lower energies (less than 12 keV).
2. The secondary peak (phase ~ 0.2) decreases in strength with energy and disappears at $\sim$12 keV.
3. At high energies (greater than 12 keV), the profile shows a single peaked structure with a large pulse fraction.
4. A narrow low energy peak (less than 2 keV) is seen coincident with the pulse minima at higher energies (phase ~ 0.46).

These features have been reported previously using *RXTE* observations by Doroshenko et al. (2011), Devasia et al. (2011a), and Nespoli & Reig (2011). Owing to the better energy resolution, and the broader energy coverage, especially below 3 keV, the *Suzaku* data show a more detailed and clearer picture of the energy dependence of the pulse profiles. Suchy et al. (2011) analyzed *Suzaku* data using much wider energy bins than ours to probe the energy dependence.

2.4.2 VELA X-1

The energy dependent pulse profiles of the source are shown in Figure 2.2. The figure shows that the pulse profiles have complex energy dependent structures, with upto five peaks in the XIS energy band which merge to two asymmetric peaks in the PIN energy band. With a careful examination of the pulse profiles, the following characteristics can be observed:

1. The first two peaks in the low energy profiles at phases ~ 0.2 and 0.5 merge to become a single asymmetric peak (phase ~ 0.3) at ≥ 12 keV. The next three peaks of the low energy profiles at phases ~ 0.6, 0.8 and 1 merge to become the second high energy peak (phase ~ 0.9) after 12 keV.

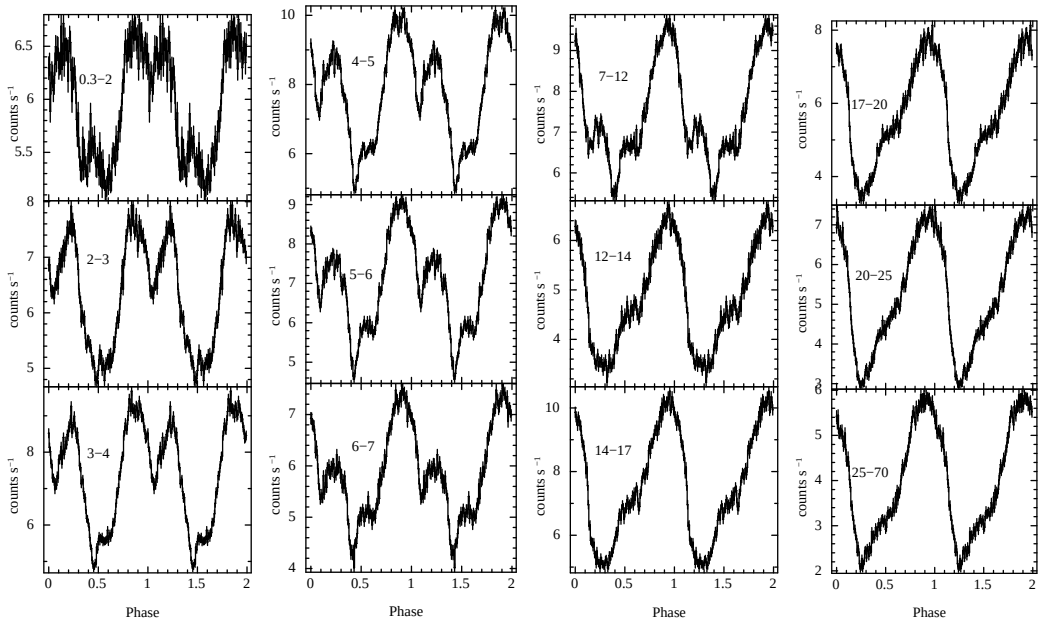

Figure 2.1: Energy dependent pulse profiles of 1A 1118-61 using the XIS and PIN data. Captions inside the figure (in units of keV) represent the energy range for which the profiles were created. The pulse profiles in the 0.2–12 keV energy range are made from the XIS data (data from all the three XISs are added together), where as profiles in the 12–70 keV range are obtained from the PIN data.

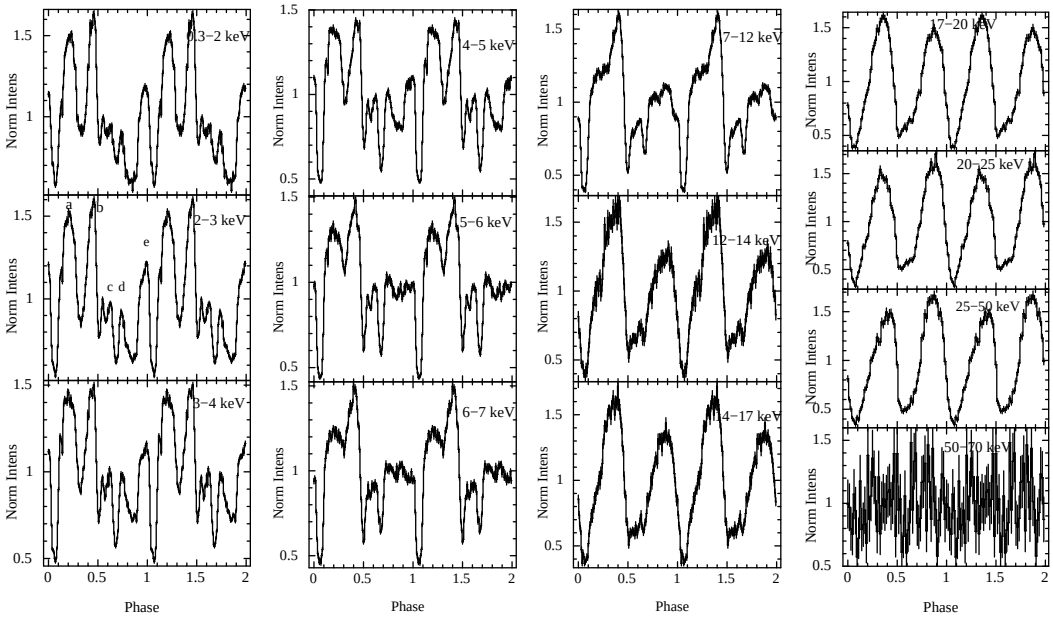

Figure 2.2: Energy dependent pulse profiles of Vela X-1 using XIS & PIN data. Captions inside the figure represent the energy range for which the profiles were created. The pulse profiles in the 0.2–12 keV energy range are made from the XIS data (data from all the three XISs are added together), where as profiles in the 12–70 keV range are obtained from the PIN data.

2. The dip at phase ~ 0.3 decreases with energy and disappears at ~ 12 keV.

3. The dip at phase ~ 0.7 however increases with energy upto 5 keV after which it shows a decreasing trend and disappears at ~ 14 keV.

4. The dip at phase ~ 0.9 also decreases with energy and disappears at ~ 7 keV.

5. There is also an indication of a dip like structure at the lowest energies (≤ 5 keV) between phase 0.5-0.6. The strong energy dependence of the pulse profiles have been probed previously by Doroshenko et al. (2011) using data from the same *Suzaku* observation in four energy bands which confirmed the structure of the complex pulse profiles.

2.4.3 A0535+26

The energy dependent pulse profiles of the source are shown in Figure 2.3. The pulse profiles are complex in structure with narrow dips in the low energy ranges ≤ 12 keV

which morphed to become a simpler, more sinusoidal profile at higher energies. The following characteristics are observed with a careful examination of the profiles.

1. A narrow dip at phase ~ 0.1, which decreases in strength with energy and disappears at energies ≥ 14 keV.

2. Indication of another sharp dip at phases ~ 0.2–0.3, which is evident only at the lowest energy range ($\leq$ 2keV).

3. The emission component between phases 0.5–0.7 becomes weaker and weaker with energy and finally disappears at ~ 17 keV. As a result the main dip of the profile (at phase ~ 0.6) is narrower at lower energies (≤ 12 keV) and broader at higher energies

The energy dependence is very similar to that found during the 2005 *Suzaku* observation (Naik et al., 2008). The profile is however, very different from the simple sinusoidal profile at all energies found during the quiescence phase of the source (Mukherjee & Paul, 2005; Negueruela et al., 2000), or the double peaked profile extending upto higher energies during its giant outbursts (Mihara, 1995; Kretschmar et al., 1996).

2.4.4 XTE J1946+274

The energy dependent pulse profiles of the source are shown in Figure 2.4. The pulse profiles show a clear double peaked structure which extends upto the high energies. The following characteristics can be observed in more detail.

1. At the lowest energy ranges (0.3–4 keV), the peak (phase ~ 0.5) increases in strength with energy and the dip at phase ~ 0.8 increases in strength.

2. Between 4–7 keV, the same dip mentioned above decreases in strength and the two peaks are almost equal in strength.

3. Between 7–17 keV, this dip (phase ~ 0.8) disappears and a new, much weaker dip appears at ~ 0.9 which is probably the true interpulse region between the pulses.

4. At the highest energies (25–70 keV), the second peak at phase ~ 0.1 becomes much weaker.

The energy dependence of the pulse profiles of XTE J1946+274 is very similar to that investigated by Wilson et al. (2003) during the 1998 outburst of the source.

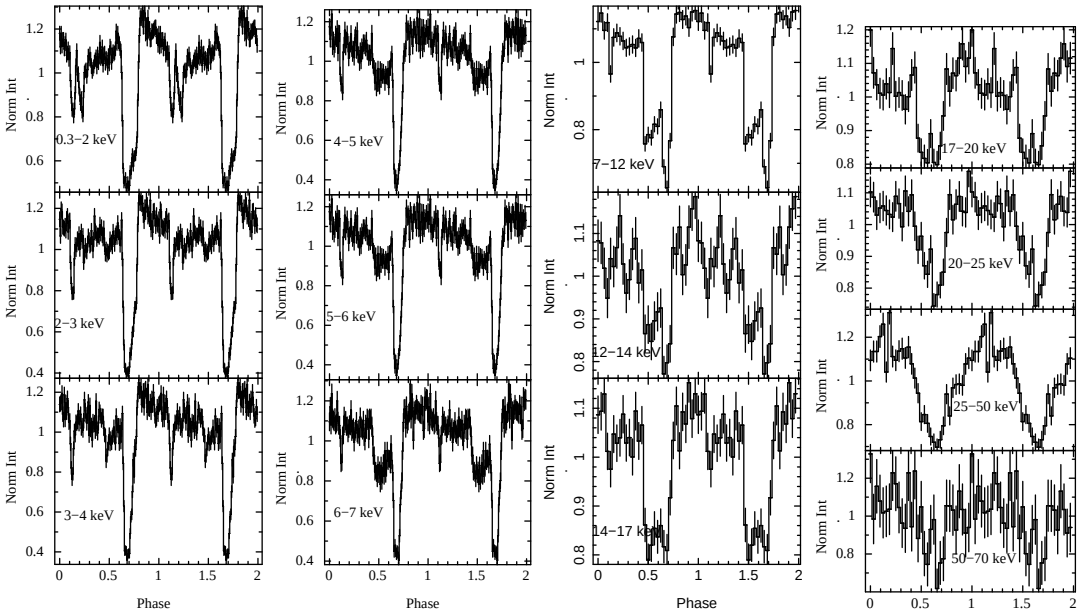

Figure 2.3: Energy dependent pulse profiles of A 0535+26 using XIS & PIN data. Captions inside the figure represent the energy range for which the profiles were created. The pulse profiles in the 0.2–12 keV energy range are made from the XIS data (data from all the three XISs are added together), where as profiles in the 12–70 keV range are obtained from the PIN data.

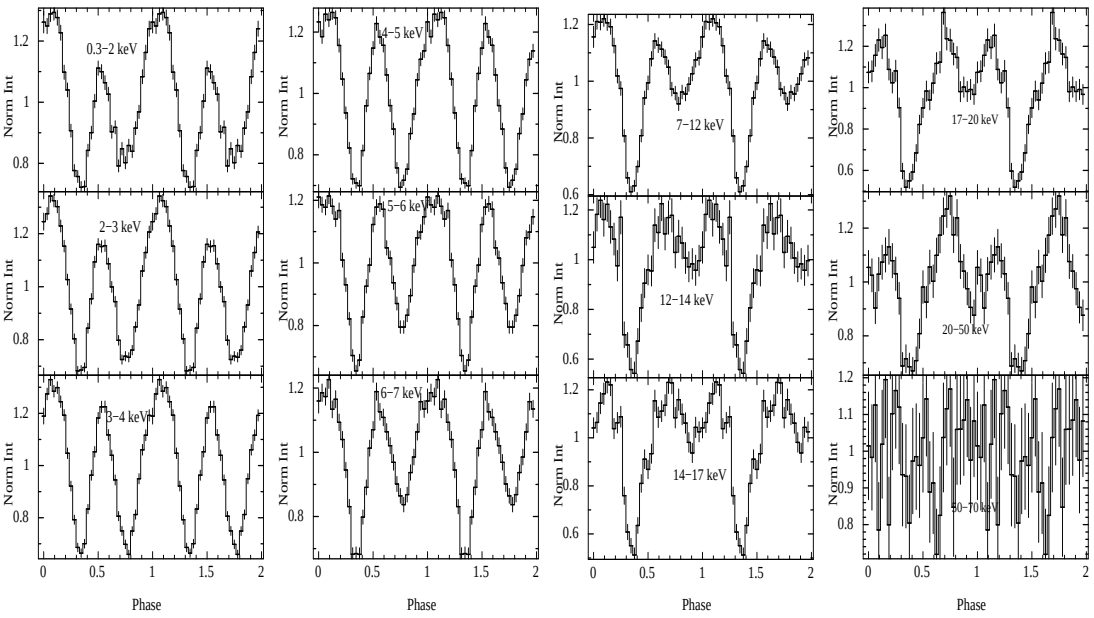

Figure 2.4: Energy dependent pulse profiles of XTE J1946+274 using XIS & PIN data. Captions inside the figure represent the energy range for which the profiles were created. The pulse profiles in the 0.2–12 keV energy range are made from the XIS data (data from all the three XISs are added together), where as profiles in the 12–70 keV range are obtained from the PIN data.

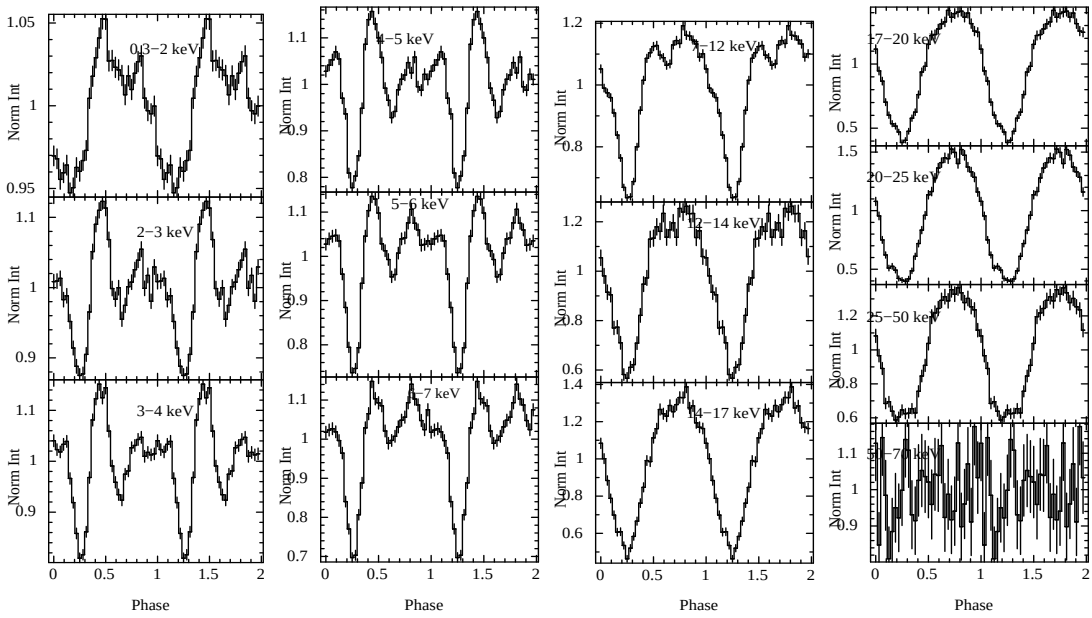

Figure 2.5: Energy dependent pulse profiles of 4U 1626-67 using XIS & PIN data. Captions inside the figure represent the energy range for which the profiles were created. The pulse profiles in the 0.2–12 keV energy range are made from the XIS data (data from all the three XISs are added together), where as profiles in the 12–70 keV range are obtained from the PIN data.

2.4.5 4U 1626-67

The energy dependent pulse profiles of the source are shown in Figure 2.5. The pulse profile is complex and multi peaked at low energies and evolves to a simple sinusoidal profile at higher energies. The nature of the average pulse profile (2-60 keV) from the 1996 data as given in Jain et al. (2010) is consistant with that found by us. The following characteristics are observed with a careful examination of the profiles.

1. Three dips are seen in the profile at phases ~ 0.3 (main dip) and $\sim$ at 0.6 and 0.9 respectively. The dips appear shallower at the lowest energies < 2 keV probably due to the presence of soft excess emission.

2. The pulse profiles after ~ 12 keV are featureless and sinusoidal in nature.

2.4.6 EXO 2030+375

In EXO 2030+375, pulsations are detected upto very high energies, and the dips in the profile are very strong and clearly distinguishable at least upto the hard X-rays (high energy ranges). The XIS and HXD/PIN profiles, though look similar, the structure and depths of the dips are found to be different. However, the difference is very clearly visible in the HXD/GSO profile. Figure 2.6 shows the energy dependent pulse profiles of the source upto 600 keV. pulsations are detected upto $\sim$ 100 keV, and the dips in the profile are very strong and clearly distinguishable at least upto 70 keV. The following characteristics can be observed in more detail.

1. Four dips are seen in the profile at phases $\sim$ 0.1, 0.3, 0.45 and 0.7. All the dips appear shallower at the lowest energies $<$ 2 keV, indicating the presence of a soft excess emission in the source.

2. The first peak at phase $\sim$ 0.6 (between the interpulse dip at phase $\sim$ 0.7) becomes stronger with energy upto 10 keV, after which it decreases in strength and merges with the pulse profile after $\sim$ 55 keV. It appears from the figure that the interpulse dip (phase $\sim$ 0.7) appears due to the evolution of the strength of the first peak of the profile and is not a real dip feature.

3. The dips at all other phases are clearly distinguishable up to $\sim$40 keV. Beyond this energy, the width and depth of the dips in the pulse profiles decrease gradually up to $\sim$70 keV. Beyond $\sim$70 keV, however, the dips become indistinguishable and the pulse profiles appear smooth and single peaked.

The presence of dips in the pulse profiles up to $\sim$70 keV is rarely seen in the accretion powered X-ray pulsars. The shape of the pulse profiles obtained from *Suzaku* observation are found to be different from that obtained from $RXTE$ (Reig & Coe, 1999b; Sasaki et al., 2010), $JEM-X$ (Martínez Núñez et al., 2003), $INTEGRAL$ (Klochkov et al., 2008b) observatories, though a few of these observations were carried out during the 2006 giant outburst, and this *Suzaku* observation is during a type I outburst of the source where the accretion rate and geometry are expected to be different.

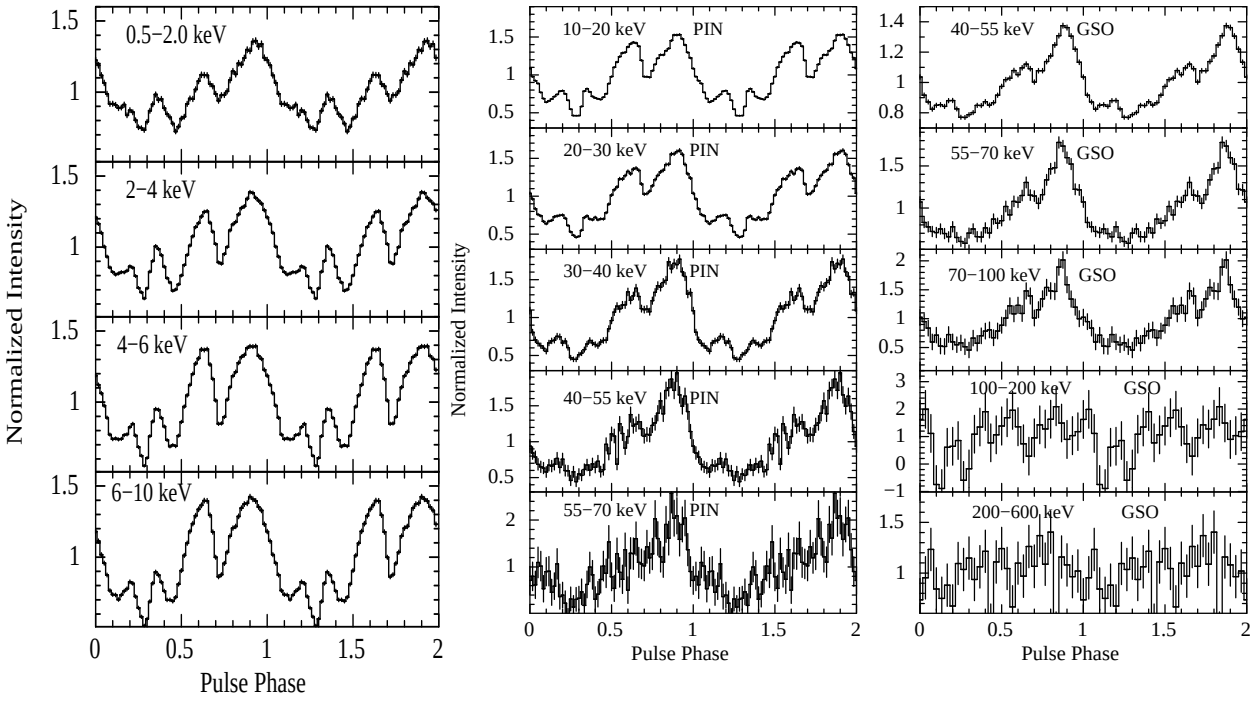

Figure 2.6: Energy dependent pulse profiles of EXO 2030+375 using XIS (left), PIN (middle) & GSO data (right). Captions inside the figure represent the energy range for which the profiles were created. The pulse profiles in the 0.2–12 keV energy range are made from the XIS data (data from all the three XISs are added together), where as profiles in the 12–70 keV range are obtained from the PIN data, and 40–600 keV from the GSO data.

2.4.7 GX 1+4

The pulse profile of GX 1+4 has characteristic low energy dips which has been attributed to accretion column eclipses (Galloway et al., 2001). The dips are intensity as well as energy dependent and has been studied with *BeppoSAX* observation by Naik et al. (2005). The low energy dip like features disappear after $\sim$ 12 keV, after which it morphed into a single sinusoidal profile. The energy dependent pulse profiles of the source are shown in Figure 3.12. The following characteristics are observed in detail.

1. There are two dip like features at phases $\sim$ 0.2 and 0.6 in the low energy profiles ($<$ 12 keV) apart from the main dip at phase $\sim$ 0.9.

2. The broad dip like feature at phase $\sim$ 0.2 gets stronger with energy while the narrower dip at phase $\sim$ 0.6 appears to decrease in strength. After 12 keV, pulse profile morphed to become a simple sinusoidal profile.

Although GX 1+4 is commonly categorized as a low energy dip source, the dip at phase $\sim$ 0.2 gets stronger with energy in contrary to the low energy dips seen in the other sources. This aspect has been investigated in detail in Chapter 4. Further, pulsations are detected upto 70 keV in this source as seen from the figure. This has also been confirmed from the *Integral* observation of the source analyzed by Ferrigno et al. (2007).

2.5 Energy dependence of pulse profiles with no low energy dips

Energy resolved pulse profiles classified as "non dip" sources were created as given in Table 2.2 by folding the light curves in different energy bands with the obtained pulse periods of the respective sources. The pulse profiles in the energy range of 0.3-12 keV were created using all the three XISs (0, 1 & 3), and in the 10-70 keV range were created from the PIN data. In this category of sources (namely GX 1+4, GX 301-2 and 4U 1907+09) the pulse profiles do not exhibit the low energy dips, although they show complex evolution with energy (w.r.t to the relative strength of the peaks and predominance of one particular component in specific energy ranges). The following characteristics are observed with a careful examination of the profiles of each source.

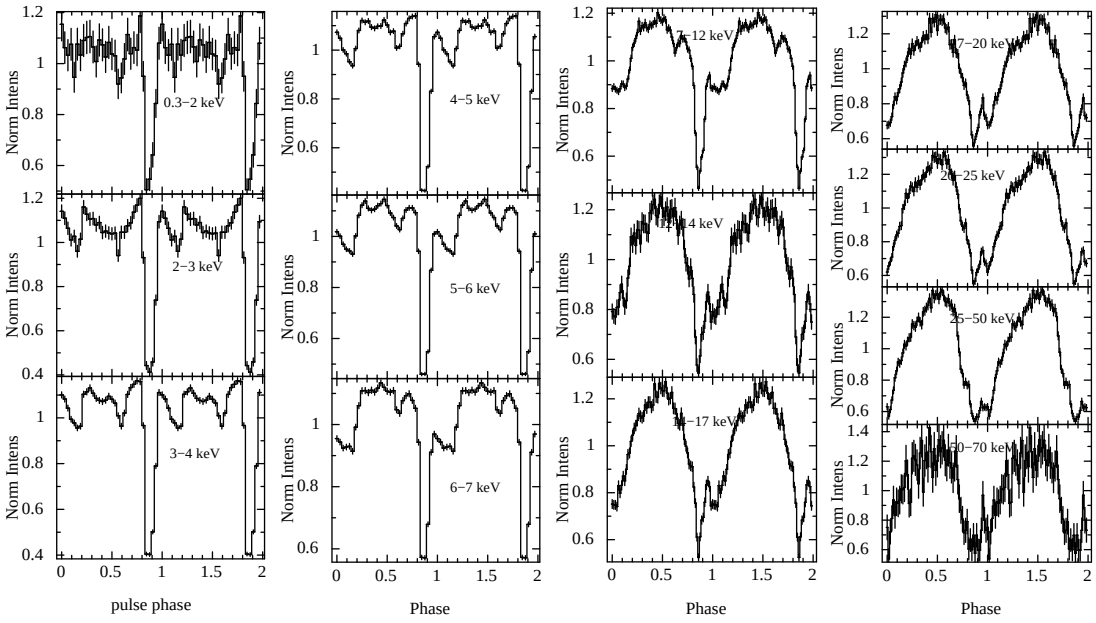

Figure 2.7: Energy dependent pulse profiles of GX 1+4 using XIS & PIN data. Captions inside the figure represent the energy range for which the profiles were created. The pulse profiles in the 0.2–12 keV energy range are made from the XIS data (data from all the three XISs are added together), where as profiles in the 12–70 keV range are obtained from the PIN data.

2.5.1 GX 301-2

GX 301-2 has a very strong and variable absorption along its line of sight as is also discussed in the spectroscopy results of this source in Chapter 3. The energy dependent pulse profiles of the source are shown in Figure 2.8. The pulse profile exhibits a broad single peaked structure at low energies, which morphed to become a double peaked structure at higher energies. The relative intensity and predominance of the peaks change with energy. The following characteristics can be observed in more detail.

1. The low energy pulse profiles (< 3 keV) show the presence of a single broad peak which becomes narrower with energy. The pulse profiles < 3 keV are smeared in nature. This may be due to the strong and significant residuals below 2-3 keV seen in the spectrum (refer Chapter 3), probably **either due to reprocessing or the spectral leakage of the photons at lower energies creating a low energy tail.** This issue is already discussed in Suchy et al. (2012) who have analyzed the

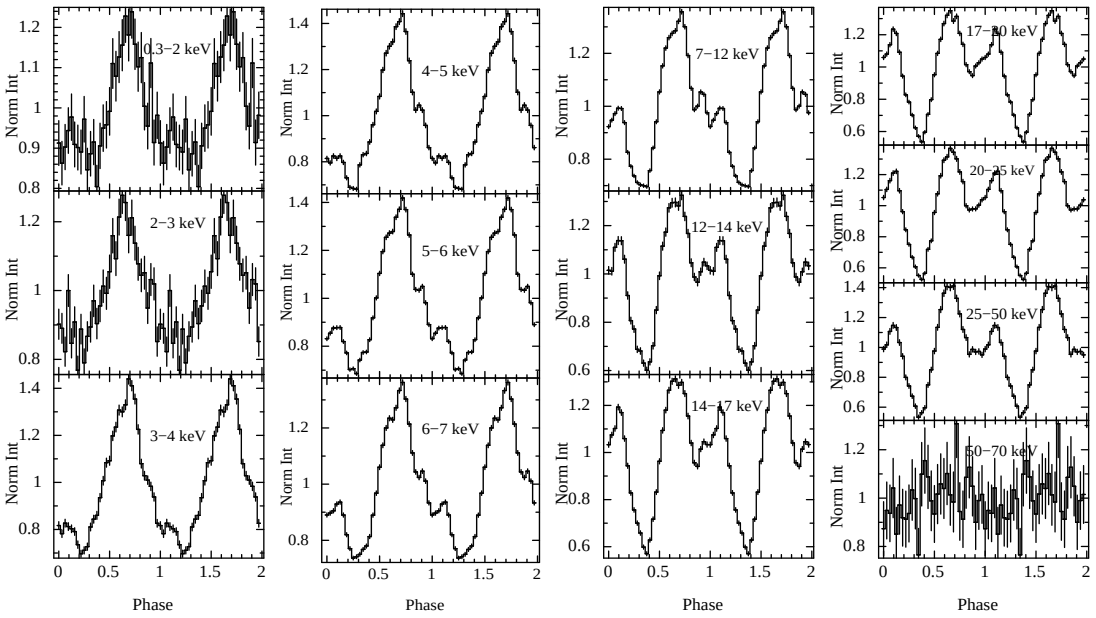

Figure 2.8: Energy dependent pulse profiles of GX 301-2 using XIS & PIN data. Captions inside the figure represent the energy range for which the profiles were created. The pulse profiles in the 0.2–12 keV energy range are made from the XIS data (data from all the three XISs are added together), where as profiles in the 12–70 keV range are obtained from the PIN data.

same *Suzaku* observation.

2. A second peak appears at around phase ~ 0.1 after ~ 3 keV which gradually grows in intensity with increasing energy. It decreases a little in strength after 25 keV. This may be due to the presence of the cyclotron resonance scattering feature in the source in this energy range as is discussed later.

The energy dependence of GX 301-2 have been studied before with the same observation by Suchy et al. (2012). Although they presented the pulse profiles in much wider energy bands, the dependence hinted is the same. This evolution of the pulse profile from the single peaked structure at lower energies to a double peaked structure is in contrary to that found in most accretion powered pulsars and as is also seen in the case of most sources presented in the previous section. This also further indicates strong energy dependence of the beaming pattern, as the high energy pulse profiles reflect the true emission and beaming pattern of the pulsar.

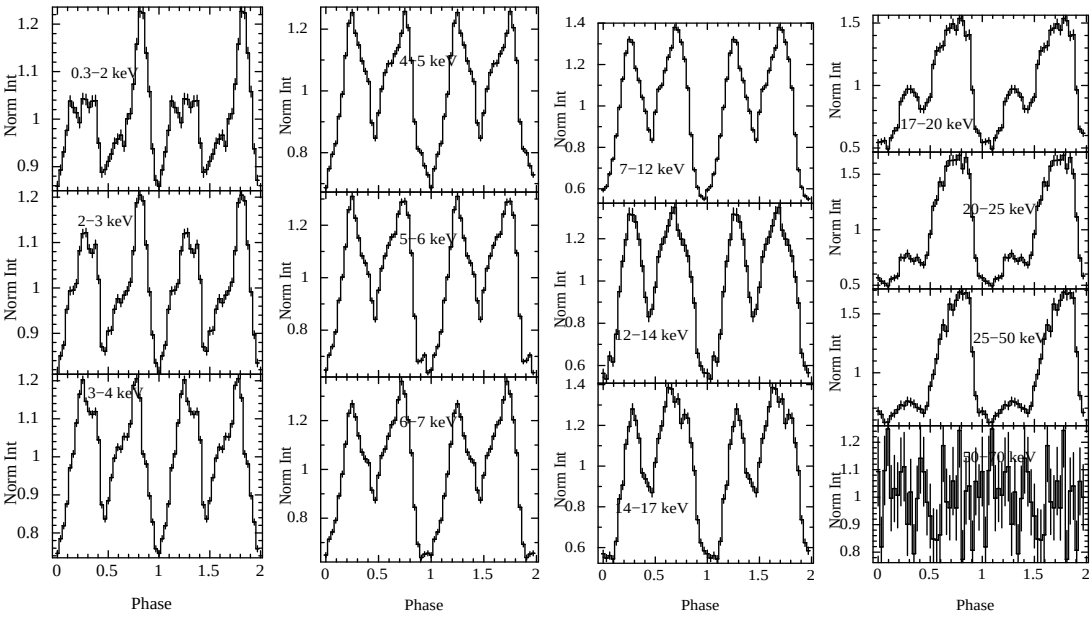

Figure 2.9: Energy dependent pulse profiles of 4U 1907+09 using XIS & PIN data. Captions inside the figure represent the energy range for which the profiles were created. The pulse profiles in the 0.2–12 keV energy range are made from the XIS data (data from all the three XISs are added together), where as profiles in the 12–70 keV range are obtained from the PIN data.

2.5.2 4U 1907+09

4U 1907+09 exhibits highly energy dependent pulse profiles and is double peaked in nature as seen in Figure 2.9. The following characteristics can be seen in more detail.

1. The first peak is flattened in the lowest energy ranges (< 2 keV) after which it remains almost constant in intensity and width upto ~ 17 keV. The first peak decreases in intensity after this energy range and the pulse profile evolves to a single peaked profile with a small hump between phases 0.1–0.4 after ~ 25 keV.

2. The second peak of the profile broadens in width upto 4 keV after which is remains almost constant in nature.

The energy dependence of the pulse profiles of 4U 1907+09 indicates highly energy dependent beaming pattern in the source. The evolution of the pulse profile further hints that the second peak is dominantly producing the hard X-ray photons in the source and may be of an intrinsically different nature.

2.5.3 Discussion & Summary

In this Chapter, the results of the evolution of the pulse profiles with energy are presented for many bright accretion powered pulsars which have long observations with *Suzaku* . The study is done into two categories; in the first one pulse profiles having complex low energy dips are studied and in the second one, the energy dependent pulse profiles which show variation in the relative strength of the different components with energy are studied. The following points can be summarized from this investigation.

- Most of the sources pulsate upto 50 keV except for EXO 2030+375 and GX 1+4. Pulsations are detected upto 70 keV for GX 1+4 and in the case of EXO 2030+375, pulsations are detected upto as high as 100 keV. This confirms that these are exceptionally hard X-ray sources as are also indicated in the earlier works.

- Presence of an additional peak in 1A 1118-61 and shallower dips as in 4U 1626-67 and EXO 2030+375 in the lowest energies (< 2 keV), indicates the presence of soft excess emission in the spectrum of the source. This is typically a blackbody emission either from the base of the accretion column or by reprocessing in the atmosphere of the system and is explained in more detail in Chapter 3.

- The study of the pulse profiles of EXO 2030+375 presents us with very interesting results, as the dips in the profiles are detected upto very high energy ranges upto ~ 100 keV. This indicates the possibility of the presence of very hot ionized reprocessing matter in the atmosphere of the binary system and is explored in detail in Chapter 4.

- **The study of the pulse profiles of GX 1+4 reveals a broad dip like feature which increases in strength with energy in contrary to the common trend of the dips decreasing in strength with energy.**

- Studying the pulse profiles of GX 301-2, GX 1+4 and 4U 1907+09 further hints that the beaming patterns could be highly energy dependent in these sources. Complex beam structures have been explored before by Kraus (2001); Blum & Kraus (2000) and more recently by Becker et al. (2012). Modeling the energy dependent pulse profiles of these sources would further give us the crucial clues on the formation of complex beaming pattern and hence the accretion geometry in these sources.

Chapter 3

Broadband X-ray spectroscopy of accretion powered X-ray pulsars

3.1 Spectral formation in accretion powered pulsars: Its broadband nature

Accretion powered X-ray pulsars are **some** of the most powerful sources of X-ray radiation in our Galaxy. **Their luminosity lie within** $10^{33} - 10^{35} \mathrm{erg\,s^{-1}}$ **during quiscence, and can even rise upto** $10^{38} \mathrm{erg\,s^{-1}}$ **during the active state,** and they radiate this energy in a broad energy range of $\sim$ 0.1-100 keV. This broadband nature of the energy spectrum originates from multiple and complicated **processes** which occur near the neutron star surface, where the infalling accreted matter is brought to rest and the X-ray are emitted by **conversion of** the gravitational potential energy to heat energy. The theory of X-ray pulsar spectral formation was originally proposed by Davidson (1973) as a scenario where most of the infalling matter accreted from the neutron star passes through a radiative, radiation dominated shock region and settles on the two poles of the neutron star forming dense "thermal mounds" just above the neutron star surface and a column of the decelerating plasma above it. The mound being optically thick emits mostly blackbody photons which are further upscattered and Comptonized by the infalling plasma and diffuse and escape through the walls of the accretion column. The escaping photons carry away the kinetic energy of the plasma hence allowing it to come to rest on the neutron star surface. These photons undergo further scattering and reprocessing either in the accretion mound or column or in the circumstellar material of the

binary system as it reaches our line of sight. As a result of this, signatures of various processes that occur near the neutron star are also imprinted on it.
One of the most important process in this regard are the broad absorption like features found in the energy spectrum due to the resonant scattering of the continuum photons with the electrons, that are quantized into Landau levels in the presence of high magnetic fields. These "Cyclotron Resonance Scattering features (CRSF) will be discussed in detail in Chapter 5 and will also comprise a bulk of the results presented and discussed in this thesis hereafter. Another important process is the reprocessing of the X-rays either by the circumstellar material or the accretion disk. Depending on the density, **metal abundance** and ionization state of the reprocessing region, narrow emission line features of Fe, Si, O, Ne etc. can also be found. The energy spectrum of accretion powered pulsars thus present to us a bonanza of features in a broad energy band starting from the very low energy reprocessed emission ($\leq$ 1keV) to the high energy Comptonized photons and CRSF lines ($10 - 100$keV). The complete modeling of the energy spectrum should include free-free emission and absorption, Comptonization, cyclotron lines and **various** emission lines.

3.2 Theoretical models of spectral formation:

There have been several attempts to model the energy spectra of accretion powered pulsars. Yahel (1980) calculated the spectra from accreting magnetized neutron stars by including the escaping photons from the optically thin parts of the accretion column. Nagel (1981) solved the radiative transfer equations in a hot magnetized plasma including the effect of Comptonization and redistribution of photons due to cyclotron resonance scattering. Meszaros & Nagel (1985a,b) calculated in their series of papers the X-ray spectra, cyclotron line shapes and pulse shapes of accretion powered pulsars assuming a slab and column geometry for the accretion columns. Klein et al. (1996) calculated radiative transfer for supper-Eddington accretion onto highly magnetized neutron stars and indicated the development of instabilities in the settling plasma below the shock dominated region. Their calculations further indicated that this would enhance the radiative transport efficiency. None of these models however proved to be a good description of the X-ray spectra of accreting pulsars which were characterized by a low energy turnover of

the powerlaw (**representing an unscattered Planck spectrum**) nature, and a high energy cutoff at 20-30 keV. Other features like the CRSFs and the Fe lines are superposed on it. Becker et al. (2005); Becker & Wolff (2005) took a step forward by proposing a new model of spectral formation by introducing "Bulk Motion Comptonization" (henceforth BMC) of the seed photons produced in the accretion mound due to collisions with the rapidly infalling plasma in the accretion column. Although the resultant spectrum is characterized by a powerlaw along with a low energy turnover at low energies, it lacks the the high energy cutoff feature in the spectra. The powerlaw index in these cases is always ≥ 2 to avoid infinite photon energy density. This model has therefore been successful in describing a few steep spectrum sources like X-Persei and GX 304-1 (Becker et al., 2005; Becker & Wolff, 2005). Becker & Wolff (2007) improved the model by including the effect of "Thermal Comptonization" along with the BMC as it now reproduced a flatter spectrum with a high energy quasi exponential cutoff feature in its spectra. This model successfully reproduced the spectra of some bright X-ray pulsars like Cen X-3, Her X-1 and SMC X-1 and more recently for 4U 0115+63 (Ferrigno et al., 2009).
There have also been attempts to model the CRSF features analytically by assuming certain physics and geometry of the line forming region by Araya & Harding (1999); Araya-Góchez & Harding (2000); Schönherr et al. (2007) and more recently by Nishimura (2008, 2011); Mukherjee & Bhattacharya (2012a,b). The details of these models are given in Chapter 5. Nevertheless, a complete model for X-ray spectral formation in accretion powered pulsars incorporating all the physical processes is still **awaited**. In the absence of this, it is a common trend to model the energy spectrum phenomenologically by multiple components that would describe its broadband nature.

3.3 Phenomenological spectral models: The need for multicomponent modeling

Phenomenological models usually consist of a powerlaw with quasi exponential high energy cutoffs of various functional forms. The most widely used models are a power-law with a **high energy** exponential cutoff or as a broken power-law (White et al., 1983; Mihara, 1995; Coburn, 2001). A combination of two powerlaws with different photon indices but common cutoff energy value called the Negative and Positive powerlaws with Exponential model (NPEX model Mihara (1995); Makishima et al. (1999)) may also be

used. A thermal Comptonization model is another model which describes the spectra of these sources well. To describe the low energy turnover **apart from the intrinsic low energy cutoff**, region of the spectrum, additional absorption column density of cold matter along our line of sight or a local absorption component like a partial covering absorber is used. A blackbody component may also be used to describe the low energy excess, **often observed in sources with low column density or absorbing material**. In addition to the continuum, Gaussian or Lorentzian multiplicative profiles are used to describe the CRSF absorption profiles and additive Gaussian profiles are used to describe Gaussian emission lines. This clearly brings out the need for multicomponent spectral modeling of the broadband spectra of accretion powered pulsars. The details of the different continuum spectral models used are given below. They are all part of the XSPEC package in HEASOFT either as a standard or a local model.

Powerlaw High Energy cutoff model

The functional form of the powerlaw high energy cutoff model is as follows:
I(E) can be expressed as

$$I(E) = \begin{cases} E^{-\Gamma}, & \text{if } E \leq Ec \\ E^{-\Gamma} \exp(\frac{Ec-E}{Ef}), & \text{if} E \geq Ec \end{cases}$$

Where Γ is the power-law photon index, Ec is the cutoff energy and Ef is the e-folding energy of the exponential roll-over. This model although a very simple one and has been used extensively to effectively describe the continuum spectrum of many sources suffers from the disadvantage of the abrupt break or "cusp" at Ec which may give rise to artifacts at the cutoff energy.

Cutoff powerlaw model

This is a limiting case of the powerlaw highecut model with a very low cutoff energy value in the limit $Ec- > 0$. I(E) can be expressed as The functional form of the powerlaw high energy cutoff model is as follows:

I(E) can be expressed as

$$I(E) = \begin{cases} E^{-\Gamma}, & \text{if } E \leq Ec \\ E^{-\Gamma} \exp(\frac{-E}{\beta}), & \text{if} E \geq Ec \end{cases}$$

Where Γ is the power-law photon index and β is the e-folding energy of the exponential roll-over. This is also widely used.

Powerlaw with a smoothed high energy cutoff 'newhcut' model

This is a modified version of the powerlaw high energy cutoff model, where in order to avoid the abrupt break at Ec, I(E) has a smoothed region of width W between the low-energy range $E \leq Ec - W/2$ and the high-energy range $E \geq Ec + W/2$ described by a third-degree polynomial function, to obtain a function that is continuous with its derivatives (Burderi et al., 2000). The mathematical form of the function is

$$I(E) = \begin{cases} E^{-\Gamma}, & \text{if } E \leq Ec - W/2 \\ AE^3 + BE^2 + CE + D, & \text{if } Ec - W/2 \leq E \leq Ec \\ E^{-\Gamma} \exp(\frac{Ec-E}{Ef}), & \text{if } E \geq Ec + W/2 \end{cases}$$

Powerlaw with Fermi Dirac cutoff (FDCUT) model

This is a powerlaw with a form of the exponential cutoff energy that resembles the Fermi-Dirac function and hence its name. It was first introduced by Tanaka (1986) and has been used widely since. The functional form is

$$I(E) = \begin{cases} E^{-\Gamma}, & \text{if } E \leq Ec \\ \frac{E^{-\Gamma}}{\exp(\frac{Ec-E}{Ef})+1}, & \text{if} E \geq Ec \end{cases}$$

Where Γ is the power-law photon index, Ec is the cutoff energy and Ef is the e-folding energy of the exponential roll-over. **The advantage of this model over high energy cutoff is that the e-folding energy is a smoother function, and does not have a discontinuity at** $E = E_c$

NPEX

The functional form of this model is as follows:
$I(E) = (A1E^{-\Gamma 1} + A2E^{-\Gamma 2}) \exp(\frac{-E}{KT})$
A1 and $\Gamma 1 \geq 0$ are the normalizations and photon index of the negative powerlaw and A2 and $\Gamma 2 \geq 0$ are the normalizations and photon index of the positive powerlaw. KT is the e-folding energy. This model has a physical meaning and it approximates an unsaturated Comptonized spectrum which commonly describes the accretion powered pulsars (Mihara, 1995; Makishima et al., 1999). For $\Gamma 2 = 2.0$ it can approximate the Wien peak. For this reason, while fitting this model to the spectrum of accretion powered pulsars , $\Gamma 2$ value is fixed at 2.0 while $\Gamma 1$ and other parameters are varied.

Thermal Comptonization: CompTT

This is an analytic model describing Comptonization of soft photons in a hot plasma (Titarchuk, 1994). It has the seed blackbody temperature, the electron temperature, and the optical depth as the parameters of the fitting model and it is valid for both optically thin and thick regions. There is an additional parameter responsible for fixing the geometry of the Comptonizing region, which can be disk like or spherical in nature. For modeling the spectra of accretion powered pulsars , this parameter is kept ≥ 1 which applies to a spherical geometry. Although it is not a correct approximation for the accretion column geometry, this is the closest to the expected conical/cylindrical geometry.

For modeling the CRSF either a Gaussian or a pseudo-Lorentzian profile is multiplied with the continuum spectrum. The Gaussian profile has the form
$G(E) = \exp(-\tau \exp(\frac{-(E-Ec)^2}{2\sigma^2}))$
where Ec is the line energy, σ is the line width and τ the optical depth of the line profile. The Lorentzian profile has the form
$G(E) = \exp\left\{-\frac{D(WE/Ec)^2}{(E-Ec)^2+D^2}\right\}$
Ec, D & W denotes the centroid energy, depth and width of the fundamental. There in an offset between the centroid energy of the two models, since the centroid energy of the Lorentzian description is not coincident with the minimum of the line profile (Nakajima et al., 2010); $E_{ga} = E_{lor}\{1 + (W_{lor}/E_{lor})^2\}$, **where E_{ga} is the centroid energy of the Gaussian function, and E_{lor} and W_{lor} and the centroid energy and width of**

the Lorentzian function.

The analytical form of the a typical model comprising of all the components used to fit the spectra of accretion powered pulsars are as follows:

$\mathrm{F(E)} = \exp^{-\sigma(\mathrm{E})\mathrm{N_{H1}}}(((\mathrm{N1} + \mathrm{N2}\ e^{-\sigma(E)\mathrm{N_{H2}}}) * G(E))\ I(E) + Gau)$

where I(E), G(E) have forms already described before and N_{H1} and N_{H2} describes the line of sight and partial covering local absorption respectively, and Gau is the Gaussian emission line for the emission lines like Fe etc. in the low energy spectrum.

3.4 Requirements for broadband spectroscopy

Broadband capability and high sensitivity are the foremost requirements for performing broadband spectroscopy of accretion powered pulsars .*Suzaku* is a Japanese satellite launched in 2005 which covers the 0.2-600 keV energy range. It has two sets of instruments on board, four X-ray Imaging Spectrometers XISs (Koyama et al., 2007) covering the 0.2-12 keV range, the Hard X-ray Detector (HXD) having PIN diodes (Takahashi et al., 2007) covering the energy range of 10–70 keV, and GSO crystal scintillators detectors covering the 70–600 keV energy band. It has good to moderate sensitivity in the entire energy band, and is therefore currently the best suited instrument for this purpose. The details of the instruments and its different observing modes and capabilities are given in Chapter 1.

3.5 Observations

For probing the broadband nature of the spectrum in accretion powered pulsars , we have analyzed *Suzaku* observations of several sources which had moderately long exposures. For sources with more than one observation, we have analyzed the brighter/longer observation except for 4U 1907+09 for which there were two long and comparatively bright observation available, and data from both the observations were analyzed. The log of the observations along with their exposure time and observation mode is given in table 3.1.

Table 3.1: Observation details

Source name	Time	Observation Id	Exposure (Ks)	Pointing	XIS mode	XIS counts counts/s/XIS	PIN counts counts/s
1A 1118-61	2009-01-15	403049010	49.7	H	N,1	24	24.2
Vela X-1	2008-06-(17 & 18)	403045010	103	H	N,1	36	12.9
A0535+26	2009-08-24	404054010	52	H	B,1	3.6	1.9
XTE J1946+274	2010-10-11	405041010	51	H	N,1	3.1	1.2
4U 1907+09	2006-05-02	401057010	123	X	N ,1	3.9	1.5
4U 1907+09	2007-04-(19, 20 & 21)	402067010	158	H	N,0	8.1	2.4
GX 301-2	2009-01-(05, 06 & 07)	403044020	62	H	N,1	10.2	14.0
4U 1626-67	2006-03-(09, 08 & 11)	400015010	72	X	N,2	5.6	1.8
Cen X-3	2008-12-(08, 09 & 10)	403046010	48	H	B,1	14.3	14.3
Her X-1	2008-02-(21 & 22)	102024010	34	X	B,0	1.0	12.2
EXO 2030+375	2007-07-29	402068010	57	H	B,1	16.3	16.2
GX 1+4	2010-10-02	405077010	97	H	N,1	6.5	4.5

^{X} 'XIS nominal'; ^{H} 'HXD nominal'

^{N} Normal clock; ^{B} Burst clock ; ^{0} no window; ^{1} $\frac{1}{4}$ window; ^{2} $\frac{1}{8}$ window

3.6 Reduction & Analysis

We have used the data processed with *Suzaku* data processing pipeline ver. 2.3.12.25. For extracting the XIS and HXD/PIN spectra, we used cleaned event data. The cleaned events of the XIS data were screened for standard criteria [1]. We extracted the XIS light spectra from these cleaned events by selecting a circular region of $4'$ around the source centroid. We also extracted the background spectra by selecting a region of the same size $18'$ away from the source centroid. Response files and effective area files were generated by using the FTOOLS task 'xisresp'. For HXD/PIN background, simulated 'tuned' non X-ray background event files (NXB) corresponding to January 2009 were used to estimate the non X-ray background[2], and the cosmic X-ray background was simulated as suggested by the instrument team[3] applying appropriate normalizations for both the cases. Response files for the respective observations were obtained from the *Suzaku* Guest Observer Facility.[4]. Each of the sources were checked for possible effects of pileup as mentioned separately for all the sources.

[1]See http://heasarc.nasa.gov/docs/suzaku/analysis/abc/node9.html for standard screening criteria

[2]http://heasarc.nasa.gov/docs/suzaku/analysis/pinbgd.html

[3]http://heasarc.nasa.gov/docs/suzaku/analysis/pin_cxb.html

[4]http://heasarc.nasa.gov/docs/heasarc/caldb/suzaku/ and used for the HXD/PIN spectrum

Spectral Analysis

We performed pulse phase averaged spectral analysis using spectra from the front illuminated CCDs (XISs-0 and 3), back illuminated CCD (XIS-1), and the PIN. Spectral fitting was performed using *XSPEC* v12.6.0. The energy ranges chosen for the fits were 0.8–10 keV for the XISs, and 12-70 keV for the PIN spectra. We neglected the 1.75–2.23 keV energy range in order to take out the artificial structures in the XIS spectra at around the Si edge and Au edge. After appropriate background subtraction we fitted the spectra simultaneously with all the parameters tied, except the relative instrument normalizations which were kept free.

3.7 1A 1118-61

The hard X-ray transient pulsar 1A 1118-61 was observed with *Suzaku* , once at the peak of the outburst and once in its decline phase 13 days later. For this analysis we have used the data at the peak of the outburst as is specified in table 3.1.
Observations of a bright source like 1A 1118-61, especially at the peak of the outburst should be checked for possible effects of pileup. Suchy et al. (2011) had applied the tool 'pile_estimate.sl' to estimate the pileup fraction in XIS and had excluded regions of the CCDs with pileup fraction above 5%. We checked for the effect of pileup by extracting spectra with the central $10''$ and $15''$ radii removed, and generated their corresponding responses. Comparing these two spectra with the original spectrum, we observe that the spectral shape remains almost the same in all the cases and the change in photon index is only $\sim$0.02 for the XISs, where this effect is the most pronounced for XIS-3. Hence, our results are not expected to vary significantly due to this effect. The XIS spectra were rebinned by a factor of 5 from 0.8–6 keV and 7–10 kev. However due to the presence of a narrow iron line, the spectrum was rebinned only by a factor of 2 in the 6–7 keV energy range. The PIN spectra were rebinned by a factor of 4 in the 12–70 keV range.

3.7.1 Broadband Continuum modeling

This source shows narrow dips in its low energy pulse profiles as discussed in Chapter 2 which is thought to arise from absorption by some local neutral matter, probably the accretion stream phase locked with the neutron star. A partial covering absorber 'pcfabs'

model in *XSPEC* needs to be added to the spectral model to account for this purpose. We initially tried to fit the continuum with a partial covering high-energy cutoff model (similar modeling for this source has been done in Devasia et al. (2011a)) which gave a very low value of high-energy cutoff (~ 3 keV) for some of the phase bins while performing pulse phase resolved spectroscopy described later in Chapter 4. High energy cutoff in this scenario is equivalent to the cutoff power-law model. Hence we fitted the broad band energy spectrum of 1A 1118-61 with a partial covering cutoff power-law model with an interstellar absorption and a Gaussian line for an Fe $K\alpha$ feature at 6.4 keV and a weaker Fe $K\beta$ feature at 7.1 keV. In addition, a broad cyclotron absorption feature was also found in the spectra at 49 ± 0.5 keV. This feature was fitted with the *XSPEC* standard model 'cyclabs' which is a cyclotron absorption line having a Lorentzian profile. We also tried to fit the CRSF with a Gaussian model 'gabs'. Apart from the slight offset in the centroid energy of the two models as described in Section 3.3, the other parameters like the depth and the width were consistent within error bars. The fits are also similar. We however considered a Lorentzian profile for the CRSFs for the rest of the thesis after verifying the consistency between the Lorentzian and Gaussian profiles.

Presence of the broad cyclotron feature at $\sim$ 55 keV had already been reported from *RXTE* observations (Doroshenko et al., 2011) and from these *Suzaku* observations (Suchy et al., 2011). Although the spectral fitting using the partial covering cutoff power-law model provided a good fit to the data with no systematic residual patterns, and a reduced χ^2 of 1.91 for 874 d.o.f, the CRSF obtained was very deep and wide. A width of 19.2 ± 1.1 keV seems to be somewhat unphysical. We then tried to fit the spectra with the other standard continuum models like powerlaw with 'fdcut', CompTT and NPEX models. The best fits were obtained with the 'NPEX' and 'FDCUT' model. The reduced χ^2 obtained were 1.89 for 873 d.o.f and 1.80 for 872 d.o.f respectively, providing a better fit than the cutoff power-law model. The CRSF centroid energy is at $\sim$ 47 keV for both the models, and more importantly the CRSF parameters indicate a shallower and narrower line for these models, with a width of 7.23 ± 1.6 and 13.7 ± 2.0 for the 'NPEX' and 'FDCUT' model respectively. This indicates that 'NPEX' and 'FDCUT' provides a more physical and reasonable fit to the spectra of 1A 1118-61. The partial covering parameters, $N_{\rm H2}$ and $Cv_{\rm fract}$ are consistent for both the models. The broad 10 keV Gaussian feature as reported in Suchy et al. (2011) was also not required in our continuum modeling. This may **arise** from imperfect continuum modeling as discussed in Coburn et al. (2002) and has been discussed later. Figure 3.1 shows the best fit

continuum models and Table 3.2 shows the best fitting parameters.

Table 3.2: Best fitting phase averaged spectral parameters of 1A 1118-61. Errors quoted are for 99 per cent confidence range.

parameters	NPEX	FDCUT
$N_{\rm H1}^{a}$ (10^{22} atoms cm^{-2})	0.80 ± 0.01	0.86 ± 0.01
$N_{\rm H2}^{b}$ (10^{22} atoms cm^{-2})	$12.9^{+0.5}_{-0.6}$	$10.9^{+0.5}_{-0.4}$
$Cv_{\rm fract}$	0.29 ± 0.01	$0.29^{+0.01}_{-0.009}$
PowIndex	–	0.56 ± 0.01
E-folding energy (keV)	–	10.9 ± 0.2
E-cut energy (keV)	–	$19.9^{+0.9}_{-0.8}$
$powerlaw_{\rm norm}^{c}$	–	0.13 ± 0.01
NPEX Γ1	0.22 ± 0.02	–
NPEX Γ2	-2.0 (frozen)	–
NPEX KT (keV)	$6.57^{+0.13}_{-0.08}$	–
$NPEX_{\rm norm}$ 1^{c}	0.11 ± 0.01	–
$NPEX_{\rm norm}$ 2^{c}	$4.8e^{-4} \pm 3.9e^{-5}$	–
$E1_{\rm cycl}$	$46.6^{+1.0}_{-0.9}$	47.9 ± 1.1
$D1_{\rm cycl}$	$0.37^{+0.04}_{-0.05}$	$0.7^{+0.5}_{-0.2}$
$W1_{\rm cycl}$	$7.2^{+2.0}_{-1.5}$	$13.7^{+2.3}_{-2.0}$
FeK_{β} energy (keV)	7.10 ± 0.03	7.11 ± 0.02
Iron line eqwidth (eV)	23.9 ± 3.2	18.9 ± 4.2
FeK_{α} energy (keV)	6.41 ± 0.01	6.41 ± 0.01
Iron line eqwidth (eV)	55.6 ± 4.6	55.4 ± 5.3
Flux (XIS) ^{d} (0.3-10 keV)	2.4 ± 0.3	2.4 ± 0.3
Flux (PIN) ^{e} (10-70 keV)	1.02 ± 0.30	1.02 ± 0.31
reduced χ^2/d.o.f	1.89/873	1.80/872

^{a} Denotes the Galactic line of sight absorption ^{b} Denotes the local absorption by the partial covering absorber 'pcfabs'.

^{c} photons $\mathrm{keV}^{-1}\,\mathrm{cm}^{-2}\,\mathrm{s}^{-1}$ at 1 keV

^{d} $10^{-9}\,\mathrm{ergs\,cm}^{-2}\,\mathrm{s}^{-1}$ and are in 99 % confidence range.

^{e} $10^{-8}\,\mathrm{ergs\,cm}^{-2}\,\mathrm{s}^{-1}$ and are in 99 % confidence range.

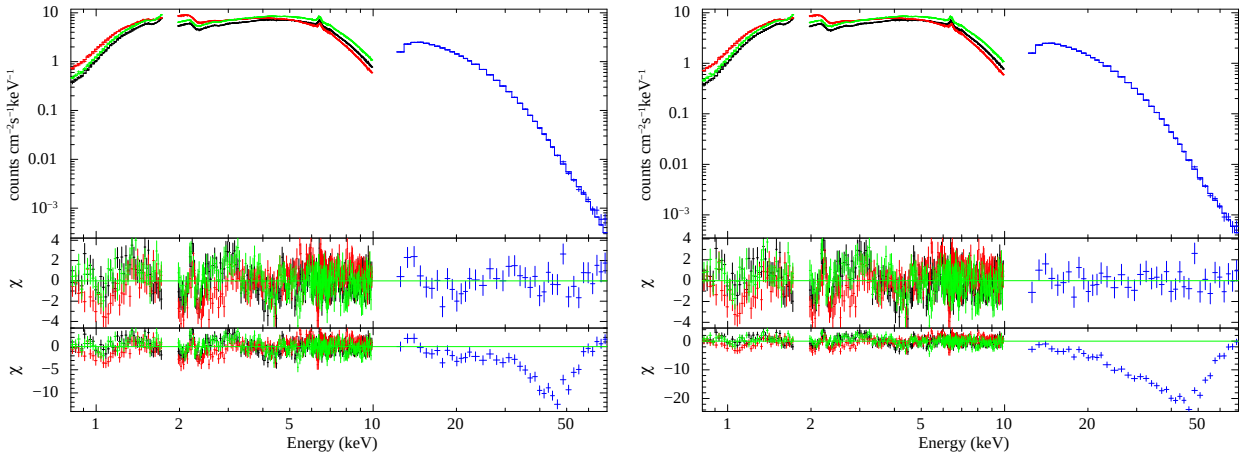

Figure 3.1: First panel of both the figures show the phase averaged spectrum of 1A 1118-61 with the best fit continuum models, the second panel shows the residuals after inclusion of the CRSF and Fe lines, and the third panel shows the residuals without inclusion of the CRSF. The left figure shows the results obtained with the NPEX model and the right one shows the same obtained with the FDCUT model.

3.8 Vela X-1

Vela X-1 has been observed with *Suzaku* on June 17-18 2008 (Obs. Id–403045010). **The useful exposure this observation was $\sim$ 103 ks**.

In order to check for pileup correction, the value obtained was higher than that of Crab Nebula count rate of 36 ct/sq arcmin/s (CCD exposure), and the radius at which this value equals 36 in the PSF is about 15-16 arcsec. Thus the check performed showed a case of moderate photon pile up, and 15 pixels from the image center were removed to account for this effect. The XIS spectra were rebinned by a factor of 6 from 0.8-6 keV and 7-10 keV, and by a factor of 2 between 6-7 keV. The PIN spectra were rebinned by a factor of 2 upto 22 keV, by 4 upto 45 keV, and 6 upto 70 keV.

3.8.1 Light curves & hardness ratio

Figure 3.2 shows the light curves of Vela X-1 rebinned with the timebin equal to the pulse period as obtained from the XIS and PIN data respectively. The light curves show that the source is highly variable. Panel 3 of the same figure shows the hardness ratio

(ratio of PIN counts to XIS counts) for the entire stretch. Except for the brief initial stretch at the beginning, the hardness ratio remains nearly constant upto the first 90000 s after which it is more variable with an increasing trend. For this above mentioned constant hardness ratio stretch, arrows in panel 1 also show the "off-states" in the XIS light curve as presented in Doroshenko et al. (2011). Since the main aim of this work is to perform pulse phase resolved spectroscopy to probe the spectral parameters with changing viewing angle, we took only this stretch of constant hardness ratio excluding the stretches **having sudden drop in intensity or** the "off-states" for further analysis. This would ensure that our results would be free from any systematic effects of phase average spectral variability.

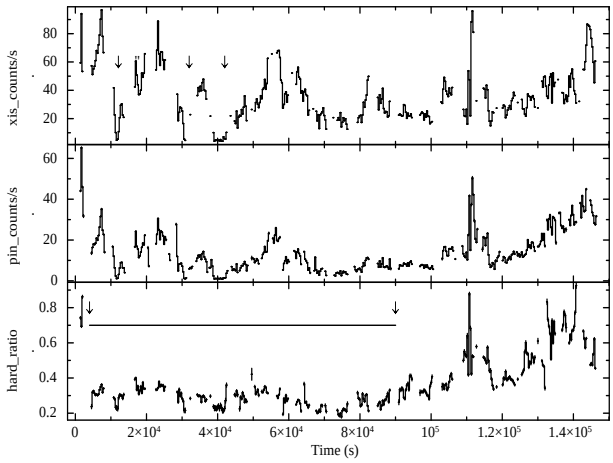

Figure 3.2: The first panel shows the light curve of Vela X-1 obtained with Suzaku for one of the XIS in the energy band of 0.3-12 keV. The second panel shows the same obtained in the PIN energy band(10-70 keV). The time binning is equal to the pulse period. The bottom panel shows the hardness ratio. The arrows and the dash indicates the time range of the data which were selected on the basis of constant hardness ratio for further analysis.

3.8.2 Intensity dependence of the pulse profiles

As already mentioned earlier, since the main aim of this work is to probe the pulse phase dependence of the spectral parameters, we also checked for the intensity dependence of the pulse profiles to avoid averaging over data having different intensity dependence. Intensity dependent pulse profiles were created using both XIS (0.3-12 keV) and PIN

(10-70 keV) for the above mentioned stretch of the data having similar hardness ratio and excluding the "off-states". Pulse profiles were created in three intensity windows having characteristic XIS count rates ≤ 20 c s^{-1}, 20-50 c s^{-1} and ≥ 50 c s^{-1} by applying intensity filtering. Figure 3.3 shows the intensity dependent pulse profiles in the XIS and PIN energy band respectively. The XIS and the PIN profiles also show similar characteristics in all the intensity bands except for a slightly larger pulse fraction in XIS at low count rate (≤ 20) and in PIN at medium count rate (20-50). The XIS pulse profile created with counts greater than 50 however differs considerably, with the dips and peaks in some phases not coinciding as can be seen from the figure, the dip in the highest intensity profile at phase ~ 0.6 coincides with a peak in the other intensity band profiles. To avoid this intensity dependence we averaged over data only in the intensity band of ≤ 50 c s^{-1} to perform spectral analysis.

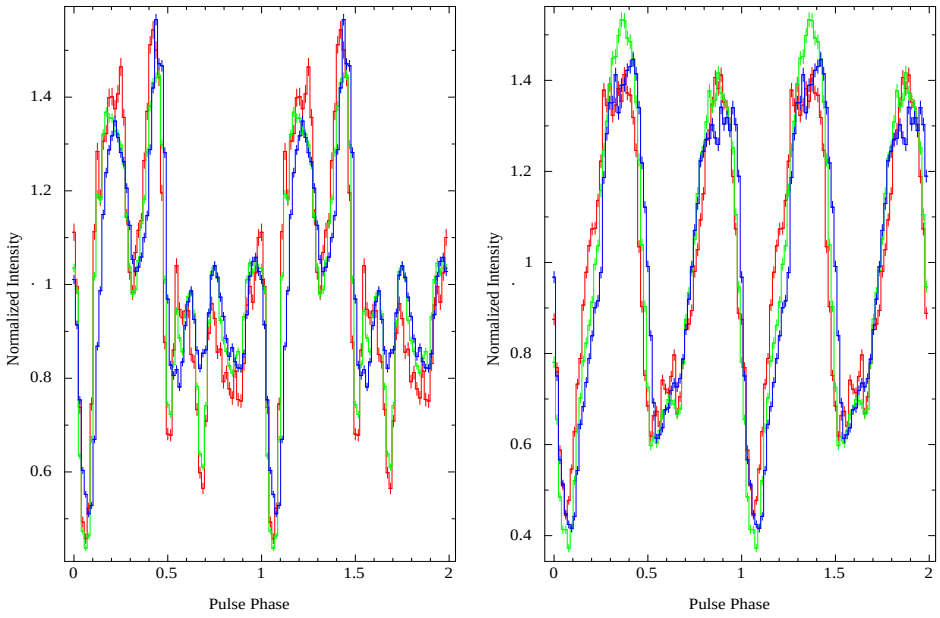

Figure 3.3: Intensity dependent pulse profiles of Vela X-1. The left panel shows the pulse profiles (0.3-12 keV) using XIS data & the right panel shows the pulse profile (10-70 keV) using PIN data. The pulse profiles in red shows the profile with XIS count rate ≤ 20 c s^{-1}, the one in green with 20-50 c s^{-1}, and the one in blue ≥ 50 c s^{-1}

3.8.3 Broadband Continuum modeling

We tried to fit the spectrum with all the continuum models described above. The best fits were obtained with both the high-energy cutoff 'highecut' model and 'CompTT' assuming a spherical geometry for the Comptonizing region (Titarchuk, 1994). In both the cases along with the Galactic line of sight absorption, a partial covering absorption model 'pcfabs' was applied to take into account the intrinsic absorption local to the neutron star. A Gaussian line was also used to model the narrow Fe kα feature found at 6.4 keV.
In addition, two absorption features were found at 25 and 50 keV, which are the CRSF fundamental and harmonic as found previously for this source. These were modeled with Lorentzian profiles. Figure 3.4 shows the best-fitting spectra along with the residuals. Since the energy spectrum has a strong pulse phase dependence, we do not expect the pulse phase averaged spectrum to fit well to a simple continuum model. The best fit had a reduced χ^2 of 2.03 for 831 d.o.f for the 'highecut' model and 1.92 for 832 d.o.f for the 'CompTT' model respectively. The value of the additional absorption component (N_{H2}) and the covering fraction (Cv_{fract}) are higher for the 'CompTT' model. The fundamental CRSF has similar parameters for both the models except for a slightly wider line in the case of the 'CompTT' model. The harmonic is however much deeper and wider in the case of 'CompTT' model. However, in the 'highecut' model, the energy and depth of the fundamental ($E1_{\rm cycl}$ and $D1_{\rm cycl}$) could not be constrained completely independent of the $E_{\rm cut}$ parameter. This is because of the very close value of the $E_{\rm cut}$ and $E1_{\rm cycl}$. However, the consistency of the CRSF parameters variation with pulse phase obtained from both the continuum models give give us added confidence on the suitability of these continuum models to fit the spectra of Vela X-1. This has been discussed in Chapter 5.

The continuum model used by Doroshenko et al. (2011) is slightly different from ours since they used a combination of powerlaw and CompTT model while we have used a partial covering CompTT model. As a result, the Galactic line of sight absorption (N_{H1}) value obtained in our analysis is lower, and the comptonization parameters are also different. The cyclotron parameters however match well and are consistent with each other within error bars. Keeping in mind that E_{cycl} from the Lorentzian description does not define the minimum of the line profile (Nakajima et al., 2010) , from the values of E_{cycl} and $E2_{cycl}$ we obtained with the Lorentzian (cyclabs) model, the corresponding minimum of the line profile are calculated to be at 26.8 keV and 56.3 keV which are

consistent with the values obtained by Doroshenko et al. (2011) within error bars. The depth and width of the cyclotron lines are also consistent. Figure 3.4 shows the best fit continuum models and Table 3.3 shows the best fitting parameters.

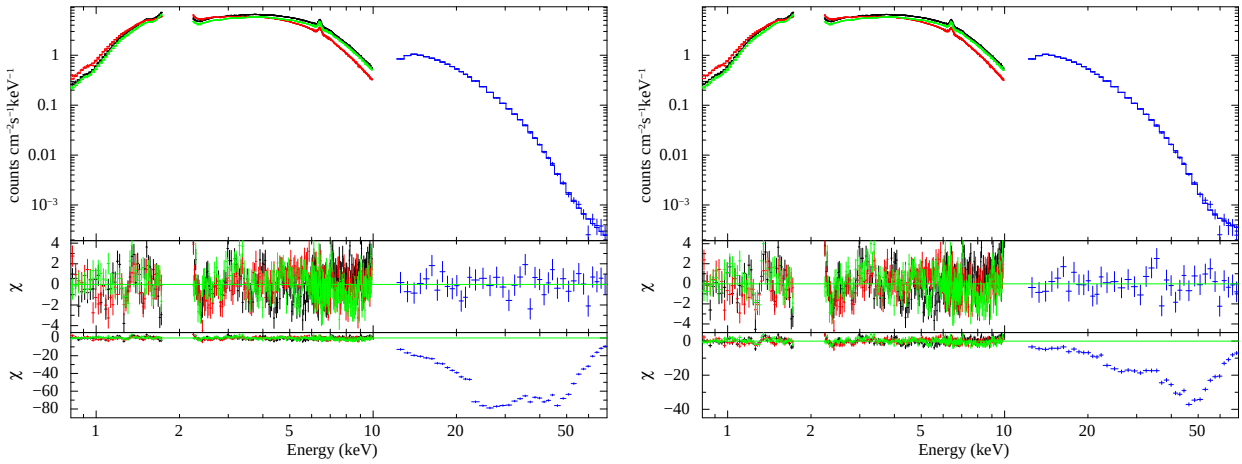

Figure 3.4: The different panels in the figure depict the same as in Figure 3.1 for Vela X-1. The left figure shows the results obtained with the Highecut model and the right shows the same obtained with the CompTT model.

3.9 A0535+26

A0535+26 was observed twice with *Suzaku* (Mitsuda et al., 2007) on September 14–15 2005 during the declining phase of the second normal outburst of 2005 and August 24 2009 during the decline of the 2009 normal outburst. We have chosen the 2009 observation (Obs. Id–404054010) for our analysis because of the longer duration (exposure $\sim$ 52 ks) and its 'HXD nominal' pointing position which is more suitable for CRSF studies, although the count rates were comparable for both the observations.

The XIS data of A0535 +26 had value of 3 $ct/sq\,arcmin/s/CCD\,exposure$ at the image peak, and showed no evidence of significant pile-up. The XIS spectra were rebinned by a factor of 6 from 0.8-6 keV and 7-10 keV, and by a factor of 2 between 6-7 keV. The PIN spectrum was rebinned by a factor of 2 upto 22 keV, by 4 upto 45 keV, and 6 upto 70 keV.

Table 3.3: Best fitting spectral parameters of Vela X-1 with a partial covering high-energy cutoff model. Errors quoted are for 99 per cent confidence range.

parameters	Highecut	CompTT
$N_{\rm H1}^{a}$ (10^{22} atoms cm^{-2})	1.38 ± 0.01	1.05 ± 0.02
$N_{\rm H1}^{a}$ (10^{22} atoms cm^{-2})	$4.00^{+0.27}_{-0.26}$	$6.30^{+0.30}_{-0.29}$
Cv_{fract}	0.38 ± 0.01	0.451 ± 0.008
PowIndex	1.19 ± 0.01	–
E-folding energy (keV)	$16.1^{+1.7}_{-1.5}$	–
E-cut energy (keV)	24.6 ± 0.8	–
$powerlaw_{norm}$ [c]	0.190 ± 0.001	–
$CompTT_{0}$ (keV)	–	0.49 ± 0.01
CompTT kT (keV)	–	10.6 ± 0.1
CompTT τ	–	10.95 ± 0.01
$CompTT_{norm}$ [c]	–	0.062 ± 0.001
$\rm E1_{cycl}$ (keV)	24.1 ± 1.0	$24.4^{+1.7}_{-1.6}$
$\rm D1_{cycl}$	0.26 ± 0.04	0.28 ± 0.05
$\rm W1_{cycl}$ (keV)	$4.8^{+1.9}_{-1.4}$	$7.7^{+3.0}_{-2.3}$
$\rm E2_{cycl}$ (keV)	$50.5^{+3.4}_{-2.7}$	$48.7^{+1.3}_{-1.2}$
$\rm D2_{cycl}$	$0.94^{+0.33}_{-0.28}$	$1.82^{+0.18}_{-0.17}$
$\rm W2_{cycl}$ (keV)	$10.00^{+4.3}_{-3.3}$	$19.3^{+3.8}_{-2.9}$
Iron line energy (keV)	$6.41\pm$ 0.01	$6.41\pm$ 0.01
Iron line eqwidth (eV)	56.8 $\pm$2.3	56.7 $\pm$2.2
Flux (XIS) [d] (0.3-10 keV)	1.53 ± 0.01	1.53 ± 0.01
Flux (PIN) [e] (10-70 keV)	4.12 ± 0.01	4.11 ± 0.01
reduced χ^2/d.o.f	2.03/831	1.92/832

[a] Denotes the Galactic line of sight absorption [b] Denotes the local absorption by the partial covering absorber 'pcfabs'.

[c] photons $\rm keV^{-1}\,cm^{-2}\,s^{-1}$ at 1 keV

[d] $10^{-10}\,\rm ergs\,cm^{-2}\,s^{-1}$ and are in 99 % confidence range.

[e] $10^{-10}\,\rm ergs\,cm^{-2}\,s^{-1}$ and are in 99 % confidence range.

3.9.1 Broadband Continuum modeling

We tried to fit the spectrum with all the continuum models described in section 3.3. For A0535+26 the best fits were obtained with the NPEX, powerlaw and the 'CompTT'

model (assuming spherical geometry for the comptonizing region). The powerlaw model however did not require a 'highecut' to fit the energy spectra. Including the GSO spectra in the fitting, the relative normalization of the GSO with respect to XIS showed that the flux in the GSO band (50-200 keV) was overestimated ~ 4 times without the inclusion of a 'highecut' in the spectrum. As inclusion of the GSO spectrum is not possible for phase resolved studies due to its limited statistics, and a spectrum of an accretion powered pulsar without a cutoff at higher energies is not viable, we have carried out further analysis with the 'NPEX' and 'CompTT' models. In both the cases, along with the Galactic line of sight absorption, a partial covering absorption model 'pcfabs' was applied to take into account the local absorption evident at certain pulse phases, which is evident in the pulse profiles and is local to the neutron star in Chapter 2. A Gaussian line was also used to model the narrow Fe kα feature found at 6.4 keV. In addition, a deep and wide feature found at ~ 45 keV was modeled with a Lorentzian profile, which is the CRSF found previously in this source (Caballero et al., 2007). The CRSF parameters were also consistant within error bars for both the continuum models, the centroid energy being only slightly higher for the 'powerlaw' model. The reduced χ^2 obtained for the models were 1.25 and 1.26 for 839 and 840 d.o.f respectively with no systematic residual pattern. Figure 3.5 shows the best fit continuum models and Table 3.4 shows the best fitting parameters.

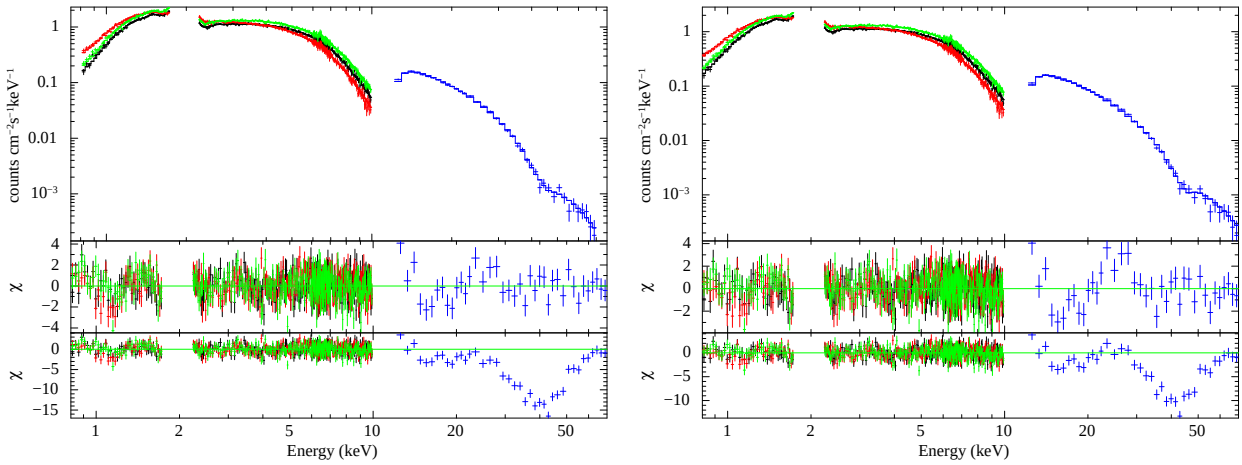

Figure 3.5: The different panels in the figure depict the same as in Figure 3.1 for A0535+26. The left figure shows the results obtained with the NPEX model and the right one shows the same obtained with the CompTT model.

Table 3.4: Best fitting phase averaged spectral parameters of A 0535+26. Errors quoted are for 99 per cent confidence range.

Model	A 0535+26	
parameters	NPEX	CompTT
$N_{\rm H1}^{a}$ (10^{22} atoms cm^{-2})	0.59 ± 0.02	$0.31^{+0.04}_{-0.03}$
$N_{\rm H2}^{b}$ (10^{22} atoms cm^{-2})	$3.7^{+0.3}_{-0.4}$	7.4 ± 1.1
$Cv_{\rm fract}$	0.49 ± 0.01	0.37 ± 0.02
$CompTT_{\rm T0}$ (keV)	–	0.52 ± 0.04
CompTT KT (keV)	–	$14.7^{+2.0}_{-1.5}$
CompTT τ	–	$7.3^{+0.4}_{-0.5}$
$CompTT_{\rm norm}$ ^{c}	–	0.008 ± 0.001
NPEX $\alpha 1$	$1.01^{+0.05}_{-0.04}$	–
NPEX $\alpha 2$	-2.0 (frozen)	–
NPEX KT (keV)	$11.5^{+1.2}_{-1.1}$	–
$NPEX_{\rm norm}$ 1^{c}	$0.041^{+0.002}_{-0.001}$	–
$NPEX_{\rm norm}$ 2^{c}	$4.94e-6 \pm 1.25e-6$	–
$E1_{\rm cycl}$	$42.6^{+0.9}_{-0.8}$	$43.2^{+0.8}_{-0.6}$
$D1_{\rm cycl}$	$1.3^{+0.3}_{-0.2}$	$1.4^{+0.4}_{-0.3}$
$W1_{\rm cycl}$	$7.2^{+2.3}_{-1.8}$	$4.9^{+1.4}_{-1.2}$
Iron line energy (keV)	6.41 ± 0.01	6.41 ± 0.01
Iron line eqwidth (eV)	23.4 ± 4.6	24.3 ± 5.3
Flux (XIS) ^{d} (0.3-10 keV)	3.05 ± 0.04	3.05 ± 0.05
Flux (PIN) ^{e} (10-70 keV)	8.14 ± 0.02	8.14 ± 0.03
reduced χ^2/d.o.f	1.25/839	1.26/837

^{a} Denotes the Galactic line of sight absorption ^{b} Denotes the local absorption by the partial covering absorber 'pcfabs'.

^{c} photons $\mathrm{keV}^{-1}\,\mathrm{cm}^{-2}\,\mathrm{s}^{-1}$ at 1 keV

^{d} $10^{-10}\,\mathrm{ergs\,cm^{-2}\,s^{-1}}$ and are in 99 % confidence range.

^{e} $10^{-10}\,\mathrm{ergs\,cm^{-2}\,s^{-1}}$ and are in 99 % confidence range.

3.10 XTE J1946+274

XTE J1946+274 was observed on October 11 2010 (Obs. Id–405041010) just after the peak of the September/October 2010 type I (see Chapter 1 for details on outbursts of

BeXRBs) outburst. The observation had an exposure of $\sim$ 51 ks.
The XIS data of XTE J1946+274 had a value of 2 $ct/sq\,arcmin/s/CCD\,exposure$ at the image peaks, and showed no evidence of significant pile-up. The XIS spectra were rebinned by a factor of 6 from 0.8-6 keV and 7-10 keV, and by a factor of 2 between 6-7 keV. Due to poorer statistics in the PIN spectrum of XTE J1946+274, higher rebinning factors of 2, 6, and 10 were applied as in the case of A 0535+26.

3.10.1 Broadband Continuum modeling

We tried to fit the spectrum with all the continuum models described above. For XTE J1946+274, best fits with similar values of reduced χ^2 were obtained with the 'highecut', 'NPEX' and 'CompTT' model.'Pcfabs' was applied to take into account the local absorption of the neutron star and a Gaussian line was also used to model the narrow Fe kα feature found at 6.4 keV. A deep and wide residual was found at $\sim$ 38 keV, at the same energy as the CRSF discovered by Heindl et al. (2001). As discussed previously, the CRSF was modeled with a Lorentzian profile. The 'highecut' and 'NPEX' models gave consistant values of the CRSF parameters, but the 'CompTT' model required a much shallower and narrow profile. Moreover, all the parameters of the 'CompTT' model could not be constrained well for this source, probably due to the poorer quality of the PIN data. We have thus carried out the further analysis of this source with the two former models. For the best fitting models, the reduced χ^2 was 1.09 and 1.11 respectively for 826 d.o.f. Without the inclusion of the CRSF, the difference in χ^2 ($\Delta\ \chi^2$) was 150 and 119 respectively for the same models. The best-fitting values for the spectral models for both the sources are given in Table 3.5. Figure 3.6 shows the best-fit spectra of the source with both the continuum models.
Müller et al. (2012) however have reported analysis of the *RXTE* , *Integral* and *Swift* observations during the same outburst of this source. Instead of a line at 36 keV, they found a weak evidence of a CRSF at $\sim$ 25 keV. It may be worthwhile mentioning in this context that the *Suzaku* PIN data has better sensitivity than *INTEGRAL* ISGRI at this energy range, and hence may be better suited for CRSF detection. We have carefully checked the statistical significance and possible systematic errors associated the CRSF.

Statistical significance: To estimate the detection significance of the CRSF we tried to fit the PIN spectrum only with the 'highecut' model with its powerlaw index frozen to the value obtained from the best fitting broadband spectrum. The addition of the

CRSF improved the χ^2 from 51.56 to 28.13 for 20 d.o.f corresponding to an F value of 16.7, and a F-test false alarm probability of 6×10^{-4}.

Possible systematic errors: At first, we checked the reproducibility of the NXB using the earth occultation data (Fukazawa et al., 2009). We extracted the spectra using the earth occultation data in three energy bands centering the CRSF and compared ratio of the count rates with the NXB. The ratio obtained were 1.3, 1.2 and 1.2 at $10-28$, $28-48$ and $48-70$ keV respectively indicating the lack of any energy dependent feature that can be introduced by the simulated X-ray background. We also included a systematic uncertainty of 3% on the PIN spectrum to check the detection of the CRSF. The line was still detected, but the uncertainty in the depth of the feature increased by 23%. The detection of pulse phase dependence of this feature as discussed in section 3.3.2 is also in favor of its presence since the background data is not expected to vary over the pulse phase. Finally, to verify the existence of the CRSF in a model independent manner, we divided the PIN spectrum of a pulse phase with the deepest CRSF, by the same of a pulse phase with the shallowest CRSF detected (see Chapter 5). Figure 3.6 shows the ratio plot of the two spectra. Although the quality of the data is not good after 40 keV, the dip at $\sim$ 30-35 keV is clearly seen indicating the presence of the CRSF.

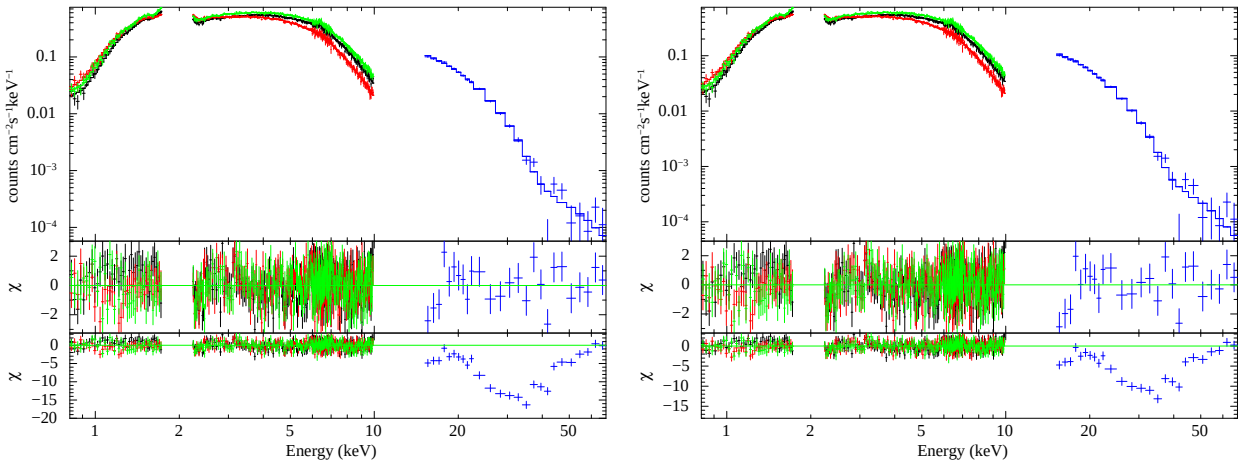

Figure 3.6: The different panels in the figure depict the same as in Figure 3.1 for XTE J1946+274. The left panel shows the results obtained with the Highecut model and the right panel shows the same obtained with the NPEX model.

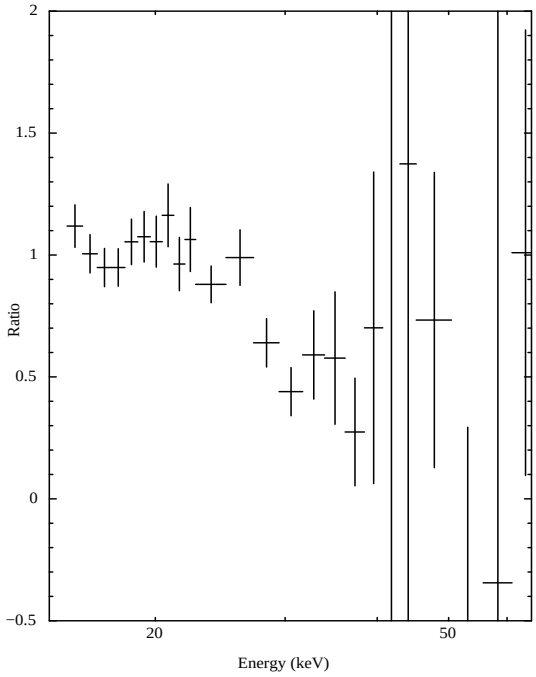

Figure 3.7: Ratio of counts of the energy spectrum with the shallowest cyclotron line to counts of the spectrum with the deepest cyclotron line in XTE J1946+274. Though the ratio of the counts after 40 keV have large error bars due to statistical limitations, the dip in counts at $\sim$ 30-40 keV is clearly visible indicating the presence of the CRSF

Table 3.5: Best fitting phase averaged spectral parameters of XTE J1946+274. Errors quoted are for 99 per cent confidence range.

Model	XTE J1946+274	
parameters	highecut	NPEX
$N_{\rm H1}^{a}$ (10^{22} atoms cm^{-2})	1.3 ± 0.03	$1.27^{+0.03}_{-0.04}$
$N_{\rm H2}^{b}$ (10^{22} atoms cm^{-2})	$5.9^{+0.9}_{-0.8}$	$9.0^{+2.7}_{-1.7}$
$Cv_{\rm fract}$	0.27 ± 0.04	$0.17^{+0.04}_{-0.05}$
PowIndex	$1.09^{+0.05}_{-0.04}$	–
E-folding energy (keV)	$25.6^{+2.8}_{-2.3}$	–
E-cut energy (keV)	$7.0^{+0.7}_{-0.3}$	–
$powerlaw^{c}_{\rm norm}$	0.021 ± 0.001	–
NPEX $\alpha 1$	–	$0.70^{+0.08}_{-0.10}$
NPEX $\alpha 2$	–	-2.0 (frozen)
NPEX KT (keV)	–	$13.3^{+2.4}_{-2.7}$
$NPEX_{\rm norm}$	–	$0.014^{+0.002}_{-0.001}$
$NPEX_{\rm norm}$ 2^{c}	–	$2.34^{d} \pm 1.5$
$E1_{\rm cycl}$	$38.3^{+1.6}_{-1.4}$	$38.6^{+1.9}_{-1.8}$
$D1_{\rm cycl}$	$1.7^{+0.4}_{-0.3}$	$1.5^{+0.6}_{-0.4}$
$W1_{\rm cycl}$	$9.6^{+3.7}_{-3.1}$	$8.6^{+5.4}_{-3.3}$
Iron line energy (keV)	6.41 ± 0.022	6.41 ± 0.02
Iron line eqwidth (eV)	29.1 ± 4.9	28.4 ± 5.2
Flux (XIS) ^{d} (0.3-10 keV)	1.80 ± 0.02	1.80 ± 0.02
Flux (PIN) ^{e} (10-70 keV)	3.47 ± 0.01	3.59 ± 0.0
reduced χ^2/d.o.f	1.09/826	1.11/826

^{a} Denotes the Galactic line of sight absorption ^{b} Denotes the local absorption by the partial covering absorber 'pcfabs'.

^{c} photons $\mathrm{keV}^{-1}\,\mathrm{cm}^{-2}\,\mathrm{s}^{-1}$ at 1 keV

^{d} $10^{-10}\,\mathrm{ergs\,cm^{-2}\,s^{-1}}$ and are in 99 % confidence range.

^{e} $10^{-10}\,\mathrm{ergs\,cm^{-2}\,s^{-1}}$ and are in 99 % confidence range.

3.11 4U 1907+09

4U 1907+09 was also observed twice with *Suzaku*, once on May 2006, and again on April 2007. We have analyzed both the observations in this thesis, henceforth referred as Obs.1

and Obs. 2 respectively. Obs.1 had an exposure of $\sim$ 57 ks and Obs. 2 had an exposure of $\sim$ 158 ks.

For 4U 1907+09, Obs.1 did not show any evidence of pile-up. For obs.2 however, the value obtained was higher than that of Crab Nebula count rate of 36 $ct/sq\,arcmin/s/CCD\,exposure$, and the radius at which this value equals 36 in the PSF is about 15-16 arcsec. Thus the check performed showed a case of moderate photon pile-up, and 15 pixels from the image center were removed to account for this effect. The XIS spectra were rebinned by a factor of 6 from 0.8-6 keV and 7-10 keV, and by a factor of 2 between 6-7 keV. The PIN spectrum was rebinned by a factor of 2 upto 22 keV, by 4 upto 45 keV, and 6 upto 70 keV.

3.11.1 Light curves and hardness ratio

4U 1907+09 is a variable X-ray source showing flaring and dipping activity in the timescales of minutes to hours (in 't Zand et al., 1997). Figures 3.8 shows the XIS and PIN light curves along with the hardness ratio for both the observations. As can be seen from the figure Obs. 1 shows a clear dip near the middle of the observation. For Obs. 2, the light curves show two flaring features in between and a dip in the last $\sim$ 10 ks of the observation. These features were also mentioned in Rivers et al. (2010), while performing time resolved spectroscopy of the same *Suzaku* observations, and were probed further by them to investigate the spectral variability with time. The flares and dips may, however affect our results of pulse phase resolved spectroscopy. As is seen, for Obs. 1 the hardness ratio remains more or less constant throughout the observation. We have therefore taken the entire stretch of the observation for our analysis. For Obs. 2, which is of a much longer duration, we have thus compared the pulse profiles and the energy spectra in these stretches individually with that from the rest of the observation. Though the pulse profiles look very similar in all the stretches, the energy spectra is harder with an increased absorption in the last stretch of the observation containing the dip. Thus, we took only the stretch of the observation excluding the dips for further analysis.

3.11.2 Broadband Continuum modeling

For both the observations, best fits were obtained with the 'highecut', 'NPEX' and 'compTT' model with comparable values of reduced χ^2 and similar residual patterns.

Rivers et al. (2010) also obtained similar results with the 'highecut', 'fdcut' and 'NPEX' model. A comparison between the NPEX model parameters obtained in our analysis and those reported in Rivers et al. (2010) reveals very consistant set of parameter values for Obs.1, but a softer less absorbed spectra obtained by us in the case of Obs.2. This is expected, since for Obs. 2 we have excluded the the last stretch of data from our analysis which had a more harder and absorbed spectra. Two Gaussian lines were also used in both the observations to model the narrow Fe kα and Fe kβ feature found at 6.4 and $\sim$ 7.1 keV respectively. In addition, a relatively shallow and narrow feature found at $\sim$ 18 keV was modeled with a Lorentzian profile which is the CRSF previously detected in this source (Makishima & Mihara, 1992; Makishima et al., 1999). As also discussed in Rivers et al. (2010), the first harmonic of the CRSF at $\sim$ 36 keV could not be detected in the PIN spectra probably due to the statistical limitation of the data in this energy range. **Fixing the energy of the first harmonic at twice the fundamental and its width at twice the fundamental width, the upper limit obtained on the depth was 0.7 for both the models.**

For both the observations, the CRSF fundamental parameters obtained with the 'NPEX' and 'CompTT' models were consistant within error bars with that found by Rivers et al. (2010). The 'highecut' model however required a deeper CRSF in both the cases to fit the spectra. The reduced χ^2 obtained for the models were 2.01, 1.22 and 1.23 for 1123, 1124 and 1124 d.o.f for Obs.1 and 1.62, 1.51 and 1.69 for 832, 837 and 838 d.o.f for Obs.2 in case of highecut, NPEX and CompTT respectively with no systematic residual patterns. Due to the compatibility of the CRSF parameters obtained with the 'NPEX' and CompTT models, we have carried out further phase resolved analysis using these two models. Figure 3.9 and 3.10 shows the best-fit spectra for 4U 1907+09. Obs.1 exhibits a higher value of $CompTT_{\rm T0}$ and lower NPEX Γ1 indicating a harder spectrum than Obs.2. Table 3.6 shows the best fitting parameters for both the observations.

3.12 GX 301-2

GX 301-2 is in an eccentric orbit (e=0.462) with an orbital period of 41.498 $\pm$0.002 days (Koh et al., 1997). The underlying orbital variability follows a consistent pattern (see Figure 3.11): shortly ($\sim$ 1.4 d) before the periastron passage the neutron star encounters a gas stream from the companion resulting in an extended X-ray flare, the activity

Table 3.6: Best fitting phase averaged spectral parameters of 4U 1907+09. Errors quoted are for 99 per cent confidence range.

Model	2006		2007	
parameters	NPEX	CompTT	NPEX	CompTT
$N_{\rm H1}^{a}$ (10^{22} atoms cm^{-2})	2.51 ± 0.03	1.92 ± 0.03	1.97 ± 0.01	1.62 ± 0.03
$CompTT_{\rm T0}$ (keV)	–	0.66 ± 0.01	–	0.47 ± 0.01
CompTT KT (keV)	–	4.7 ± 0.1	–	4.80 ± 0.04
CompTT τ	–	15.4 ± 0.2	–	14.9 ± 0.1
$CompTT_{\rm norm}$ ^{c}	–	0.011 ± 0.001	–	0.032 ± 0.001
NPEX $\alpha 1$	0.59 ± 0.03	–	0.84 ± 0.02	–
NPEX $\alpha 2$	-2.0 (frozen)	–	-2.0 (frozen)	–
NPEX KT (keV)	4.4 ± 0.1	–	4.41 ± 0.04	–
$NPEX_{\rm norm}$ 1^{c}	0.021 ± 0.001	–	0.072 ± 0.001	–
$NPEX_{\rm norm}$ 2^{c}	$8.50e-5 \pm 6.80e-6$	–	$2.47e-4 \pm 7.5e-6$	–
$E1_{\rm cycl}$	17.9 ± 0.3	$17.8^{+0.3}_{-0.4}$	$17.9^{+0.2}_{-0.1}$	18.1 ± 0.2
$D1_{\rm cycl}$	0.71 ± 0.06	0.68 ± 0.06	0.68 ± 0.03	0.61 ± 0.03
$W1_{\rm cycl}$	$3.0^{+0.8}_{-0.7}$	$2.9^{+0.8}_{-0.7}$	3.3 ± 0.4	2.8 ± 0.4
Iron line energy (keV)	7.03 ± 0.02	7.02 ± 0.02	$7.10^{+0.03}_{-0.02}$	$7.10^{+0.03}_{-0.04}$
Iron line eqwidth (eV)	5.91.9	6.4 ± 1.8	10.7 ± 2.9	7.9 ± 2.6
Iron line energy (keV)	6.41 ± 0.022	6.41 ± 0.02	$6.420^{+0.008}_{-0.010}$	$6.420^{+0.007}_{-0.009}$
Iron line eqwidth (eV)	59.1 ± 7.3	60.1 ± 8.3	51.7 ± 3.6	43.8 ± 1.7
Flux (XIS) ^{d} (0.3-10 keV)	1.84 ± 0.02	1.84 ± 0.02	4.75 ± 0.06	4.74 ± 0.06
Flux (PIN) ^{e} (10-70 keV)	3.43 ± 0.01	3.44 ± 0.01	6.87 ± 0.02	6.91 ± 0.02
reduced χ^2/d.o.f	1.22/1124	1.23/1124	1.51/837	1.69/838

^{a} Denotes the Galactic line of sight absorption ^{b} Denotes the local absorption by the partial covering absorber 'pcfabs'.
^{c} photons $\mathrm{keV}^{-1}\,\mathrm{cm}^{-2}\,\mathrm{s}^{-1}$ at 1 keV
^{d} $10^{-10}\,\mathrm{ergs\,cm}^{-2}\,\mathrm{s}^{-1}$ and are in 99 % confidence range.
^{e} $10^{-10}\,\mathrm{ergs\,cm}^{-2}\,\mathrm{s}^{-1}$ and are in 99 % confidence range.

decreases during the periastron passage and reaches a minimum shortly after that. The X-ray luminosity slowly increases over the orbit again until a second minimum is encountered near the apastron where the spiral shaped gas stream is intercepted a second time. The overall change in luminosity through the orbit is about a factor of ten. The high mass X-ray binary GX 301-2 was observed twice with *Suzaku* ; once on August 25, 2008 in the lowest flux part of the binary orbit, and a much longer observation ($\sim$ 62 Ks) on January 5, 2009 at phase 0.2 after the minima (see Figure 3.11) For this analysis we have used the second observation as is specified in table 3.1.
The XIS data of GX 301-2 at this orbital phase had a value of 14 $ct/sq\,arcmin/s/CCD\,exposure$ at the image peaks, and showed no evidence of significant pile-up. The XIS spectra were rebinned by a factor of 6 from 0.8-6 keV and 7-10 keV, and by a factor of 2 between 6-7 keV. The PIN spectrum of was binned by a factor of 3 throughout its energy range.

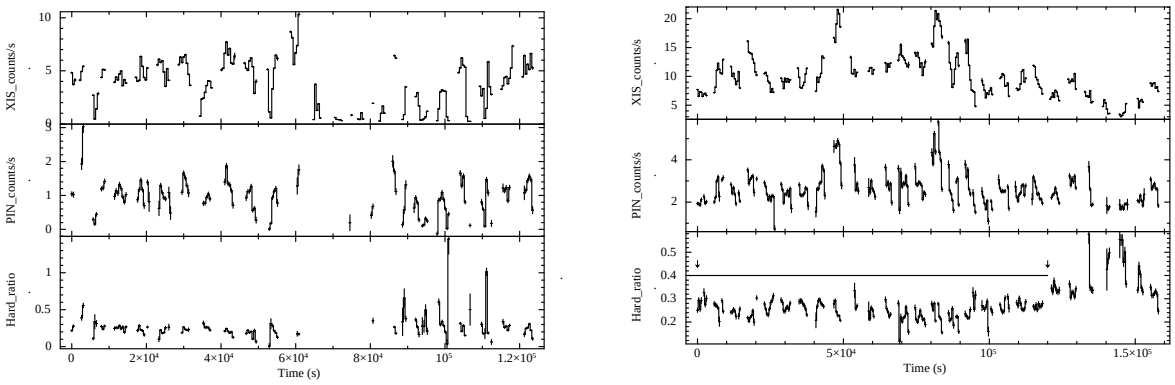

Figure 3.8: Light curves of 4U 1907+09 for the two *Suzaku* observations . The left panel corresponds to Obs. 1 and the right panel to Obs. 2. The first panels in each figure shows the light curve for one of the XIS in the energy band of 0.3-12 keV. The second panel shows the same obtained in the PIN energy band(10-70 keV). The time binning is equal to the respective pulse period of the source as described in Chapter 2. The bottom panel shows the hardness ratio. The arrows in the hardness ratio for the bottom figure indicate the stretch for which data was chosen to perform phase resolved analysis.

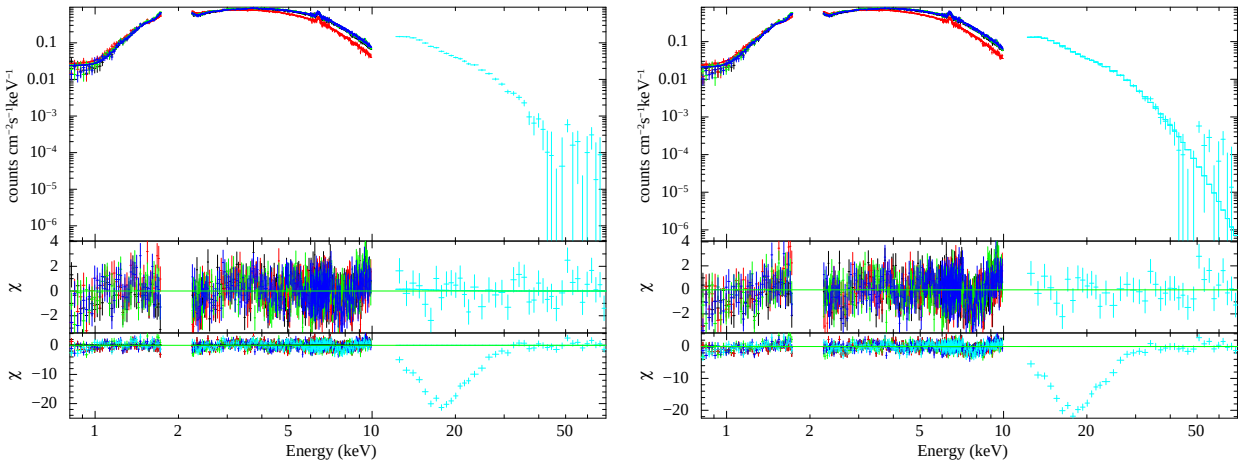

Figure 3.9: The different panels in the figure depict the same as in Figure 3.1 for Obs.1 of 4U 1907+09. The left panel shows the results obtained with the NPEX model and the right panel shows the same obtained with the CompTT model.

3.12.1 Broadband Continuum modeling

GX 301-2 has a very strong and variable absorption along its line of sight and an extremely strong FeK_{α} line. This source shows strong and significant residuals below 2-3

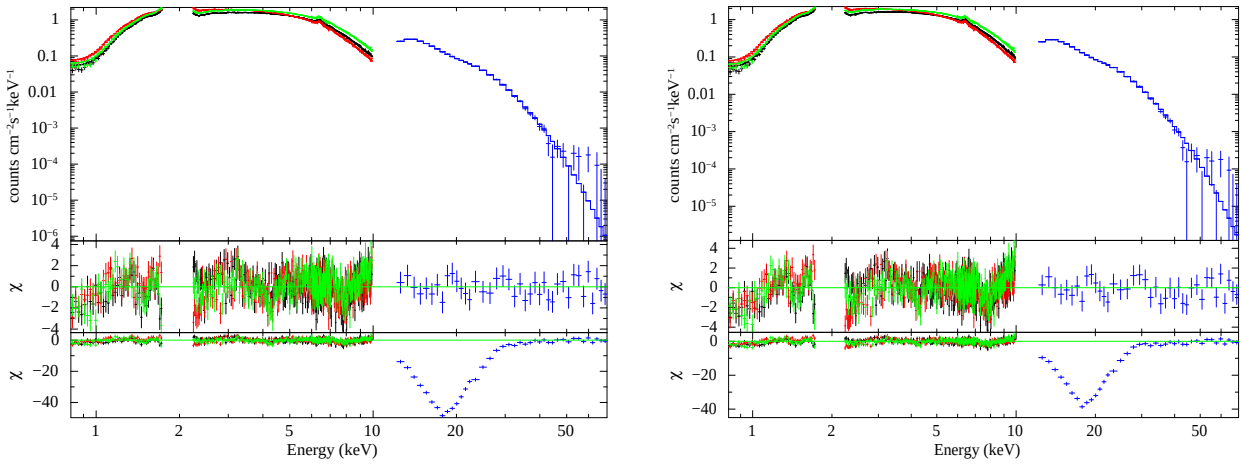

Figure 3.10: The different panels in the figure depict the same as in Figure 3.1 for Obs.2 of 4U 1907+09. The left panel shows the results obtained with the NPEX model and the right panel shows the same obtained with the CompTT model.

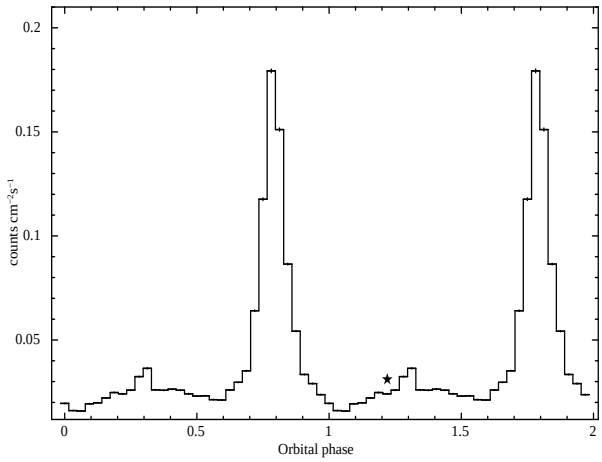

Figure 3.11: The left panel shows the Swift/BAT (15-150 keV) light curve folded with the orbital period of 41.48 days. The star indicates the phase at which the *Suzaku* observation was made.

keV, probably due to the spectral leakage or reprocessing at lower energies. This issue is already discussed in Suchy et al. (2012) who have analyzed the same *Suzaku* observation. Following their suggestion, we have ignored the low energy part of the spectrum below 3 keV, as is also mentioned in Chapter 2.

The source also shows complex low energy pulse profiles with absorption dips which

is thought to arise from the strong, variable and clumpy nature of the stellar wind (Kreykenbohm et al., 2004; Mukherjee & Paul, 2004). An additional partial covering absorber 'pcfabs' model in *XSPEC* needs to be added to the spectral model to account for this. We tried to fit the spectrum with all the continuum models described above. The best fits were obtained with the 'FDCUT' and 'HIGHECUT' model. In addition, a deep and broad cyclotron absorption feature was also found in the spectra at 36 keV. This feature was fitted with the *XSPEC* standard model 'cyclabs' which is a cyclotron absorption line having a Lorentzian profile. The fit however provided an unrealistically broadened line of $\sim$ 20 keV. A better fit with a narrower line was provided with the *XSPEC* Gaussian model 'gabs' for this source. The reduced χ^2 obtained by fitting these models were 1.92/640 d.o.f and 1.96 for 661 d.o.f respectively. The fit also improved significantly with the smoothed cutoff continuum model 'NEWHCUT' probably due to the very close $E_{\rm cut}$ and $E1_{\rm cycl}$ energy for this source, which not only introduces a strong correlation between the two parameters but also leaves residual like structures close to this energy. The reduced χ^2 also improved with the 'NEWHCUT' model with a value of 1.86 for 638 d.o.f, proving to be the best continuum model for this source. The CRSF parameters were also best constrained with this model, with a slightly lower centroid energy and σ value than in the case of 'FDCUT' model. This is the only source for which we did not find agreement between the CRSF parameter values for different spectral models. However, the spectrum of this source is very complicated and highly absorbed, and the continuum modeling of this source may also not be perfect although the continuum parameters were similar for both the models. The strong FeK_α emission line and FeK_β line found in the source were accounted by Gaussian emission lines. In addition a Ca K_α was also found in the spectrum. Figure 3.12 shows the best-fit spectra and Table 3.7 shows the best fitting parameters

3.13 4U 1626-67

The low mass X-ray binary 4U 1626-67 was observed twice with *Suzaku* , once just before its torque reversal in 2006 March, and once after the reversal in 2010 September. **Although the source was $\sim$ 3 times brighter during the second observation**, the first observation had a much longer exposure time of $\sim$ 72 Ks, and hence is used for our analysis.

Table 3.7: Best fitting phase averaged spectral parameters of GX 301-2. Errors quoted are for 99 per cent confidence range.

parameters	FDCUT	Newhcut
$N_{\rm H1}^{a}$ (10^{22} atoms cm^{-2})	$12.0^{+5.3}_{-1.8}$	$16.5^{+2.2}_{-2.3}$
$N_{\rm H2}^{b}$ (10^{22} atoms cm^{-2})	$20.4^{+2.6}_{-3.6}$	$17.4^{+1.3}_{-1.0}$
$Cv_{\rm fract}$	$0.94^{+0.03}_{-0.09}$	$0.89^{+0.04}_{-0.06}$
PowIndex	0.93 ± 0.01	0.95 ± 0.01
E-folding energy (keV)	$4.0^{+0.4}_{-0.3}$	5.1 ± 0.1
E-cut energy (keV)	$36.5^{+0.6}_{-0.7}$	29.8 ± 0.1
$powerlaw^{c}_{\rm norm}$	0.14 ± 0.01	0.151 ± 0.004
$E1_{\rm cycl}$	$36.3^{+1.5}_{-1.2}$	31.7 ± 0.1
$\sigma_{\rm cycl}$	8.3 ± 0.4	6.1 ± 0.1
$\tau_{\rm cycl}$	$13.4^{+2.3}_{-1.9}$	$16.5^{+2.0}_{-1.6}$
FeK_{β} energy (keV)	7.07 ± 0.01	7.08 ± 0.01
Iron line eqwidth (eV)	19.4 ± 2.2	19.5 ± 2.2
FeK_{α} energy (keV)	6.39 ± 0.01	6.39 ± 0.01
Iron line eqwidth (eV)	129.0 ± 4.9	128.9 ± 4.3
$E_{Ca}K_{\alpha}$ (keV)	3.69 ± 0.01	3.69 ± 0.01
$E_{Ca}K_{\alpha}$ eqwidth (eV)	16.9 ± 6.2	16.2 ± 5.9
Flux (XIS) [d] (0.3-10 keV)	8.23 ± 0.07	8.23 ± 0.07
Flux (PIN) [e] (10-70 keV)	5.36 ± 0.17	5.31 ± 0.18
reduced χ^2/d.o.f	1.92/645	1.87/657

[a] Denotes the Galactic line of sight absorption [b] Denotes the local absorption by the partial covering absorber 'pcfabs'.

[c] photons $\mathrm{keV}^{-1}\,\mathrm{cm}^{-2}\,\mathrm{s}^{-1}$ at 1 keV

[d] $10^{-10}\,\mathrm{ergs}\,\mathrm{cm}^{-2}\,\mathrm{s}^{-1}$ and are in 99 % confidence range.

[e] $10^{-9}\,\mathrm{ergs}\,\mathrm{cm}^{-2}\,\mathrm{s}^{-1}$ and are in 99 % confidence range.

The XIS data of 4U 1626-67 had a value of 2 $ct/sq\,arcmin/s/CCD\,exposure$ at the image peaks, and showed no evidence of significant pile-up. The XIS spectra were rebinned by a factor of 8 from 0.8-6 keV and 7-10 keV, and by a factor of 2 between 6-7 keV. The PIN spectrum of was binned by a factor of 2 upto 22 keV, by 6 upto 45 keV, and 10 upto 70 keV.

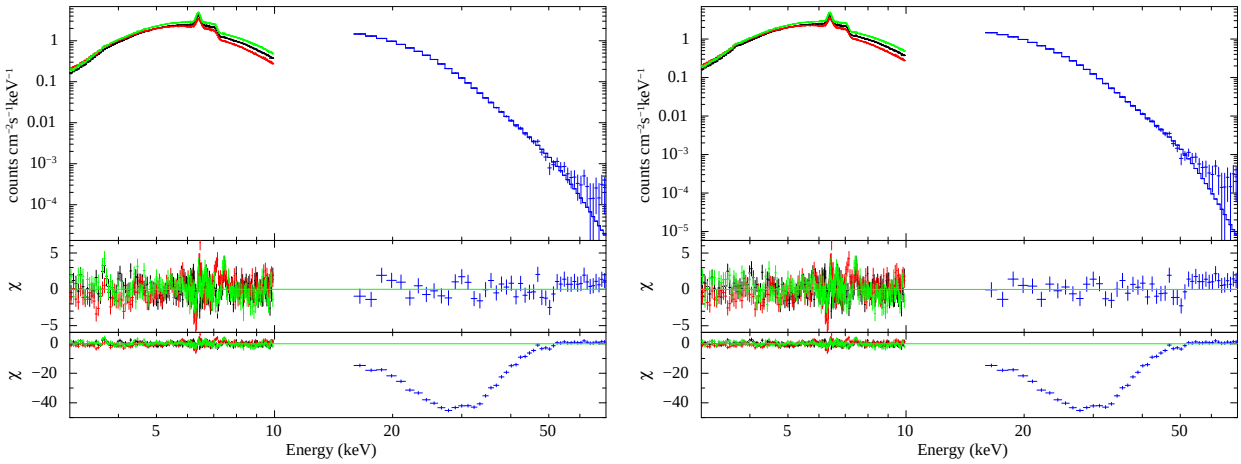

Figure 3.12: The different panels in the figure depict the same as in Figure 3.1 for GX 301-2. The left panel shows the results obtained with the FDCUT model and the right panel shows the same obtained with the newhcut model.

3.13.1 Broadband Continuum modeling

The broadband spectroscopy of 4U 1626-67 for both the *Suzaku* observations have been performed before by Camero-Arranz et al. (2012). They have fitted the continuum spectra with a powerlaw high-energy cutoff model and an additional low energy blackbody component. 4U 1626-67 shows complex energy dependent pulse profiles similar to many of the sources discussed here and we have included an additional partial covering absorber 'pcfabs' model to account for this. The low energy blackbody component is thus not required in our case. We could not constrain the $N_{\rm H1}$ value **and fixed it to the interstellar Galactic column density towards 4U 1626-67**.

We have obtained the best fits with the partial covering 'NPEX' and 'CompTT' models and did not find the high energy cutoff model a good description of the spectra as it shows signatures of systematic residuals. A deep an narrow absorption feature at $\sim$ 35 keV fitted with the *XSPEC* standard model 'cyclabs' which is a cyclotron absorption line having a Lorentzian profile. The line detected were however narrower and the partial absorption parameters lesser for the 'NPEX' model. The addition of a broad FeK_{α} emission line did not improve our fit as indicated in Camero-Arranz et al. (2012). We however found evidence of a strong line complex at $\sim$ 1 keV as indicated by Camero-Arranz et al. (2012). The two lines detected by us were Ne He α and Ne Ly

α, and Gaussian emission lines were added to account for these. The best fitted spectra had reduced χ^2 values of 1.79/899 d.o.f and 1.47/899 d.o.f for the 'NPEX' and 'Comptt' models respectively. Figure 3.13 shows the best-fit spectra and Table 3.13.1 shows the best fitting parameters.

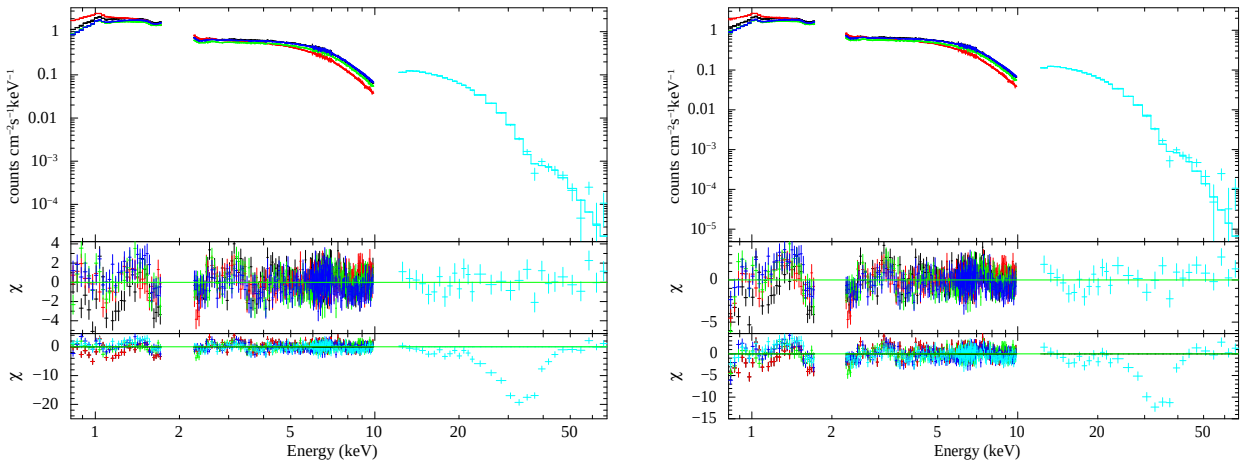

Figure 3.13: The different panels in the figure depict the same as in Figure 3.1 for 4U 1626-67. The left panel shows the results obtained with the CompTT model and the right panel shows the same obtained with the NPEX model.

3.14 Cen X-3

The high mass X-ray binary Cen X-3 was observed with *Suzaku* from December 8 2008 to December 10 2008 covering the entire binary orbit for 97 Ks. Half of the observation however consisted of the source in the low intensity states and the eclipse duration. As is evident from figure 3.14, the beginning $\sim$ 100 s, and the last 10^4 s consisted of the eclipse, with low intensity dips in between the observation. To perform the analysis, we have discarded the low count stretches of the observation which consisted of the beginning $\sim$ 100 s stretch and the last 7×10^4 s of the observation, since although it does not add to the statistics of the data, these time segments show some signatures of change in spectral shape. We have therefore analyzed the stretch of data with constant hardness ratio and spectral shape, and the effective exposure obtained was $\sim$ 48 Ks.

The XIS data had a value of 24 $ct/sq\,arcmin/s/CCD\,exposure$ at the image peaks, and showed no evidence of significant pile-up. The XIS spectra were rebinned by a

Table 3.8: Best fitting phase averaged spectral parameters of 4U 1626-67. Errors quoted are for 99 per cent confidence range.

parameters	CompTT	NPEX
$N_{\rm H1}^{a}$ (10^{22} atoms cm^{-2})	$0.09(fixed)$	$0.09(fixed)$
$N_{\rm H2}^{b}$ (10^{22} atoms cm^{-2})	8.3 ± 0.3	$12.8^{+0.7}_{-0.6}$
$Cv_{\rm fract}$	0.27 ± 0.01	0.35 ± 0.01
$CompTT_{\rm T0}$ (keV)	0.23 ± 0.04	–
CompTT KT (keV)	6.4 ± 0.2	–
CompTT τ	15.4 ± 0.2	–
$CompTT_{\rm norm}$ [c]	0.010 ± 0.001	–
NPEX Γ1	–	0.87 ± 0.01
NPEX Γ2	–	$-2.0(frozen)$
NPEX KT (keV)	–	5.4 ± 0.1
$NPEX_{\rm norm}$ 1[c]	–	0.023 ± 0.001
$NPEX_{\rm norm}$ 2[c]	–	$6.63e^{-5} \pm 2.99e^{-6}$
$E1_{\rm cycl}$	$35.3^{+0.6}_{-0.5}$	$35.1^{+0.6}_{-0.5}$
$D1_{\rm cycl}$ [d]	$1.6^{+0.4}_{-0.2}$	$1.6^{+0.8}_{-0.4}$
$W1_{\rm cycl}$	$4.1^{+1.3}_{-1.0}$	$2.5^{+1.0}_{-0.9}$
$NeHe_{\alpha}$ energy (keV)	0.92 ± 0.01	0.92 ± 0.01
$NeHe_{\alpha}$ eqwidth (eV)	7.7 ± 0.7	3.9 ± 0.3
$NeLy_{\alpha}$ (keV)	1.02 ± 0.01	1.02 ± 0.01
$NeLy_{\alpha}$ eqwidth (eV)	23.4 ± 6.9	16.2 ± 5.9
Flux (XIS) [e] (0.3-10 keV)	1.92 ± 0.03	1.96 ± 0.03
Flux (PIN) [f] (10-70 keV)	4.03 ± 0.01	3.91 ± 0.01
reduced χ^2/d.o.f	1.47/899	1.79/899

[a] Denotes the Galactic line of sight absorption [b] Denotes the local absorption by the partial covering absorber 'pcfabs'.

[c] photons $\mathrm{keV}^{-1}\,\mathrm{cm}^{-2}\,\mathrm{s}^{-1}$ at 1 keV

[d] $*10^{-7}$; [c] denotes the optical depth of the feature.

[e] $10^{-10}\,\mathrm{ergs\,cm^{-2}\,s^{-1}}$ and are in 99 % confidence range.

[f] $10^{-9}\,\mathrm{ergs\,cm^{-2}\,s^{-1}}$ and are in 99 % confidence range.

factor of 8 from 0.8-6 keV and 7-10 keV, and by a factor of 2 between 6-7 keV. The PIN

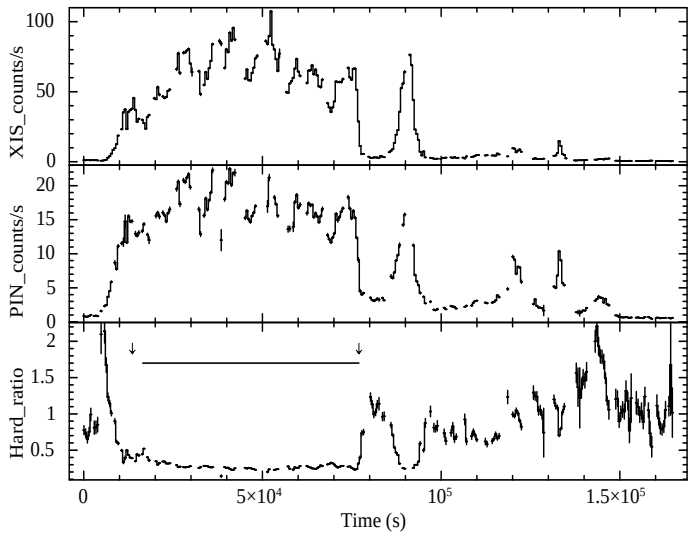

Figure 3.14: Top panel shows the XIS light curve (0.3–10 keV) for the entire *Suzaku* observation showing the "dip" and the "eclipse" durations. The middle panel shows the PIN light curve (10–70 kev) for the same. The bottom panel shows the hardness ratio (PIN counts/ XIS counts) for the entire duration of the observation .The arrows indicate the stretch of the observation that was used for the analysis.

spectrum of was binned by a factor of 2 upto 22 keV, by 4 upto 45 keV, and 6 upto 70 keV.

3.14.1 Broadband Continuum modeling

The broadband spectroscopy of Cen X-3 using the same *Suzaku* observation has been performed before by Naik et al. (2011b) who performed broadband spectroscopy at different phases of the binary orbit. We have however done the same in the entire stretch of the observation after discarding the low count stretches. The source has a high, variable wind and therefore varying absorption along the binary orbit. We have included the 'pcfabs' model in this case to account for this effect. We tried to fit the spectrum with all the continuum models as for the other sources. Naik et al. (2011b) have obtained the best fit with the partial covering high-energy cutoff model throughout the binary orbit. We have however found the partial covering NPEX and CompTT to provide better fits, with the reduced $\chi^2 > 3$ in the case of the high-energy cutoff model. In addition, a very deep and broad cyclotron absorption feature was also found in the spectra at ~ 30 keV. This feature was fitted with the *XSPEC* standard model 'cyclabs' which is a cyclotron

absorption line having a Lorentzian profile. The fit however provided an unrealistically broadened line of > 20 keV. A better fit with a narrower line was provided with the Gaussian model 'gabs' for this source. Three Fe K emission line features were found as also reported in Naik et al. (2011b) at 6.4, 6.7 and 6.97 keV. Gaussian emission lines were added to the spectrum to account for these. In addition, we also detected a Fe L line at 0.82 keV, and Ne line complex at 0.98 keV. The best fits had reduced χ^2 values of 1.92/679 d.o.f and 2.64/683 d.o.f for the CompTT and NPEX models respectively. The CompTT model provides the best fit with very well constrained values of the CRSF parameters, although the values of the CRSF parameters obtained from the NPEX model are agreeable with these values. There is however a discrepancy between the pcfabs parameters, with the CompTT model consistent with a high $N_{\rm H2}$ value of ~ 95 and the NPEX model consistent with a low value of $N_{\rm H2}$ value of ~ 4. The $Cv_{\rm fract}$ values are comparable. Figure 3.15 shows the best-fit spectra and Table 3.9 shows the best fitting parameters.

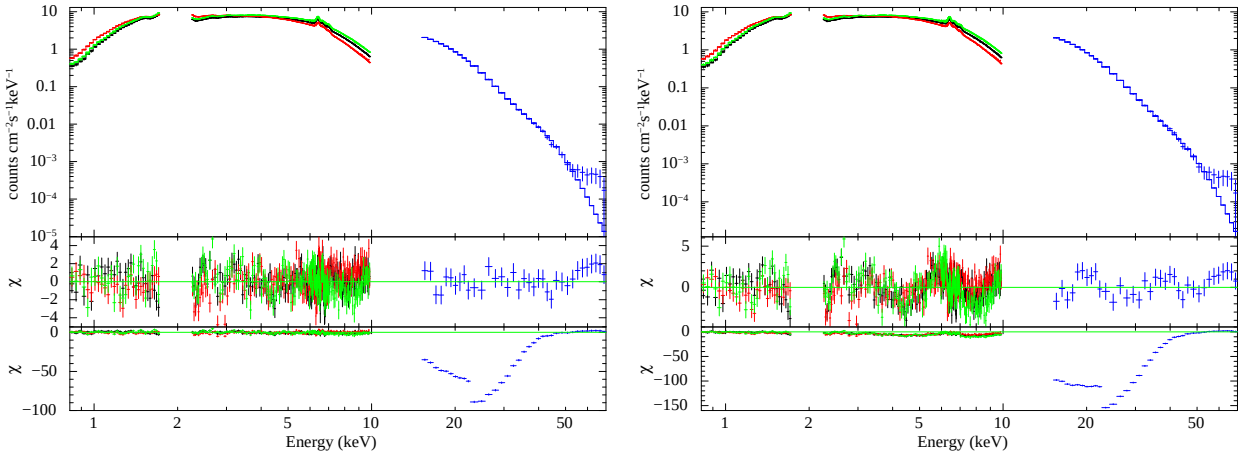

Figure 3.15: The different panels in the figure depict the same as in Figure 3.1 for Cen X-3. The left panel shows the results obtained with the CompTT model and the right panel shows the same obtained with the NPEX model.

3.15 Her X-1

Her X-1 was initially observed twice with *Suzaku* , once during 2005 October and once during 2006 March. Both observations were chosen carefully to avoid eclipses, and the

source was in its "on-state" (which corresponds to high X-ray flux) during both. The results corresponding these observations are presented in Enoto et al. (2008). It was further observed for a longer duration in 2008 during its on state. At the time of writing thesis, we have analyzed the 2008 data for our work. The source was subsequently also observed in 2010 and 2012, and the work to analyze those results are ongoing.
The XIS data had a value of 1 $ct/sq\,arcmin/s/CCD\,exposure$ at the image peaks, and showed no evidence of significant pile-up. The XIS spectra were rebinned by a factor of 8 from 0.8-6 keV and 7-10 keV, and by a factor of 2 between 6-7 keV. The PIN spectrum of was rebinned by a factor of 4 throughout its energy range.

3.15.1 Broadband Continuum modeling

The broadband spectroscopy of Her X-1 using the 2005 2006 *Suzaku* observations have been performed before by Enoto et al. (2008). They have used the NPEX model to fit the continuum spectra. We tried to fit the spectrum with all the continuum models as for the other sources. In addition we also added the partial covering absorber pcfabs, which is consistent with the source having a complex energy dependent pulse profile with dips that disappear at higher energies (Deeter et al., 1998). We have found the NPEX, the high-energy cutoff and the FDCUT models to be the best description of the spectrum of this source. The CompTT model did not provide a good fit and the model parameters could not be constrained well. Even after adding the partial covering pcfabs, there was some excess at low energies ($<$ 1 keV) for which we added an additional blackbody component of temperature $\sim$ 0.1 keV. We could not constrain the $N_{\rm H1}$ value since it is very low and **fixed it to the value of interstellar Galactic column density towards Her X-1.** The local absorption column density value $N_{\rm H2}$ however turned out to be very high and could not be constrained very well for all the spectral models. The high value of $N_{\rm H2}$ is however consistent with the dips extending to higher energies ($>$ 20 keV).

A weak FeK_α emission line was detected. A Ne IX line was also detected around 0.94 keV. In addition, a very deep and broad cyclotron absorption feature was also found in the spectra at $\sim$ 39 keV. This feature was fitted with the *XSPEC* standard model 'cyclabs' which is a cyclotron absorption line having a Lorentzian profile. This line however could not be constrained with the high-energy cutoff model. With the NPEX and FDCUT models too, the addition of 'cyclabs' model resulted in unrealistically broadened lines of

$>$ 15 keV. A better fit with narrower lines were provided with the Gaussian model 'gabs' for this source. The CRSF centroid energy and σ were consistent for both the models although the FDCUT model required a very high τ value for the fit. The final best fits for the spectrum were thus obtained with the partial covering NPEX and FDCUT models model with the gabs model, the emission lines and the blackbody component. The best fits corresponded to reduced χ^2 values of 1.05/682 d.o.f and 1.06/682 d.o.f respectively with the FDCUT and NPEX models. Figure 3.16 shows the best-fit spectra Table 3.10 shows the best fitting parameters.

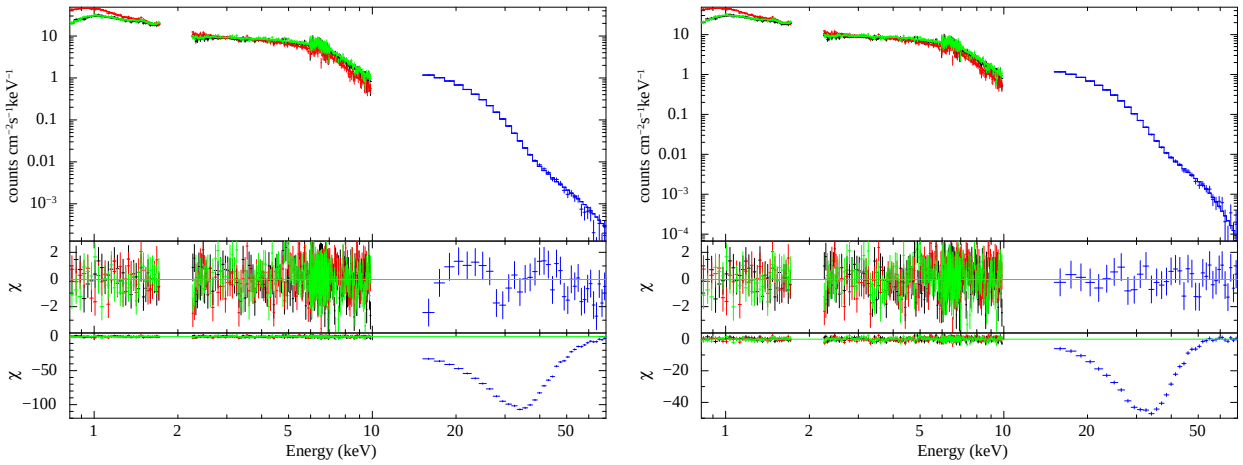

Figure 3.16: The different panels in the figure depict the same as in Figure 3.1 for Her X-1. The left panel shows the results obtained with the FDCUT model and the right panel shows the same obtained with the NPEX model.

3.16 EXO 2030+375

The transient Be/X-ray binary pulsar exo 2030+375 observed on 2007 May 14 at the peak of its regular type I outburst. The XIS data of EXO 2030+375 showed no evidence of significant pile-up, although the source was very bright during the time of the observation . This is due to the fact that the observation was fixed at $\frac{1}{4}$ window 'burst' mode. The XIS spectra were rebinned by a factor of 6 from 0.8-6 keV and 7-10 keV, and by a factor of 2 between 6-7 keV. The PIN spectrum was binned by a factor of 4 throughout its energy range. The GSO spectrum was binned with the fixed grouping scheme provided

by the instrument team [5].

3.16.1 Broadband Continuum modeling

As for the other sources, we tried to fit the spectrum with all the continuum models described above. All the other continuum models, except the 'highecut' model provides unacceptable fits to the spectrum. Apart, from very high values of reduced χ^2 (> 3) for the other continuum models, the residuals after fitting shows a broad dip like feature between 20-30 keV, which can be fitted with a shallow but unphysically broad CRSF at $\sim$ 24 keV. The 'highecut' model however does not produce any residual at that energy indicating that the residual might be an artifact due to incorrect continuum modeling. In addition we also added a partial covering absorber pcfabs, which is consistent with the source having a complex energy dependent nature of its pulse profile (Refer Chapter 2). As the observation was during the peak of the Type I outburst and the pulsar being bright at hard X-rays, the presence of several emission lines is expected in the spectrum. Therefore, we added Gaussian functions at above energies to the spectral model and re-fitted the spectra. Though these emission lines are weak, addition of these lines to the model improved the simultaneous spectral fitting with reduced χ^2 of 1.59 (for 638 dof). Further, since the dips in the pulse profile extend upto very high energies ($\sim$ 100 keV) for this source, we were motivated to use a partially ionized (*zxipcf* model in XSPEC; Reeves et al. 2008) absorber. Using the partially ionized absorber component in the spectral model, the ionization states of the absorbing medium and the corresponding covering fraction can be investigated. The *zxipcf* model component in $XSPEC$ uses a grid of $XSTAR$ (Kallman et al. 2004) photoionized absorption models for absorption. The free parameters in this model are N_{H2} (in 10^{22} cm^{-2}), Cv_{fract} (covering fraction), and the ionization parameter ξ (erg cm s^{-1}; Reeves et al. 2008). The spectral fitting was improved marginally with the use of partially ionized partial covering absorber with a reduced χ^2 of 1.51 (for 637 dof). The ionization parameter indicates the presence of moderately ionized matter ($log(\xi) \sim 1.56$) as a local absorber to the photons produced from the accretion column. Figure 3.17 shows the best-fit spectra Table 3.11 shows the best fitting parameters.

[5] http://heasarc.gsfc.nasa.gov/docs/suzaku/analysis/gsobgd64bins.dat

It may be noted in this context that the spectral fitting of the *RXTE* observations of the pulsar during 2006 June giant outburst showed the presence of a cyclotron resonance feature centered at ∼11 keV (Wilson et al., 2008). A cyclotron resonance line at ∼63 keV was reported at certain pulse phase ranges of the pulsar from the *INTEGRAL* observations during same giant outburst (Klochkov et al., 2008a). From *RXTE* observations of the pulsar at relatively lower luminosity level, a spectral feature was detected at ∼36 keV and ascribed to a cyclotron absorption feature (Reig & Coe, 1999b). However, in our best fit spectral model, no such absorption feature was present at above energies. Therefore, we did not include any additional cyclotron absorption component to the spectral fitting.

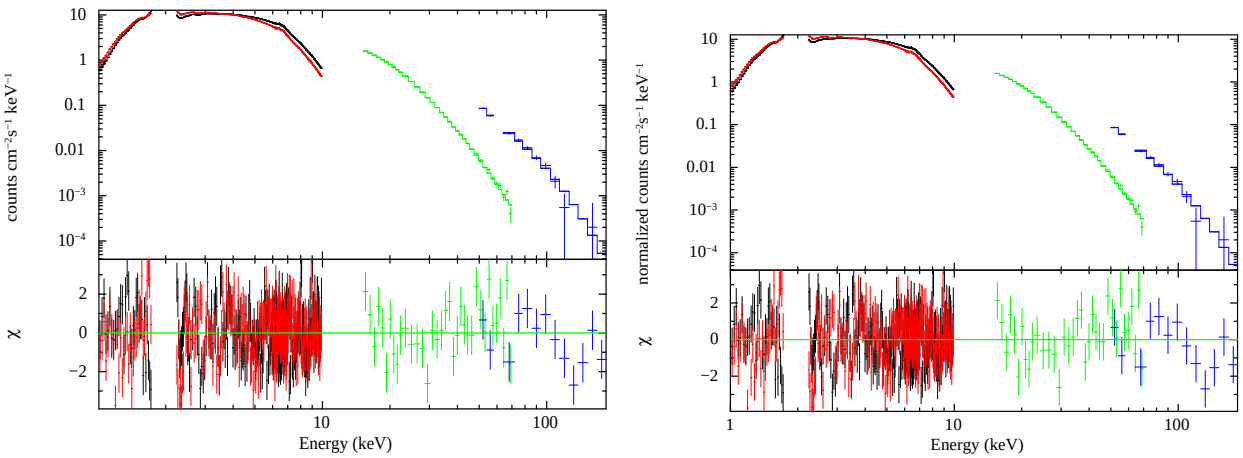

Figure 3.17: The different panels in the figure depict the same as in Figure 3.1 for EXO 2030+375. The left panel shows the results obtained with the neutral absorber model and the right panel shows the same obtained with the ionized absorber model.

3.17 GX 1+4

GX 1+4 was observed with *Suzaku* for ∼ 100 Ks on 2010 October 02. The XIS data had a value of 6 $ct/sq\,arcmin/s/CCD\,exposure$ at the image peaks, and showed no evidence of significant pile-up. The XIS spectra were rebinned by a factor of 6 from 0.8-6 keV and 7-10 keV, and by a factor of 2 between 6-7 keV. The PIN spectrum was binned by a factor of 2 upto 22 keV, by 4 upto 45 keV, and 6 upto 70 keV.

3.17.1 Broadband Continuum modeling

High resolution X-ray spectroscopy of GX 1+4 was performed by Paul et al. (2005) using *Chandra* observations. We present here the results of broadband spectroscopy of the source. As for the other sources, we tried to fit the spectrum with all the continuum models. As is mentioned in Chapter 1, the source being highly absorbed, we fitted the energy spectra in the range > 2 keV. The best fit was obtained with the 'NPEX' model, with the 'highecut', 'CompTT' and 'FDCUT' models yielding unacceptable results. In addition a very strong FeK_α and a FeK_β emission lines were detected in the energy spectrum. The hard nature of the X-ray spectrum and a very strong Fe fluorescent emission motivated us to fit the spectrum with the *XSPEC* model 'pexrav', which is an exponentially cut off power law spectrum reflected from neutral material (Magdziarz & Zdziarski, 1995). The 'pexrav' model provided a marginally better fit then the 'NPEX' model with the reduced χ^2 values being 1.84/708 d.o.f and 1.85/707 d.o.f respectively. This is an indication that the X-ray spectrum of GX 1+4 is Compton reflection dominated (occurs when the X-ray impinges upon a slab of cold matter, probably circumstellar matter in this case). This has also been pointed out by Rea et al. (2005) from the *BeppoSAX* observation of the source at different intensity states.

Although the pulse profiles show low energy dip like structures (refer Chapter 2), we did not require an additional partial covering absorber to fit the spectrum. This aspect is discussed in detail in the next chapter. We also did not find any evidence of a CRSF in the energy spectrum as hinted in Ferrigno et al. (2007). Figure 3.18 shows the best-fit spectra and Table 3.12 shows the best fitting parameters.

3.18 Discussion & Summary

In this chapter the results of the broadband spectroscopy of accretion powered pulsars are presented. All the bright sources observed with *Suzaku* for long exposures have been analyzed. For each source, the parameter values obtained with different continuum and line models are presented and compared. The models which give us physical as well as consistant results are chosen as the best suited continuum models for the particular source. Table 3.13 summarizes the results obtained from the broadband spectroscopy of these sources.

In the process of trying to fit the energy spectrum with different continuum models we

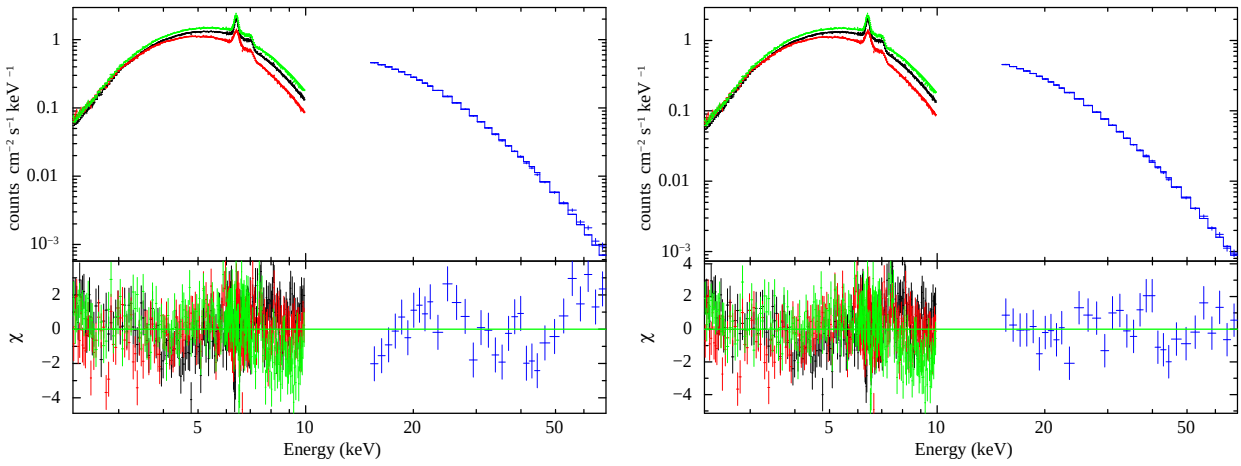

Figure 3.18: Phase averaged spectrum of GX 1+4 with the best fit continuum models after inclusion of all the emission lines. The left panel shows the results obtained with the 'npex' model and the right panel shows the same obtained with the 'pexrav' absorber model. First panel of both the figures show the phase averaged spectrum of GX 1+4 with the best fit continuum models, the second panel shows the residuals.

have also noticed certain trends in continuum model fitting. The 'highecut' 'FDCUT' and 'Newhcut' models being very simple models with less number of parameters, is a good choice to model the continuum in case of moderate or poor statistics like XTE J1946+274. Which of the three was a better fit depended on the particular source itself. For example 'FDCUT' and 'Newhcut' were better continuum models in the case of GX 301-2 since the very close $E_{\rm cut}$ and $E1_{\rm cycl}$ energy possibly introduced some artificial correlation between the parameter values for the 'Highecut' model. But in general the 'Highecut' and the 'Newhcut' models provided very similar fits with similar parameter values for only a slightly better reduced χ^2 value as also in the case of XTE J1946+274. The 'CompTT' on the hand which is a more physical description of the spectra and has a reasonable number of free parameters is better for continuum fitting specially for phase resolved spectroscopy described in later chapters only if the statistical quality of the data is reasonably good. This is probably the reason why it described the spectra very well for Vela X-1, A 0535+26, 4U 1907+09 and Cen X-3, and failed to constrain the continuum well in the case of XTE J1946+274. The 'NPEX' model on the other hand, although being a phenomenological model has a clear physical meaning and approximates the photon number spectrum for an unsaturated Comptonization (Sunyaev & Titarchuk,

1980; Meszaros, 1992), is useful for all the sources with significantly different statistical quality except for Vela X-1 and GX 301-2 where it provided unacceptable fits. EXO 2030+375 also fits well only to a 'highecut' model inspite of the data quality being very high. **One more exception is GX 1+4 which is described well by a reflection dominated 'pexrav' model due to its hard spectrum and exceptionally strong FeK_α emission of equivalent width $\sim$ 150 eV**.

The CRSFs are well fitted with both Gaussian and Lorentzian profiles for all the sources except for GX 301-2, Cen X-3 and Her X-1 where Lorentzian profile 'Cyclabs' resulted in unphysical broad absorption lines. It is also worth mentioning that we did not require any broad absorption or emission feature at $\sim$ 10 keV to fit the spectrum of any sources as required in the *Suzaku* observations of 1A 1118-61 (Suchy et al., 2011), 4U 1907+09 (Rivers et al., 2010) and *RXTE* observations of GX 301-2 (Suchy et al., 2008). We suspect it may be a result of imperfect modeling of the continuum spectrum, as is also mentioned in Coburn et al. (2002).

Lastly, *Suzaku* with its broadband capability and high sensitivity is ideal to probe the detailed spectrum of the accretion powered pulsars which were observed with the same for long exposures. It provides us the great opportunity to study pulse phase resolved variations of the spectra for slow pulsars, particularly, with respect to its CRSF features, which are highly sensitive to continuum modeling and requires careful modeling of the broadband spectrum for reliable results. It also allows us to study the pulse phase resolved variations of the narrow dip like features in the pulse profiles in these sources as described in Chapter 2, which is accounted by an additional partial absorbing component in their spectrum. The next two chapters, 4 and 5 are dedicated to the study of the pulse phase resolved variations of these features in the spectra of slow accretion powered pulsars with the aid of the broadband continuum modeling results obtained in this chapter.

Table 3.9: Best fitting phase averaged spectral parameters of Cen X-3. Errors quoted are for 99 per cent confidence range.

parameters	CompTT	NPEX
$N_{\rm H1}^{a}$ (10^{22} atoms cm^{-2})	$1.00^{+0.10}_{-0.08}$	1.22
$N_{\rm H2}^{b}$ (10^{22} atoms cm^{-2})	0.8 ± 0.3	3.9 ± 0.1
$Cv_{\rm fract}$	0.43 ± 0.02	0.57 ± 0.01
$CompTT_{\rm T0}$ (keV)	0.66 ± 0.02	–
CompTT KT (keV)	4.6 ± 0.1	–
CompTT τ	16.3 ± 0.2	–
$CompTT_{\rm norm}$ ^{c}	0.21 ± 0.01	–
NPEX Γ1	–	$1.16^{+0.04}_{-0.03}$
NPEX Γ2	–	$-2.0(frozen)$
NPEX KT (keV)	–	$4.5^{+0.2}_{-0.1}$
$NPEX_{\rm norm}$ 1^{c}	–	$0.51^{+0.06}_{-0.03}$
$NPEX_{\rm norm}$ 2^{c}	–	0.002 ± 0.001
$E1_{\rm cycl}$	30.2 ± 0.1	$31.0^{+1.5}_{-1.0}$
$\sigma_{\rm cycl}$	$7.9^{+0.6}_{-0.5}$	$10.5^{+2.8}_{-1.2}$
$\tau_{\rm cycl}$	$17.9^{+0.7}_{-0.6}$	$30.9^{+15.8}_{-10.2}$
FeK_{α} energy (keV)	6.39 ± 0.01	6.39 ± 0.01
Iron line eqwidth (eV)	61.7 ± 7.4	63.1 ± 8.2
Fe XXV energy (keV)	6.69 ± 0.02	6.69 ± 0.02
Iron line eqwidth (eV)	37.0 ± 2.9	40.5 ± 4.7
Fe XXVI energy (keV)	6.98 ± 0.01	6.98 ± 0.01
Iron line eqwidth (eV)	5.1 ± 3.6	7.3 ± 4.5
FeL_{α} energy (keV)	0.82 ± 0.01	0.82 ± 0.01
FeL_{α} eqwidth (eV)	37.6 ± 5.4	36.1 ± 4.7
$NeLy_{\alpha}$ (keV)	0.98 ± 0.01	0.98 ± 0.01
$NeLy_{\alpha}$ eqwidth (eV)	18.14 ± 3.38	19.24 ± 4.22
Flux (XIS) ^{d} (0.3-10 keV)	2.28 ± 0.28	2.28 ± 0.28
Flux (PIN) ^{e} (10-70 keV)	5.36 ± 0.20	5.49 ± 0.21
reduced χ^2/d.o.f	1.92/679	2.64/683

^{a} Denotes the Galactic line of sight absorption ^{b} Denotes the local absorption by the partial covering absorber 'pcfabs'. ^{c} photons $\rm keV^{-1}\,cm^{-2}\,s^{-1}$ at 1 keV ^{d} 10^{-9} ergs $\rm cm^{-2}\,s^{-1}$ and are in 99 % confidence range. ^{e} 10^{-9} ergs $\rm cm^{-2}\,s^{-1}$ and are in 99 % confidence range.

Table 3.10: Best fitting phase averaged spectral parameters of Her X-1. Errors quoted are for 99 per cent confidence range.

parameters	FDCUT	NPEX
$N_{\rm H1}^{a}$ (10^{22} atoms cm^{-2})	0.02 (fixed)	0.02 (fixed)
$N_{\rm H2}^{b}$ (10^{22} atoms cm^{-2})	62.9 ± 27.4	89.4 ± 30.7
$Cv_{\rm fract}$	$0.21^{+0.14}_{-0.09}$	0.49 ± 0.11
PowIndex	$0.91^{+0.02}_{-0.03}$	–
E-folding energy (keV)	6.2 ± 1.5	–
E-cut energy (keV)	$35.6^{+6.1}_{-4.1}$	–
$powerlaw_{\rm norm}^{c}$	$0.15^{+0.04}_{-0.02}$	–
NPEX $\alpha 1$	–	0.2 ± 0.1
NPEX $\alpha 2$	–	$-2.0(frozen)$
NPEX KT (keV)	–	6.0 ± 0.2
$NPEX_{\rm norm}$ 1^{c}	–	$0.51^{+0.04}_{-0.03}$
$NPEX_{\rm norm}$ 2^{c}	–	$5.93e^{-4} \pm 0.0001$
$E1_{\rm cycl}$	$38.5^{+2.2}_{-0.9}$	$39.1^{+0.8}_{-0.9}$
$\sigma_{\rm cycl}$	$8.2^{+1.1}_{-0.8}$	7.2 ± 0.7
$\tau_{\rm cycl}$	31.7 ± 7.8	$19.8^{+4.6}_{-4.1}$
Bbody KT (keV)	0.13 ± 0.02	$0.15^{+0.04}_{-0.01}$
Bbody $Norm^{f}$	$0.003^{+0.002}_{-0.001}$	$0.003^{+0.002}_{-0.001}$
FeK_{α} energy (keV)	6.41 ± 0.02	6.41 ± 0.02
Iron line eqwidth (eV)	14.9 ± 5.5	24.5 ± 6.1
$NeIX$ (keV)	0.94 ± 0.01	0.94 ± 0.01
$NeIX$ eqwidth (eV)	18.8 ± 3.6	11.7 ± 4.6
Flux (XIS) ^{d} (0.3-10 keV)	2.5 ± 0.7	2.5 ± 0.7
Flux (PIN) ^{e} (10-70 keV)	4.57 ± 0.14	4.55 ± 0.14
reduced χ^2/d.o.f	1.05/682	1.06/682

^{a} Denotes the Galactic line of sight absorption ^{b} Denotes the local absorption by the partial covering absorber 'pcfabs'. ^{c} photons $\rm keV^{-1}\,cm^{-2}\,s^{-1}$ at 1 keV ^{d} 10^{-9} ergs $\rm cm^{-2}\,s^{-1}$ and are in 99 % confidence range. ^{e} 10^{-9} ergs $\rm cm^{-2}\,s^{-1}$ and are in 99 % confidence range.

^{f} in units of L_{39}/D_{10}^{2}, where L_{39} is the source luminosity in units of 10^{39} ergs^{-1} , D_{10} is the distance to the source in units of 10 kpc

Table 3.11: Best fitting phase averaged spectral parameters of EXO 2030+375. Errors quoted are for 99 per cent confidence range.

Model	Neutral absorber	Partially ionized absorber
$N_{\rm H1}^{a}$ (10^{22} atoms cm^{-2})	2.04 ± 0.01	2.07 ± 0.01
$N_{\rm H2}^{b}$ (10^{22} atoms cm^{-2})	40.9 ± 3.3	45.4 ± 2.8
$Cv_{\rm fract}$	0.13 ± 0.01	0.23 ± 0.01
$log(\xi)$	——	1.56 ± 0.15
PowIndex	1.33 ± 0.01	1.37 ± 0.01
E-folding energy (keV)	21.2 ± 0.2	21.5 ± 0.2
E-cut energy (keV)	12.4 ± 0.2	11.0 ± 0.8
Emission lines		
Si XIII		
Line energy (keV)	2.01 ± 0.01	2.01 ± 0.01
Line width (keV)	0.001	0.001
Line eq. width (eV)	2	2 ± 2
Si XIV		
Line energy (keV)	2.50 ± 0.03	2.51 ± 0.02
Line width (keV)	0.13 ± 0.03	0.14 ± 0.02
Line eq. width (eV)	11	13
S XV		
Line energy (keV)	3.19±0.01	3.19±0.01
Line width (keV)	0.11±0.02	0.12±0.01
Line eq. width (eV)	8	10
Fe K_{α}		
Line energy (keV)	6.39±0.01	6.4±0.02
Line width (keV)	$0.01^{+0.02}_{-0.01}$	0.05±0.02
Line eq. width (eV)	7	19
Fe XXVI		
Line energy (keV)	6.61±0.01	6.66±0.02
Line width (keV)	0.20±0.02	0.08±0.03
Line eq. width (eV)	51	25
Flux (XIS) [d] (0.3-10 keV)	$2.94^{+0.07}_{-0.06}$	$2.94^{+0.08}_{-0.09}$
Flux (PIN) [e] (10-70 keV)	$5.92^{+0.13}_{-0.12}$	$5.92^{+0.15}_{-0.13}$
Flux (GSO) [f] (70-200 keV)	$2.53^{+0.05}_{-0.05}$	$2.54^{+0.04}_{-0.07}$
reduced χ^2/d.o.f	1.59/638	1.51/637

[a] Denotes the Galactic line of sight absorption [b] Denotes the local absorption by the partial covering absorber 'pcfabs'.
[c] photons $\rm keV^{-1}\,cm^{-2}\,s^{-1}$ at 1 keV
[d] $10^{-9}\,\rm ergs\,cm^{-2}\,s^{-1}$ and are in 99 % confidence range.
[e] $10^{-9}\,\rm ergs\,cm^{-2}\,s^{-1}$ and are in 99 % confidence range.
[f] $10^{-9}\,\rm ergs\,cm^{-2}\,s^{-1}$ and are in 99 % confidence range.

Table 3.12: Best fitting phase averaged spectral parameters of GX 1+4. Errors quoted are for 99 per cent confidence range.

parameters	PEXRAV	NPEX
$N_{\rm H1}^{a}$ (10^{22} atoms cm^{-2})	13.96 ± 0.08	$13.54^{+0.04}_{-0.09}$
PowIndex	0.86 ± 0.01	–
E-folding energy (keV)	30.5 ± 0.7	–
Rel_{refl}	0.29 ± 0.06	–
$pexrav_{\rm norm}^{c}$	0.056 ± 0.001	–
NPEX $\alpha 1$	–	0.52 ± 0.01
NPEX $\alpha 2$	–	$-2.0(frozen)$
NPEX KT (keV)	–	10.9 ± 0.2
$NPEX_{\rm norm}$ 1^{c}	–	0.045 ± 0.001
$NPEX_{\rm norm}$ 2^{c}	–	$1.0e^{-5} \pm 1.0e^{-6}$
FeK_{α} energy (keV)	6.39 ± 0.01	6.39 ± 0.02
Iron line eqwidth (eV)	149 ± 12	151 ± 11
FeK_{β} energy (keV)	7.04 ± 0.01	7.04 ± 0.02
Iron line eqwidth (eV)	29 ± 2	30 ± 4
Flux (XIS) ^{d} (0.3-10 keV)	4.71 ± 0.05	4.70 ± 0.05
Flux (PIN) ^{e} (10-70 keV)	3.12 ± 0.07	3.11 ± 0.08
reduced χ^2/d.o.f	1.84/708	1.85/707

^{a} Denotes the Galactic line of sight absorption ^{c} photons $\mathrm{keV}^{-1}\,\mathrm{cm}^{-2}\,\mathrm{s}^{-1}$ at 1 keV ^{d} $10^{-10}\,\mathrm{ergs\,cm}^{-2}\,\mathrm{s}^{-1}$ and are in 99 % confidence range. ^{e} $10^{-9}\,\mathrm{ergs\,cm}^{-2}\,\mathrm{s}^{-1}$ and are in 99 % confidence range.

Table 3.13: Summary of broadband spectroscopy of accretion powered pulsars

Source	Best fit continuum models	Patial covering absorber	CRSF keV	Emission lines	Comments
1A 1118-61	NPEX & FDCUT	Y	47	FeK_α & FeK_β	Cutoffpl provides good fit but very broad CRSF
Vela X-1	Highecut & CompTT	Y	24 & 50	FeK_α	Ratio of CRSF harmonics > 2
A 0535+26	NPEX & CompTT	Y	43	FeK_α	Powerlaw provides good fit but flux overestimated ~ 4 times in the GSO band
XTE J1946+274	Highecut & NPEX	Y	38	FeK_α	CRSF reconfirmed at 38 keV.
4U 1907+09	NPEX & CompTT	N	18	FeK_α & FeK_β	CRSF harmonic at ~ 36 keV not detected.
GX 301-2	FDCUT & Newhcut	Y	36	FeK_α & FeK_β & Ca K_α	Highly absorbed spectrum.
4U 1626-67	NPEX & CompTT	Y	35	Ne He_α & He Ly_α	Interstellar absorption value fixed.
Cen X-3	NPEX & CompTT	Y	30	FeK_α, Fe XXV1, Fe Ly_α & Ne Ly_α	–
Her X-1	FDCUT & NPEX	Y	38	FeK_α & Ne IX	Interstellar absorption fixed.
EXO 2030+375	Highecut (partial and neutral absorber)	Y	N	FeK_α, Fe XXVI, Si XII, Si XIV, Si XV	CRSF not detected evidence for ionized partial absorber
GX 1+4	NPEX & PEXRAV	N	N	FeK_α & FeK_β	Reflection dominated spectrum in accretion powered pulsars .

Y – Yes ; N– No

Chapter 4

Pulse phase resolved spectroscopy: A powerful tool to probe the dips in the low energy pulse profile

4.1 Dips in pulse profiles

As discussed extensively in Chapter 2, many accretion powered pulsars show a drop in intensity over a narrow phase range, commonly referred to as dips in their pulse profiles. These can be attributed to the accretion column or the stream blocking our line of sight at some viewing angles to the neutron star. For the sources for which the energy dependent pulse profiles were investigated in detail in Chapter 2 to trace the evolution of the narrow low energy dips, we have carried out pulse phase-resolved spectroscopy in narrow phase bins to explain its complex nature and quantify the absorption local to the environment of the neutron star. This is a very important tool to probe the dips and its nature, and can have important implications on the properties of the accretion stream, its density, ionization state and clumpiness.

4.2 Results

In this Chapter we have presented the results of the pulse phase resolved spectroscopy of the continuum parameters in some bright accretion powered pulsars with *Suzaku* observations. The main emphasis is to be able to quantify and explain the narrow dips

in their pulse profiles with the partial covering absorber 'pcfabs' model in *XSPEC*, which needs to be added to the spectral model to account for this local absorption. The same set of observations that were used for the phase averaged analysis were used in the phase resolved case. The same duration of the observations as mentioned in Chapter 3 were also used for the analysis taking care of the luminosity variation and spectral variability wherever required. To investigate this we extracted the phase resolved spectra with 25 independent phase bins (except in the case of XTE J1946+274 as discussed later), applying phase filtering in the FTOOLS task XSELECT. For the phase resolved analysis we used the same background spectra and response matrices as was used for the phase averaged spectrum for both the XIS's and the PIN data. We also fitted the spectra in the same energy range and rebinned them by the same factor as in phase averaged case. All the individual spectra for the respective sources were fitted with the best fit continuum and line models discussed in Chapter 3, and the analytical expressions of the spectral models are also given in the same chapter. The value of the Galactic absorption (N_{H1}) and the Fe line width were frozen to the phase averaged values for the two respective model components. We froze the cyclotron parameters of the corresponding phase bins to the best-fit values obtained from the investigation of the cyclotron line parameters using $\frac{3}{25}$ pulse phases or two neighbouring phase bins as described in Chapter 5. Below are summarized the results of pulse phase resolved spectroscopy of the continuum parameters of some sources. The phases of the dips in the pulse profile and the corresponding changes in the the local absorption component (N_{H2}) and the covering fraction (Cv_{fract}) are with respect to the low energy XIS (0.3-10 keV) pulse profile. The pattern of variation of the other continuum parameters are with respect to the hard energy PIN (10-70 keV) profile unless otherwise indicated. For a detailed description of the pulse profiles at different energy bands and its evolution with energy refer to Chapter 2.

4.2.1 1A 1118-61

Phase resolved spectroscopy of Obs. 1 was carried out with the 'NPEX' and 'FDCUT' continuum models. Figure 4.1 shows the composite pulse profiles in the low and high energy band showing the location of the narrow dips in the low energy XIS pulse profile. Figure 4.2 shows the continuum parameters as a function of the pulse phase for the two models. The results obtained as seen from the figure for both the models are as follows.

1. At the dip in the pulse profile at phase ~ 0.1, there is sudden increase in the value

of the local absorption component (N_{H2}) with a corresponding dip in the value of the covering fraction (Cv_{fract}). This indicates the presence of a very dense clump of matter along our line of sight at that phase. The value of N_{H2} is higher for the 'NPEX' model although the Cv_{fract} shows a slightly lower value for the 'FDCUT' model.

2. At the main dip in the pulse profile at phase $\sim 0.4-0.5$ there is an increase in the value of N_{H2} as well as Cv_{fract}. This is commensurate with this being the phase corresponding to the most prominent dip in the pulse profile. At phase ~ 0.4 just before the main dip there is a drop in Cv_{fract} for both the models.

3. Photon index Γ and α also shows similar trends with the pulse phase for both the models. The spectrum is harder near the pulse peak and softer at the off pulse regions. This is also evident in the pulse profiles of the same observation.

4. The Folding energy E_{fold} is maximum between phase $0.1-0.2$ and shows a minima between phase $0.4-0.5$. kT also shows the maxima and minima at the same phases although the pattern of variability is a little different.

5. The cutoff energy E_{cut} shows a sudden increase between phase $0.1-0.2$ corresponding to the phase where the E_{fold} also peaks. It cannot be however constrained well between phases $0.2-0.4$.

6. The powerlaw and the 'NPEX' normalisations show significant variations with the pulse profile.

4.2.2 VELA X-1

Phase resolved spectroscopy was carried out with the 'highecut' and 'CompTT' continuum models. Figure 4.3 shows the composite pulse profiles in the low and high energy band showing the location of the narrow dips in the low energy XIS pulse profile. Figure 4.4 shows the continuum parameters as a function of the pulse phase for the two models. The results obtained as seen from the figure for both the models are as follows.

1. At the dips at phase ~ 0.3 and phase ~ 0.9 of the low energy XIS profile, there is a sudden increase in the value of the local absorption component (N_{H2}). The dip being larger at phase 0.3 the corresponding value of N_{H2} is also larger.

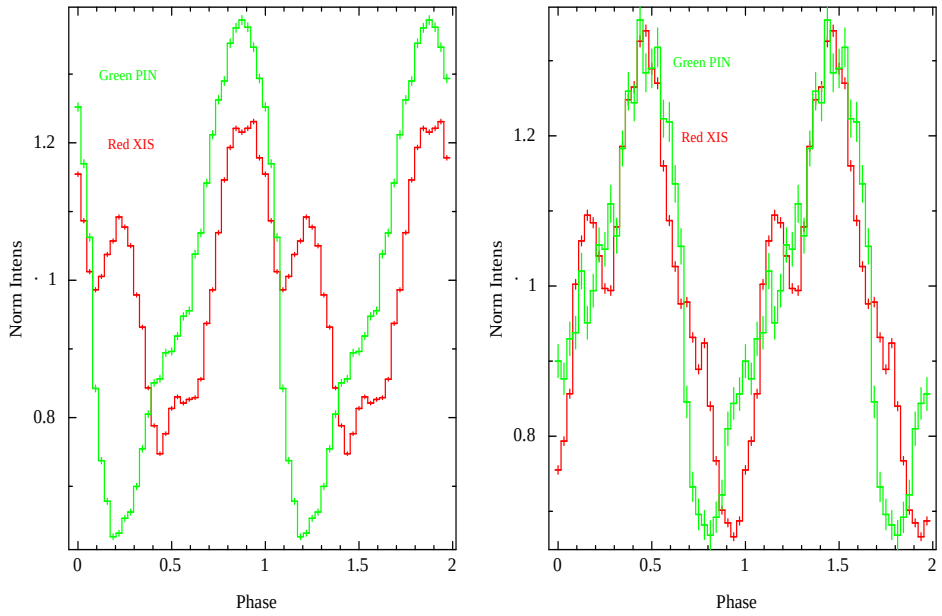

Figure 4.1: Left panel and right panel in the figure shows the background subtracted low energy XIS (0.3–10 keV) and the high energy PIN (10–70 keV) pulse profiles of Obs. 1 and Obs. 2 respectively of 1A 1118-61, showing the narrow dips in the pulse profile in the XIS band and its absence in the PIN band. In all the figures in this chapter, the pulse profiles denote normalised intensity unless mentioned otherwise.

2. At the main dip of the XIS profile between phase 0.5-0.6, there is also an indication of an increase of N_{H2} with a high covering fraction (Cv_{fract}). Similar to the case as in 1A 1118-61, this is consistent with this being the phase corresponding to the most prominent dip in the pulse profile.

3. The dip at phase $\sim$ 0.7 of the XIS profile has somewhat different characteristics and extends upto 20 keV. The 'highecut' model shows a very high value of N_{H2} and a very small Cv_{fract} at this phase. The 'CompTT' model however does not show any significant change in the values of N_{H2} or Cv_{fract}, but a very high optical depth (τ).

4. The value of Cv_{fract} shows somewhat different pattern of variation for the two models. For the 'highecut' model, the phases where N_{H2} is high usually has a small Cv_{fract}, but for the 'CompTT' model there is an indication of correlation between the two parameters.

5. In general the optical depth (τ) increases and the low-energy seed temperature

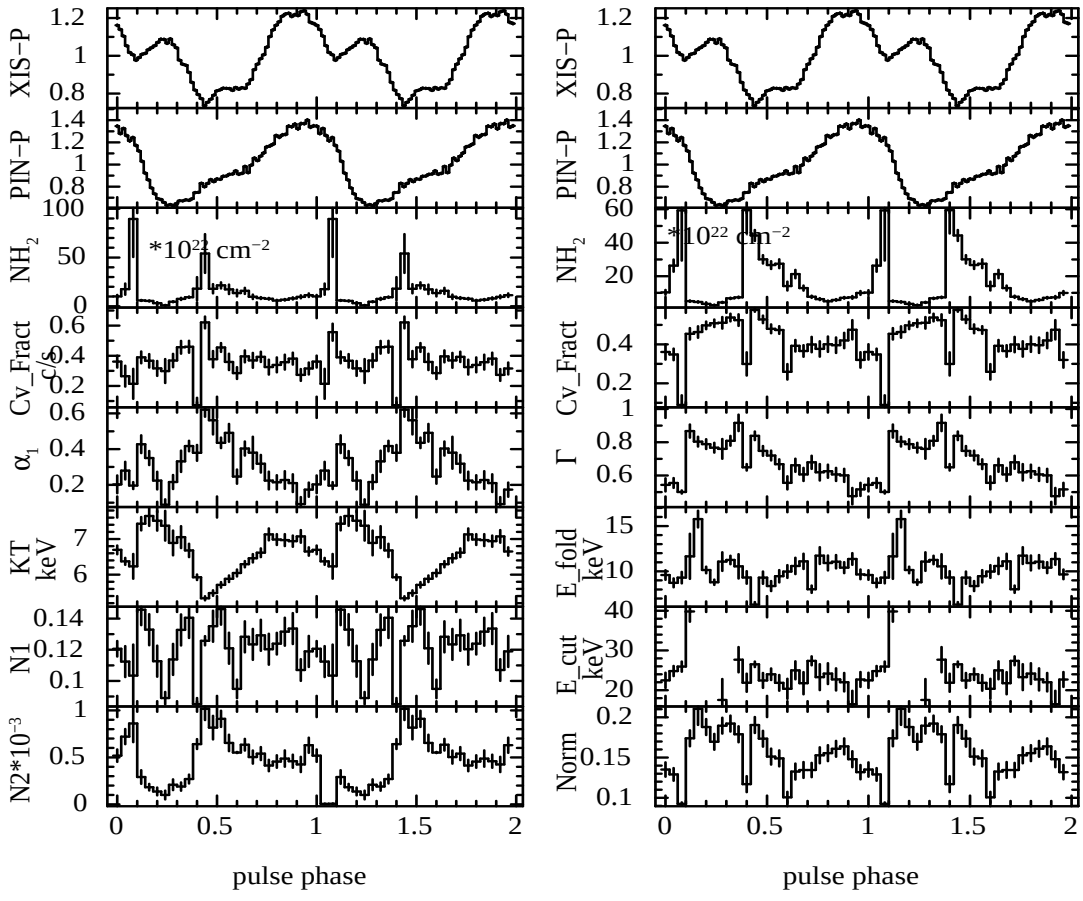

Figure 4.2: Variation of the spectral parameters with phase along with the pulse profile (0.3-12 keV for XIS and 10-70 keV for PIN) in 1A 1118-61. The pulse profiles of the pulsar are shown in top two panels of both sides of the figure, respectively. The left panel shows the variation using the model 'NPEX' and the right panel shows the same using the model 'FDCUT'.

(T_{seed}) falls at the dips of the XIS pulse profile.

6. The powerlaw photon index (Γ) shows a strong dependence on the pulse profile. It is hardest at high energy PIN pulse profile peaks and softest at the off pulse phases. Similar spectral hardening at the pulse peaks was found for this source previously by Kreykenbohm et al. (1999).

7. The folding energy (E_{fold}) varies with the pulse phase with the values peaking at the ascending and descending phases of the PIN pulse profile, and their minimum at the pulse peaks. The Cutoff-energy (E_{cut}) also varies with the pulse phase.

8. The electron temperature (kT) is highest at the ascending and descending phases of the PIN pulse profile at phases $\sim$ 0.1, 0.5, 0.7 and 1. It is lower in the off pulse regions.

9. The optical depth (τ) and kT however shows strong anti-correlation with each other throughout the pulse phase. This may imply that the statistics of the data are not good enough to determine the variation of these two parameters independently.

10. Both the power law normalizations and the CompTT normalizations shows a variability pattern with the values peaking at the peaks of the XIS pulse profile.

4.2.3 A0535+26

Phase resolved spectroscopy was carried out with the 'NPEX' and 'CompTT' continuum models. Figure 4.5 shows the composite pulse profile in the low and high energy band showing the location of the narrow dips in the low energy XIS pulse profile. The variation of the continuum parameters are shown as a function of pulse phase in Figure 4.6. Both the models give a consistent picture of the change in partial covering absorber and covering fraction (N_{H2} or Cv_{fract}) with the pulse phase. The results obtained as seen for the figure from both the models are as follows:

1. At the dip at phase $\sim$ 0.1 there is a moderate increase in the value of N_{H2} with no increase in Cv_{fract}. This is consistent with this dip extending upto only $\sim$ 7 keV in this source (Refer Chapter 2 for the detailed energy evolution of the same).

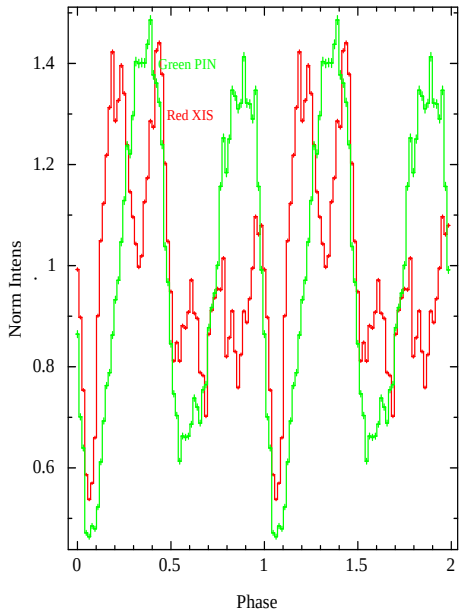

Figure 4.3: Figure showing the background subtracted low energy XIS (0.3–10 keV) and the high energy PIN (10–70 keV) pulse profile of Vela X-1 showing the narrow dips in the pulse profile in the XIS band and its absence in the PIN band.

2. There is a dip like structure between phase $\sim 0.2 - 0.3$ which prominent only at the lowest energies (< 2 keV). No significant change in N_{H2} or Cv_{fract} is seen at that phase range as is expected.

3. The main dip of the XIS profile between phase 0.6-0.7 is associated with an increase in both the N_{H2} and Cv_{fract} values. This is in agreement with this dip being the most prominent one in the XIS profile. Also the pattern of change in N_{H2} and Cv_{fract} values near this phase range is the same as the structure of the main dip.

4. There is no change in the N_{H2} or Cv_{fract} values at the apparent dip at phase ~ 0.5. As is also seen from Figure 4.5, this can be rather explained by a soft emission peak between phase $\sim$ 0.5–0.6. This is further supported by a very soft powerlaw slope (high Γ) at that phase.

5. Photon index Γ is in general low near the pulse peaks and high at the off pulse phases, indicating a harder spectra near the pulse peak.

6. Electron temperature KT does not show much variations with the pulse phase, but the optical depth τ is highest at the main dip at phase 0.6–0.7.

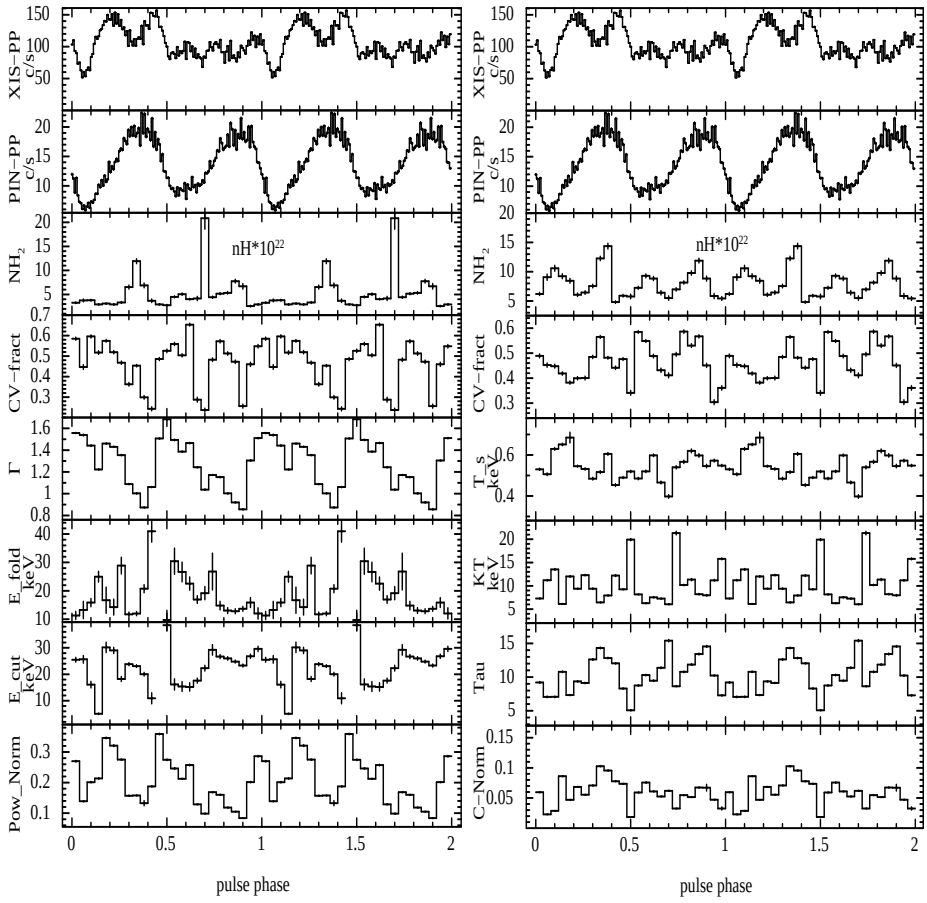

Figure 4.4: Same as in Figure 4.2 in Vela X-1. The left panel shows the variation using the model 'highecut' and the right panel shows the same using the model 'CompTT'. The pulse profiles denote the normalized intensity.

.

7. Both the NPEX normalizations and the CompTT normalizations shows a variability pattern with pulse profiles.

4.2.4 XTE J1946+274

Due to a short pulse period of 15.75 s in this source (Refer Chapter 2), 25 independent phase bin extraction was not possible, specially for the XIS data. We proceeded with the extracting of 25 overlapping but 8 independent phase bins for extraction of both XIS and PIN data for this source. Phase resolved spectroscopy was carried out with the 'Highecut' and 'NPEX' continuum models. Figure 4.7 shows the composite pulse

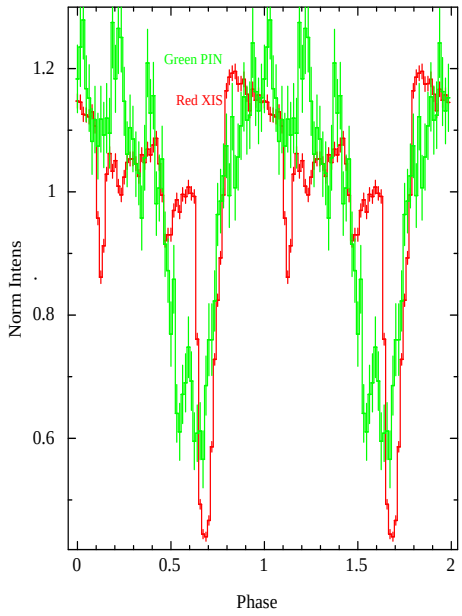

Figure 4.5: Figure showing the background subtracted low energy XIS (0.3–10 keV) and the high energy PIN (10–70 keV) pulse profile of A 0535+26 showing the narrow dips in the pulse profile in the XIS band and its absence in the PIN band.

profile in the low and high energy band showing the location of the narrow dips in the low energy XIS pulse profile. The variation of the continuum parameters are shown as a function of pulse phase in Figure 4.8. Both the models provide a very consistent picture in the change of N_{H2} and Cv_{fract} parameters. The results obtained as seen for the figure from both the models are as follows.

1. The N_{H2} has a double peaked structure with a smaller peak around phase $\sim 0.3 - 0.4$ around the main dip of the XIS profile and a bigger peak at phase ~ 0.8 corresponding to the dip in the pulse profile at the same phase.

2. The Cv_{fract} also shows a double peaked profile with one of its peaks coinciding with the dip at phase ~ 0.8 and another in the phase range of 0.4–0.5. This increase in the Cv_{fract} is closer to the peak of the XIS profile. This may be an indication of some absorption at the lowest energies 0.3–3 keV, as the XIS peak at phase ~ 0.5 shows a decrease in its strength at the same energy range.

3. Photon index Γ and α also shows similar trends with the pulse phase for both the models. It is flat up to phase ~ 0.3 after which it peaks at ~ 0.4 near the off pulse regions of the pulse profiles and then shows an increasing trend again.

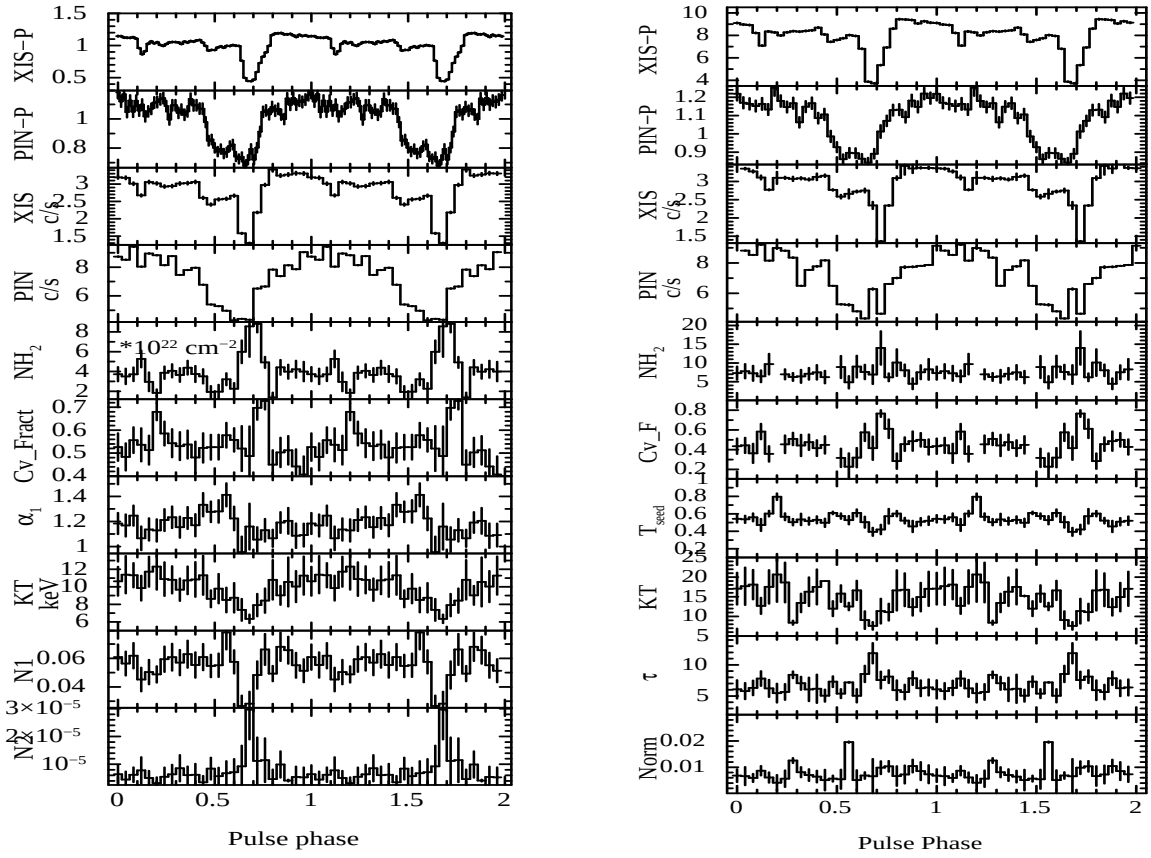

Figure 4.6: Same as in Figure 4.2 in A 0535+26. The left panel shows the variation using the model 'NPEX' and the right panel shows the same using the model 'CompTT'.

4. The Folding energy E_{fold} does not vary significantly with the pulse phase, while the electron temperature KT peaks at ~ 0.8 coinciding with the dip in the XIS profile at the same phase range.

5. Both the NPEX normalizations and the CompTT normalizations shows a variability pattern with pulse profiles.

4.2.5 EXO 2030+375

In case of EXO 2030+375, the X-ray pulsations are clearly seen up to $\sim$ 100 keV (See Chapter 2). The dips in the pulse profile are very strong and clearly distinguishable up to $\sim$ 70 keV. The presence of dips in the pulse profiles up to $\sim$70 keV is rarely seen in accretion powered X-ray pulsars, and this source presents us the rare opportunity

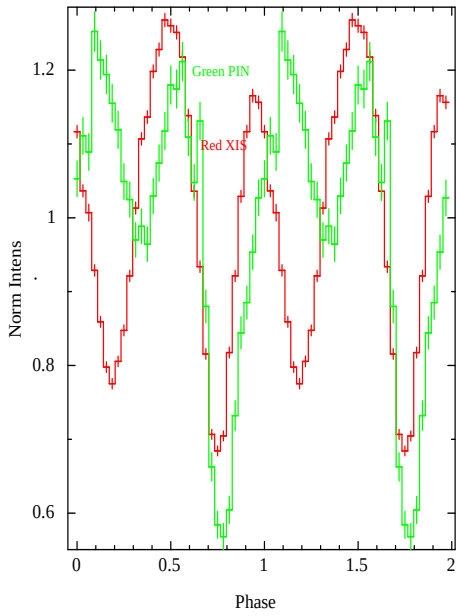

Figure 4.7: Figure showing the background subtracted low energy XIS (0.3–10 keV) and the high energy PIN (10–70 keV) pulse profile of XTE J1946+274 showing the narrow dips in the pulse profile in the XIS band and its absence in the PIN band.

to probe the nature of these high energy dips. Figure 4.9 shows the composite pulse profile in the low and high energy band showing the location of the narrow dips in the pulse profile at both the low (XIS) and high (PIN) energy pulse profiles. Four dips are seen in the pulse profile at phases $\sim$ 0.1, 0.3 ,0.45 and 0.7. From the evolution of the pulse profiles with energy (Refer Chapter 2) it it seen that only the dip at $\sim$ 0.7 can be a manifestation of the evolution in strength of the first peak in the pulse profile (see Chapter 2 for details). The other dips disappear at much higher energies, and cannot be traced due to the limited statistics at higher energies. Phase resolved spectroscopy was carried out with the neutral as well as partially ionized absorber along with the 'highecut' continuum model. The variation of the continuum parameters are shown as a function of pulse phase in Figure 4.10.

1. At the dip at phase $\sim$ 0.1 there is an increase in the value of N_{H2} as well as the Cv_{fract}. The N_{H2} shows a higher value for the neutral absorber model as expected. Both the models however have a similar value for the Cv_{fract}. The ionized absorber model indicates the presence of a highly ionized matter at that phase with $\xi \simeq 100$.

2. The dip at phase $\sim$ 0.3 showing an increase in N_{H2} with a steep increase in the

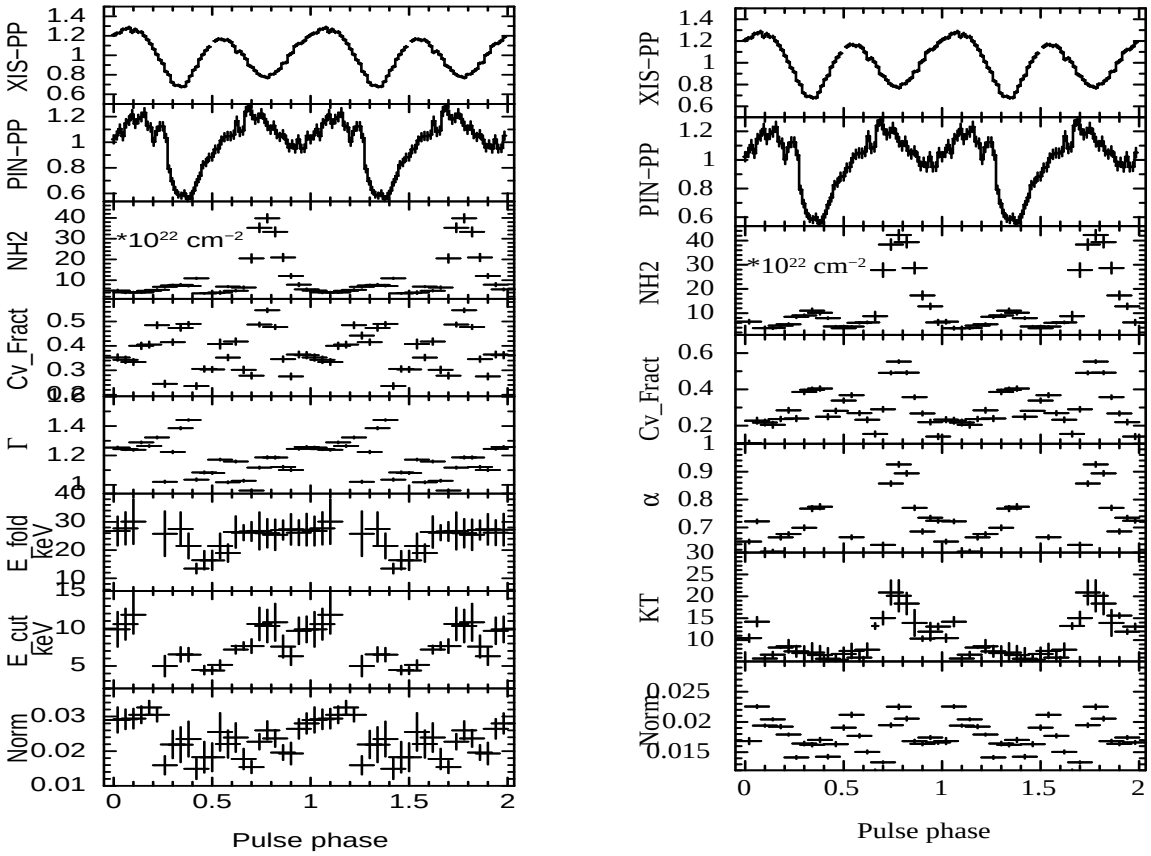

Figure 4.8: Same as in Figure 4.2 in XTE J1946+274. The left panel shows the variation using the model 'highecut' and the right panel shows the same using the model 'NPEX'.

Cv_{fract} value. Similar as to the dip at phase ~ 0.1, N_{H2} shows a higher value for the neutral absorber model. Cv_{fract} is $\simeq 0.6$ for both the models indicating it to be the deepest dip in the pulse profile. This is also confirmed from Figure 4.9. The ionized absorber model indicates the presence of a highly ionized matter at that phase with $\xi \simeq 100$ as in the previous case.

3. The dip at phase ~ 0.45 shows an increase in N_{H2} of the same order as in the dip at phase ~ 0.3 for the neutral absorber model, but a maximum value of N_{H2} for the ionized absorber model. The Cv_{fract} for both the models is also lower than at the previous dips indicating the presence of a very dense clumpy matter at that phase. The ionized absorber model further indicates that the matter is highly ionized.

4. The dip at phase ~ 0.7 shows no significant increase in the value of N_{H2} or Cv_{fract}

for the neutral absorber model and only a slight increase in Cv_{fract} for the ionized absorber model. This is in agreement with the dip being only a manifestation of the evolution of strength of the first peak of the pulse profile and not a real dip feature caused by absorption. The ionized absorber model however indicates that the matter is highly ionized ($\xi \simeq 100$).

5. The photon index Γ has a very similar pattern of variation for both the models. In General the spectrum is harder near the pulse peak and softer in the off pulse regions.

6. The Folding energy E_{fold} also has similar pattern of variations for both the models with no clear trend visible. The cutoff energy E_{cut} cannot be constrained well for both the models.

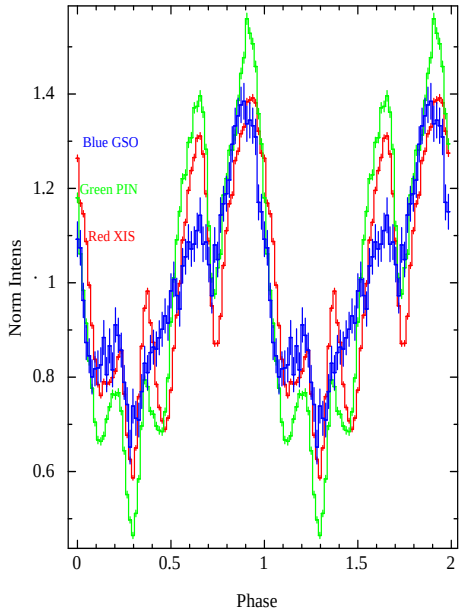

Figure 4.9: Figure showing the background subtracted low energy XIS (0.3–10 keV) and the high energy PIN (10–70 keV) & GSO (40–600 keV) pulse profiles of EXO 2030+375 showing the narrow dips in the pulse profile which extend upto very high energies in this source (Upto the PIN energy band).

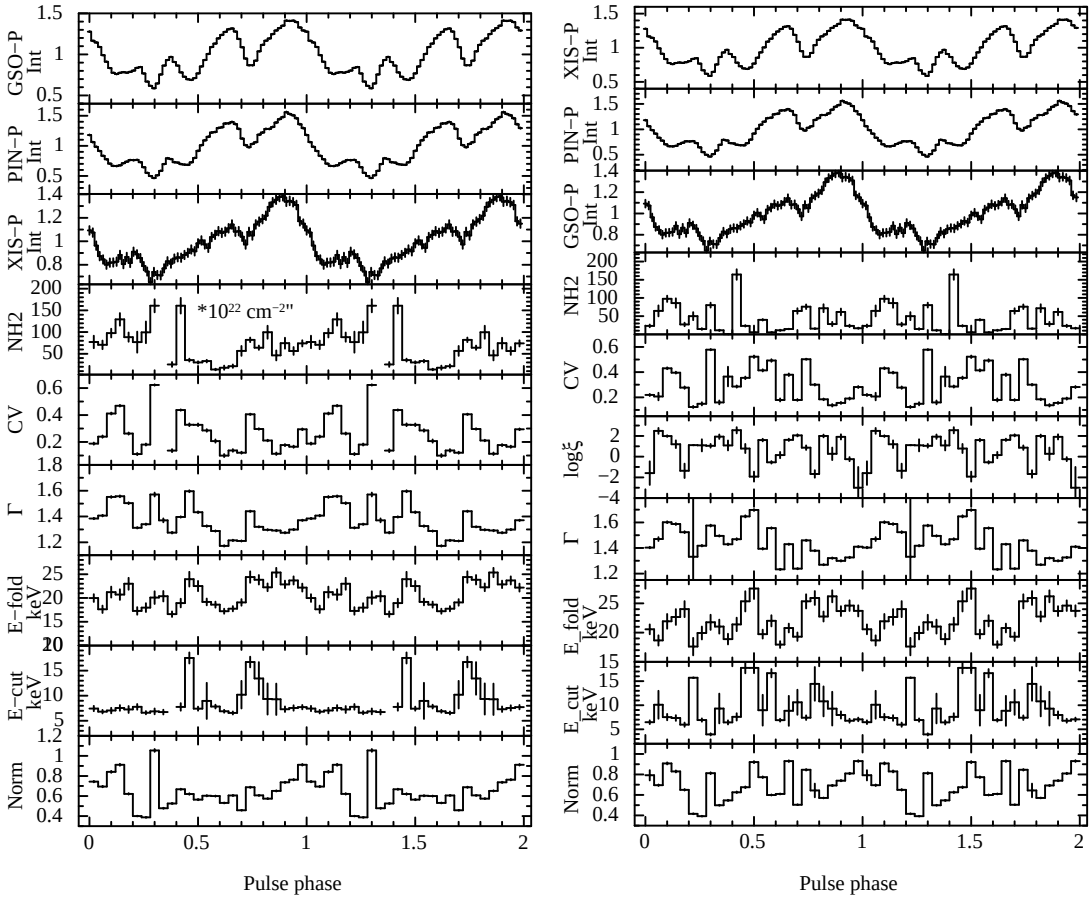

Figure 4.10: Variation of the spectral parameters with phase along with the pulse profile (0.3-12 keV for XIS, 10-70 keV for PIN and 40-600 keV for GSO) in EXO 2030+375. The pulse profiles of the pulsar are shown in top three panels of both sides of the figure, respectively. The left panel shows the variation using the model 'highecut' with neutral absorber and the right panel shows the same using the model 'highecut' with a partially ionized absorber.

4.2.6 GX 1+4

The source GX 1+4 is different in nature, since although we see the dip like structures in the low energy pulse profiles as compared to its absence in the high energy bands (Figure 4.11), an additional partial absorbing component is not required to fit the energy spectrum (Refer Chapter 3). Therefore to investigate the structures in the pulse profiles, phase resolved spectroscopy was carried out with the 'NPEX' and 'PEXRAV' continuum models. The variation of the continuum parameters are shown as a function of pulse phase in Figure 4.12. The parameters exhibit a very consistent pattern of variation for both the continuum models as follows.

1. The 'NPEX' photon index α and the 'PEXRAV' photon index Γ follow the trend of the low energy XIS pulse profile. The spectra are thus the softest at the phase 0/1 and hardest near the off pulse regions ($\sim$ phase 0.9). This is in support of the fact that the broad dip like feature at phase ~ 0.2 may actually be a soft emission peak which disappears at higher energies. The spectra is also hardest near phase ~ 0.6 as is also seen in the low energy pulse profile as a paucity of photons in that phase range. The origin of this dip like feature is however not very clear.

2. The KT of the 'NPEX' model and the e-folding energy of the 'PEXRAV' model also have similar patterns of variations like the photon index parameters.

3. The reflection coefficient Rel_{refl} cannot be constrained well in the phase resolved data.

4.3 Discussion & Summary

In this chapter we have presented the results of pulse phase resolved spectroscopy of the continuum parameters in some bright accretion powered pulsars . The first four sources studied (i.e. 1A 1118-61, Vela X-1, A 0535+26 and XTE J1946+274) exhibit narrow dips in their pulse profiles which gradually disappear at higher energy ranges. All these sources exhibit dip like features upto $\sim$ 12 keV, as the lower energy photons are more susceptible to reprocessing by absorption and scattering in the local medium of the neutron star. The fifth source studied, i.e. EXO 2030+375 show dips which are clearly distinguishable upto 70 keV, which could perhaps arise from a hotter, partially ionized

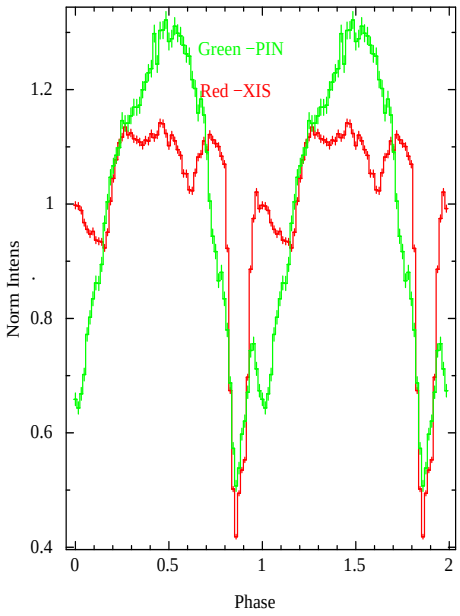

Figure 4.11: Figure showing the background subtracted low energy XIS (0.3–10 keV) and the high energy PIN (10–70 keV) pulse profile of XTE GX 1+4 showing the pulse profile in the XIS band and its absence in the PIN band.

matter. Indeed, the use of partial covering partially ionized absorber gives a marginally better fit for the source as seen in Chapter 3 and the phases corresponding to the dips show a higher degree of ionization. GX 1+4, the last source studied in different in nature and the dip like features in its low energy pulse profile cannot be explained by a partial covering absorber. These features may actually be additional soft emission components at those phases.

The presence of a high value of the local absorption component (N_{H2}) with a lower covering fraction Cv_{fract} as seen in some phases corresponding to the dips for some sources, could indicate the presence of a dense clump of matter. This could further indicate that the accretion stream or column (which is phase locked with the neutron star and is responsible for producing these dip like features) is clumpy in nature. These dense clumps may fall into our line of sight at some viewing angles and absorb/scatter away the radiation (prefarably the low energy photons) emitted from the accretion powered pulsars . The column density, covering fraction and the ionization fraction would manipulate the process locally and define the nature of the individual dips.

For all the sources except GX 1+4, the spectra hardens near the peak of the hard X-ray (PIN: 10-70 keV) pulse profile, indicating a deeper view to the inner parts of the

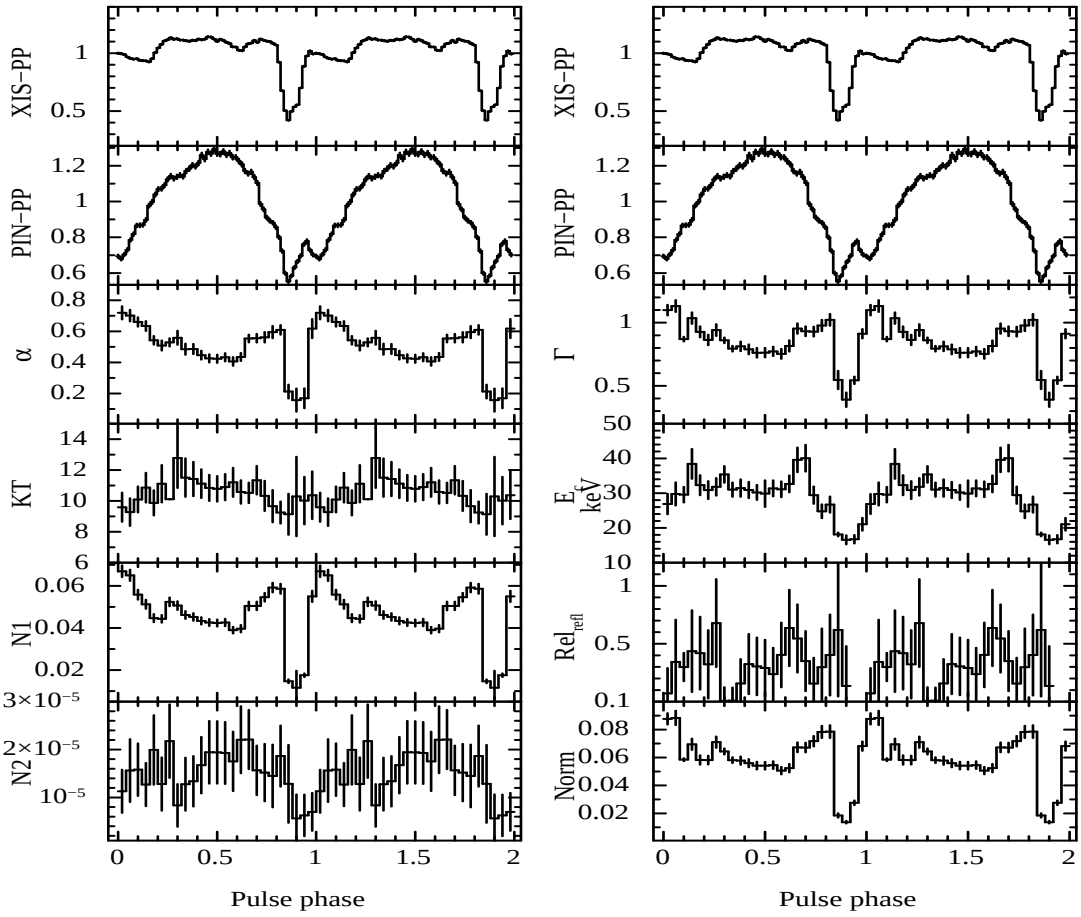

Figure 4.12: Same as in Figure 4.2 in GX 1+4. The pulse profiles of the pulsar are shown in the top two panels of both sides of the figure, respectively. The left panel shows the variation using the model 'NPEX', and the right panel shows the same using the model 'PEXRAV' model.

accretion column at that phase which could be true for a pencil type of beaming pattern. The phase resolved variations of the CRSF parameters (in Chapter 5) in A 0535+26 and XTE J1946+274 also hint the same, although a fan type of beaming pattern is indicated for Vela X-1.

Chapter 5

Pulse phase resolved spectroscopy of CRSF

5.1 Formation of cyclotron resonance scattering feature

The strong magnetic fields of accretion powered pulsars of the order of $\sim 10^{12}$ G plays a crucial role in the formation of the X-ray spectrum of these sources. Near the neutron star where the magnetic field dominates **the flow of matter**, the soft photons produced in the thermal mound are Comptonized in the accretion shock emitting X-ray and Gamma ray photons. **Due to the effect of the non spherical emission zone and the scattering cross sections of the photons which are altered in the presence of strong magnetic fields (i.e. acquire different dependencies depending whether they escape parallel or perpendicular to the magnetic field vector (Becker, 1998)), different beaming patterns of radiation, "Fan" or "Pencil" are produced depending on the rate of mass accretion on the neutron star and hence the luminosity produced**. The details of these have been discussed in Chapters 1 and 3. Another unique characteristic which arises due to the modification of the cross section by the magnetic field is the formation of the cyclotron resonance scattering feature (henceforth CRSF). The Comptonized photons also undergo scattering with the electrons in the **mildly** relativistic plasma in the accretion column. In presence of magnetic fields the electrons exhibit a helical trajectory with the Larmor radius and

the corresponding Larmor frequency as given by

$$r_b = \frac{m_e v_\perp}{eB} \tag{5.1}$$

and

$$\omega_b = \frac{eB}{mc} \tag{5.2}$$

where m_e is the mass of the electron, $v_\perp$ the perpendicular component of velocity of the electron, e, the charge of an electron and B, the magnetic field strength.

At high magnetic fields of the order of the critical magnetic field strength (cyclotron energy equal to the electron rest mass energy), $B_{crit} = \frac{m^2c^3}{e\hbar} = 44 \times 10^{12}$ G, the Larmor radius becomes of the order of the De Broglie radius of **the electron in the plasma**. A relativistic quantum mechanical treatment becomes necessary as the electron's perpendicular momenta are quantized into discrete Landau levels given by

$$\frac{p_\perp}{mec} = n\frac{B}{B_{crit}} \tag{5.3}$$

The scattering cross section is therefore resonant at the energy separation of these Landau levels. Since the cross section is very high at these resonances and the Landau levels are thermally broadened, a photon with its energy close to the Landau level separation may not escape the line forming region and is consequently observed as an absorption feature in the energy spectrum at

$$E_n = (m_e c^2)\frac{\sqrt{1 + 2n\frac{B}{B_{crit}}\sin^2\theta} - 1}{\sin^2\theta} \times \frac{1}{1+z} \tag{5.4}$$

Here m_e is the electron mass c the speed of light, θ the direction between the incident photon and the magnetic field vector, z gravitational radius corresponding to the line forming region ($z = \frac{1}{\sqrt{1-\frac{2GM}{Rc^2}}} - 1$).

$n = 1$ corresponds to the cyclotron fundamental and the corresponding harmonics are given by n=2,3,4 etc. **The above expression also indicates that the line energy is angular dependent.**

The presence of the CRSF was first theoretically predicted by Gnedin & Sunyaev (1974), even before it was discovered observationally. Subsequently, the formation of CRSFs have been numerically solved by Araya & Harding (1999); Araya-Góchez & Harding (2000); Schönherr et al. (2007) ,and the properties of the line at different viewing

angles and emission regions have been quantified. To give a clearer idea Figure 5.1 shows the resonant cross sections at different viewing angles as computed for a particular set of physical parameters in the emission region (Araya & Harding, 1999).

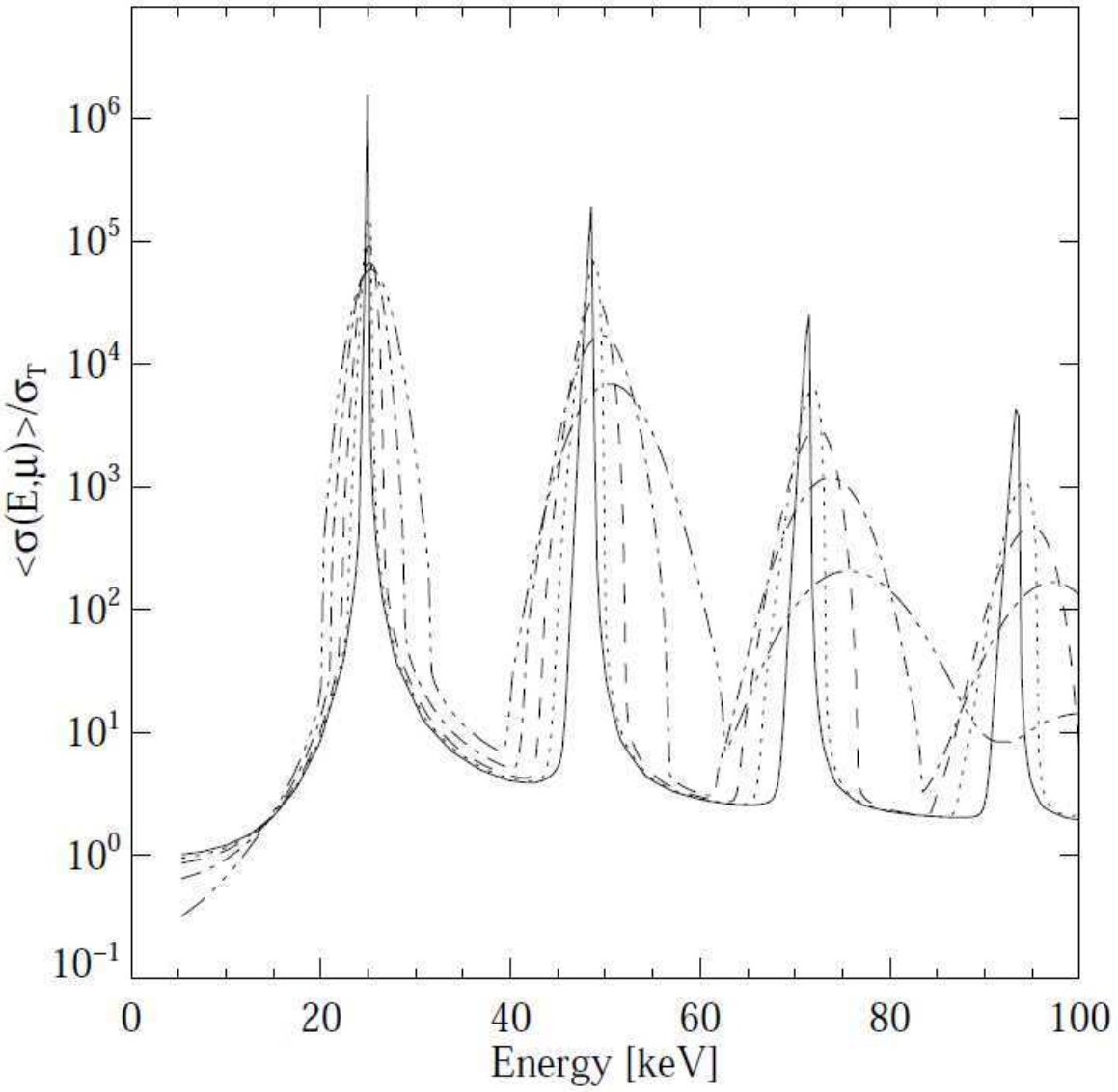

Figure 5.1: Cross sections for Compton scattering in presence of strong magnetic fields in terms of σ_T, for a particular set of physical parameters. Here $B/B_{crit} = 0.05$, $KT = 3$ keV. The profiles are shown for different θ w.r.t magnetic field. Solid, dotted, dashed, dashed-dotted, and dash and triple dotted lines correspond to $\cos\theta = 0.005, 0.2, 0.375, 0.625, 0.875$. This figure has been taken from Araya & Harding (1999)

5.2 Significant observational results of cyclotron resonance scattering feature

Due to the gravitational redshift near the neutron star, the CRSF are actually observed at $E_{obs} = E(1+z)$. For typical neutron star parameters, $z \sim 0.3$.
Cyclotron line was first discovered in the source Her X-1 Trümper et al. (1977). Initially thought to be in emission at ~ 53 keV, it was later inferred to be in absorption at 40 keV based on theoretical arguments (Nagel, 1981). Figure 5.2 shows the first cyclotron line **measurement** in the spectrum of Her X-1.

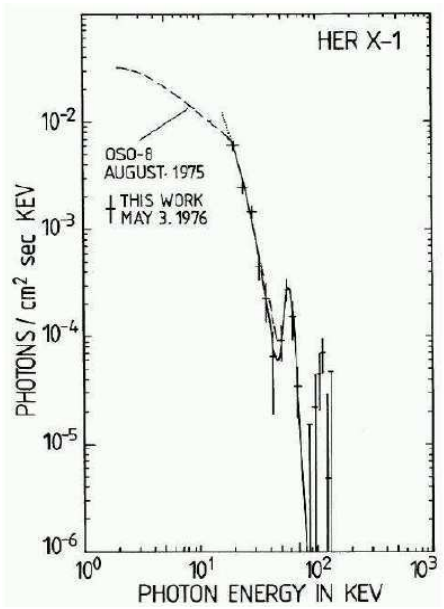

Figure 5.2: The energy spectrum of Her X-1 taken from Trümper et al. (1977) showing the first CRSF detection.

This provided the first direct measurement of the magnetic field strength of a neutron star. **A pioneer in the observational studies of cyclotron resonance scattering feature has been the satellite *Ginga* (Mihara, 1995), and CRSFs in many sources have been discovered by this space mission**. Subsequently with the satellites *RXTE* , *BeppoSAX*, *Integral*, and specially *Suzaku* providing high quality spectral data over a broad energy range, there have been discovery of new sources and a great deal of followup observations of sources, specially in their outbursts and bright states, and detailed studies on CRSFs have been carried out leading to significant advancements

in this field. At the time of writing this thesis, 19 CRSF sources have been discovered with magnetic fields measured ranging from 10–50 keV (Pottschmidt et al., 2012). Table 5.1 give a complete list of CRSF sources discovered so far [1]. In some sources multiple CRSFs have been discovered : six lines in 4U 0115+63 (Santangelo et al., 2000; Heindl et al., 2004) and three lines in V 0332+53 (Pottschmidt et al., 2005). Anharmonic spacing between the lines have been found in many sources where the ratio of the harmonics deviate from the expected value of 2. Deviations < 2 can be explained by relativistic corrections as in 4U 0115+63 (Santangelo et al., 2000) and > 2 by superposition of many lines as in Vela X-1 (Kreykenbohm et al., 2002) and A 0535+26 (Caballero et al., 2007). The same set of observations for the respective sources have also confirmed that the fundamental profile usually appears shallower than its corresponding higher order harmonic. There have also been reports of more complex CRSF profiles (deviating from a standard Gaussian or Lorentzian profile) as the fundamental in V 0332+53 (Nakajima et al., 2010). Significant variations of the CRSF parameters have been observed with luminosity on pulse to pulse timescales as well as on longer timescales. Except for A 0535+26, all the other sources seem to exhibit either a correlation or anti-correlation with the flux (Mihara et al., 2004; Staubert et al., 2007; Tsygankov et al., 2007; Klochkov et al., 2011, 2012), indicating two different accretion regimes in these sources depending on the source's luminosity and also on its critical luminosity which is a function of the magnetic field strength of the neutron star. The higher the field strength, the higher is its corresponding critical luminosity. More details of these are provided in Becker et al. (2012). Another important recent discovery has been the evidence of a secular decay in the centroid of the line energy and hence the magnetic field of the neutron star in Her X-1 (Staubert, 2013). This has been found for the first time in any source and could indicate signatures of field burial due to accretion. Signatures of variability of the CRSF with the superorbital period has also been indicated in the same work for this source.

An important characteristic of the CRSF variability with the neutron star rotational period or the pulse phase. This characteristic, measured with the pulse phase resolved spectroscopy is a very important tool which provides a wealth of information on the emission region and the magnetic field geometry of the neutron star. This is discussed in detail in this Chapter and the results

[1] http://www.sternwarte.uni-erlangen.de/wiki/doku.php?id=cyclo:start

are presented. Another interesting aspect is probing the beaming pattern near the cyclotron line energy of the particular source as a huge cross section difference is encountered at this energy range as already discussed. In the latter section of this chapter, a systematic study is performed to probe the pulse profiles near their cyclotron resonance scattering feature energies of the sources studied in Chapter 3 which showed CRSF features.

Table 5.1: cyclotron resonance scattering feature Table

Source name	Energy (keV)	Companion	Source Type(P/T)[2]
Swift J1626.6-5156	10	Be	T
4U 0115+63	14, 24, 36, 48, 62	BO.5 Ve	T
4U 1907+09	18, 38	B2 III-IV	P
4U 1538-52	22, 47	B0I	P
Vela X-1	24, 51	B0.5Ib	P
V 0332+53	27, 51, 74	O8.5 Ve	T
Cep X-4	28	B1.5 Ve	T
Cen X-3	30	O6.5II	P
X Per	29	B0 IIIVe	P
RX J0440.9+4431	32	Be	T
MXB 0656-072	33	O9.7 Ve	T
XTE J1946+274	36	B0-1 V-IVe	T
4U 1626-67	37	WD?	P
GX 301-2	37	B1.2Ia	P
Her X-1	41	A9-B	P
1A 0535+26	45, 100	O9.7 IIe	T
1A 1118-61	50, 110 ?	O9.5IV-Ve	T
GX 304-1	54	B2 Vne	P
GRO J1008-57	76	B1-B2	T

5.3 Pulse phase resolved spectroscopy of cyclotron resonance scattering feature and its importance

Inherently the angular dependence of the cyclotron resonance scattering feature cross section is expected to result in variations of a few % for the cyclotron parameters with the viewing angle of the neutron star or the pulse phase as evident in Equation 5.4 (See also Schönherr et al. (2007) and references therein). In addition, as the CRSF depends on the physical parameters of the region like the plasma temperature, the optical depth and the geometry of the region, projections of different parts of the accretion column having different physical properties at different viewing angles, can also result in variations of the CRSF parameters with pulse phase.

Pulse phase resolved spectroscopy of the cyclotron parameters have been performed for some sources previously, for example in Her X-1 (Soong et al., 1990; Enoto et al., 2008; Klochkov et al., 2008b), 4U 1538-52 (Robba et al., 2001), 4U0115+63 (Heindl et al., 2000), Vela X-1 (Kreykenbohm et al., 1999, 2002; La Barbera et al., 2003), Cen X-3 (Suchy et al., 2008), and more recently in GX 301-2 (Suchy et al., 2012), 1A 1118-61 (Suchy et al., 2011) and 4U 1626-67 (Iwakiri et al., 2012). In this Chapter we show for the first time the phase resolved variations of the CRSF parameters in XTE J1946+274. For the other sources more careful and detailed results have been obtained.

5.4 Requirements for phase resolved spectroscopy

Performing pulse phase resolved spectroscopy of the CRSF parameters requires some crucial issues to be taken care of which are mentioned below:

1. **cyclotron resonance scattering feature is usually broad, extending sometimes upto $\sim$ 10 keV or more around the center, and often shallow in depth. Detection of this, first of all requires a broadband spectrum, preferably extending to low energies like 1 keV so that absorption column density and in some cases, partial covering absorption are well constrained. Therefore a major requirement is careful modeling of the broadband continuum spectrum and obtaining consistent and physically reliable parameters of the continuum for the different models.** The continuum model should not introduce any artificial systematic or residual like structures

in the spectrum which can be modelled as a part of the cyclotron line. This issue has been described extensively in Chapter 3 for all the sources for which the results are presented here. *Suzaku* , with its broadband energy coverage and good spectral resolution is most ideally suited in this regard. **It may be noted that the past mission *BeppoSAX* was also suitable in this regard due to its broadband energy range.**

2. The CRSF parameters should preferably give consistent results for both the Gaussian and the Lorentzian profile. In cases where one of the model gives any unphysical value of the CRSF parameters, the other model should be preferred. For example in GX 301-2, Her X-1 and 4U 1626-67, a Gaussian profile is preferred. The CRSF parameters should not show any correlation with any of the continuum parameters or with its other parameters which might introduce an artificial dependence in the results. This issue is discussed with respect to GX 301-2 and Vela X-1 in Chapter 3.

3. The stretch of the observation chosen for the analysis should be free from any luminosity or spectral variability to ensure we are mapping the variability with the viewing angle alone. This has also been discussed in Chapter 3.

5.5 Results

In this section, we present the results of pulse phase resolved analysis of the CRSF parameters of some bright accretion powered pulsars **for which long observations were made with** *Suzaku* . The same set of observations that were used for the phase averaged analysis were used in the phase resolved case. The same duration of the observations as mentioned in Chapter 3 were also used for the analysis taking care of the luminosity variation and spectral variability wherever required. To investigate this we performed pulse phase resolved spectroscopy, applying phase filtering in the FTOOLS task XSELECT. For the phase resolved analysis we used the same background spectra and response matrices as was used for the phase averaged spectrum for both the XIS's and the PIN data. We also fitted the spectra in the same energy range. The data are also rebinned the same way as in the phase averaged case unless stated otherwise. In all the cases phase resolved spectra were generated with the phases centered around as in the case of 25 independent bins but at thrice their widths. This resulted in 25 overlapping

bins out of which only 8 were independent. All the individual spectra for the respective sources were fitted with the best fit continuum and line models discussed in Chapter 3. The value of the Galactic absorption (N_{H1}) and the Fe line centroids and widths were frozen to the phase averaged values since they are not expected to vary with the viewing angle.

5.5.1 1A 1118-61

Phase resolved spectroscopy was carried out with the 'FDCUT' and 'NPEX' continuum models and a Lorentzian profile for the CRSF. Due to limited statistics we were unable to constrain all the parameters, and froze the width of the CRSF harmonic to the phase averaged value of the respective models and varied the rest of the parameters with pulse phase. Figure 5.3 shows the variation of the cyclotron parameters of the source using the best fit models as a function of pulse phase. The variation of the parameters have very similar pattern for the different models used for the source except in the phase range 0.5–0.8 where there is a disagreement between the parameter $D1_{\rm cycl}$. The following features can be seen from the Figure 5.3. The results are compared with respect to the high energy PIN profile (10–70 keV) shown in panel two of the same figure.

1. The energy ($E1_{\rm cycl}$) varies by 30% ($\sim$ 43–56 keV). The pattern of variation of the energy parameter ($E1_{\rm cycl}$) follows the PIN pulse profile roughly, except for a smaller hump at phase $\sim$ 0.4.

2. The depth ($D1_{\rm cycl}$) shows more or less consistent values at the rise and the peak of the PIN pulse profile. It however shows an increase near the falling edge of the pulse profile (phase 0.0–0.2). There is a discrepancy between the values of $D1_{\rm cycl}$ especially in the phase range where it remains constant (phase 0.5–0.8) with the parameters obtained with the NPEX model showing systematically lower values.

5.5.2 VELA X-1

Phase resolved spectroscopy was carried out with the 'highecut' and 'CompTT' continuum models and two separate Lorentzian profiles for the CRSFs. Due to limited statistics we were unable to constrain all the parameters, and froze the width of the CRSF harmonic to the phase averaged value of the respective models and varied the rest of the parameters with pulse phase. For phases close to or at the off pulse regions, the

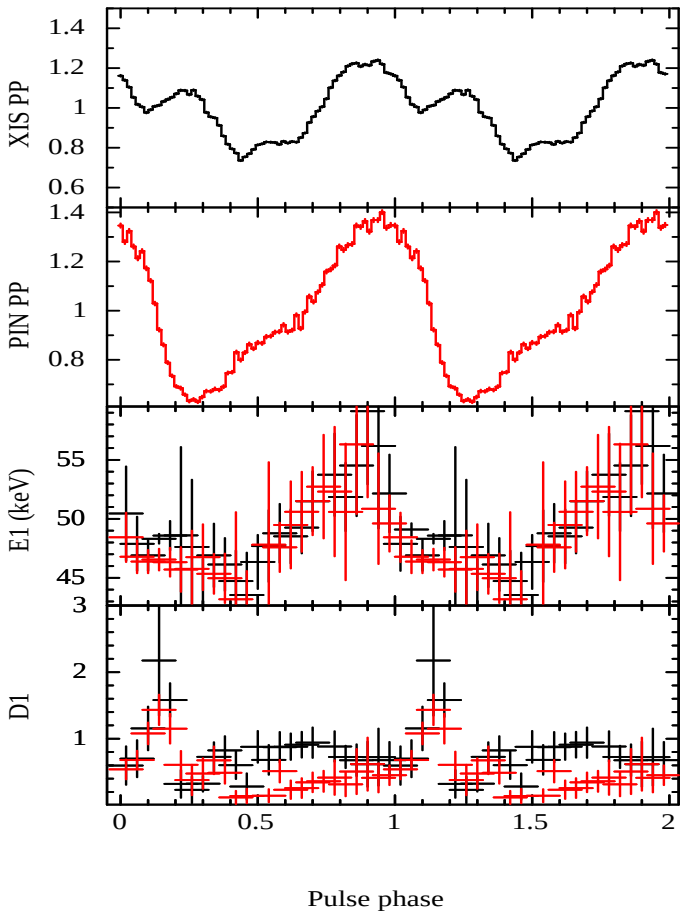

Figure 5.3: Variation of the cyclotron line parameters as is obtained with the two models for 1A 1118-61. The top two panels indicate the normalized intensities of the low energy XIS (0.3-10 keV) and high energy PIN (10-70 keV) pulse profiles. The black points denote the parameters as obtained with the 'FDCUT' model and the red points denote the parameters as obtained with the 'NPEX' model. Only 8 of the 25 bins are independent. **All the error bars in this and similar figures henceforth are at 99 % confidence level.**

CRSFs are weak and sometimes cannot be detected in the spectra for either or both of the continuum models. Figure 5.4 shows the variation of the cyclotron parameters for both the models as a function of pulse phase. Despite statistical limitations in the data to constrain the CRSF fundamental energy and depth independent of the cutoff energy in the 'highecut' model, the variation of the CRSF parameters have very similar pattern for both the 'highecut' and the 'CompTT' model. This gives us **high level of** confidence on the obtained results. The results also follow the trend as obtained previously

by Kreykenbohm et al. (2002) using *RXTE* but they did not have enough sensitivity to probe these features in detail. The following features can be seen from the Figure 5.4. The variation is compared with respect to the high energy PIN pulse profile (10–70 keV) shown in panel two of the same figure. Figure 5.5 shows the ratio of the two line energies $E2_{\rm cycl}/E1_{\rm cycl}$ with pulse phase.

1. The energy of the fundamental $E1_{\rm cycl}$ varies by a large amount with pulse phase, with the values varying between 22 keV in the off pulse region to 28 keV in the ascending phase of the second pulse. It has a decreasing trend with phase for the first pulse with nearly constant values for the second pulse, except for the ascent of the second pulse at phase ~ 0.7 where $E1_{\rm cycl}$ peaks in value.

2. The depth of the fundamental $D1_{\rm cycl}$ varies almost by a factor of three with the pulse phase, with the deepest lines near the pulse peaks and shallowest in the off pulse regions. Its value peaks near the ascending edges of the first pulse (phase $\sim$ 0.2-0.4) and the ascending edge of the second pulse (phase ~ 0.7). The lines are in general deeper for the first pulse.

3. The width of the fundamental $W1_{\rm cycl}$ varies almost by a factor of two. The width is maximum at the rising edges of the two pulse peaks at phases ~ 0.1 and 0.7.

4. The energy of the second harmonic $E2_{\rm cycl}$ varies between values of 48 keV to 62 keV. The values are maximum at the descending phase of both the pulses.

5. The depth of the second harmonic $D2_{\rm cycl}$ varies by a factor of 2 with the deepest harmonics found at the same phases as the phases having maximum $E2_{\rm cycl}$.

6. The ratio of the two line energies $E2_{\rm cycl}/E1_{\rm cycl}$ has significant pulse phase dependence (Figure 5.5) with an average value of ~ 2.1, maximum of ~ 2.6 near the pulse peaks at phase ~ 0.4 and ~ 0.9 and minimum of ~ 1.7 near the off pulse regions at phase ~ 0.8.

5.5.3 A0535+26

Phase resolved spectroscopy was carried out with the 'NPEX' and 'CompTT' continuum models and a Lorentzian profile for the CRSF. Due to limited statistics we were unable to constrain all the parameters, and froze the width of the CRSF harmonic to the phase

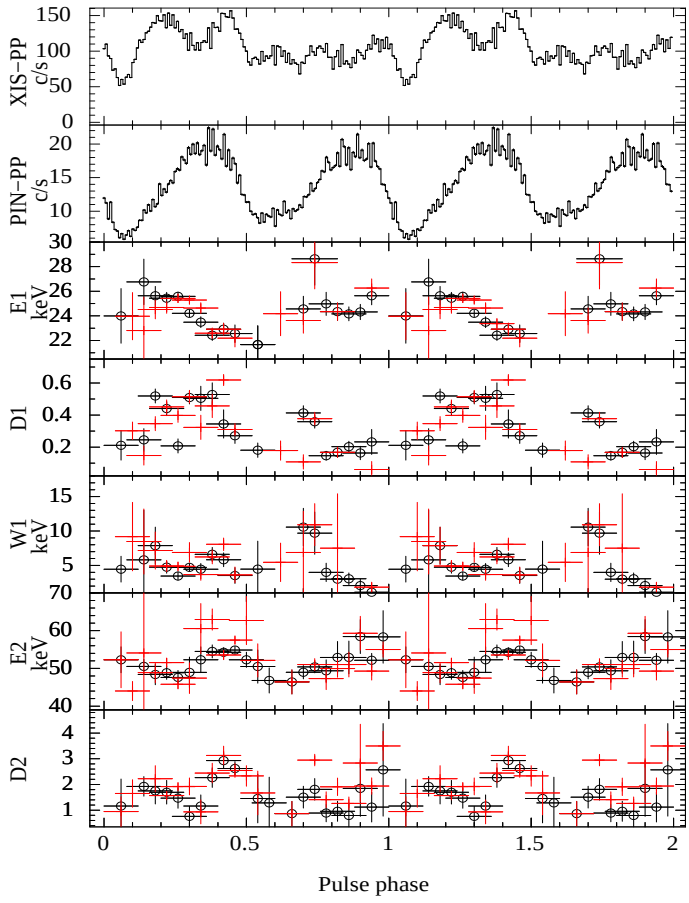

Figure 5.4: Same as in Figure 5.3 in Vela X-1. The black points with 'circle' denote the parameters as obtained with the highecut model The red points denote the points as obtained with the CompTT model. Only 8 of the 25 bins are independent.

averaged value of the respective models and varied the rest of the parameters with pulse phase. Figure 5.6 shows the variation of the cyclotron parameters of the source using the best fit models as a function of pulse phase. The variation of the parameters have very similar pattern for the different models used for the source which gives us a high level of confidence on the obtained results. The following features can be seen from the Figure 5.6. The results are compared with respect to the high energy PIN profile (10–70 keV) shown in panel two of the same figure.

1. the energy ($E1_{\rm cycl}$) varies by 14% ($\sim$ 43–50 keV). The pattern of variation of both the energy ($E1_{\rm cycl}$) and depth ($D1_{\rm cycl}$) has a gradually increasing trend with the

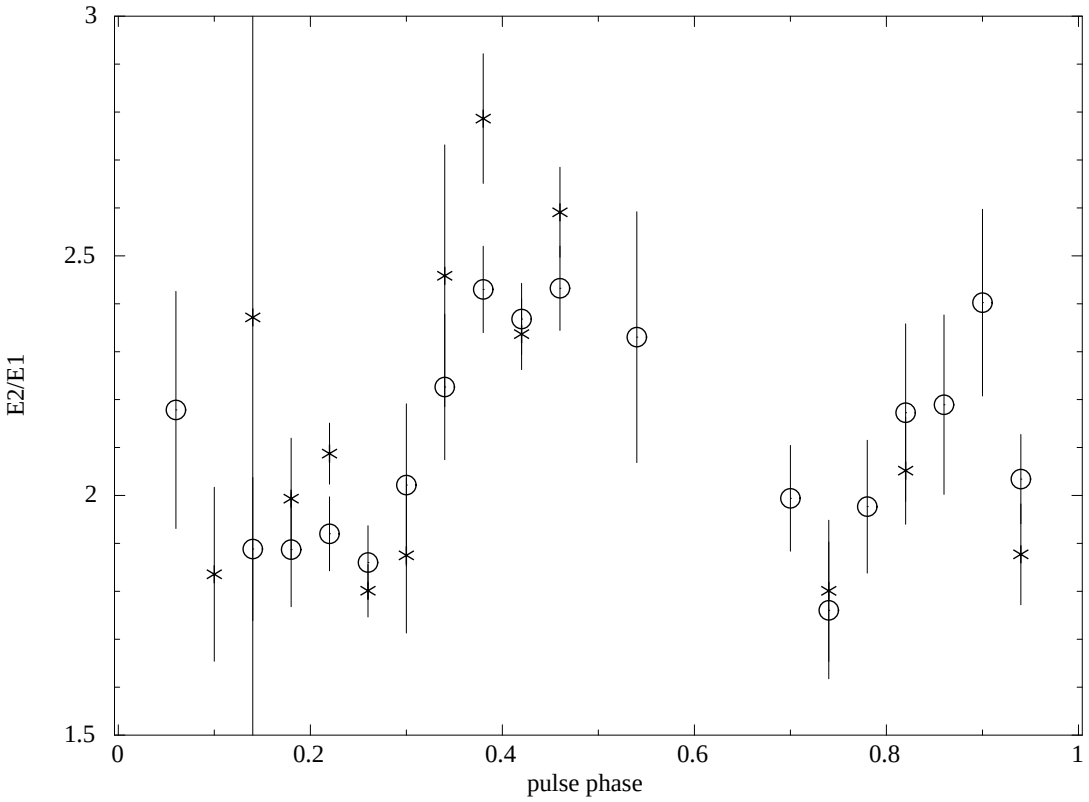

Figure 5.5: Variation of the ratio of the two cyclotron lines E2/E1 for Vela X-1 as is obtained by fitting the two models. The variation of the parameter as obtained from the high energy cutoff model is denoted by the symbol 'circle'. Variation of the parameter as obtained from the CompTT model is denoted by the symbol 'star'.

pulse profile and drops off abruptly in the off-pulse region (phase ~ 0.6), increasing again where the pulse profile picks up.

2. The depth ($D1_{\rm cycl}$) cannot be constrained at some phases by both the models, and at the off pulse phase at ~ 0.6, only the 'CompTT' is able to constrain the depth. It has a very sharp pattern of variation, varying between ~ 0.8–4, and it is shallowest near the pulse peak and deepest near the pulse minima.

5.5.4 XTE J1946+274

Phase resolved spectroscopy was carried out with the 'Highecut' and 'NPEX' continuum models and a Lorentzian profile for the CRSF. Due to limited statistics we were unable to constrain all the parameters, and froze the width of the CRSF harmonic to the phase

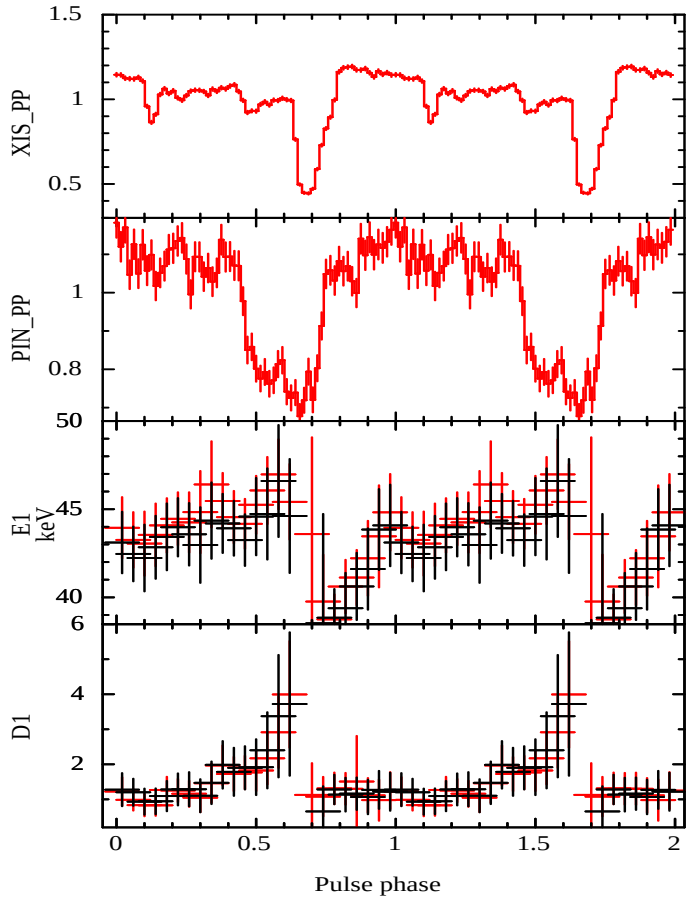

Figure 5.6: Same as in Figure 5.3 in A 0535+26. The black points denote the parameters as obtained with the 'NPEX' model The red points denote the parameters as obtained with the CompTT model. Only 8 of the 25 bins are indepenent.

averaged value of the respective models and varied the rest of the parameters with pulse phase. Figure 5.7 shows the variation of the cyclotron parameters of the source using the best fit models as a function of pulse phase. The variation of the parameters have very similar pattern for the different models used for the source which gives us a reasonable amount of confidence on the obtained results. The following features can be seen from the Figure 5.7. The results are compared with respect to the high energy PIN profile (10–70 keV) shown in panel two of the same figure.

1. The energy ($E1_{\rm cycl}$) varies about 36%. It's value is generally higher in the first pulse with the values peaking near the first peak (phase$\sim$ 0.7–0.8), and a decreasing trend near the second pulse.

2. The depth ($D1_{\rm cycl}$) varies between 1–3. It is deepest at the interpulse regions at phase $\sim$ 1.0 and shallow between phase 0.5–0.8 near the first peak. Due to limited statistics, specially of the PIN spectra, the CRSF parameters however cannot be constrained at the main dip, and at the ascending edges of the first peak (phase $\sim$ 0.5–0.7).

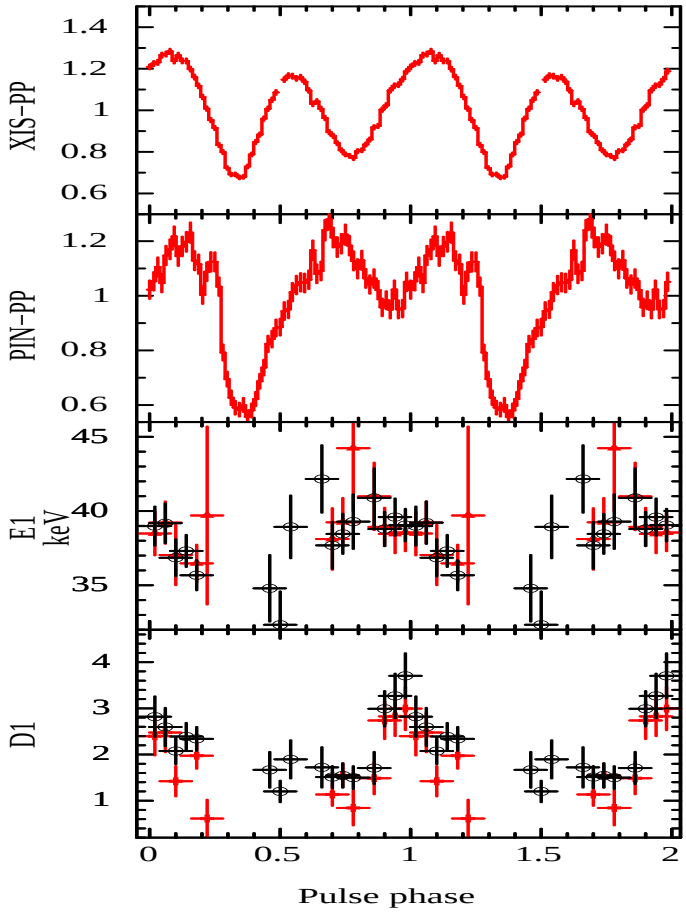

Figure 5.7: Same as in Figure 5.3 in XTE J1946+274. The black points denotes the parameters as obtained with the 'Highecut' model The red points denote the parameters as obtained with the NPEX model. Only 8 of the 25 bins are independent.

5.5.5 4U 1907+09

For 4U 1907+09, pulse phase resolved spectroscopy was carried out with the two *Suzaku* observations which had a factor of two difference in luminosity. Phase resolved spectroscopy was carried out with the 'NPEX' and 'Comptt' continuum models and a Lorentzian

profile for the CRSF. For Obs. 1, all the CRSF parameters like $E1_{\rm cycl}$, $D1_{\rm cycl}$ and $W1_{\rm cycl}$ could be constrained for this source, probably due to the longest observation duration available for it and a low cyclotron energy compared to the other sources. Only the $E1_{\rm cycl}$ and $D1_{\rm cycl}$ could be constrained for the Obs. 2 having a comparatively shorter exposure time.

Figure 5.8 shows the variation of the cyclotron parameters for both the observations of the source using the best fit models as a function of pulse phase. The variation of the parameters have very similar pattern for the different models used for the source which gives us a **high level** of confidence on the obtained results. The most striking **feature** is that the variations of $E1_{\rm cycl}$ and $D1_{\rm cycl}$ follow the same pattern with the pulse phase, although there is a factor of two difference in the luminosity between the two observations. The following features can be seen from the Figure 5.8. Both the observations have the same phase reference (both start from respective phase 0). The results are compared with respect to the high energy PIN profiles (10–70 keV) shown in panel two of the same figure. The $E1_{\rm cycl}$ and $D1_{\rm cycl}$ variations can be seen from both the observations, and the $W1_{\rm cycl}$ variations from Obs. 1.

1. The energy $E1_{\rm cycl}$ varies by $\sim 19\%$. Its value is maximum near the peak of the first pulse (20 keV at phase ~ 0.3), and again at the ascending edge of the second pulse (phase ~ 0.6), the minimum being at the second pulse peak (15 keV at $\sim$ phase 0.7–0.8).

2. The depth $D1_{\rm cycl}$ has a clear double peaked pattern with the peaks corresponding to the ascending edge of the first pulse and the peak of the second pulse (phase $\sim 0.1 - 0.2$ and 0.7 respectively). It is minimum near the pulse minima (phase $\sim$ 0.9). $E1_{\rm cycl}$ varies between 0.2–1.4 and is generally greater for the first pulse.

3. The width ($W1_{\rm cycl}$) has a similar pattern of variation as $E1_{\rm cycl}$, and peaks at similar phases with values varying within 7 keV.

5.5.6 GX 301-2

Phase resolved spectroscopy was carried out with the 'FDCUT' and 'Newhcut' continuum models with a Gaussian profile for the CRSF. **For this source, the optical depth τ could not be constrained well at all pulse phases and was fixed to the**

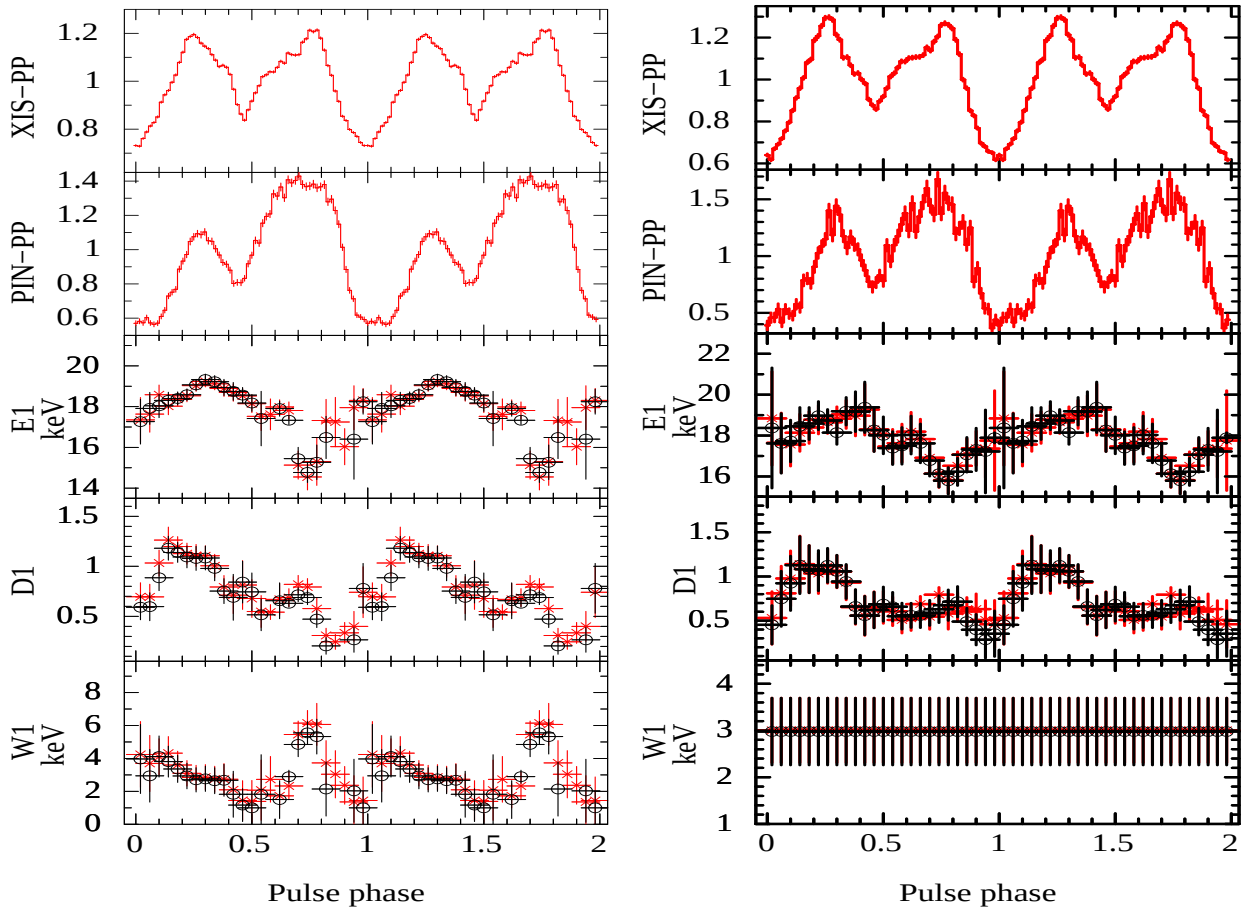

Figure 5.8: Same as in Figure 5.3 for the two observation in 4U 1907+09. The black points denotes the parameters as obtained with the 'NPEX' model The red points denote the parameters as obtained with the 'CompTT' model. Only 8 of the 25 bins are independent.

phase averaged value. The CRSF width σ was varied instead. Although there is a discrepancy between the parameters obtained with the two continuum models (as is also discussed in detail in Chapter 3), we have presented the results obtained with the 'Newhcut' model since it gives better constrained values of the CRSF parameters. Figure 5.9 shows the variation of the cyclotron parameters of the sources using the best fit model as a function of pulse phase. The following features can be seen from the Figure 5.9. The results are compared with respect to the high energy PIN profile (10–70 keV) shown in panel two of the same figure.

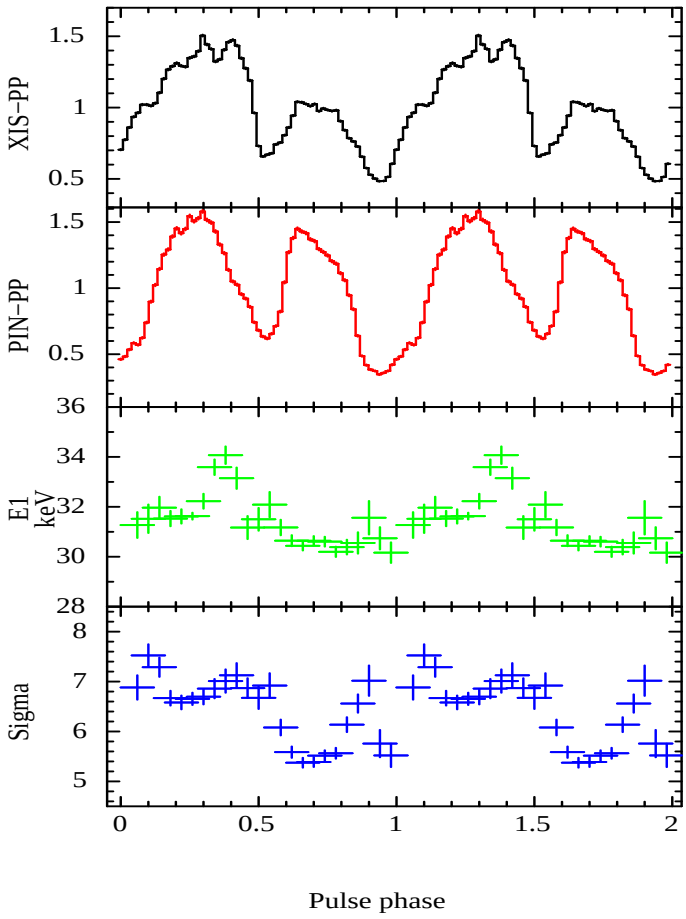

Figure 5.9: Same as in Figure 5.3 in GX 301-2 as obtained with the 'Newhcut' model. The top two panels indicate the normalized intensities of the low energy XIS (0.3-10 keV) and high energy PIN (10-70 keV) pulse profiles. Only 8 of the 25 bins are independent.

1. The energy $E1_{\rm cycl}$ varies by $\sim 13\%$. Its value is maximum just before the peak of the first pulse (34 keV at phase ~ 0.35), after which it decreases and maintains a consistent value of ~ 30 keV for the second pulse.

2. The width of the CRSF σ has a more complicated profile. It is maximum at phase ~ 0.1 near the rising edge of the first peak with a second maxima just after the phase where the $E1_{\rm cycl}$ peaks at the falling edge of the first pulse (phase ~ 0.4–0.5). After this it has a decreasing trend with the minima at the second peak (phase 0.6–0.7).

5.5.7 4U 1626-67

Phase resolved spectroscopy was carried out with the 'NPEX' and 'CompTT' continuum models and a Lorentzian profile for the CRSF. Due to limited statistics we were unable to constrain all the parameters, and froze the width of the CRSF harmonic to the phase averaged value of the respective models and varied the rest of the parameters with pulse phase. Figure 5.10 shows the variation of the cyclotron parameters of the source using the best fit models as a function of pulse phase. The pattern of variation obtained is consistent with that found in Coburn (2001); Iwakiri et al. (2012) where strong almost constant values of CRSF are found at the peak of the pulse and is not detectable in the off pulse regions. Thus the CRSF parameters cannot be constrained at the off pulse regions. The variation of the parameters also have very similar pattern for the different models used which give us added confidence on our obtained results. The following features can be seen from the Figure 5.10. The results are compared with respect to the high energy PIN profile (10–70 keV) shown in panel two of the same figure.

1. The energy $E1_{\rm cycl}$ varies by $\sim 12\%$. Its value is maximum ($\sim$ 37 keV) just after the peak of the pulse profile at phase 0.9 with a smaller peak ($\sim$ 35 keV) at phase ~ 0.6 .

2. The pattern of variation of the depth $D1_{\rm cycl}$ is very similar to that of the pulse profile, and remains almost constant at phases 0.5–0.9 (i.e. the region of the peak of the pulse profile) and becomes shallower near the falling edge of the pulse (phases 0.1 and 0.3). The line is not detected at the off pulse regions.

5.6 Model independent verification of the pulse phase dependence of CRSF

In order to verify the pulse phase dependence of the cyclotron resonance scattering feature in the above mentioned sources (Figures 5.3 to 5.10) in a model independent manner, we calculated the ratio of the following (i) PIN spectrum of the pulse phase with the deepest CRSF, by the same of the pulse phase with the shallowest CRSF as seen in the figures 5.3 to 5.10 (i) same for the pulse phase with the highest CRSF energy to the pulse phase with the lowest CRSF energy. For Vela X-1 the ratios were calculated for the fundamental CRSF, and in the case of GX 301-2 where the depth was kept fixed

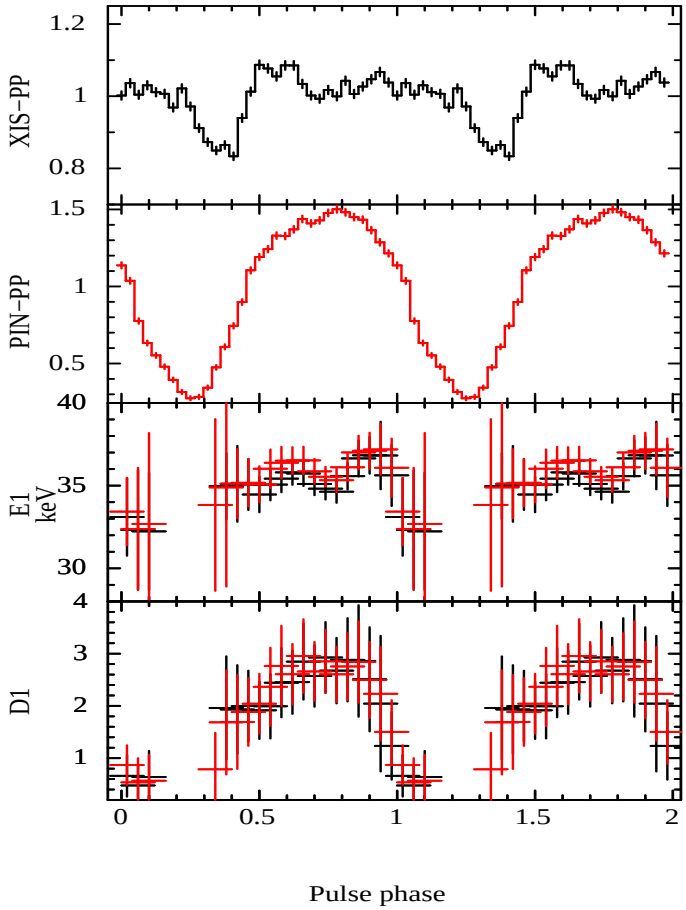

Figure 5.10: Same as in Figure 5.3 in 4U 1626-67. The black points denotes the parameters as obtained with the 'NPEX' model and the red points denote the parameters as obtained with the 'CompTT' model. Only 8 of the 25 bins are independent.

at the phase averaged value at all the pulse phases, the ratio of spectra corresponding to the widest to the narrowest CRSF was calculated.

The ratio plot of spectra for the phases corresponding to the deepest and shallowest CRSF is also shown in Chapter 3 to verify the existence of the CRSF in XTE J1946+274. Figures 5.11 and 5.12 show the ratio plots of the spectra for each source. The ratio plots for the CRSF energies (Figure 5.11) show dip like features or systematic trends near the CRSF energies of the corresponding sources. The features are most prominent for A 0535+26, GX 301-2 and 4U 1626-67 all of which have a deep CRSF detected in their spectrum. The ratio plot of the CRSF depths (Figure 5.12) also show dip like features near the corresponding CRSFs of the sources. As in the previous case, the dip is most

prominent for GX 301-2 and 4U 1626-67. A 0535+26 having a deep but narrow CRSF a narrow but prominent dip is seen at $\sim$ 35 keV. Another interesting observation is that although the dip at $\sim$ 18 keV for 4U 1907+09 is not very prominent (the source has a very shallow and narrow CRSF), a clear dip is seen at $\sim$ 40 keV, near the first harmonic of the CRSF. This motivated us to look more carefully at our phase resolved spectra, especially at the phase ranges where the ratio plot was made. Indeed, for the spectra near the peak of the second pulse profile at phase range 0.7–0.8, clear dip like residuals are seen at $\sim$ 40 keV. An attempt to constrain the line however failed due to poor statistics of the source at higher energies. This hints the presence of the first harmonic of the CRSF in 4U 1907+09 after Cusumano et al. (1998), and further indicates that the harmonic too exhibits pulse phase dependence, being stronger at the peak of the second pulse.

5.7 Variation of the pulse profiles around the cyclotron line

As the scattering cross sections are significantly altered and increases by a large factor near the cyclotron resonance scattering feature (Araya & Harding, 1999; Araya-Góchez & Harding, 2000; Schönherr et al., 2007), the corresponding beam patterns and hence the pulse profiles are also expected to change near the corresponding resonance energies of the accretion powered pulsars . Such probes have been attempted before by Tsygankov et al. (2006); Lutovinov & Tsygankov (2009); Ferrigno et al. (2011). Significant changes near the cyclotron line energy have been reported before in a couple of sources (V 0332+53 Tsygankov et al. (2006) and 4U 0115+63 Ferrigno et al. (2011)). 4U 0115+63 shows significant changes of its shape near the pulse peak at the CRSF fundamental and its corresponding harmonics. V 0332+53 also shows an asymmetrical single peaked structure near its fundamental CRSF energy in contrary to the otherwise double peaked profile. Lutovinov & Tsygankov (2009) studied both the intensity and energy dependence from the pulse profiles in the hard X-ray range (20-100 keV) using *Integral* observation . **More interestingly, they have tried to see the changes in the profiles near the CRSF. The main result of the work is that there is a general trend of increase of the pulse fractions with energy for all the sources, with a local maxima near the CRSF energy for some sources.** We have studied the energy dependent

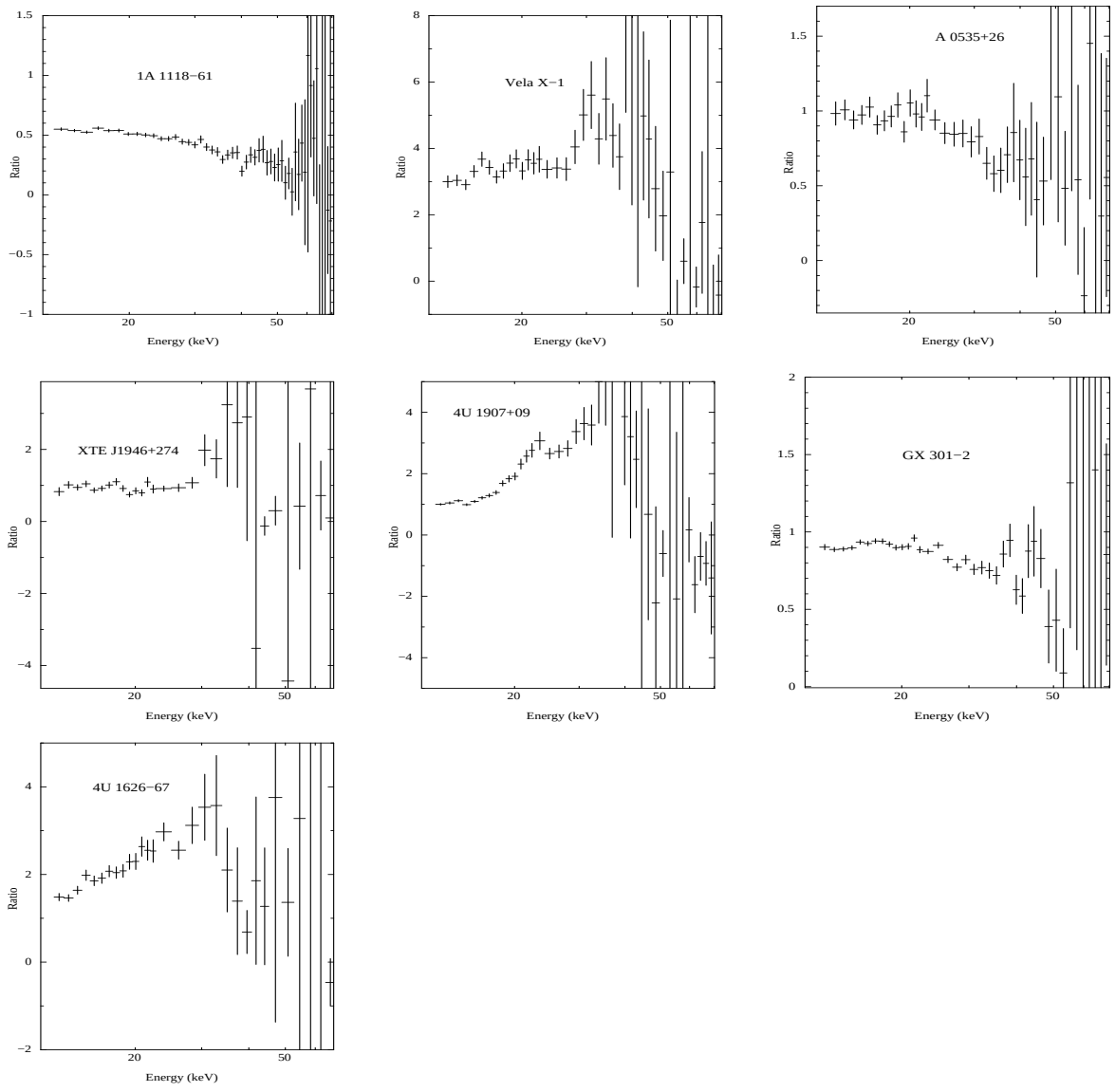

Figure 5.11: Plots for ratio of the PIN spectra for sources at phases corresponding to the lowest CRSF energy to the highest CRSF energy.

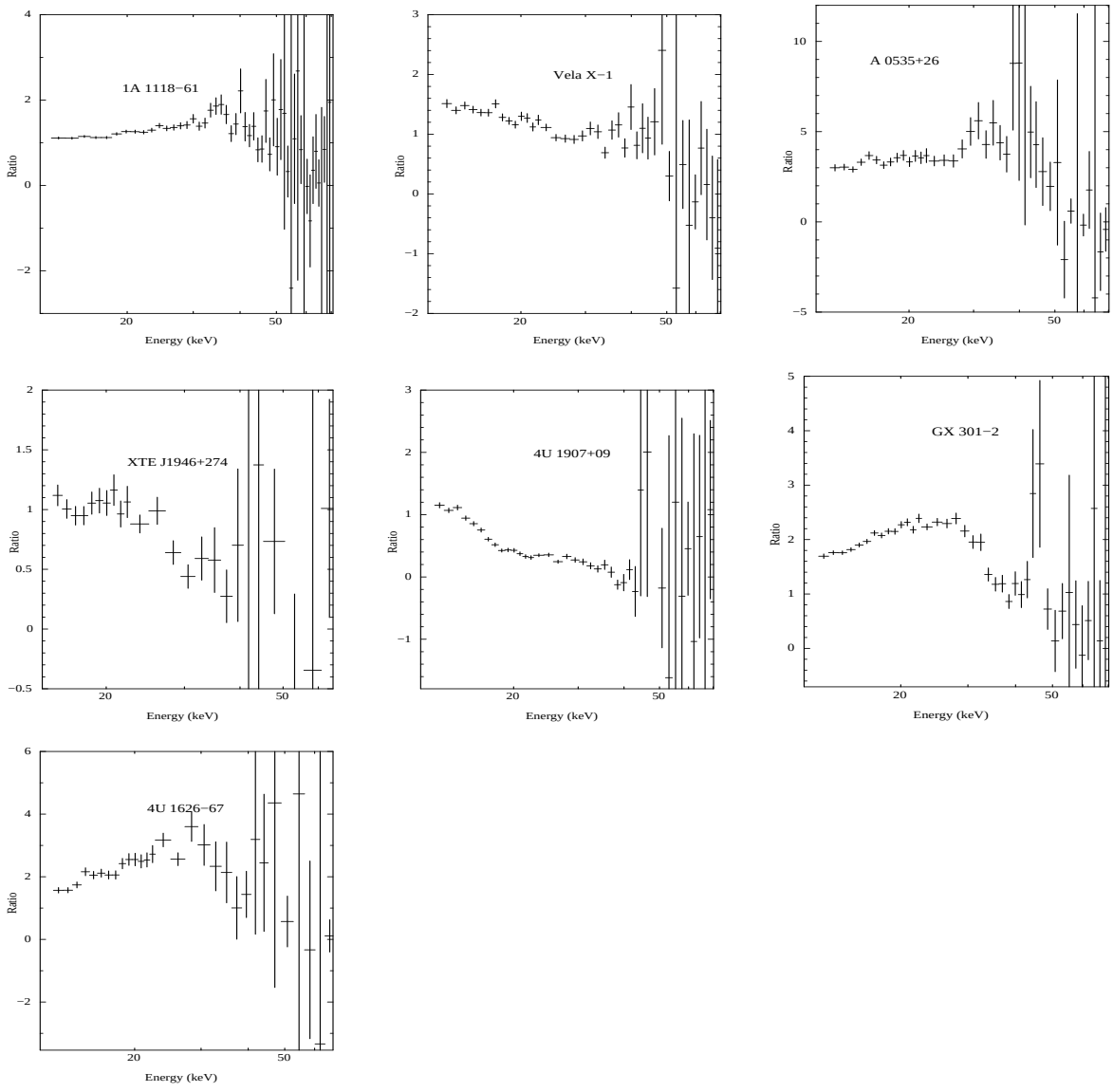

Figure 5.12: Same as in Figure 5.11 at phases corresponding to the deepest to the shallowest CRSF (widest to narrowest for GX 301-2).

evolution of the pulse profiles near the CRSF energy of all the X-ray binaries with a confirmed CRSF, and for which long *Suzaku* observations were available (See Table 3.1 of Chapter 3). Apart from the sources which were covered in Lutovinov & Tsygankov (2009), we have also studied some sources like XTE 1946+274, 1A 1118-61 and GX 304-1 that were not probed with the *Integral* data.

5.7.1 Timing Analysis

We have used the *Suzaku* HXD-PIN data for the analysis. For GX 304-1 which has a higher CRSF among the other sources, we have also used HXD-GSO data (50-70 keV). We have extracted light curves in different energy bands after background subtraction and deadtime correction See [3]. Arrival times of all the photons were corrected to the barycenter of the solar system. For Her X-1 and Cen X-3 having short orbital periods, the arrival times were corrected for the orbital motion.

Energy dependent light curves of the sources have been extracted according to the energy of the CRSF measured from its corresponding spectra. Pulse periods have been measured by the χ^2 maximization technique. The best estimate of the period for Her X-1 and Cen X-3 are tabulated in Table 5.2.

The light curves in different energy bands have been folded with the best obtained periods to create the pulse profiles for the different sources. The pulse profile near the CRSF is centered around the CRSF energy with a width equal to the FWHM of the feature measured from the spectrum in Chapter 3.

Table 5.2: Determined pulse periods

Source name	Period (s)
Her X-1	1.23774389 s (T0= 53648.4893, P^a_{orb}=1.7001 d)
Cen X-3	4.80461737 s (T0=54808.13541,P^a_{orb}= 2.0870 d)

[a] Orbital period in days

5.7.2 Results: Energy Dependence of the high energy pulse profiles near the CRSF

Figures 5.13, 5.14, 5.15, 5.16, 5.17, 5.18,5.19, 5.20, 5.21 and 5.22 shows the pulse profiles of different sources in the PIN-HXD energy band (10-70 keV) and the PIN-GSO band

[3]http://heasarc.gsfc.nasa.gov/docs/suzaku/analysis/abc/node10.html

(< 70 keV). The pulse profiles at the CRSF energies are marked in red, and the profiles at all other energies (higher and lower) are marked in green. The main results are the following'

1. GX 301-2, 1A 1118-61 and Her X-1 shows some distinct change in the pulse profile near the CRSF energy. The higher and lower energy (w.r.t CRSF) profiles are similar.

2. XTE J1946+274 and A0535+26 shows enhanced beaming and change in shape of the pulse profile near the CRSF band but we do not have enough statistics at higher energies to probe the change thereafter.

3. Cen X-3 shows featureless profile near the CRSF at $\sim$ 28 keV. But it is highly beamed with a shift in the peak at higher energies (34-50 keV).

4. 4U 1626-67 is quite featureless with energy (this source has a shallow a narrow line at 37 keV).

5. Two other sources which seem to featureless near the CRSF fundamental are 4U 1907+09 and Vela X-1. It is noteworthy that both have shallow and narrow lines at 18 and 24 keV respectively. The increase in pulsation for 4U 1907+09 coincides with the possible harmonic CRSF (though it is not detected in the spectra of the same *Suzaku* observation).

6. GX 304-1 shows a phase shift in the pulse profile near the CRSF energy. The CRSF of this source being at $\sim$ 54 keV, we cannot probe the profile at energies higher than the CRSF. For this source, we have not plotted the pulse profiles together, since the pulsed fraction is drastically lower in the GSO band (50-70 keV profile).

   For all of these sources the maximum beamed pulse profiles are in the range of 20-50 keV.

5.8 Discussion & Summary

In **the first part of** this Chapter we have presented the results of pulse phase resolved spectroscopy of the CRSFs in some bright accretion powered pulsars with *Suzaku* observation . The strength of our results lie in the fact that we have obtained similar pattern

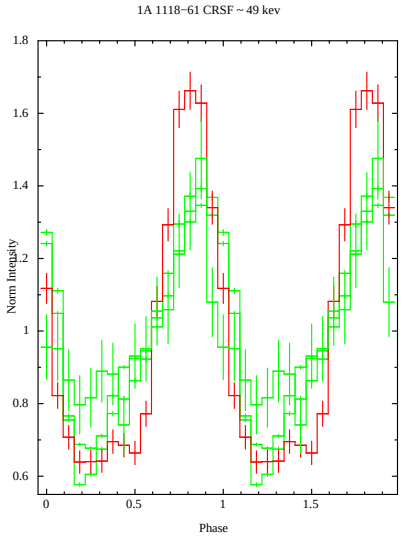

Figure 5.13: Energy dependent pulse profiles for 1A 1118-61 during the peak of an outburst. For all the sources, the pulse profile near the CRSF energy is marked in red, and the others in green. For all the sources the pulse profiles denote normalized intensity.

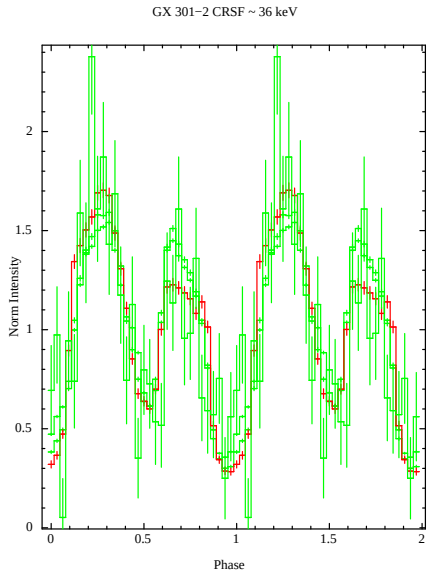

Figure 5.14: Same as in Figure 5.13 for GX 301-2.

of variation of the CRSF parameters for all the sources with more than one continuum model. In the above sections, we have described in detail the pattern of variations of the cyclotron resonance scattering feature parameters with the pulse phase. **The results indicate complex dependence, and typical variations with phase are 10–30**

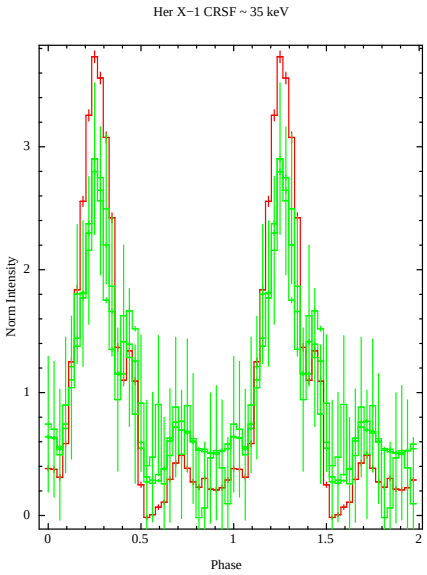

Figure 5.15: Same as in Figure 5.13 for Her X-1.

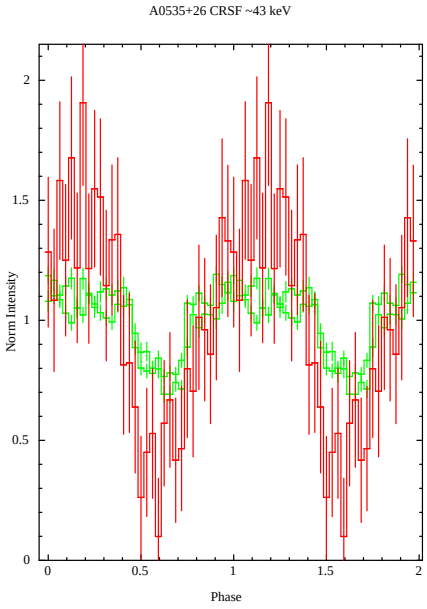

Figure 5.16: Same as in Figure 5.13 for A 0535+26.

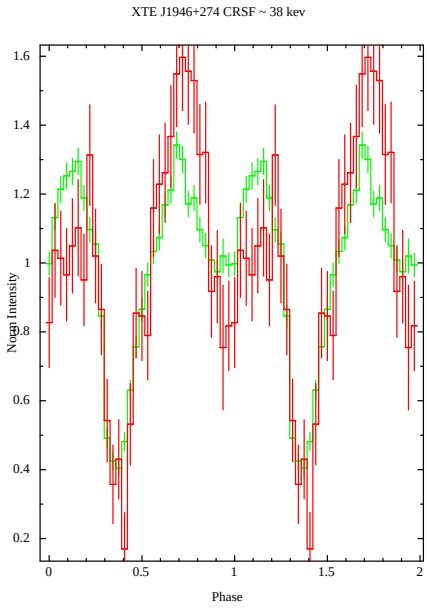

Figure 5.17: Same as in Figure 5.13 for XTE J1946+274.

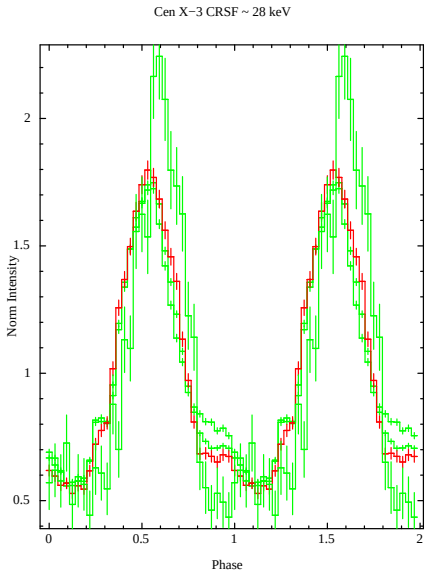

Figure 5.18: Same as in Figure 5.13 for Cen X-3.

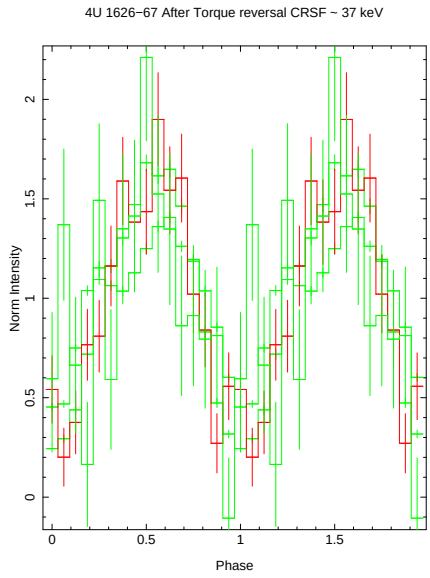

Figure 5.19: Same as in Figure 5.13 for 4U 1626-67.

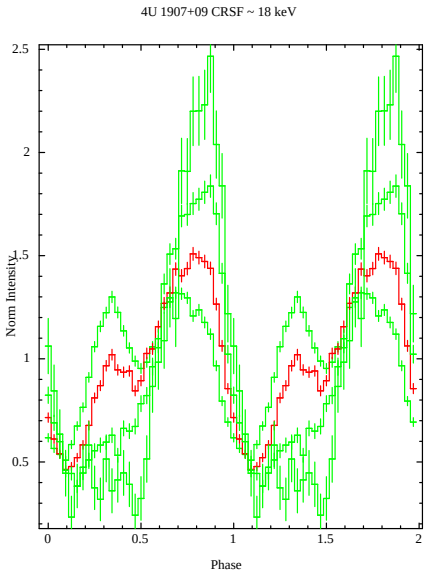

Figure 5.20: Same as in Figure 5.13 for 4U 1907+09. The first peak disappears with increasing energy. The pulse profile is beamed and becomes a single peaked structure at $\sim$ 36 keV.

% or more. Such high percentage of variation cannot be definitely explained by the change in viewing angle alone, and if explained by the changing projections at different viewing angles of different parts of the accretion column, requires a large gradient in the physical parameters across the emission region. Similarly, a change in the CRSF centroid

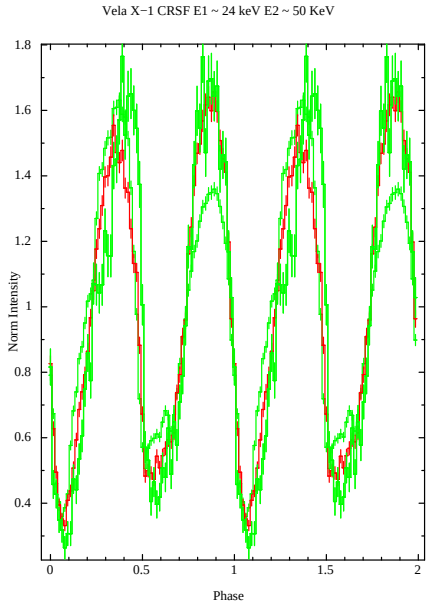

Figure 5.21: Same as in Figure 5.13 for Vela X-1. The second peak is in general stronger at higher energies with a phase shift in the first peak after 30 keV.

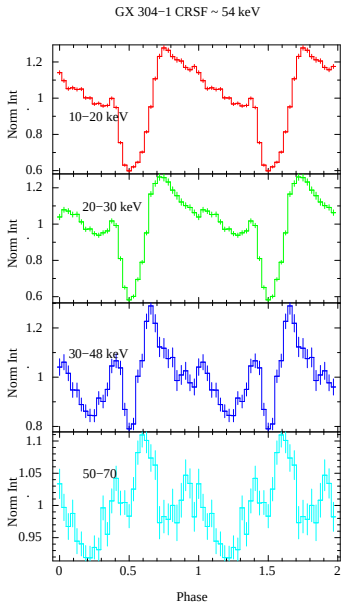

Figure 5.22: Energy dependent pulse profiles for GX 304-1. The pulse profile in the last panel (50-70 keV) corresponds to the profile at the CRSF energy and shows a phase shift w.r.t to the profiles at other energies.

energy due to the change in the height of the emission region (and hence the magnetic field strength) at different viewing angles requires an accretion column of height several kilometers. Such explanations are therefore not very plausible. Alternately the results can be explained by large polar cap regions (with a wide opening angle of $50 - 60°$.), or a more complex configuration of magnetic field consisting of high gradients, and non dipolar components (Nishimura, 2008; Mukherjee & Bhattacharya, 2012a,b). It has also been recently proposed that superposition of cyclotron resonance scattering feature , from different line forming regions can give rise to this large factor of variation in the CRSF parameters (Nishimura, 2011). Moreover the effect of gravitational light bending due to the strong gravity near the neutron star surface (Leahy, 2003) may smear the pulse phase dependence results with a particular viewing angle having contributions from multiple emission regions.

There are also no reliable theoretical modeling available till date which has been able replicate the physically observable CRSFs and its variations very accurately. Monte carlo simulations of the line forming region often suffer from the problem of very strong emission wings in the fundamental CRSF which are not observed in reality. **The absence of emission wings in the data may although, also be due to limited energy resolution of the present day instruments, or due to the smearing effect of superposition of many cyclotron lines.** The fan or pencil beam patterns depending on the sources luminosity (as discussed in Chapter 1) are also ideal approximations of the beaming of the radiation and both may also coexist from an accretion column, with the base of the column emitting the fan like beam pattern and the top emitting pencil like beam pattern. Kraus (2001); Leahy (2004) have interpreted the observed pulse profiles of Cen X-3 and Her X-1 as a combination of pencil and fan like beaming patterns of radiation emitted from the accretion column on the surface of the neutron star. In this case a higher percentage of variation of the CRSF parameters are acceptable with the beaming patterns changing within one rotational phase of the neutron star. In this scenario, the phases indicating narrower and deeper CRSFs at higher centroid energies may refer to the region dominated by fan beaming pattern and the ones indicating more broader and shallower CRSFs at lower energies to the region dominated by pencil beaming pattern (Refer to Schönherr et al. (2007) for the expected angular dependence of the CRSFs with viewing angle). This situation is further complicated by the contribution from both the poles of the neutron star adding up to the beaming profile at certain favorable viewing angles. Another important point worth considering is the accretion geometry itself.

Conventionally, the accretion geometry has been assumed to be an emitting region of slab or cylinder on the surface of the neutron star (Meszaros & Nagel, 1985b). However, this is just a **simplifying** assumption and the actual geometry would depend on the structure of the region where the accreted matter couples to the magnetic field lines and further on the nature of the region where the matter gets decelerated on the neutron star surface. Ring shaped mounds and partially filled or hollow accretion columns may result if the filling factor and hence the threading region is smaller. Emission from more of these complicated geometries have been calculated in Kraus (2001), Leahy (2003) and references therein. Simulations of CRSF line forming regions must be carried out with more of these geometries and compared with the observational results.
We have not tried to carry out a detailed theoretical modeling of the sources and have left it for a future work. However in the next few paragraphs we will provide a few explanations of the variations of the CRSF parameters from very simple arguments.

5.8.1 1A 1118-61

The pulse phase dependence of 1A 1118-61 have been obtained for the first time in detail for this source. Suchy et al. (2011) had performed phase resolved spectroscopy of the continuum and cyclotron parameters with the same *Suzaku* observation in three phase bins, centered around the pulse peaks and the dips. They had obtained different results for the phase variations of the CRSF with the 'cutoffpl' and the 'CompTT' model. Our results are consistent with the trend suggested with the 'CompTT' model. The 'cutoffpl' model anyway as we have shown in Chapter 3 is not a very good description of the 1A 1118-61 spectra and results in unphysically broad CRSF lines.
The CRSF parameters in 1A 1118-61 vary by a large amount (30 % for the energy and factor of two for the depth). This either implies a more complicated magnetic field geometry (non-dipolar) or more complex geometry and beaming pattern.

5.8.2 Vela X-1

Pulse phase resolved spectroscopy of the CRSFs in Vela X-1 was performed previously by Kreykenbohm et al. (2002) using the two *RXTE* observations, but they did not have enough sensitivity to probe the variations in detail. We have obtained very detailed results of the variations of the CRSFs in Vela X-1 exploiting the broadband capability and the high sensitivity of the *Suzaku* observation added with a vary careful analysis

to mitigate the effect of variability due to change in the spectrum or luminosity in the results. Moreover we have found the evidence of the variations in the ratio of the two line energies with the pulse phase for the first time in this source, which is an interesting result. This indicates that the respective CRSF fundamental and the first harmonic forming regions are changing with the pulse phase. As is mentioned before, the ratio of the two line energies is > 2 at many phases. According to Nishimura (2011), This would favor a line forming region with a large polar cap or of a greater height. The fundamental would be formed at a higher site and second harmonic primarily around the bottom. As a result $E2/E1 > 2$ is expected. Nishimura (2011) further predicts a shallow and narrow fundamental and a deeper and wider second harmonic would imply large viewing angle w.r.t the magnetic field. A fan like beam would be expected for Vela X-1 in this case.

5.8.3 A 0535+26

Pulse phase resolved variations of the CRSF in A 0535+26 was performed by Caballero et al. (2008) using *Integral* observation . They reported the variation of the CRSF in six phase bins and also detected the first harmonic of the line at $\sim$ 100 keV at some pulse phases. Our results are compatible with that reported by the authors, although we have not detected the first harmonic of the CRSF with the *Suzaku* observation . At the same time we have obtained more detailed and sensitive results for the variation of the fundamental line with pulse phase.

The energy of the CRSF does not vary by a large fraction, although the depth varies by almost a factor of four. Since the correlation of the deepest and shallowest CRSFs with the pulse profile of the source can provide some idea about the beaming pattern of the source at that luminosity, the trend of shallowest lines near the pulse peak and deepest near the off pulse as found in A 0535+26 favors a pencil beam geometry.

5.8.4 XTE J1946+274

Pulse phase dependence of the CRSF parameters have been obtained for the first time in this source. Although the statistics of this observation is not as good as in the other sources, it is sufficient to detect a clear phase dependence of the cyclotron line parameters with the pulse phase. The CRSF parameters vary by a large fraction in this source. Following the argument given for the case of A 0535+26, the trend of shallowest

lines near the pulse peak and deepest near the inter pulse regions favors a pencil beam geometry for the source in this luminosity.

5.8.5 4U 1907+09

For 4U 1907+09, analysis of the same *Suzaku* observations have been performed before by Rivers et al. (2010). We have done a detailed and careful analysis emphasizing mainly on the results of the CRSF variations with pulse phase. The most interesting result obtained for this source is that the CRSF parameters show the same pattern of variation for the two observations having factors of two difference in luminosity. This has important implications on the change in the beaming pattern of radiation with luminosity and hints that the beaming pattern remains constant for this luminosity range. Similar results obtained at different luminosity levels would be crucial to establish the change in beaming pattern of the sources with luminosity as proposed in Becker et al. (2012).
The CRSF parameters vary by a large amount in this source. Further, in similar light of the arguments stated in the case of A 0535+26 and XTE J1946+274, deepest and widest lines found near the peak and shallowest and narrowest near the off-pulse as found in 4U 1907+09 favors a fan beam geometry for the emission. **Another interesting result is the presence of the first harmonic clearly seen in the ratio plot of the PIN spectra at the phases corresponding to the deepest and shallowest fundamental. This is the second time the presence of the first harmonic has been indicated in this source after Cusumano et al. (1998).**

5.8.6 GX 301-2

Pulse phase resolved spectroscopy of the CRSF in GX 301-2 have been performed before from *RXTE* observation (Kreykenbohm et al., 2004) and from *Suzaku* observation (Suchy et al., 2012) in six and ten phase bins respectively. Both the works have used the 'FDCUT' continuum model for their results. We have obtained a consistently similar picture of the phase resolved variations of the CRSF in this source with the 'Newhcut' model. The maxima and the minima of the CRSF parameters are in agreement with the previous works although the pattern of variation is sharper and steeper. This might also be due to the higher resolution of our results with the 25 overlapping phase bins in compared to the previous cases.
Although The CRSF parameters do not vary by a large amount in this source, the sharp

pattern of variations are indicative of the existence of sharp gradients in the physical parameters of the emission region or a non dipolar magnetic field (**i.e. the presence of higher order multipoles.**).

5.8.7 4U 1626-67

Pulse phase resolved spectroscopy of the CRSF in GX 301-2 have been performed before from *RXTE* observation (Coburn, 2001) and from *Suzaku* observation (Iwakiri et al., 2012) using the NPEX and FDCUT models respectively. The results from the *RXTE* observation claim that the CRSF parameters are constant near the peak of the pulse and is weak or non detectable at the off pulse regions. This trend is similar to that found in our results, although the higher resolution of our results probably allow us to distinguish two peaks in the CRSF energy near the peak of the pulse profile. The results from the *Suzaku* observations (Iwakiri et al., 2012) claim the detection of a cyclotron emission feature rather than the absorption feature at the dim phase (falling edges) of the pulse profile. The authors justify their results with the decrease in the optical depth of the accretion column at these phases which makes the line appear in emission rather than in absorption. We however find an absorption (Gaussian) profile for the CRSF is consistent with the line at all phases and do not add a emission profile at the dim phases. Moreover the optical depth and width (τ and σ) obtained by Iwakiri et al. (2012), is not consistent with our results, as they find an increasing trend of τ near the falling edges of the peak in contrary to a decreasing trend in the depth of the profile found by us.
The CRSF parameters in this source do not vary by a large factor and the picture is consistent with a simple fan beam pattern of radiation with deeper CRSFs near the peak of the profile and shallower at the falling edges. The CRSF centroid energy $E1_{\rm cycl}$ is also higher near the peaks as expected from a fan beam pattern (emission from lower regions of the column having higher magnetic field strength.)

In the last section of this chapter, we have probed the pulse profiles of accretion powered pulsars near their corresponding cyclotron resonance scattering feature energies. Although a general trend of increase in the pulse fraction is noticed at higher energies (20–50 keV), there is a distinct change in shape and pulse fraction in the pulse profiles of some sources like GX 301-2, 1A 1118-61 and Her X-1. Interestingly, all of these sources exhibit a

deep CRSF in their energy spectra. On the other hand sources like Vela X-1, 4U 1907+09 and 4U 1626-67, which are quite featureless near their CRSF fundamental energies have a relatively shallow fundamental in their spectra. GX 304-1 on the other hand exhibits a phase shift near its CRSF energies. These features need to be studied and modeled in detail, and correlated studies of the pulse profile variation near its cyclotron resonance scattering feature energies along with the phase resolved measurements can provide a consistent picture of the magnetic and emission geometry in these sources.

Chapter 6

Thomson X-ray polarimeter, prospects for compact objects

6.1 Introduction

Since the birth of X-ray astronomy, sensitivity/capability of timing, spectral, and spatial observations of the X-ray sources have improved by several orders of magnitude and have provided us with a wealth of information regarding the X-ray sky. X-ray polarimetry however, continues to remain a fairly unexplored domain with only one definitive polarization measurement available made with OSO 8 in 1976 (Weisskopf et al., 1976) of the Crab nebula (P = 19± 1.0 per cent). Polarization angle was consistent with measurements at other wavelengths and consistent with the synchrotron nature of the radiation. It also provided upper limits of 13.5 and 60 per cent for the pulse phase averaged degree of polarization in two X-ray accretion powered pulsars Cen X-3 & Her X-1 respectively (Silver et al., 1979). Although Radio and Optical astronomers extensively use polarimetry to probe into the radiation mechanism and geometry of sources, X-ray astronomy is far behind in this regard which would provide some crucial information regarding the radiation mechanism, source geometry, inclination and magnetic fields etc. Sensitive X-ray polarimetry could also be used as a probe for fundamental physics since it gives information on matter under extreme gravitation or magnetic fields. It could also solve degeneracy between different theoretical models which cannot be solved by timing and spectroscopy studies alone. Various emission mechanisms like synchrotron, non-thermal bremsstrahlung etc. give rise to high degree of polarization. Other emission processes for

polarization could be scattering of initially unpolarized radiation in asymmetric plasmas or disks. Vacuum birefringence through extreme magnetic fields or the phenomenon of Compton dragging can also give rise to polarization. The potential sources of X-ray polarization are accretion and rotation powered pulsars, thermal or reflected emission from the accretion disk. Cosmic acceleration sites such as supernovae remnants and jets in Active Galactic Nuclei or microquasars are also sources of polarization.
In recent times there have been significant development in X-ray polarization measurement techniques (Costa et al., 2008; Bellazzini et al., 2006). Various X-polarimetry missions are under development. Out of them the most significant ones are the *GEMS* mission (Swank et al., 2008) and the X-ray Imaging Polarimetry Explorer (XIPE) (Soffitta et al., 2013), which is based on photoelectron polarimeter technique for measurement of polarization in the soft X-rays. In the hard X-rays too, various Compton X-ray polarimeters have been proposed, to name a few the X-Calibur (Compton Scattering polarimeter) (Beilicke et al., 2012), GRAPE (Gamma-Ray Polarimeter Experiment) (McConnell et al., 2009), and several balloon borne hard X-ray polarimeters like HX-POL (Lee et al., 2010), PoGOLite (Pearce et al., 2012) etc.
In 2008, a proposal was submitted to the Indian Space Research Organization (ISRO) for a dedicated small satellite experiment for measuring X-ray polarization in the $5-30$ kev range. This will be based on the principle of polarization measurement by anisotropic Thomson scattering of X-rays and will be sensitive to the bright X-ray sources. This instrument will compliment the polarization measurements in the soft X-ray band by photoelectron polarimeter and in the hard X-ray band by the Compton polarimeter and allow measurement of polarization over a wide energy range.

Here we calculate the Minimum Detectable polarization (MDP) that we would get with the X-ray polarimeter experiment for polarization from different sources, a) the thermal emission from the accretion disk for some of the galactic black hole sources during their thermal dominated spectral states, b) the hard reflection dominated emission from the black hole binaries during their Comptonization dominated spectral states, and c) accretion powered X-ray pulsars.

Apart from the MDP, the error in measurement of the angle of polarization for particular detection significance limits is also calculated. We have done a very detailed analysis and calculation in case of the polarization expected from the black hole binaries in their thermally dominated state due to the following reasons:

1. Sources with strong X-ray polarization like accretion powered pulsars or reflection dominated emission from the accretion disk etc., are expected to have a fairly high degree of polarization and are sources of hard X-rays which are most suited for observation by the Thomson X-ray polarimeter. Galactic black hole binaries however, have a soft spectra in their thermally dominated state and typically peak at $1-3$ kev. In this state there is also expected to be very little flux above ~ 10 kev. The radiation itself is also not polarized to a high degree except in the innermost parts of the accretion disk in some cases. This makes its detection by the Thomson polarimeter difficult.

2. Black hole binaries have different spectral states and display state transitions in which either the thermal or the non thermal component dominates the X-ray flux. They are also mostly transient sources which go into outburst once in a while during which they make their transition to the thermally dominated soft state. Therefore, detection of polarization from the black hole binaries in their thermal state would also be constrained by the condition of one of the sources going into outburst/state transition during the lifetime of the mission.

6.2 Proposed Experiment

6.2.1 Objective

A Thomson scattering X-ray polarimeter has been developed and a small satellite mission with a similar payload is under consideration by ISRO. It is based on the principle of anisotropic Thomson scattering of X-ray photons working in the $5-30$ kev (with Lithium scatterer) and $8-30$ kev (with Beryllium scatterer). Thomson scattering and the intensity distribution of the scattered photons is measured as a function of azimuthal angle. Polarized X-ray will produce an azimuthal modulation in the count rate as seen from Figure 6.1. The total configuration will be rotated about the viewing axis. A laboratory model has been made and tested successfully, an engineering model has been designed and fabrication of the same is in the final stages which has been designed for a flight unit [1]. The instrument configuration consists of four detector elements which are multi wire proportional counters placed on the sides of a disk like scattering element

[1] http://www.rri.res.in/$\tilde{}$bpaul/polix.html

Table 6.1: Instrument specifications of the Thomson X-ray Polarimeter

Description	Value
Photon collection area	1017 cm^2
Energy range	5–30 keV
Field of view	$3^\circ \times 3^\circ$ flat topped 0.2°
Detectors	Proportional counters
Total weight	$\sim$ 100 kgs
Overall dimension	$\sim 650 \times 650 \times 550$ mm^3
Power	50 Watt
Data generation rate	50 Gbits/day
Scattering element	Li/Be
Life time	3–5 years

made of Le or Be (typically having a low atomic number). The geometry of the scatterer is optimized to obtain the maximum scattering efficiency (Vadawale et al., 2010). The field of view of the system is confined to $3^\circ \times 3^\circ$ by a flat topped collimator having a flat topped response of 0.2°. The system configuration is given in Figure 6.2. Given below is a table (Table 6.1) on the instrument specifications. It has a sensitivity of $2-3$ per cent MDP in a $50-100$ mCrab source for an exposure of one million seconds (Rishin, 2010). The proposed experiment will be useful in measuring the degree and direction of X-ray polarization of a few ($\simeq 50$) bright cosmic X-ray sources including accretion powered binary X-ray pulsars, galactic black hole candidates, rotation powered pulsars and magnetars, SNRs and Active Galactic Nuclei.

6.2.2 Design and polarization measurement technique

Though the most sensitive polarization measurement devices are based on photoelectron track imaging, they require to be coupled with high throughput X-ray mirrors due to a small detector size. They also cover a softer energy range. The proposed scattering experiment is based on the well established technique of X-ray polarization measurement using Thomson scattering which has moderate sensitivity over a relatively large bandwidth suited in the energy band of our interest. The experiment configuration consists of a central low Z (Lithium, Lithium Hydride or Beryllium) scatterer surrounded by xenon filled X-ray proportional counters as X-ray detectors which collects the scattered X-ray

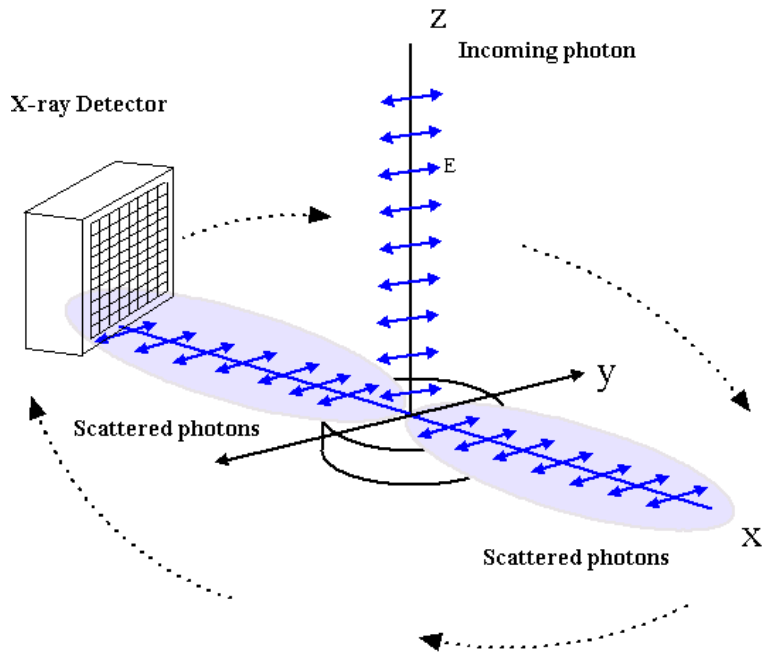

Figure 6.1: Figure showing the the intensity distribution of the scattered photons is measured as a function of azimuthal angle

photons. The instrument is rotated along the viewing axis leading to the measurement of the the azimuthal distribution of the scattered X-ray photons which gives information on polarization. The sensitivity of this experiment is dependent on a) collecting area b) scattering and detection efficiency c) detector background and d) modulation factor of the instrument.

Sensitivity and Minimum Detectable polarization of the Thomson scattering X-ray Polarimeter

The experiment is based on the principle that the differential Thomson scattering cross section for polarized radiation has an azimuthal dependence. The expression for differential cross section is given by

$$\mathrm{d}\sigma = \mathrm{r}_e^2(1 - \sin^2\theta\,\cos^2\phi)\mathrm{d}\theta\mathrm{d}\phi \tag{6.1}$$

where θ is the angle between the direction of the incident and scattered photon, ϕ is the angle between the scattering plane defined by the direction and the electric field vector of the incident photon, r_e is the classical electron radius. The resultant azimuthal

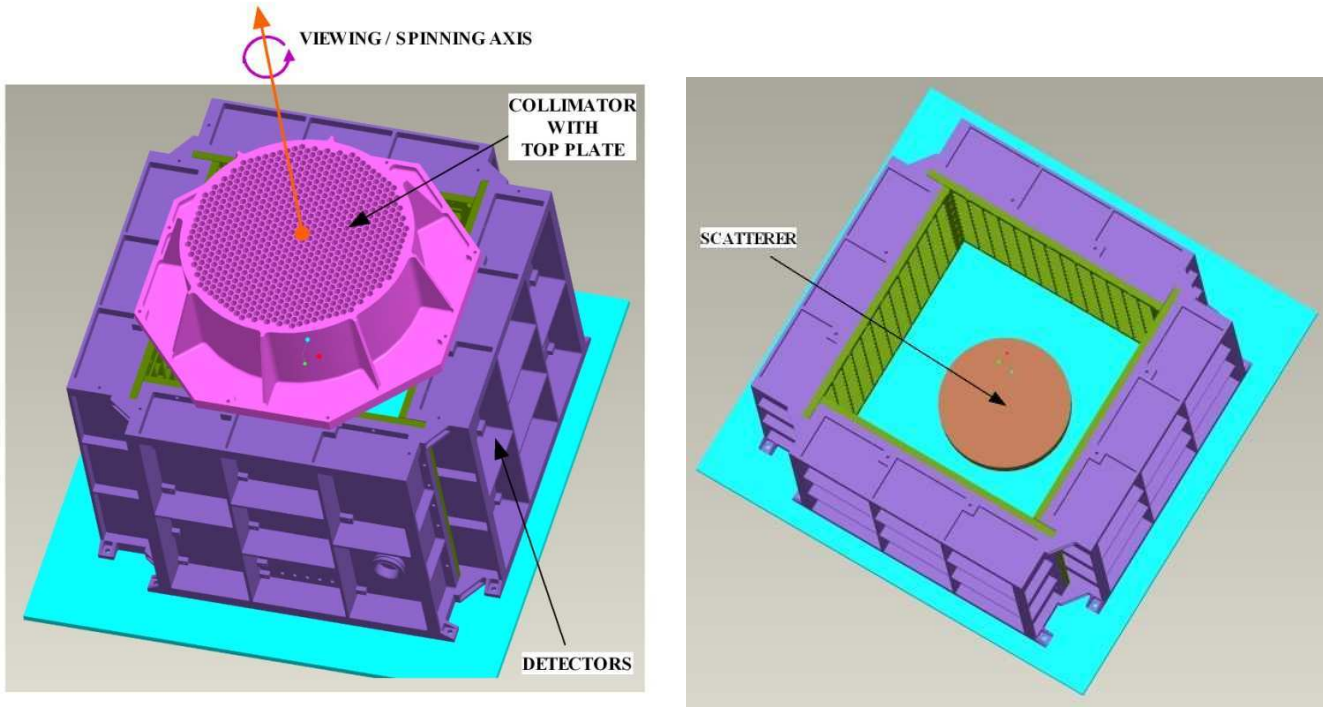

Figure 6.2: Figure shows the configuration of the Thomson Polarimeter. Here the detector elements are flat multi-wire proportional counters placed on four sides of a disk-like scattering element made of Be or Li.

distribution follows the integral of the differential cross section and is given by

$$\mathrm{C}(\phi) = \mathrm{B} + \mathrm{A}\sin(2\phi - \mathrm{P}) \tag{6.2}$$

A and B are constants and ϕ is the azimuthal coordinate and P the angle of polarization of the incident radiation.

The modulation factor μ for the pattern is expressed as

$$\mu = \frac{\mathrm{C_{max}} - \mathrm{C_{min}}}{\mathrm{C_{max}} + \mathrm{C_{min}}} \tag{6.3}$$

The degree of polarization for the incident beam is defined as

$$\mathrm{P_{pol}} = \frac{\mu_p}{\mu_{100}} \tag{6.4}$$

where μ_p is the observed modulation factor and μ_{100} is the modulation factor of the instrument in the absence of background for a 100 per cent polarized radiation

Minimum Detectable polarization (MDP) of the measurement for 99 per cent confidence level is given as (Weisskopf et al., 2010) -

$$\mathrm{MDP}_{99} = \frac{4.29}{\mu_{100}\mathrm{S}}\sqrt{\frac{(\mathrm{S}+\mathrm{B})}{\mathrm{T}}} \tag{6.5}$$

where S is the total source counts in the units of counts/sec given as $\mathrm{S} = \mathrm{R}_{src} * \mathrm{A}_c * \epsilon$; R_{src} being the rate of incident photons per unit area, ϵ is the overall detection efficiency and A_c the collecting area. B is the total background counts in the same unit given as $\mathrm{B} = \mathrm{R}_{bkg} * \mathrm{A}_d$; R_{bkg} being the total rate of background photons per unit area, A_d being the total detector area., T the integration time. (Following M. Weisskopf et al. 2010), For a required detection significance of $\mathrm{n}_\sigma = 3$ (99.73 percent confidence level) & 5 (99.99994 per cent confidence level) the MDP is calculated to be -

$$\mathrm{MDP}_{3_\sigma} = \frac{4.86}{\mu_{100}\mathrm{S}}\sqrt{\frac{(\mathrm{S}+\mathrm{B})}{\mathrm{T}}} \tag{6.6}$$

&

$$\mathrm{MDP}_{5_\sigma} = \frac{7.57}{\mu_{100}\mathrm{S}}\sqrt{\frac{(\mathrm{S}+\mathrm{B})}{\mathrm{T}}} \tag{6.7}$$

So for a given observation of particular S and B the parameters T determines the MDP at nσ level.

This is the expression for the MDP that we get for one day of observations for T secs integration time. To improve our polarization detectability we should intergrate it for more number of days . So the net MDP obtained for n days of observation each of T secs for a 5σ detection significance is given by

$$\mathrm{MDP}_{\mathrm{net}} = \frac{7.57}{\mu_{100}S_{net}}\sqrt{\frac{(\mathrm{S}_{\mathrm{net}}+\mathrm{B}_{\mathrm{net}})}{\mathrm{T}}} \tag{6.8}$$

where S_{net} and B_{net} are the net source and background counts obtained by integration over n days given by

$$\mathrm{S_{net}} = \sum_{i=1}^{n} \mathrm{S}_i \quad \& \quad \mathrm{B_{net}} = \sum_{i=i}^{n} \mathrm{B}_i \tag{6.9}$$

6.3 Expected polarization from Accreting black holes in their thermal state

One of the earliest work on the expected polarization properties of thermal emission from the accretion disk was done by (Rees, 1975). It predicted linear polarization with the electric field vector lying in the plane of the disk due to electron scattering in its plane parallel atmosphere. This was predicted according to Chandrasekhar (1960) calculations for plane scattering atmosphere where polarization degree depends on the angle of inclination of the system, the maximum value being $\simeq$ 12 per cent for edge on systems. Sunyaev & Titarchuk (1985) showed that the polarization of the disk photons depend on the optical thickness of the disk. Connors et al. (1980) computed X-ray polarization features from the standard accretion disk using general relativistic treatment which predicted energy dependent rotation in the plane of polarization in the inner parts of the accretion disk closer to the black hole. Dovčiak et al. (2008) extended this work by including the effect of optical depth and scattering atmosphere on the expected polarization signal. Li et al. (2009) showed the use of polarization information obtained of the thermal emission from the accretion disk to infer the inclination of the inner region of the disk. Schnittman & Krolik (2009) computed X-ray polarization from accreting black holes in their thermally dominated state using a Monte Carlo ray tracing code in General Relativity. For direct radiation from the disk it reproduces Chandrasekhar's results for the outer part of the disk. There is a decrease in the degree of polarization and energy dependent rotation in the plane of polarization in the innermost regions due to general relativistic effects. However, for the returning radiation there would be a rotation in the plane of polarization by ninety degrees at a transition radius, and an enhancement in polarization which can provide a good estimate of the black hole spin and also map the temperature of the inner accretion disk and its emissivity profile.

6.3.1 Analysis and Results

We have calculated the expected MDP from five galactic black hole candidates during their transition to the soft spectral state in the three energy bands of $6-9$, $9-11$, and $11-15$ keV. MDP was computed during the days when the blackbody temperature was highest (hence the source most thermally dominated) during the outbursts/state transitions of the sources. Equation 6.7 and 6.8 is used to calculate the MDP and MDP_{net} in the case of a 5σ statistical detection. The MDP_{net} value is also calculated for a 3σ statistical detection given by equation 6σ only in the $11-15$ KeV range, since it may not be detected for a 5σ detection in all cases in this band.

The values of the parameters used for the calculation are as follows :- $\mathrm{n}_\sigma = 5$; modulation factor for 100 per cent polarization for our experiment $\mu = 0.4$; integration time T = 43 200 secs (assuming a duty cycle of 50 per cent in a low altitude near equatorial orbit). The source counts S and background counts B are obtained from spectral fitting of the Rossi X-ray Timing Explorer *RXTE*/PCA (Zhang et al., 1993; Jahoda et al., 1996) spectra in the $3-30$ KeV range during the specified period of the outburst/state transition of the source. The Proportional Counter Array (PCA) has five xenon filled proportional counter detectors, sensitive in the range of $2-60$ KeV, and has an effective area of 6500 cm^2 at 6 KeV. The *RXTE*/PCA spectral data were fitted using *XSPEC* to a model consisting of interstellar absorption (Morrison & McCammon, 1983) plus a multicolor blackbody accretion disk (Mitsuda et al., 1984; Makishima et al., 1986) and a power-law component. In addition, an iron line and a Fe absorption edge was applied to some data sets. A systematic error of 0.5 per cent was also added in quadrature with the error. For the source counts $\mathrm{S} = \mathrm{R}_{src} * \mathrm{A}_c * \epsilon$, R_{src} is obtained from the blackbody count rate obtained by the spectral fitting of the data. $\mathrm{A}_c = 1017$ cm^2 (collecting area for our experiment). Following Cowsik & et al. (2010), the energy dependent efficiency ϵ is calculated for both Lithium and Beryllium scatterer. **At first the mean free path for scattering is calculated for both Li and Be at different energy ranges assuming the total mean free path to be the sum of photoelectric absorption mean free path and Thompson scattering mean free path. The photoelectric absorption cross section for the respective elements and energy ranges are taken from the NIST database [2]. After that the probability of back scattering of the X-ray photons are calculated** assuming a disk shaped scattering element with an

[2] www.nist.gov.in

Table 6.2: Energy dependent efficiency for Li & Be scatterer

Energy range(Kev)	Efficiency(Li)	Efficiency(Be)
6-9	9.4 per cent	4.0 per cent
9-11	16.1 per cent	8.5 per cent
11-15	21.7 per cent	14.4 per cent

optical depth of unity for Thomson scattering. The values obtained in the three energy bands of interest for both the materials of the scatterer are tabulated in Table 6.2
The background consists of the detector internal background B1. The power-law non thermal component of the flux B2 could also be polarized to a significant fraction having an energy dependence and could provide crucial information on the physics and geometry of the power-law photon emitting regions and also on the properties of the black hole (Schnittman & Krolik, 2009). However in this work we have considered this component of the flux as a background, due to the following reasons :

1. Black hole binaries in their low hard states would give us information on the polarization of the power-law photon emitting regions i.e. the corona and also on the black hole parameters. This is however expected to differ significantly from the polarization obtained from the thermal photons in the inner parts of the accretion disks obtained in the high soft states. Therefore a difference in the polarization information obtained in the two states would clearly distinguish between the two components. The power-law photons are likely to have only small energy dependence, and, in particular, a continuous change of the polarization angle with the energy is typical of the GR effects near the black hole.

2. Moreover in the thermal dominated (high soft) spectral states of the black hole binaries, the emission from the disk dominates over the power-law photon emitting regions and hence the polarization signal can be thought to come predominantly from the accretion disk of the source. There is however, a possibility of some dilution of the polarization signal in the thermal states due to the non-thermal power-law component.

Therefore B = B1+B2. B1 is calculated from the background obtained from the spectral fitting of the PCA spectra with the area scaled for the polarimeter detector . Hence

$$\mathrm{B1} = \frac{\mathrm{Counts_{AvgPCA}(counts/sec)}}{\mathrm{A_{PCATotal}}} * \mathrm{A_{xpolTotal}}$$

$$\mathrm{S_{net}} = \sum_{i=1}^{n} \mathrm{S_i} \quad \& \quad \mathrm{B_{net}} = \sum_{i=1}^{n} \mathrm{B1_i} + \mathrm{B2} * \mathrm{n} \tag{6.10}$$

This gives us an estimate of best MDP that we could have achieved by integration during that particular outburst/transition of the source using the X-ray Polarimeter. Calculating the MDP in the three energy bands of interest also enables us to do spectro polarimetry that would be crucial to map the energy dependent rotation in the plane of polarization in the inner parts of the accretion disk and possibly the transition radius where there would be a ninety degrees rotation in the plane of polarization. This would be essential to calculate the parameter space of the black holes and give an estimate of its spin and emissivity profile.
Results for the five black hole candidates for which the MDP is calculated is given below.

6.3.2 GRO J1655-40

GRO J1655-40 in an X-ray transient which was first discovered in July 1994 when it went into an outburst and was detected by the Burst and Transient Source Experiment (BATSE) on board *CGRO* in the $20-100$ KeV band. (Harmon et al., 1995). It is a Low Mass X-ray Binary (LMXB) having the mass of the compact object $\mathrm{M} = 7.02 \pm 0.22 M_{\odot}$ (Orosz & Bailyn, 1997). It has also shown signatures of ejection of superluminal jets. It showed an increased X-ray activity in the late February 2005 as it entered into a new outburst (Markwardt & Swank, 2005). As the outburst evolved the X-ray spectrum passed through various spectral states of low/hard, high/soft, very high states. Figure 6.3 shows the one day averaged All Sky Monitor (ASM) daily light curve of this source during the outburst in the $1.5-12$ KeV energy band.

For the MDP calculation the data was analysed in two stretches MJD $53\,442-53\,449$ & MJD $53\,511-53\,525$, when the spectrum was found to be the most blackbody dominated in all the three energy bands of our interest. Figure 6.4 shows the best-fitting spectrum of the source on two days. The first spectrum is of MJD 53 514, when the source was blackbody dominated and was hence included in the analysis of the MDP. The second spectrum is of MJD 53 503 which is mostly power-law dominated in the energy bands

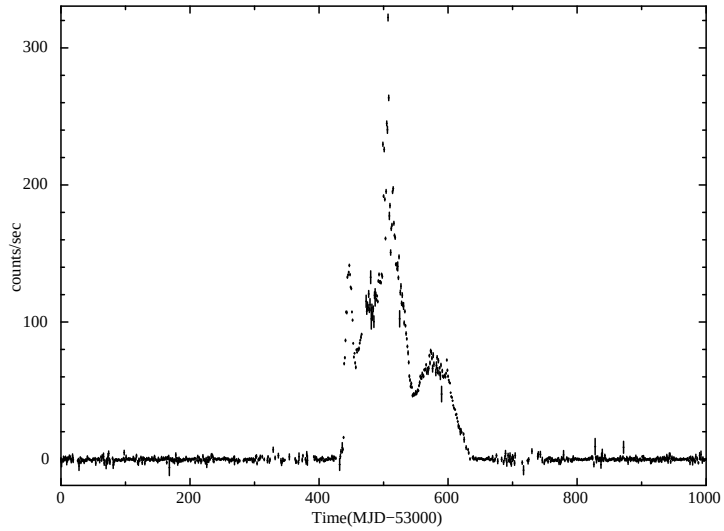

Figure 6.3: One day averaged long term ASM light curve of GRO J1655 − 40 showing the 2005 outburst of GRO J1655 − 40.

of our interest and hence have not been added in the analysis. Figure 6.5 & 6.6 shows the two components (thermal & non-thermal) of the flux during the outburst and also the MDP in the three energy bands for the two stretches analysed during the outburst. Although the MDP calculated on individual days for the source may exceed 100 per cent on some days (which means that polarization in the source cannot be detected with a 5σ statistical detection on those days), specially in the $11 - 15$ KeV band and in some days in the $9 - 11$ KeV band, the net MDP obtained by integrating over all the days can be constrained to a much smaller and reasonable value. However in the figures showing the MDP calculated, the days exceeding 100 per cent MDP have not been plotted.

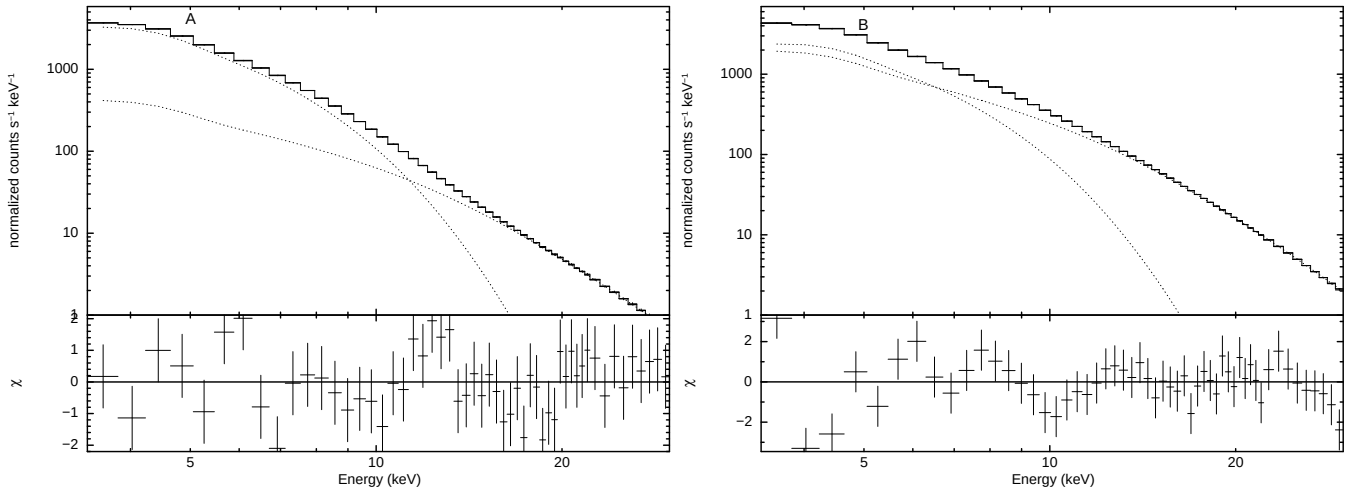

Figure 6.4: Figure A shows the X-ray energy spectrum of GRO J1655-40 in a disc dominated state on MJD 53514 fitted with the disk blackbody, powerlaw and interstellar absorption. Figure B shows the X-ray energy spectrum of GRO J1655-40 in a power-law dominated state on MJD 53503 fitted with the disk blackbody, powerlaw and interstellar absorption

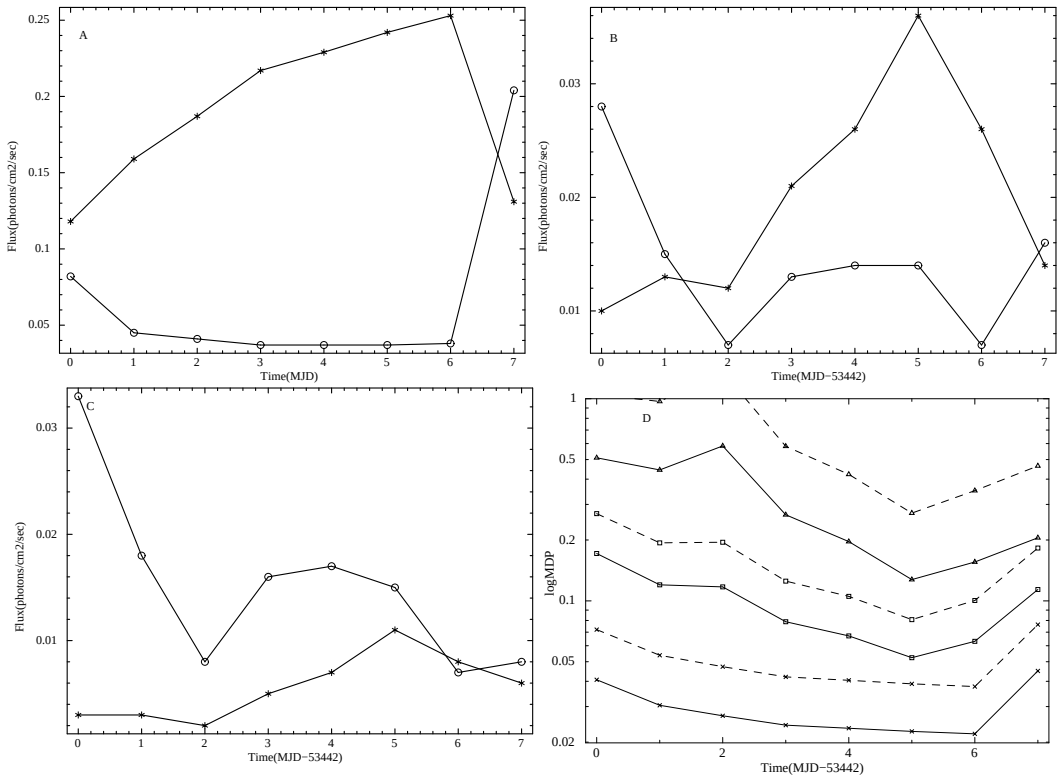

Figure 6.5: Figure A, B, C shows the blackbody and the powerlaw fluxes in the three energy bands for GRO J1655-40 in one stretch of its outburst in $6-9$ KeV, $9-11$ KeV, & $11-15$ KeV respectively. star indicates the blackbody flux and circle the powerlaw flux. Figure D shows the value of the MDP in the three energy bands for this source during the same time. Cross indicates MDP in $6-9$ KeV square indicates MDP in $9-11$ KeV & triangle indicates MDP in $11-15$ KeV.The solid line indicates calculation done with Lithium as a scatterer and dashed line indicates Beryllium as a scatterer.

6.3.3 GX 339-4

GX 339-4 is a recurrent dynamically constrained black hole candidate. It was first discovered with *OSO7* in 1972 (Markert et al., 1973b,a). Since then it has undergone several outbursts during which it passed through the various X-ray spectral states. The mass of the compact object is $\geq 5.8 M_{\odot}$ (Hynes et al., 2003). Radio jets have also been observed in the system. It entered into one of its outbursts which started early in 2002 April (Fender et al., 2002; Belloni et al., 2003, 2005). The X-ray spectrum passed through its various spectral states of low/hard intermediate and then into the high/soft state which it entered beyond MJD 52 411. The one day averaged daily ASM light curve of this source during the outburst is shown in Figure 6.7.

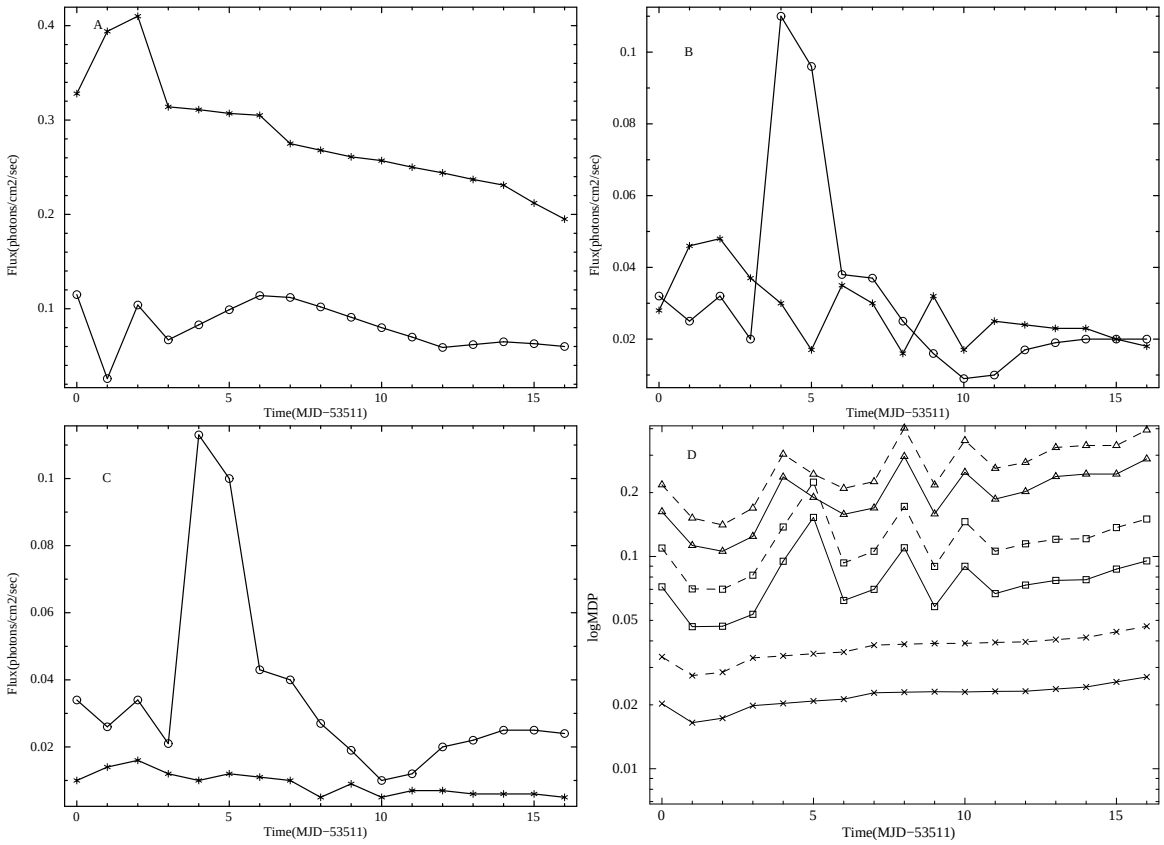

Figure 6.6: Same as Figure 6.5 for the second stretch of its outburst of GRO J1655-40 in the year 2005

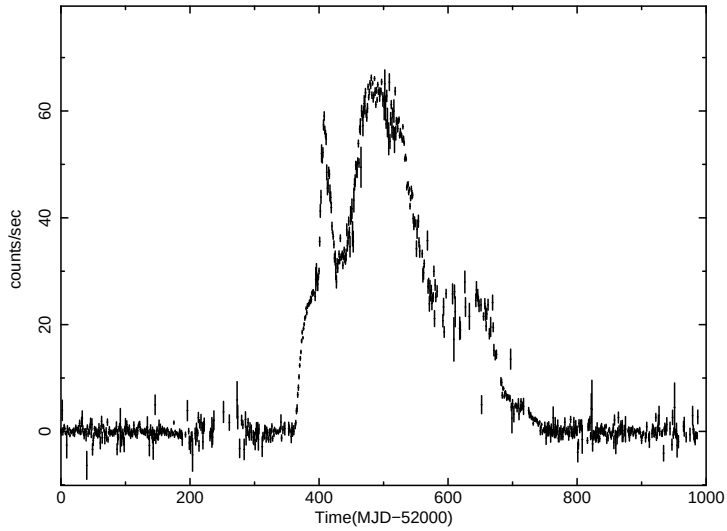

Figure 6.7: One day averaged long term ASM light curve of GX $339-4$ showing the 2002 outburst of GX $339-4$.

We have analysed the data in the stretch of MJD $52\,472 - 52\,518$ to calculate the MDP. The net MDP was found to be the lowest in this case < 1 per cent since apart from this being a very bright outburst, the source was also integrated for a long stretch $\simeq 47$ days. The comparison of the thermal and non thermal flux and the MDP obtained in the three energy bands is shown in Figure 6.8.

6.3.4 CYGNUS X-1

Cygnus X-1 is one of the brightest X-ray sources in the sky and is the most extensively investigated object among all black hole candidates. It was first discovered in a 1964 June rocket flight (Bowyer et al., 1965). The companion mass is in a range between $\simeq$ 15 $M_\odot$ (Herrero et al., 1995) & $30M_\odot$ (Gies & Bolton, 1986). This mass together with the mass function give an estimate of compact object mass between $\simeq 6.5$ & $\simeq 20M_\odot$ The X-ray spectrum undergoes a transition between the low/hard and the high/soft one. Most of the time the source is in the hard state but it makes occasional transitions to the soft state which is dominated by a soft blackbody like component. During 1996 it made a complete transition form the low/hard to the high/soft state (Cui et al., 1996; Cui, 1996; Zhang et al., 1997). However the blackbody temperature was not very high and the flux increase from its low/hard was only moderate as compared to the high/soft state transitions of the other transient black hole candidates. Figure 6.9 shows

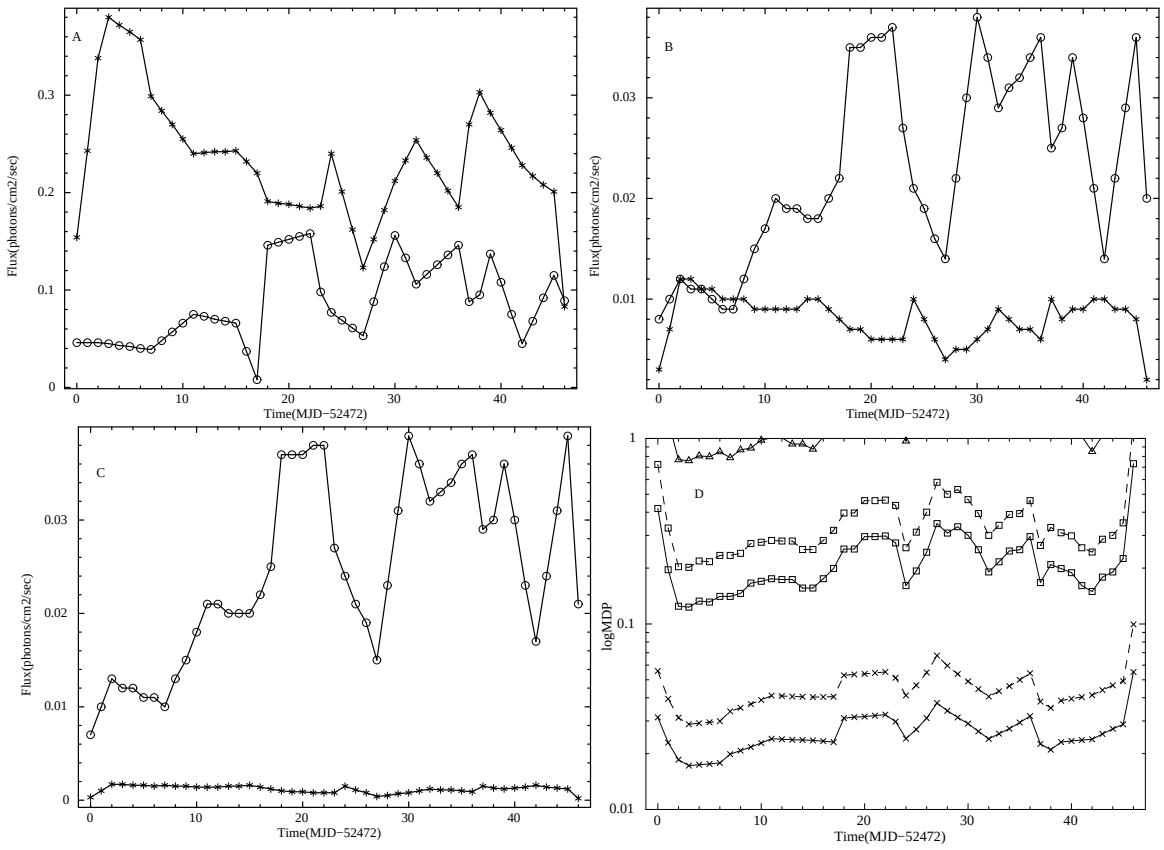

Figure 6.8: Same as Figure 6.5, for the source GX339-4 for the outburst in the year 2002

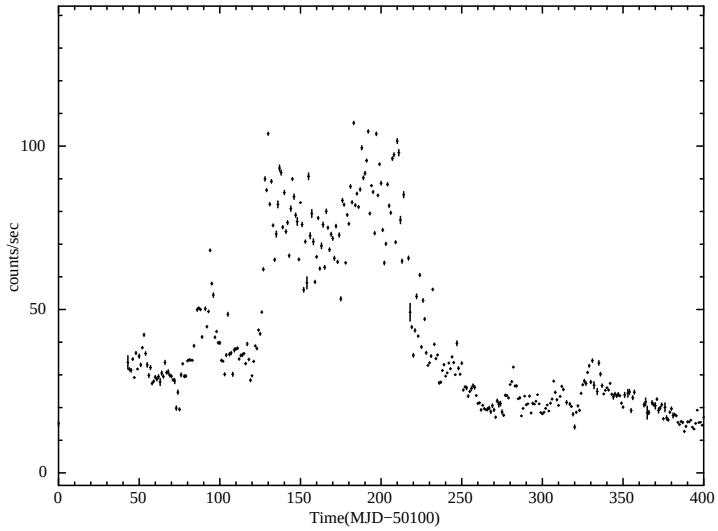

Figure 6.9: One day averaged long term ASM light curve of Cygnus X-1 showing the 1996 soft state transition of Cygnus X-1

the one day averaged ASM daily light curve of the source during it's soft state transition.

The data analysed to calculate the MDP ranged between MJD 50 225 − 50 242 & 50 250 − 50 252. The MDP_{net} integrated over all the days is higher than the upper limit on the polarization obtained by OSO-8 (Long et al., 1980) from Cygnus X-1 except in the 6 − 9 KeV with a Lithium scatterer. Therefore polarization of the thermal component of Cygnus X-1 most probably cannot be observed with the Thomson polarimeter. This is because the flux increase in the X-ray spectrum is only moderate and the power-law component of the spectrum is quite comparable to the blackbody component of the spectra on most days. Comparison of the thermal & non-thermal fluxes and the calculated MDP in the two energy bands are shown in Figure 6.10.

6.3.5 H 1743-322

H 1743-322 is a bright X-ray transient. It was first discovered with Ariel V all sky monitor in 1977 (Kaluzienski et al., 1977) and its precise position was provided by HEAO 1. Despite lack of dynamical confirmation of the mass of the compact object it is believed to be a black hole due to its spectral and temporal characteristics (Corbel et al., 2006; Kalemci et al., 2006). The source also shows relativistic jet emission. The source entered into one of its outbursts in 2003 during which it showed state transitions. The outburst was discovered by Revnivtsev et al. (2003) on March 21 using *INTEGRAL* and rediscovered a few days later by (Markwardt & Swank, 2003), and *RXTE* observations of the source was carried out during the outburst. Figure 6.11 shows the one day averaged ASM light curve of this source during its outburst.

The data was analysed from MJD 52 823 to 52 843 to calculate the MDP. Figure 6.12 shows the comparison of the two fluxes and the MDP in the three energy ranges.

6.3.6 XTE J1817-330

XTE J1817-330 was discovered as a new bright X-ray transient with the RXTE All-Sky Monitor (ASM) on 2006 January 26 (Remillard et al., 2006) with a flux of 0.93($\pm$0.03) Crab ($2-12$ KeV) and a very soft spectrum thus making it a strong black hole candidate (White & Marshall, 1984). Pointed observations with *RXTE* confirmed the soft spectrum and also hinted low absorption along the line of sight (Miller et al., 2006). Five days after the discovery of the source, its radio counterpart was identified (Rupen et al., 2006), followed by detection of counterparts at NIR, optical, and ultraviolet wavelengths (D'Avanzo et al., 2006; Torres et al., 2006a,b). The 2006 outburst lasted for approximately 160 days where the source reached a maximum of $\sim$ 1.9 Crab on 28 January 2006, following an exponential decline of the X-ray flux. Figure 6.13 shows the one day averaged ASM daily light curve of the source during its outburst.

To calculate The MDP the data was analysed between MJD 53 765 to 53 780 when *RXTE* pointed observations were available and the source was in blackbody dominated days. The MDP_{net} integrated over all the days was found to be similar to the other sources in $6-9$ KeV & $9-11$ KeV but much worse in the $11-15$ KeV energy band since the power-law flux was significantly higher and totally dominant over the blackbody flux

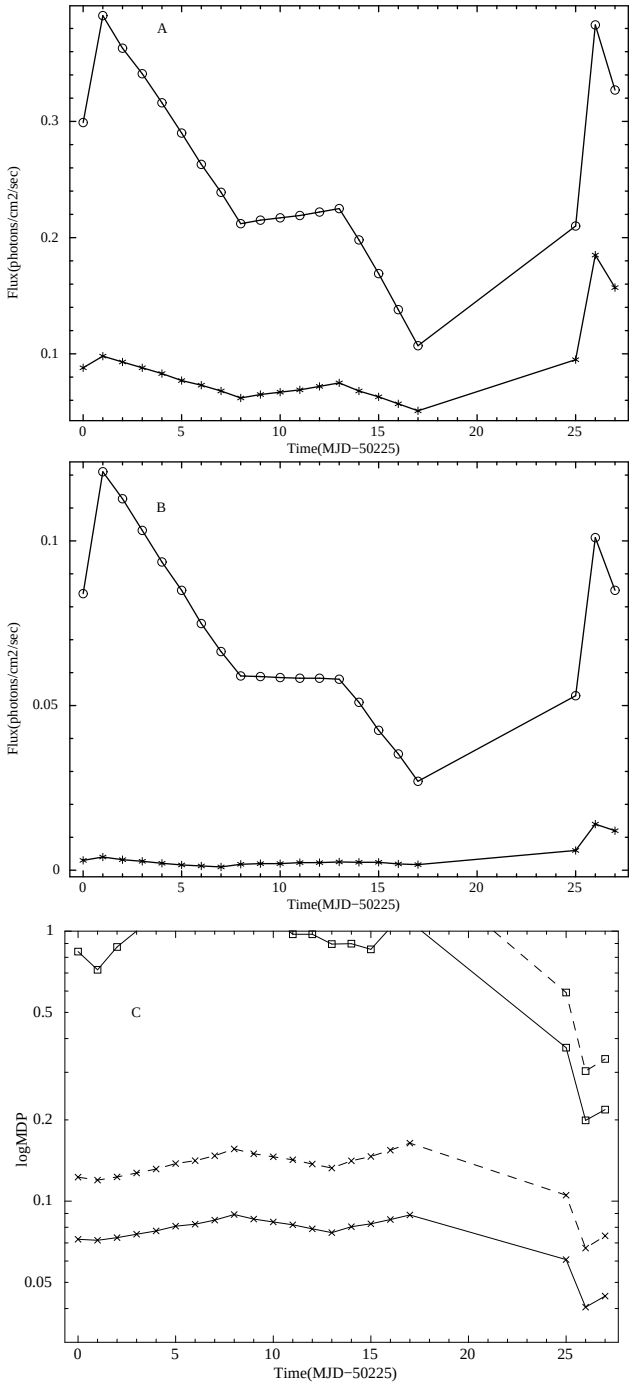

Figure 6.10: Figure A, B shows the blackbody and the powerlaw fluxes in the two energy bands for Cygnus X-1 during its soft state transition in $6-9$ KeV, & $9-11$ KeV respectively. Star indicates the blackbody flux and circle the powerlaw flux. Figure C shows the value of the MDP in the two energy bands for this source on each day. Cross indicates MDP in $6-9$ KeV square indicates MDP in $9-11$ KeV. The solid line indicates calculation done with Lithium as a scatterer and dashed line indicates Beryllium as a scatterer. The thermal emission from Cygnus X-1 is very weak in the $11-15$ KeV band and is not shown here.

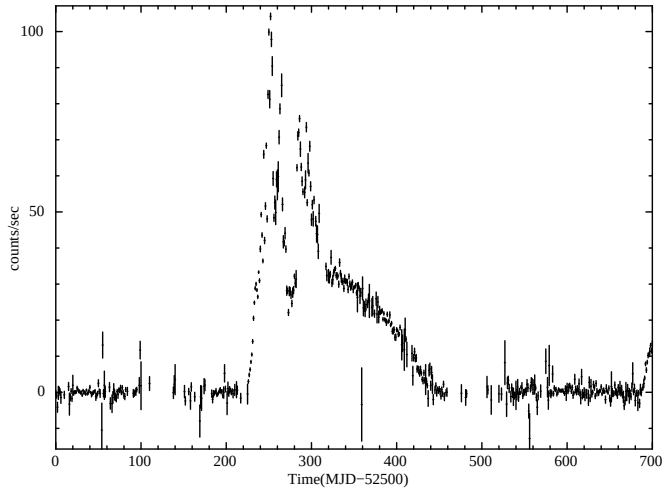

Figure 6.11: One day averaged long term ASM light curve of H 1743 − 322 showing the 2003 outburst of H 1743 − 322

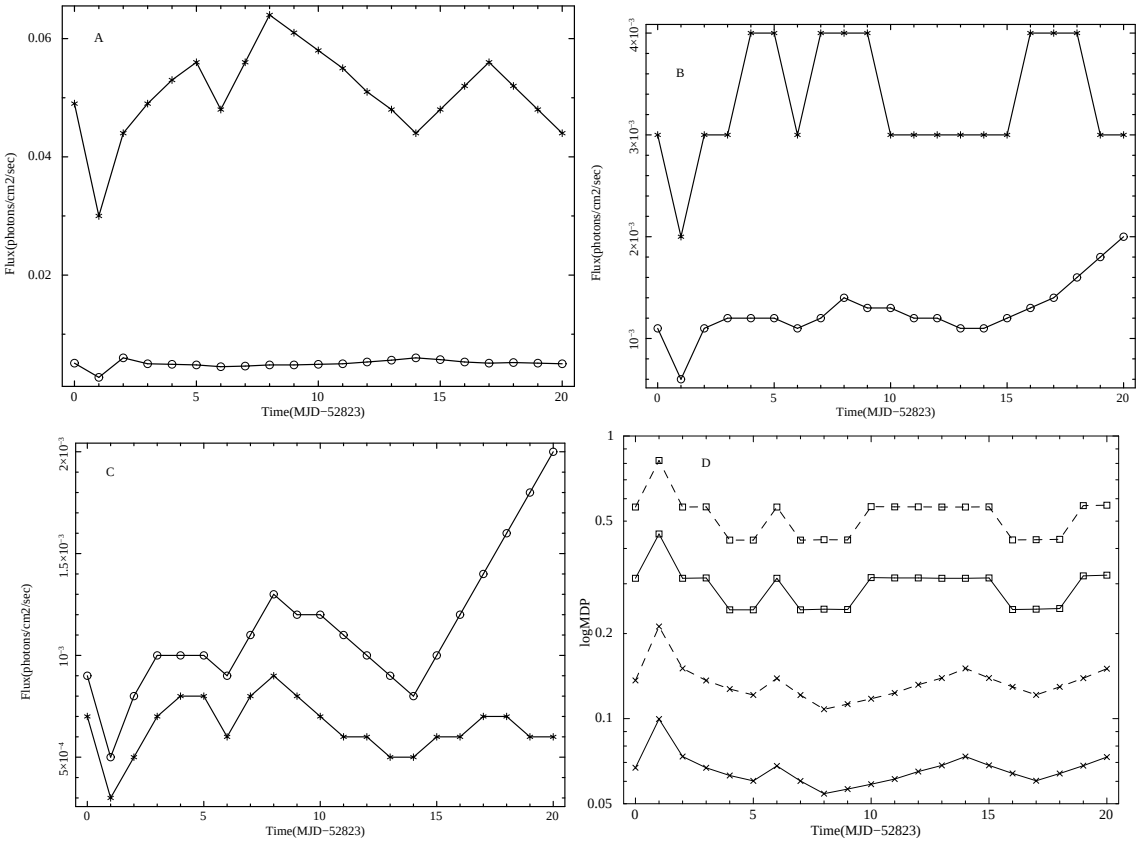

Figure 6.12: Same as Figure 6.5 for the source H1743-322 for the outburst in the year 2003

Table 6.3: Net Minimum detectable polarization calculated for all the sources during the specified **thermal emission dominated** stretches. The values are given in percentages

Source name	Net MDP 6-9 KeV		Net MDP 9-11 KeV		Net MDP 11-15 KeV		Net MDP 11-15 KeV	
MJD	5σ		5σ		5σ		3σ	
range	Li	Be	Li	Be	Li	Be	Li	Be
GRO J1655-40(53442 - 53449)	0.97	1.69	2.96	4.71	8.37	11.63	5.37	7.47
GRO J1655-40(53511 - 53525)	0.52	0.88	1.77	2.69	4.43	5.94	2.85	3.81
GX339-4(52472 - 52518)	0.36	0.62	2.92	4.67	18.10	25.10	11.62	16.11
Cyg X-1(50225 - 50242, 50250 - 50252)	1.57	2.70	15.16	23.84	-	-	-	-
H1743-322(52823 - 52843)	1.42	2.89	6.25	11.10	35.94	53.63	23.08	34.43
XTE J1817-330(53765 - 53780)	1.21	2.26	08.28	14.14	55.76	-	35.79	51.64

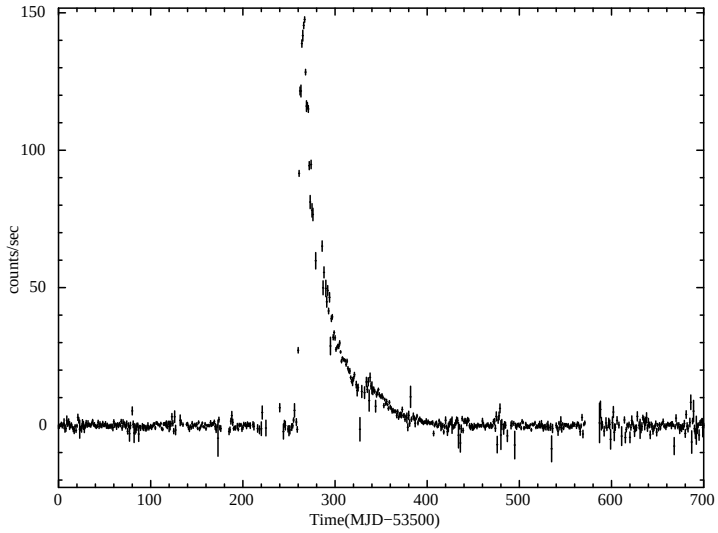

Figure 6.13: One day averaged long term ASM light curve of XTE J1817 − 330 showing the 2006 outburst of XTE J1817 − 330

over this energy band. Figure 6.14 shows the comparison of the two fluxes and the MDP in the specified energy ranges on each day during this time.

Calculated values of MDP_{net} for all the sources during the respective stretches are given in Table 6.3 as follows -

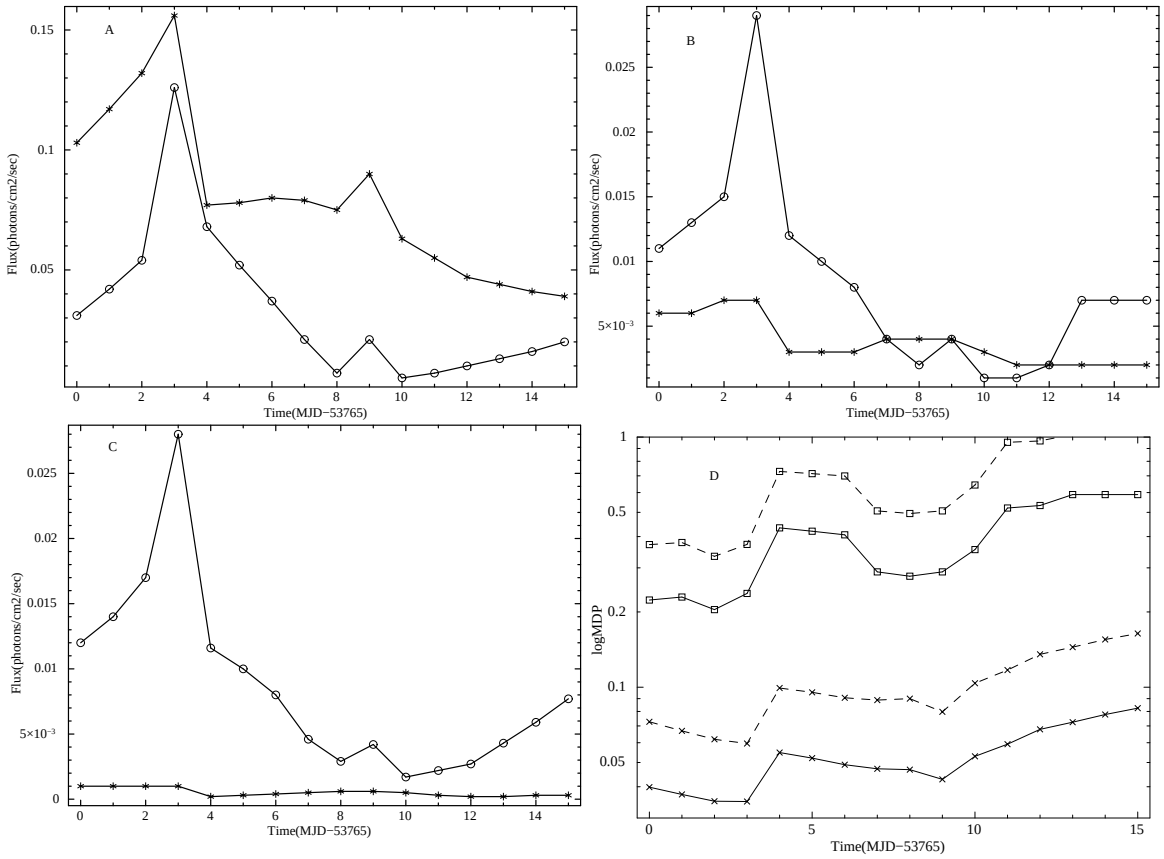

Figure 6.14: Same as Figure 6.5 for the source XTE J1817-330 for the outburst in the year 2006

6.3.7 Discussion & Conclusions

We have shown that provided some of the sources go into similar outburst/state transition during the lifetime of the mission, detection of polarization in the disk emission would be possible with the Thomson polarimeter. This can be done by performing spectro polarimetric observations in different energy bands to map the energy dependent polarization for these sources in their disk emission dominated state.
X-ray emission from the disk in accreting black holes are polarized due to electron scattering from the plane parallel atmosphere of the disk with the polarization vector lying in the plane of the disk. However, relativistic effects like beaming and gravitational lensing gives a non-trivial rotation to the integrated net polarization vector resulting in energy dependent rotation in the plane of polarization. Recent Monte Carlo Ray Tracing simulations (Schnittman & Krolik, 2009) predict a decrease in the degree of polarization along with its rotation in the inner parts of the accretion disk for direct radiation, and a net rotation of ninety degrees in the plane of polarization in the same region considering returning radiation. They have also simulated the results that would be expected with the polarization measurement taken by the *GEMS* mission polarimeter which is a photoelectron polarimeter working in the $2-10$ KeV range. Here we produce the results that we would expect to get with the Thomson polarimeter. The results could also be complimented with the *GEMS, XIPE* enabling extensive wideband spectro polarimetric studies. The main conclusions of this paper are:

1. The net MDP obtained for these sources in the three energy bands of $6-9$ KeV, $9-11$ Kev & $11-15$ KeV are in most cases less than the degree of polarization expected from accreting black holes in their thermal state from the simulations of (Schnittman & Krolik, 2009), the degree and the net rotation in the integrated polarization vector being a strong function of the black hole spin. A comparison of the net MDP presented in Table 6.3 for three different energy bands with the predicted degree of polarization (Schnittman & Krolik (2009), Figures 7 & 8) shows that for sources with favourable inclination angle (i>75 degrees) spectro-polarimetric measurements will be possible with the proposed Thomson X-ray polarimeter and these measurements will also be useful to constrain the spin parameter of the black hole. In some cases however, where the spectrum is almost entirely powerlaw dominated in the $11-15$ KeV band, the MDP obtained is above the the degree of polarization expected to be detected from such sources in case of a 5σ statistical detection. A

lower significance detection however, may be possible in such cases as a 3σ detection gives a lower achievable value of MDP. Hence spectro polarimetric observation of such sources for a few weeks during their thermally dominated spectral state would possibly enable us to map the transition radius from horizontal to vertical polarization. This could provide us with some estimates on the parameters of the black holes like their spin and/or the emissivity profile.

2. Observation of polarization in the $6-9$ KeV energy range necessitates the use of lithium as the scattering element which would set the dynamic range of the experiment to $5-30$ KeV. Use of beryllium however limits the lower energy energy threshold to 8 keV thus making observation in the $6-9$ keV band having the lowest MDP impossible. This study thus strongly supports the use of lithium as the scattering element for the Thomson polarimeter.

6.4 Expected polarization from the coronal emission in Accreting black holes

Polarization of this form is expected to be obtained in the "very high" state of accreting black holes.The most widely accepted physical interpretation of this state of black hole binaries is that of a relatively cooler thermal accretion disk surrounded by a geometrically thick "corona" of hot electrons (temperature $>$ 50 keV) (Done & Kubota, 2006). Schnittman & Krolik (2010) calculated the expected polarization in this scenario by considering different geometries for the corona and a used Monte Carlo ray-tracing code to calculate the expected polarization signature for each case. As in the case of polarization from thermal disks, the same qualitative behaviour is found, with the polarization flipping from horizontal at low energies to vertical at high energies. The polarization is be mainly due to the scattering of the photons in the hot corona, and the amount of scattering and the final energy reached is highly dependent on the scattering geometry (corona in this case). More scattering requires a more constrained geometry, which in turn naturally leads to higher polarization. Therefore, although all these different coronal geometries would roughly produce the same broadband spectra, their polarization properties would be different. The polarization from accreting black holes in their corona dominated states can provide crucial information on the physical properties of the corona, and also distinguish between different coronal geometries like the "planar

sandwich geometry", "spherical geometry" or the "clumpy corona" geometry (See Figure 6.15 for a schematic).
Another source of polarization in this hard state of the black hole binaries are the jets produced, which generates highly polarized flux in other wavelengths by the synchrotron radiation of hot electrons in a coherent magnetic field. These hot electrons can produce synchrotron self-Compton radiation in the X-ray band, also strongly polarized . This is the concept behind the "Lamp post model" (Dovčiak et al. (2012) and references therein). Dovčiak et al. (2012) studied the polarization properties of this radiation found it highly sensitive to the black hole spin, observer inclination, and the position of the primary, thus enabling in constraining these parameters.

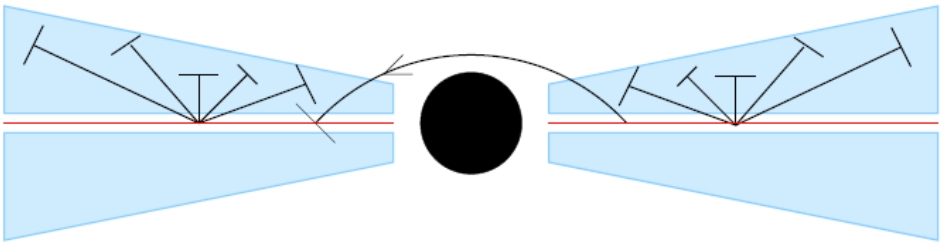

Figure 6.15: Schematic diagram of the disk and corona for the sandwich geometry. The thermal seed photons emitted from the disk are scattered by the hot electrons in the corona. Figure taken from Schnittman & Krolik (2010).

6.4.1 Analysis and Results

We have calculated the expected MDP from five galactic black hole candidates during their intermediate or VHS (very high) spectral states in the four energy bands of $6-9$, $9-11$, $11-15$ and $15-30$ keV. The VHS and intermediate spectral states are associated with the presence of an optically thick accretion disk surrounded by a powerful corona which scatters the disk photons polarising them in the process. These states are almost always associated with the transition between hard to soft spectral states or may rarely be associated with failed state transitions. Most black hole binaries during their outbursts are said to reside in these spectral states for a few days before transiting to the ultrasoft spectral state. The source is said to be in its "Very high" spectral state when the

bolometric luminosity reaches the highest during this period, and in its intermediate state when the bolometric luminosity is a few orders less than in the ultrasoft state. As an example, the transitions to the soft state in GX 3394 during the last outbursts occurred at levels somewhat below the respective global maxima, whereas during the last outbursts in XTE J1550-564 the transition to the soft state occurred at the high luminosity level (Zdziarski & Gierliński, 2004). This is the ideal spectral state to detect the polarization from the reflected hard component as discussed in the previous section. For the calculation of the MDP, the equations are parameters used are the same as in section 6.3.1. The source counts S are obtained from spectral fitting of the *RXTE* observations of Cygnus X-1, XTE J1550-564, GRS 1915+105 and GRO J1655-40 during their transition to the VHS or intermediate states. The source counts in GX 339-4 are obtained from spectral fitting of a *Suzaku* observation of the source during its VHS state. The spectral data were fitted using *XSPEC* to a model consisting of a combination of multicolor blackbody (Mitsuda et al., 1984; Makishima et al., 1986) a power-law component, and often a reflection component (model pexriv in *XSPEC*.). The values obtained in the four energy bands of interest for both the materials of the scatterer are tabulated in Table 6.4. Table 6.5 lists the MDP obtained for the different sources in the different energy bands for both the Li and Be scatterer.

6.5 results

Table 6.4: Energy dependent efficiency for Li & Be scatterer

Energy range(Kev)	Efficiency(Li)	Efficiency(Be)
6-9	9.4 per cent	4.0 per cent
9-11	16.1 per cent	8.5 per cent
11-15	21.7 per cent	14.4 per cent
15-30	27.3 per cent	24.6 per cent

6.5.1 Discussion & Conclusions

1. The results show that provided a source goes into outburst during the lifetime of the mission and we can observe it during its VHS or intermediate spectral state,

Table 6.5: Net Minimum detectable polarization calculated for 5 σ detection of the sources in a single day (integration time T = 43 200 secs). The values are given in percentages.

Source name	MDP 6-9 KeV		MDP 9-11 KeV		MDP 11-15 KeV		MDP 15-30 KeV	
–	Li	Be	Li	Be	Li	Be	Li	Be
Cyg X-1	1.8	2.8	2.2	3.6	1.7	2.2	1.4	1.5
XTE 1550-564	1.1	1.8	1.7	2.4	1.5	1.9	1.8	1.9
GRS 1915+105	1.2	2.0	2.1	3.1	2.1	2.7	3.6	3.9
GRO J1655-40	1.6	2.7	2.3	3.4	2.0	2.6	2.2	2.3
GX 339-4	2.5	4.5	3.6	5.6	2.9	3.9	3.2	3.5

we will be able to achieve an MDP of 2–5 % in all the energy bands for both Li and Be scatterers. The MDP obtained for most of the sources in the four energy bands of $6-9$ KeV, $9-11$ Kev, $11-15$ KeV and $15-30$ KeV is in most cases less than the degree of polarization expected from accreting black holes in their reflection dominated spectral states from the simulations of (Schnittman & Krolik, 2010).

2. Lowest MDP are achieved for GRS 1915+105 and XTE J1550-564 which had the highest count rates among the sources, and were also in their VHS spectral states.

3. The results improve with the use of a Li scatterer in the lower energy ranges upto 15 keV. In the harder energy range of 15–30 keV, the results are comparable as the scattering efficiencies are also comparable for both the scatterers. This indicates that the use of Li scatterer is crucial to improve the results in the lower energy ranges.

6.6 Expected polarization from Accretion powered pulsars

In contrary to the black hole sources where reflection and scattering are the primary sources of polarization, the magnetic field, its strength and geometry shapes the polarization in accretion powered pulsars where their source of emission is also strongly guided by the magnetic fields. This is mainly due to the fact that the photons acquire different opacities parallel and perpendicular to the direction of the magnetic field vector

making the photons acquire a preferential directionality. This issue is also discussed in the context of the formation of CRSF in Chapter 5. Further, since the propagation also depends on the photon energy, specially on the cyclotron resonance scattering feature of the particular sources, this makes the polarization from accretion powered pulsars a high energy dependent process as well. Calculation of polarization expected from accretion powered pulsars have been carried out by Meszaros et al. (1988). Meszaros & Nagel (1985a,b) in their series of papers calculated in detail the angle dependent cyclotron line formation and Comptonization and characteristics of the pulse profiles and spectra in accretion powered pulsars through numerical calculations of radiative transfer through strongly magnetized plasma. The authors assumed both pencil and fan beam geometry of the emitted radiation for the calculations. In Meszaros et al. (1988), these calculations are further extended to calculate the polarization properties of accretion powered pulsars for different beaming geometries (pencil and fan) from the slab and column geometry respectively. The calculations further assume a particular value of magnetic field strength, electron temperature (kT) and optical depth (τ) for the system. The polarization degree in these sources are very high and can reach typically to 80 % unlike the much weaker polarizations obtained by scattering of radiation in black hole sources. This makes them ideal sources to detect polarization. Furthermore, the crucial results of this work are that the phase measurements of the linear polarization can distinguish between and a pencil and fan beam geometry of radiation and can further provide hints of the system geometry. Phase resolved polarization measurements in different energy bands would be crucial in providing important clues in these regards. Effects of depolarization like gravitational light bending near the neutron star surface can lead to a depolarization of about ~ 10 %. The most important issues regarding polarization from accretion powered pulsars are discussed below.

1. The key signature to distinguish a pencil and fan geometry is the phase correlation between the pulse profile and the corresponding degree of polarization as a function of pulse phase. For a pencil beam pattern the maximum polarization should be in phase with the peak of the pulse profile below the corresponding CRSF energy of the source, and out of phase above the CRSF energy. The situation is exactly opposite for a fan beam pattern of emission.

2. The sweep in the angle of polarization with the pulse phase also provides similar clues in this regard. For pencil beam pattern of emission, the angle should change

from positive to negative near the pulse maximum and from negative to positive near the pulse minimum. The situation is expected to be exactly opposite for a fan beam pattern of emission.

3. Maximum degree of polarization should be observed near the CRSF energy of the particular source, and the polarization profile should be sharper around this energy.

4. Sharper polarization variations should be observed with the pulse phase for viewing angles looking preferably at one of the poles directly or at both the poles.

   Apart from these, the sweep in the polarization angle can also act as a tracer of the magnetic field geometry, and any rapid changes may be an indication of a non dipolar magnetic field.

6.6.1 Analysis & Results

As is mentioned in the previous section, a phase resolved polarization measurement preferably in different energy bands would provide the crucial clues to the beaming and geometry of accretion powered pulsars. As seen in figure 6.16, the polarization degree depends on the energy and is maximum near the CRSF energy (38.4 keV for this simulation). Since the only detailed work on the expected polarization from accretion powered pulsars so far is by Meszaros et al. (1988), we have done the calculations for a source with physical parameters similar to that assumed in their paper for a viewing angle i1,i2=45,75 degrees as shown in Figure 6.16. For this, we have have assumed the results are applicable to GX 301-2 which is an accretion powered pulsars with a CRSF at $\sim$ 38 keV (similar to that assumed in Meszaros et al. (1988)). For other sources, we have assumed a GX 301-2 like spectra with only the count rates scaled accordingly (count rates taken at the peak of their outbursts in transient sources and scaled by the count rate in GX 301-2).

We have calculated the minimum exposure time required to observe the polarization obtained from a source in eight phase bins assuming we need a 5σ detection significance between the maximum and minimum degree of polarization observed at that particular energy band for the above mentioned combination of viewing angles. We have done the calculations for 9 and 18 keV, since they fall within the band of the Thomson polarimeter and for both fan and pencil kind of beaming pattern. The maximum and the minimum observable degrees of polarization for 9 and 18 keV and for fan and pencil beam are

extracted from Figure 6.16. The calculation are done as follows:
Let $a1$,$\delta a1$ and $a2$,$\delta a2$ be the maximum and minimum detectable polarizations and its errors in measurement in a particular energy band and beam pattern. Thus $\frac{a1}{\delta a1}$ and $\frac{a2}{\delta a2}$ are the detection significance of the individual measurements Using Equation 6.7, we can write

$$\mathrm{a1} = \frac{\frac{a1}{\delta a1}}{\mu_{100} S_{net}} \sqrt{\frac{(\mathrm{S_{net}} + \mathrm{B_{net}})}{\mathrm{T}}} \tag{6.11}$$

and

$$\mathrm{a2} = \frac{\frac{a2}{\delta a2}}{\mu_{100} S_{net}} \sqrt{\frac{(\mathrm{S_{net}} + \mathrm{B_{net}})}{\mathrm{T}}} \tag{6.12}$$

Further,

$$\frac{a2 - a1}{\sqrt{\delta a1^2 + \delta a1^2}} = 5 \tag{6.13}$$

Using these equations, T is calculated assuming the following values of the other parameters.
$a1$,$\delta a1$ and $a2$,$\delta a2$ are extracted from Figure 6.16 for the two energy bands and fan and pencil beam pattern. $\mu_{100} = 0.4$ as assumed in the previous calculations.
The source counts S is obtained from spectral fitting of the *Suzaku* observations of the respective sources, the details of which are given in Chapter 3. The source and background counts and the energy dependent efficiency ϵ is calculated as in section 6.3.1. The values of ϵ obtained in the two energy bands of interest for both the materials of the scatterer are tabulated in Table 6.6.
Since the calculations are done for the time required for a 5σ detection of the maximum

Table 6.6: Energy dependent efficiency for Li & Be scatterer

Energy range(Kev)	Efficiency(Li)	Efficiency(Be)
6-12	12 per cent	6.6 per cent
12-24	25.77 per cent	21.38 per cent

difference in the polarization signal in two adjacent phase bins, one could multiply this obtained time with the number of phase bins required for measurement to get the total exposure time required. Tables 6.7 and 6.8 gives the values of the time required for observation in each phase bin.

Table 6.7: Exposure times per phase bin required at 9 keV. Time in secs

Source name	Pencil Beam		Fan Beam	
–	Li	Be	Li	Be
GX 301-2	259.9	590.1	733.1	1664.4
1A 1118-61	596.8	1479.8	1683.4	4173.9
Vela X-1	831.3	2130.6	2344.8	6009.5
A 0535+26	725.4	1834.5	2046.1	5174.3
XTE J1946+274	1073.6	2818.4	3028.1	7949.5
4U 1907+09	14184.6	43580.2	40008.2	122919.7

Table 6.8: Exposure times required at 18 keV. Time in secs

Source name	Pencil Beam		Fan Beam	
–	Li	Be	Li	Be
GX 301-2	831.0	1030.7	399.7	496.0
1A 1118-61	2548.3	3256.9	1225.7	1567.2
Vela X-1	1864.6	2360.8	896.9	1135.9
A 0535+26	2799.529	3588.4	1346.5	1726.8
XTE J1946+274	7639.1	10113.5	3674.3	4866.9
4U 1907+09	134099.4	189406.9	64500.7	91158.7

6.6.2 Discussion & Conclusions

1. All the sources except 4U 1907+09 can be observed over eight phase bins in $2-3$ days for both fan and pencil beam emissions.

2. The lower energy photons (9 keV) give better diagnostic of a pencil beam emission, while a fan beam is better probed with the hard X-ray photons (18 keV). This can be explained by the dependence of the scattering cross section and hence the opacity with the photon energy. The lower energy photons have lower opacities in the direction along the magnetic field vector (i.e. the direction along which pencil beam escapes) giving the radiation a preferred directionality and hence polarization..

3. Nevertheless the observation time for 4U 1907+09 is also likely to be much lesser than shown in Table 6.7 and 6.8, as the results are compared with calculations for a source with the CRSF energy same as in GX 301-2. The CRSF of 4U 1907+09 being $\sim$ 18 keV, the degree of polarization expected is much higher specially at 18 keV.

4. This study also strongly supports the use of lithium as the scattering element for the Thomson polarimeter as in the case of accreting black holes.

6.7 Determination of the error in the angle of polarization measurement

Since polarization from accreting black holes and accretion powered pulsars are expected to have a rotation in the net angle of polarization, determination of the error or uncertainty in the angle of polarization measurement is also necessary to specify how well one would be able to constrain the angle of polarization measurement for a specified nσ statistical detection.

To determine the error in the angle of polarization measurement we generated a modulated signal riding on a background superimposed with random errors as would be expected to obtain from the actual measurement of a polarized signal with the Thomson polarimeter. Adjusting the amplitude and background to fix the signal at specified nσ levels of detection we determined the broadening in the phase (angle of polarization) measurement i.e. the 1σ uncertainty in the polarization angle measurement at each nσ level. Similar results have been found by M. Weisskopf et al. (2010). Figure 6.17 shows the 1σ deviation in phase versus the number of sigma (σ) detection. As is seen from the figure, a 4σ statistical detection leads to an error of $\sim 20\%$ in the angle measurement which is enough to detect sweeps in the position angle specially the $0 - 90^{\circ}$ sweep as a function of pulse phase for accretion powered pulsars . This would be decisive in determining the beam pattern (fan or pencil). Similarly for the case of accreting black holes, the sweep in the angle of polarization would be detected, providing valuable inputs on the parameters of the black hole.

In the case of accretion powered pulsars , the calculation of the time required to achieve this detection was found to be less than that needed to achieve the corresponding MDP for all the sources. This hints that the decision of the exposure time required in the case of these sources would be guided by the requirement of the MDP.

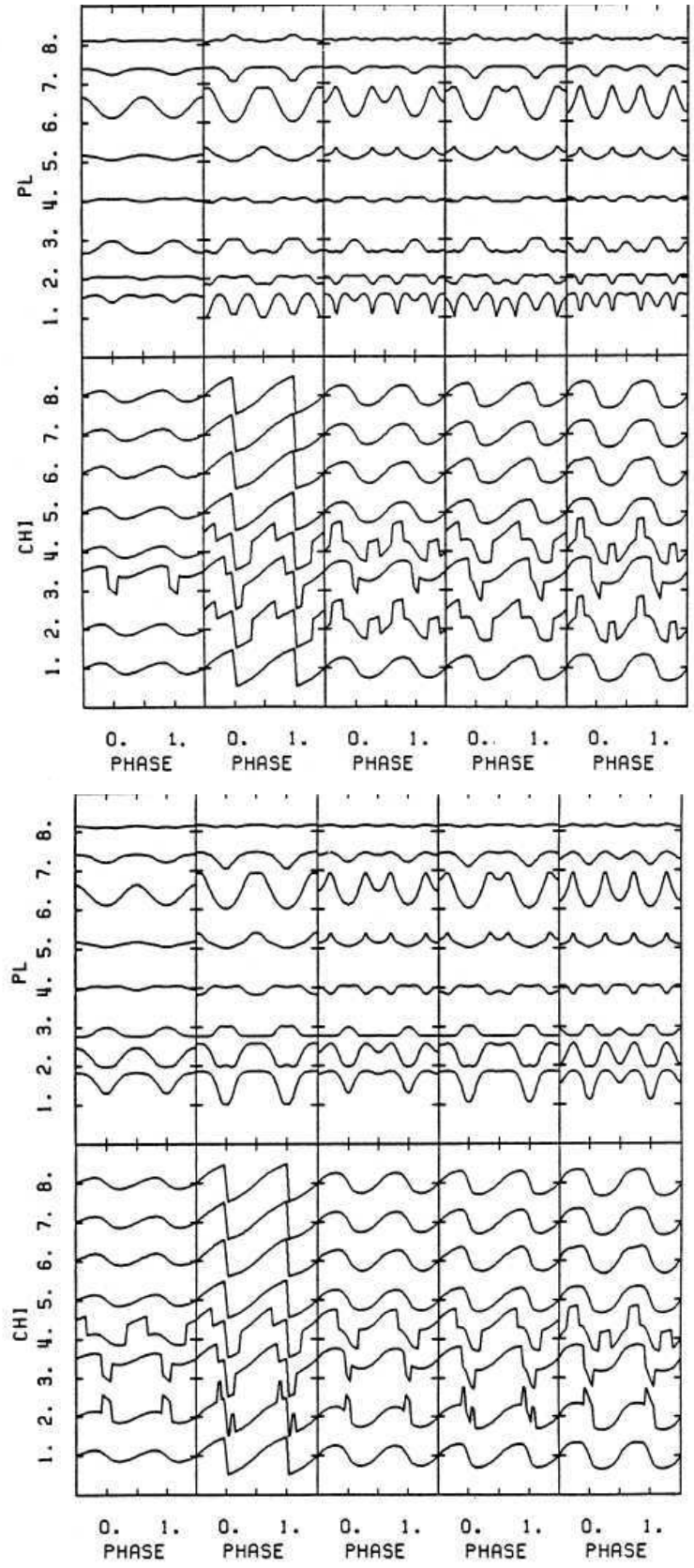

Figure 6.16: Degree and angle of polarization with pulse phase for Pencil beam and Fan beam (left and right) at different energies(1.6, 3.8, 9, 18.4, 29.1, 38.4, 51.7 and 84.7 keV from bottom to top), and for a particular combination of orientation angle of the neutron star (i1,i2=45,75). The cyclotron line energy of the neutron star is taken to be at 38 keV. Meszaros et al. (1988)

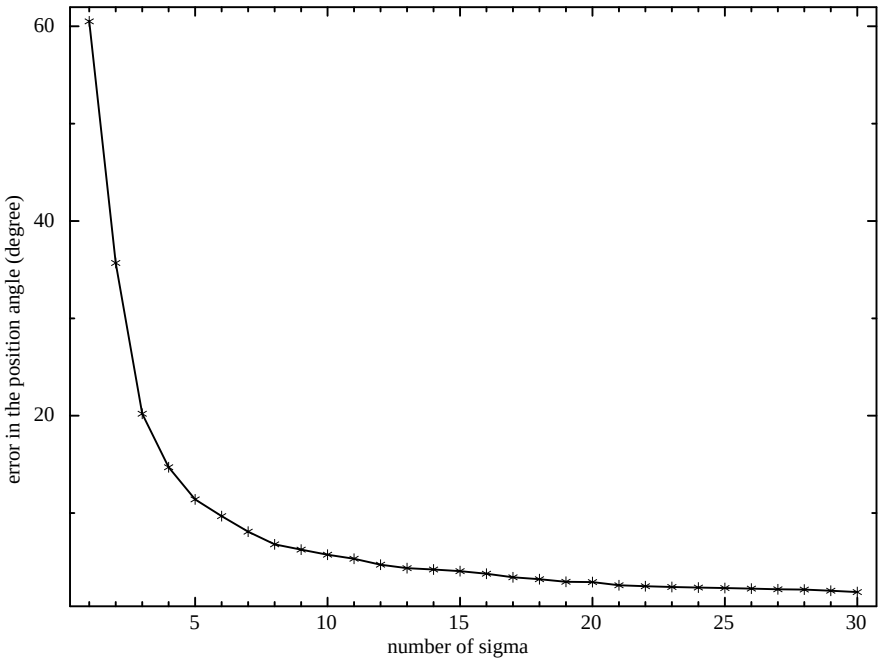

Figure 6.17: The 1σ deviation in position angle versus the number of sigma statistical detection

Chapter 7

Summary and Future work

In this thesis several aspects of accretion onto compact objects specially accretion powered pulsars are studied in detail. Chapters 2, 3, 4 and 5 are dedicated to the study of the accretion geometry and magnetic fields of accretion powered pulsars through their pulse profiles, energy spectrum and specially the CRSF features found in the energy spectra. In Chapter 6, the expected detectability of polarization of Galactic black hole and neutron star binaries are calculated for a Thomson X-ray polarimeter under consideration as a small satellite payload by ISRO. The results obtained are summarized below as follows.

- In the first section of Chapter 2 the results of the evolution of the pulse profiles are studied in two categories which are the pulse profiles having complex low energy dips and the energy dependent pulse profiles which show variation in the relative strength of the different components with energy. Low energy dips are seen in 1A 1118-61, Vela X-1, A 0535+26, XTE J1946+274 and 4U 1626-67. Dips extending upto high energies ($\sim$ 70 keV) are detected in EXO 2030+375. The study of the pulse profiles of GX 1+4 further throws light upon the nature of the energy dependence of the pulse profiles and indicates the presence of soft emission components. Soft excess emission is also detected in the lowest energy pulse profiles in 1A 1118-61, 4U 1626-67 and EXO 2030+375. In addition, studying the pulse profiles of GX 301-2, GX 1+4 and 4U 1907+09 further gives us the crucial clues that the beaming patterns could be highly energy dependent in these sources.

- In Chapter 3, the results of the broadband spectroscopy of accretion powered pulsars like 1A 1118-61, Vela X-1, A 0535+26, XTE J1946+274, 4U 1907+09, GX 301-2, 4U 1626-67, Cen X-3, Her X-1 and EXO 2030+375 are presented. For each source, the parameter values obtained with different continuum and line models are presented and compared. The models which give us physical as well as consistant results are chosen as the best suited continuum models for the particular source. In the process of trying to fit the energy spectrum with different continuum models we have also noticed certain trends in continuum model fitting as is discussed in detail in this chapter. The results obtained gives us a great opportunity to study pulse phase resolved variations of the spectra for slow pulsars, particularly, with respect to its CRSF features, which are highly sensitive to continuum modeling and requires careful modeling of the broadband spectrum for reliable results. It also allows us to study the pulse phase resolved variations of the narrow dip like features in the pulse profiles in these sources as described in Chapter 2, which is accounted by an additional partial absorbing component in their spectrum.

- In Chapter 4, pulse phase resolved spectroscopy of the continuum parameters are presented for the sources described in Chapter 2, which exhibits narrow dips in the pulse profiles. The dips are accounted by a partial covering absorber along our line of sight at those phases. All the sources except EXO 2030+375 exhibit these dip like features upto $\sim$ 12 keV, as the lower energy photons are more susceptible to reprocessing by absorption and scattering in the local medium of the neutron star. In EXO 2030+375 on the other hand the dips are clearly distinguishable upto 70 keV, which could perhaps arise from a hotter, partially ionized matter. The amount and the covering fraction of the partial covering absorber is consistent with the strength of these dips and the energies upto which they are present. For all the sources, the spectrum hardens near the peak of the hard X-ray (PIN: 10-70 keV) pulse profile, indicating a deeper view to the inner parts of the accretion column at that phase which could be true for a pencil type of beaming pattern. This pencil beam type interpretation of the beaming pattern is also consistent with that indicated from the phase resolved variations of the CRSF parameters in A 0535+26 and XTE J1946+274 as discussed in Chapter 5.

- In Chapter 5, pulse phase resolved spectroscopy of the CRSF parameters are presented for the sources discussed in Chapter 3 which are slow pulsars. The results

are presented for the first time in XTE J1946+274, and for the other sources, they are the most detailed results available till date. The robustness of the results are seen from the similar pattern of variation of the CRSF parameters obtained for all the sources with more than one continuum model. The pattern of variation of the parameters show complex dependence with phase and often vary by large factors. The variations in the CRSF parameters with phase are typically 10–30 % or more. Such high percentage of variation cannot be definitely explained by the change in viewing angle alone, and if explained by the changing projections at different viewing angles of different parts of the accretion column, requires a large gradient in the physical parameters across the emission region. Similarly, a change in the CRSF centroid energy due to the change in the height of the emission region (and hence the magnetic field strength) at different viewing angles requires an accretion column of height several Kms. Alternate explanations include a wide polar cap, a more complex configuration of the magnetic field or superposition of several CRSFs. The accretion geometry may also be complex in nature, and viewing the geometry at different viewing angles may give rise to a high percentage of variation of the CRSF parameters. Further, the results are smeared by the effect of gravitational light bending. Although we have not performed any detailed modeling of the results and leave it for a future work, we however provide a few explanations of the variations of the CRSF parameters from very simple arguments as given below.
(1) The CRSF parameters in 1A 1118-61 vary by a large amount which either implies a complicated magnetic field geometry or a more complex accretion geometry.
(2) Evidence of the variations in the ratio of the two line energies with the pulse phase is found for the first time in Vela X-1 which indicates the fundamental and harmonic line forming regions are changing with pulse phase. Moreover, the pattern of variation of the CRSF parameters indicate a fan beam pattern of emission.
(3) In A 0535+26, The energy of the CRSF does not vary by a large fraction, although the depth varies by almost a factor of four. The the pattern of variation of the CRSF parameters indicate a pencil beam pattern of emission as also hinted by the results of Chapter 4.
(4) The CRSF parameters vary by a large fraction in XTE J1946+274. The results indicate a pencil beam type of emission as also hinted by the results of Chapter 4 .
(5) The CRSF parameters vary by a large amount in 4U 1907+09. The results indicate a fan beam geometry of emission.

(6) In the case of GX 301-2, the sharp pattern of variations are indicative of the existence of sharp gradients in the physical parameters of the emission region or a non dipolar magnetic field.
In the last section of Chapter 5 the pulse profiles in these sources near their corresponding CRSF energies are studied. GX 301-2, 1A 1118-61 and Her X-1, XTE J1946+274 and A0535+26 shows enhanced beaming and change in the shape of the pulse profiles near the CRSF energies. GX 304-1 shows a phase shift in the pulse profile near the CRSF energy. 4U 1626-67, 4U 1907+09 and Vela X-1 are quite featureless near their CRSF energies.

- X-ray polarization is a fairly unexplored domain in astrophysics and is a crucial tool to solve many degeneracies regarding the accretion geometry or magnetic fields in compact objects, or the spin of the black hole which cannot be broken by timing or spectroscopic studies alone. A Thomson scattering X-ray polarimeter has been developed and a small satellite mission with a similar payload is under consideration by ISRO. In the first part of Chapter 6, the Minimum Detectable Polarization (MDP) that we would get with the X-ray polarimeter experiment is calculated for the thermal emission from the accretion disk for some of the Galactic black hole sources during their thermal dominated spectral states in different energy bands and for Li and Be scattering elements. From the study it is concluded that provided some of the sources go into similar outburst/state transition during the lifetime of the mission, detection of polarization in the disc emission would be possible with the Thomson polarimeter. This can be done by performing spectro polarimetric observations in different energy bands to map the energy dependent polarization for these sources in their disc emission dominated state.
  In the second part of the chapter, a similar study is carried out for some Galactic black hole sources during their reflection dominated spectral states. With a modest MDP of 2–5 % achievable in all the energy bands and with both the scattering elements, it is concluded that provided some of the sources are detected in their reflection dominated spectral state during an outburst, detection of energy dependent polarization would be possible with the Thomson polarimeter.

  In the third part of the chapter, the minimum exposure time required to observe the polarization obtained from accretion powered pulsars are calculated in eight phase bins assuming we need a 5σ detection significance between the maximum

and minimum degree of polarization observed at that particular energy band. It is concluded that All the sources except 4U 1907+09 can be observed over eight phase bins in $2-3$ days for both fan and pencil beam emissions. The above studies also bring out the advantage of using a lithium scatterer over a beryllium scatterer. Apart from these, the error in measurement of the angle of polarization for particular detection significance limits is also calculated.

Future work

Future work would involve more extensive studies of accretion flow and magnetic field geometry through the pulse profiles and spectra of accretion powered pulsars . Some of the projects that would naturally lead from the work done in this thesis are listed below.

- Studying the structure of the magnetic field and radiation emission geometry of neutron stars in binary systems in more detail with the NASA X-ray mission NuSTAR, and the upcoming missions ASTROSAT and ASTRO-H. The three next generation X-ray satellite missions NuSTAR (launched in June last year), ASTROSAT and ASTRO-H (both scheduled to be launched early next year) will provide an unprecedented opportunity for this study. NuSTAR and ASTRO-H are the first hard X-ray (> 10 keV) focusing satellites providing orders of magnitude improvement in the sensitivity in the hard X-ray range. ASTRO-H also has a broad band capability with extremely high energy resolution. ASTROSAT is the first X-ray satellite of its kind having broad band energy capabilities, high time resolution, increased sensitivity specially in the hard X-ray (high energy) range and a larger effective area than other satellites of its kind. Various strategies can be planned in this regard as follows:
  (1) The next generation satellites with their extremely high energy resolution are expected to resolve the CRSF shapes for the first time. These would provide important clues to the presence of magnetic field distortions, since the signatures of magnetic field distortions would be imprinted on it. The field distortions are further expected to change with the accretion rate, and tracing the shape at different luminosity levels would provide deep insights.
  (2) A systematic study to understand the spin phase dependence of the CRSFs

at different luminosity levels. Probing the spin phase dependence of the CRSF (through phase resolved studies) can map the accretion column and geometry at different viewing angles and can probe the structural changes in the same in detail. It can also more constructively verify the different accretion regimes and geometries at different luminosity levels as proposed in Becker et al. (2012).

(3) Another aspect which is practically unexplored is the evolution of the magnetic field strength and structure of these systems and the effect of the process of accretion on the magnetic field structure of the neutron stars. Evidences of magnetic field burial have been hinted in some low magnetic field millisecond pulsars and also very high magnetic field magnetars. Accretion powered pulsars also exhibit a large order of variation of luminosity and would be expected to show some signatures of this effect. A systematic study of the secular time evolution of the CRSF energies would be exciting in this regard. Some evidence of such effect has already been found in the case of Her X-1 (Staubert, 2013).

– Perform detailed modeling of the phase resolved variations of the CRSF parameters discussed in this thesis as well as those performed in future from *NuSTAR*, *ASTROSAT* and *ASTRO-H* observations, by taking into account different magnetic field geometries, accretion geometries as well as gravitational light bending.

– Make a more detailed and systematic study of the pulse profiles in accretion powered pulsars near their corresponding CRSF energies, specially for the sources which have their CRSF energies $\geq$ 50 keV and cannot be probed in detail with *Suzaku* .

Bibliography

Araya, R. A., & Harding, A. K. 1999, ApJ, 517, 334, 334

Araya-Góchez, R. A., & Harding, A. K. 2000, ApJ, 544, 1067, 1067

Ash, T. D. C., Reynolds, A. P., Roche, P., et al. 1999, MNRAS, 307, 357, 357

Bartolini, C., Guarnieri, A., Piccioni, A., Giangrande, A., & Giovannelli, F. 1978, IAU Circ., 3167, 1, 1

Baykal, A., İnam, S. Ç., & Beklen, E. 2006, MNRAS, 369, 1760, 1760

Becker, P. A. 1998, ApJ, 498, 790, 790

Becker, P. A., & Wolff, M. T. 2005, ApJ, 630, 465, 465

—. 2007, ApJ, 654, 435, 435

Becker, P. A., Wolff, M. T., & Wolfram, K. D. 2005, in Bulletin of the American Astronomical Society, Vol. 37, American Astronomical Society Meeting Abstracts, #198.01

Becker, P. A., Klochkov, D., Schönherr, G., et al. 2012, A&A, 544, A123, A123

Beilicke, M., Baring, M. G., Barthelmy, S., et al. 2012, in American Institute of Physics Conference Series, Vol. 1505, American Institute of Physics Conference Series, ed. F. A. Aharonian, W. Hofmann, & F. M. Rieger, 805–808

Bellazzini, R., Angelini, F., Baldini, L., et al. 2006, Nuclear Instruments and Methods in Physics Research A, 560, 425, 425

Belloni, T., Homan, J., Casella, P., et al. 2005, A&A, 440, 207, 207

Belloni, T., Nespoli, E., Homan, J., et al. 2003, in New Views on Microquasars, ed. P. Durouchoux, Y. Fuchs, & J. Rodriguez, 83

Beloborodov, A. M. 2002, ApJL, 566, L85, L85

Bildsten, L., Chakrabarty, D., Chiu, J., et al. 1994, in American Institute of Physics Conference Series, Vol. 304, American Institute of Physics Conference Series, ed. C. E. Fichtel, N. Gehrels, & J. P. Norris, 294–298

Bildsten, L., Chakrabarty, D., Chiu, J., et al. 1997, ApJS, 113, 367, 367

Blum, S., & Kraus, U. 2000, ApJ, 529, 968, 968

Bowyer, S., Byram, E. T., Chubb, T. A., & Friedman, H. 1965, Science, 147, 394, 394

Bozzo, E., Falanga, M., & Stella, L. 2008, ApJ, 683, 1031, 1031

Brainerd, J. J., & Meszaros, P. 1991, ApJ, 369, 179, 179

Brucato, R. J., & Kristian, J. 1972, ApJL, 173, L105, L105

Bulik, T., Gondek-Rosińska, D., Santangelo, A., et al. 2003, A&A, 404, 1023, 1023

Burderi, L., Di Salvo, T., Robba, N. R., La Barbera, A., & Guainazzi, M. 2000, ApJ, 530, 429, 429

Burnard, D. J., Arons, J., & Klein, R. I. 1991, ApJ, 367, 575, 575

Caballero, I., Kretschmar, P., Santangelo, A., et al. 2008, ArXiv e-prints, arXiv:0801.3897

—. 2007, A&A, 465, L21, L21

Caballero, I., Pottschmidt, K., Bozzo, E., et al. 2010, The Astronomer's Telegram, 2692, 1, 1

Caballero, I., Ferrigno, C., Klochkov, D., et al. 2011a, The Astronomer's Telegram, 3204, 1, 1

Caballero, I., Pottschmidt, K., Santangelo, A., et al. 2011b, ArXiv e-prints, arXiv:1107.3417

Camero-Arranz, A., Pottschmidt, K., Finger, M. H., et al. 2012, A&A, 546, A40, A40

Cemeljic, M., & Bulik, T. 1998, Acta Astronomic, 48, 65, 65

Chakrabarty, D. 1998, ApJ, 492, 342, 342

Chakrabarty, D., & Roche, P. 1997, ApJ, 489, 254, 254

Chandrasekhar, S. 1960,

Chevalier, C., & Ilovaisky, S. A. 1975, IAU Circ., 2778, 1, 1

Choi, C. S., Dotani, T., Day, C. S. R., & Nagase, F. 1996, ApJ, 471, 447, 447

Coburn, W. 2001, PhD thesis,

Coburn, W., Heindl, W. A., Rothschild, R. E., et al. 2002, ApJ, 580, 394, 394

Coe, M. J., & Payne, B. J. 1985, Astrophysics and Space Science, 109, 175, 175

Coe, M. J., Roche, P., Everall, C., et al. 1994, A&A, 289, 784, 784

Connors, P. A., Stark, R. F., & Piran, T. 1980, ApJ, 235, 224, 224

Corbel, S., Tomsick, J. A., & Kaaret, P. 2006, ApJ, 636, 971, 971

Corbet, R. H. D., Sokoloski, J. L., Mukai, K., Markwardt, C. B., & Tueller, J. 2008, ApJ, 675, 1424, 1424

Costa, E., Bellazzini, R., Bregeon, J., et al. 2008, in Society of Photo-Optical Instrumentation Engineers (SPIE) Conference Series, Vol. 7011, Society of Photo-Optical Instrumentation Engineers (SPIE) Conference Series

Cowsik, R., & et al. 2010, Hard X-ray polarimeter for small-satellite missions, ed. R. Bellazzini, E. Costa, G. Matt, & G. Tagliaferri, 345

Cox, N. L. J., Kaper, L., & Mokiem, M. R. 2005, A&A, 436, 661, 661

Crampton, D. 1974, ApJ, 187, 345, 345

Cui, W. 1996, IAU Circ., 6404, 1, 1

Cui, W., Focke, W., & Swank, J. 1996, IAU Circ., 6439, 1, 1

Cusumano, G., di Salvo, T., Burderi, L., et al. 1998, A&A, 338, L79, L79

dal Fiume, D., Orlandini, M., Cusumano, G., et al. 1998, A&A, 329, L41, L41

D'Avanzo, P., Goldoni, P., Covino, S., et al. 2006, The Astronomer's Telegram, 724, 1, 1

Davidson, K. 1973, Nature Physical Science, 246, 1, 1

Davidson, K., & Ostriker, J. P. 1973, ApJ, 179, 585, 585

Deeter, J. E., Scott, D. M., Boynton, P. E., et al. 1998, ApJ, 502, 802, 802

Devasia, J. 2012, PhD thesis,

Devasia, J., James, M., Paul, B., & Indulekha, K. 2011a, MNRAS, 414, 1023, 1023

—. 2011b, MNRAS, 417, 348, 348

Done, C., & Kubota, A. 2006, MNRAS, 371, 1216, 1216

Doroshenko, V., Santangelo, A., & Suleimanov, V. 2011, A&A, 529, A52, A52

Dovčiak, M., Muleri, F., Goosmann, R. W., Karas, V., & Matt, G. 2008, MNRAS, 391, 32, 32

—. 2012, Journal of Physics Conference Series, 372, 012056, 012056

Enoto, T., Makishima, K., Terada, Y., et al. 2008, PASJ, 60, 57, 57

Fender, R., Corbel, S., Tzioumis, T., et al. 2002, The Astronomer's Telegram, 107, 1, 1

Ferrigno, C., Becker, P. A., Segreto, A., Mineo, T., & Santangelo, A. 2009, A&A, 498, 825, 825

Ferrigno, C., Falanga, M., Bozzo, E., et al. 2011, A&A, 532, A76, A76

Ferrigno, C., Segreto, A., Santangelo, A., et al. 2007, A&A, 462, 995, 995

Finger, M. H., Camero-Arranz, A., Kretschmar, P., Wilson, C., & Patel, S. 2006, in Bulletin of the American Astronomical Society, Vol. 38, AAS/High Energy Astrophysics Division #9, 359

Frank, J., King, A., & Raine, D. J. 2002,

Fritz, S., Kreykenbohm, I., Wilms, J., et al. 2006, A&A, 458, 885, 885

Fukazawa, Y., Mizuno, T., Watanabe, S., et al. 2009, PASJ, 61, 17, 17

Fürst, F., Kreykenbohm, I., Pottschmidt, K., et al. 2010, A&A, 519, A37, A37

Galloway, D. K., Giles, A. B., Wu, K., & Greenhill, J. G. 2001, MNRAS, 325, 419, 419

Gerend, D., & Boynton, P. E. 1976, ApJ, 209, 562, 562

Giacconi, R., Kellogg, E., Gorenstein, P., Gursky, H., & Tananbaum, H. 1971, ApJL, 165, L27, L27

Giacconi, R., Murray, S., Gursky, H., et al. 1972, ApJ, 178, 281, 281

Giangrande, A., Giovannelli, F., Bartolini, C., Guarnieri, A., & Piccioni, A. 1980, A&AS, 40, 289, 289

Gies, D. R., & Bolton, C. T. 1986, ApJ, 304, 371, 371

Giles, A. B., Galloway, D. K., Greenhill, J. G., Storey, M. C., & Wilson, C. A. 2000, ApJ, 529, 447, 447

Glass, I. S., & Feast, M. W. 1973, Nature Physical Science, 245, 39, 39

Gnedin, I. N., & Sunyaev, R. A. 1974, A&A, 36, 379, 379

González-Galán, A., Kuulkers, E., Kretschmar, P., et al. 2012, A&A, 537, A66, A66

Grove, J. E., Strickman, M. S., Johnson, W. N., et al. 1995, ApJL, 438, L25, L25

Gruber, D. E., Heindl, W. A., Rothschild, R. E., et al. 2001, ApJ, 562, 499, 499

Harmon, B. A., McCollough, M. L., Zhang, S. N., Paciesas, W. S., & Wilson, C. A. 1995, IAU Circ., 6196, 1, 1

Heindl, W. A., Coburn, W., Gruber, D. E., et al. 2000, in American Institute of Physics Conference Series, Vol. 510, American Institute of Physics Conference Series, ed. M. L. McConnell & J. M. Ryan, 173–177

Heindl, W. A., Coburn, W., Gruber, D. E., et al. 2001, ApJL, 563, L35, L35

Heindl, W. A., Rothschild, R. E., Coburn, W., et al. 2004, in American Institute of Physics Conference Series, Vol. 714, X-ray Timing 2003: Rossi and Beyond, ed. P. Kaaret, F. K. Lamb, & J. H. Swank, 323–330

Herrero, A., Kudritzki, R. P., Gabler, R., Vilchez, J. M., & Gabler, A. 1995, A&A, 297, 556, 556

Hinkle, K. H., Fekel, F. C., Joyce, R. R., et al. 2006, ApJ, 641, 479, 479

Hutchings, J. B., Cowley, A. P., Crampton, D., van Paradijs, J., & White, N. E. 1979, ApJ, 229, 1079, 1079

Hynes, R. I., Steeghs, D., Casares, J., Charles, P. A., & O'Brien, K. 2003, in Bulletin of the American Astronomical Society, Vol. 35, AAS/High Energy Astrophysics Division #7, 615

in 't Zand, J. J. M., Baykal, A., & Strohmayer, T. E. 1998, ApJ, 496, 386, 386

in 't Zand, J. J. M., Strohmayer, T. E., & Baykal, A. 1997, ApJL, 479, L47, L47

Inam, S. Ç., Şahiner, Ş., & Baykal, A. 2009, MNRAS, 395, 1015, 1015

Inoue, H., Ogawara, Y., Waki, I., et al. 1984, PASJ, 36, 709, 709

Ives, J. C., Sanford, P. W., & Bell Burnell, S. J. 1975, Nature, 254, 578, 578

Iwakiri, W. B., Terada, Y., Mihara, T., et al. 2012, ApJ, 751, 35, 35

Jahoda, K., Swank, J. H., Giles, A. B., et al. 1996, in Society of Photo-Optical Instrumentation Engineers (SPIE) Conference Series, Vol. 2808, Society of Photo-Optical Instrumentation Engineers (SPIE) Conference Series, ed. O. H. Siegmund & M. A. Gummin, 59–70

Jain, C., Paul, B., & Dutta, A. 2010, MNRAS, 403, 920, 920

Janot-Pacheco, E., Ilovaisky, S. A., & Chevalier, C. 1981, A&A, 99, 274, 274

Kalemci, E., Tomsick, J. A., Rothschild, R. E., et al. 2006, ApJ, 639, 340, 340

Kaluzienski, L. J., Holt, S. S., Swank, J. H., Boldt, E. A., & Serlemitsos, P. J. 1977, in Bulletin of the American Astronomical Society, Vol. 9, Bulletin of the American Astronomical Society, 592

Kaper, L., van der Meer, A., & Najarro, F. 2006, A&A, 457, 595, 595

Kendziorra, E., Mony, B., Kretschmar, P., et al. 1992, in NASA Conference Publication, Vol. 3137, NASA Conference Publication, ed. C. R. Shrader, N. Gehrels, & B. Dennis, 217

Kendziorra, E., Kretschmar, P., Pan, H. C., et al. 1994, A&A, 291, L31, L31

Kii, T. 1987, PASJ, 39, 781, 781

Klein, R. I., Arons, J., Jernigan, G., & Hsu, J. J.-L. 1996, ApJL, 457, L85, L85

Klochkov, D., Santangelo, A., Staubert, R., & Ferrigno, C. 2008a, A&A, 491, 833, 833

Klochkov, D., Staubert, R., Santangelo, A., Rothschild, R. E., & Ferrigno, C. 2011, A&A, 532, A126, A126

Klochkov, D., Staubert, R., Postnov, K., et al. 2008b, A&A, 482, 907, 907

Klochkov, D., Doroshenko, V., Santangelo, A., et al. 2012, A&A, 542, L28, L28

Koh, D. T., Bildsten, L., Chakrabarty, D., et al. 1997, ApJ, 479, 933, 933

Kotani, T., Dotani, T., Nagase, F., et al. 1999, ApJ, 510, 369, 369

Koyama, K., Tsunemi, H., Dotani, T., et al. 2007, PASJ, 59, 23, 23

Kraus, U. 2001, ApJ, 563, 289, 289

Kraus, U., Blum, S., Schulte, J., Ruder, H., & Meszaros, P. 1996, ApJ, 467, 794, 794

Kretschmar, P., Pan, H. C., Kendziorra, E., et al. 1996, A&AS, 120, C175, C175

—. 1997, A&A, 325, 623, 623

Kreykenbohm, I., Coburn, W., Wilms, J., et al. 2002, A&A, 395, 129, 129

Kreykenbohm, I., Kretschmar, P., Wilms, J., et al. 1999, A&A, 341, 141, 141

Kreykenbohm, I., Pottschmidt, K., Kretschmar, P., et al. 2004, in ESA Special Publication, Vol. 552, 5th INTEGRAL Workshop on the INTEGRAL Universe, ed. V. Schoenfelder, G. Lichti, & C. Winkler, 333

Kreykenbohm, I., Wilms, J., Kretschmar, P., et al. 2008, A&A, 492, 511, 511

La Barbera, A., Santangelo, A., Orlandini, M., & Segreto, A. 2003, A&A, 400, 993, 993

La Barbera, A., Segreto, A., Santangelo, A., Kreykenbohm, I., & Orlandini, M. 2005, A&A, 438, 617, 617

Lamb, F. K., Pethick, C. J., & Pines, D. 1973, ApJ, 184, 271, 271

Leahy, D. A. 1991, MNRAS, 251, 203, 203

—. 2003, ApJ, 596, 1131, 1131

—. 2004, MNRAS, 348, 932, 932

Leahy, D. A., & Li, L. 1995, MNRAS, 277, 1177, 1177

Lee, K., Garson, III, A., Li, Q., et al. 2010, in Bulletin of the American Astronomical Society, Vol. 42, American Astronomical Society Meeting Abstracts #215, #387.06

Levine, A., Ma, C. P., McClintock, J., et al. 1988, ApJ, 327, 732, 732

Levine, A. M., Bradt, H., Cui, W., et al. 1996, ApJL, 469, L33, L33

Lewin, W. H. G., Ricker, G. R., & McClintock, J. E. 1971, ApJL, 169, L17, L17

Li, L.-X., Narayan, R., & McClintock, J. E. 2009, ApJ, 691, 847, 847

Liller, W. 1972, IAU Circ., 2415, 1, 1

Long, K. S., Chanan, G. A., & Novick, R. 1980, ApJ, 238, 710, 710

Lutovinov, A. A., & Tsygankov, S. S. 2009, Astronomy Letters, 35, 433, 433

Magdziarz, P., & Zdziarski, A. A. 1995, MNRAS, 273, 837, 837

Makishima, K., Maejima, Y., Mitsuda, K., et al. 1986, ApJ, 308, 635, 635

Makishima, K., & Mihara, T. 1992, in Frontiers Science Series, ed. Y. Tanaka & K. Koyama, 23

Makishima, K., Mihara, T., Nagase, F., & Tanaka, Y. 1999, ApJ, 525, 978, 978

Mangano, V. 2009, The Astronomer's Telegram, 1896, 1, 1

Maraschi, L., Huckle, H. E., Ives, J. C., & Sanford, P. W. 1976, Nature, 263, 34, 34

Markert, T. H., Canizares, C. R., Clark, G. W., et al. 1973a, ApJL, 184, L67, L67

Markert, T. H., Clark, G. W., Lewin, W. H. G., Schnopper, H. W., & Sprott, G. F. 1973b, IAU Circ., 2483, 1, 1

Markwardt, C. B., & Swank, J. H. 2003, The Astronomer's Telegram, 133, 1, 1

—. 2005, The Astronomer's Telegram, 414, 1, 1

Martínez Núñez, S., Reig, P., Blay, P., et al. 2003, A&A, 411, L411, L411

Massi, M., Ribó, M., Paredes, J. M., et al. 2004, A&A, 414, L1, L1

McClintock, J. E., Li, F. K., Canizares, C. R., & Grindlay, J. E. 1980, ApJL, 235, L81, L81

McConnell, M. L., Bancroft, C., Bloser, P. F., et al. 2009, in Society of Photo-Optical Instrumentation Engineers (SPIE) Conference Series, Vol. 7435, Society of Photo-Optical Instrumentation Engineers (SPIE) Conference Series

Meszaros, P. 1992, Journal of the British Astronomical Association, 102, 287, 287

Meszaros, P., & Nagel, W. 1985a, ApJ, 298, 147, 147

—. 1985b, ApJ, 299, 138, 138

Meszaros, P., Novick, R., Szentgyorgyi, A., Chanan, G. A., & Weisskopf, M. C. 1988, ApJ, 324, 1056, 1056

Middleditch, J., Mason, K. O., Nelson, J. E., & White, N. E. 1981, ApJ, 244, 1001, 1001

Mihara, T. 1995, PhD thesis,

Mihara, T., Makishima, K., & Nagase, F. 2004, ApJ, 610, 390, 390

Mihara, T., Yamamoto, T., Sugizaki, M., Nakajima, M., & Maxi Team. 2010, in The First Year of MAXI: Monitoring Variable X-ray Sources

Miller, J. M., Homan, J., Steeghs, D., Torres, M. A. P., & Wijnands, R. 2006, The Astronomer's Telegram, 743, 1, 1

Mitsuda, K., Inoue, H., Koyama, K., et al. 1984, PASJ, 36, 741, 741

Mitsuda, K., Bautz, M., Inoue, H., et al. 2007, PASJ, 59, 1, 1

Morrison, R., & McCammon, D. 1983, ApJ, 270, 119, 119

Motch, C., Pakull, M. W., Janot-Pacheco, E., & Mouchet, M. 1988, A&A, 201, 63, 63

Mukerjee, K., Agrawal, P. C., Paul, B., et al. 2001, ApJ, 548, 368, 368

Mukherjee, D., & Bhattacharya, D. 2012a, MNRAS, 420, 720, 720

—. 2012b, MNRAS, 420, 720, 720

Mukherjee, U., & Paul, B. 2004, A&A, 427, 567, 567

—. 2005, A&A, 431, 667, 667

Müller, S., Kühnel, M., Caballero, I., et al. 2012, A&A, 546, A125, A125

Nagase, F. 1989, PASJ, 41, 1, 1

Nagase, F., Hayakawa, S., Sato, N., Masai, K., & Inoue, H. 1986, PASJ, 38, 547, 547

Nagel, W. 1981, ApJ, 251, 288, 288

Naik, S., Paul, B., & Ali, Z. 2011a, ApJ, 737, 79, 79

Naik, S., Paul, B., & Callanan, P. J. 2005, ApJ, 618, 866, 866

Naik, S., Paul, B., Kachhara, C., & Vadawale, S. V. 2011b, MNRAS, 413, 241, 241

Naik, S., Dotani, T., Terada, Y., et al. 2008, ApJ, 672, 516, 516

Nakajima, M., Mihara, T., & Makishima, K. 2010, ApJ, 710, 1755, 1755

Negueruela, I., Reig, P., Coe, M. J., & Fabregat, J. 1998, A&A, 336, 251, 251

Negueruela, I., Reig, P., Finger, M. H., & Roche, P. 2000, A&A, 356, 1003, 1003

Nespoli, E., & Reig, P. 2011, A&A, 526, A7, A7

Nishimura, O. 2008, ApJ, 672, 1127, 1127

—. 2011, ApJ, 730, 106, 106

Okazaki, A. T., & Negueruela, I. 2001, A&A, 377, 161, 161

Orlandini, M., Fiume, D. D., Frontera, F., et al. 1998a, ApJL, 500, L163, L163

Orlandini, M., dal Fiume, D., Frontera, F., et al. 1998b, A&A, 332, 121, 121

Orosz, J. A., & Bailyn, C. D. 1997, ApJ, 482, 1086, 1086

Paul, B., Agrawal, P. C., Mukerjee, K., et al. 2001, A&A, 370, 529, 529

Paul, B., Dotani, T., Nagase, F., Mukherjee, U., & Naik, S. 2005, ApJ, 627, 915, 915

Pearce, M., Florén, H.-G., Jackson, M., et al. 2012, ArXiv e-prints, arXiv:1211.5094

Postnov, K., Shakura, N., Staubert, . R., et al. 2013, ArXiv e-prints, arXiv:1307.6026

Pottschmidt, K., Kreykenbohm, I., Wilms, J., et al. 2005, ApJL, 634, L97, L97

Pottschmidt, K., Suchy, S., Rivers, E., et al. 2012, in American Institute of Physics Conference Series, Vol. 1427, American Institute of Physics Conference Series, ed. R. Petre, K. Mitsuda, & L. Angelini, 60–67

Pringle, J. E., & Rees, M. J. 1972, A&A, 21, 1, 1

Quaintrell, H., Norton, A. J., Ash, T. D. C., et al. 2003, A&A, 401, 313, 313

Rawls, M. L., Orosz, J. A., McClintock, J. E., et al. 2011, ApJ, 730, 25, 25

Rea, N., Stella, L., Israel, G. L., et al. 2005, MNRAS, 364, 1229, 1229

Rees, M. J. 1975, MNRAS, 171, 457, 457

Reig, P., & Coe, M. J. 1999a, Memorie della Societa Astronomica Italiana, 70, 1121, 1121

—. 1999b, MNRAS, 302, 700, 700

Remillard, R., Levine, A. M., Morgan, E. H., Markwardt, C. B., & Swank, J. H. 2006, The Astronomer's Telegram, 714, 1, 1

Revnivtsev, M., Chernyakova, M., Capitanio, F., et al. 2003, The Astronomer's Telegram, 132, 1, 1

Reynolds, A. P., Quaintrell, H., Still, M. D., et al. 1997, MNRAS, 288, 43, 43

Riffert, H., Nollert, H.-P., Kraus, U., & Ruder, H. 1993, ApJ, 406, 185, 185

Rishin, P. V. e. 2010, Development of a Thomson X-ray polarimeter, ed. R. Bellazzini, E. Costa, G. Matt, & G. Tagliaferri, 83

Rivers, E., Markowitz, A., Pottschmidt, K., et al. 2010, ApJ, 709, 179, 179

Robba, N. R., Burderi, L., Di Salvo, T., Iaria, R., & Cusumano, G. 2001, ApJ, 562, 950, 950

Rosenberg, F. D., Eyles, C. J., Skinner, G. K., & Willmore, A. P. 1975, Nature, 256, 628, 628

Rothschild, R. E., Blanco, P. R., Gruber, D. E., et al. 1998, ApJ, 496, 538, 538

Rupen, M. P., Dhawan, V., & Mioduszewski, A. J. 2006, The Astronomer's Telegram, 721, 1, 1

Sako, M., Liedahl, D. A., Kahn, S. M., & Paerels, F. 1999, ApJ, 525, 921, 921

Salpeter, E. E. 1964, ApJ, 140, 796, 796

Santangelo, A., del Sordo, S., Segreto, A., et al. 1998, A&A, 340, L55, L55

Santangelo, A., Segreto, A., Del Sordo, S., et al. 2000, in Bulletin of the American Astronomical Society, Vol. 32, AAS/High Energy Astrophysics Division #5, 1230

Sasaki, M., Klochkov, D., Kraus, U., Caballero, I., & Santangelo, A. 2010, A&A, 517, A8, A8

Schnittman, J. D., & Krolik, J. H. 2009, ApJ, 701, 1175, 1175

—. 2010, ApJ, 712, 908, 908

Schönherr, G., Wilms, J., Kretschmar, P., et al. 2007, A&A, 472, 353, 353

Schreier, E., Levinson, R., Gursky, H., et al. 1972, ApJL, 172, L79, L79

Schwartz, D. A., Bleach, R. D., Boldt, E. A., Holt, S. S., & Serlemitsos, P. J. 1972, ApJL, 173, L51, L51

Silver, E. H., Weisskopf, M. C., Kestenbaum, H. L., et al. 1979, ApJ, 232, 248, 248

Smith, D. A., Takeshima, T., Wilson, C. A., et al. 1998, IAU Circ., 7014, 1, 1

Soffitta, P., Barcons, X., Bellazzini, R., et al. 2013, Experimental Astronomy, arXiv:1309.6995

Soong, Y., Gruber, D. E., Peterson, L. E., & Rothschild, R. E. 1990, ApJ, 348, 641, 641

Staubert, R. 2013, ArXiv e-prints, arXiv:1303.1922

Staubert, R., Pottschmidt, K., Doroshenko, V., et al. 2011, A&A, 527, A7, A7

Staubert, R., Shakura, N. I., Postnov, K., et al. 2007, A&A, 465, L25, L25

Steele, I. A., Negueruela, I., Coe, M. J., & Roche, P. 1998, MNRAS, 297, L5, L5

Suchy, S., Fürst, F., Pottschmidt, K., et al. 2012, ApJ, 745, 124, 124

Suchy, S., Pottschmidt, K., Wilms, J., et al. 2008, ApJ, 675, 1487, 1487

Suchy, S., Pottschmidt, K., Rothschild, R. E., et al. 2011, ApJ, 733, 15, 15

Sunyaev, R. A., & Titarchuk, L. G. 1980, A&A, 86, 121, 121

—. 1985, A&A, 143, 374, 374

Swank, J., Kallman, T., & Jahoda, K. 2008, in COSPAR Meeting, Vol. 37, 37th COSPAR Scientific Assembly, 3102

Takahashi, T., Abe, K., Endo, M., et al. 2007, PASJ, 59, 35, 35

Tanaka, Y. 1986, in Lecture Notes in Physics, Berlin Springer Verlag, Vol. 255, IAU Colloq. 89: Radiation Hydrodynamics in Stars and Compact Objects, ed. D. Mihalas & K.-H. A. Winkler, 198

Terada, Y., Mihara, T., Nakajima, M., et al. 2006, ApJL, 648, L139, L139

Thompson, T. W. J., & Rothschild, R. E. 2009, ApJ, 691, 1744, 1744

Titarchuk, L. 1994, ApJ, 434, 570, 570

Torres, M. A. P., Steeghs, D., Jonker, P. G., et al. 2006a, The Astronomer's Telegram, 733, 1, 1

Torres, M. A. P., Steeghs, D., McClintock, J., et al. 2006b, The Astronomer's Telegram, 749, 1, 1

Truemper, J., Pietsch, W., Reppin, C., et al. 1978, ApJL, 219, L105, L105

Trümper, J., Pietsch, W., Reppin, C., & Sacco, B. 1977, in Annals of the New York Academy of Sciences, Vol. 302, Eighth Texas Symposium on Relativistic Astrophysics, ed. M. D. Papagiannis, 538

Tsygankov, S. S., Lutovinov, A. A., Churazov, E. M., & Sunyaev, R. A. 2006, MNRAS, 371, 19, 19

—. 2007, Astronomy Letters, 33, 368, 368

Vadawale, S. V., Paul, B., Pendharkar, J., & Naik, S. 2010, Nuclear Instruments and Methods in Physics Research A, 618, 182, 182

van Kerkwijk, M. H., van Paradijs, J., Zuiderwijk, E. J., et al. 1995, A&A, 303, 483, 483

Vasco, D., Staubert, R., Klochkov, D., et al. 2013, A&A, 550, A111, A111

Verrecchia, F., Israel, G. L., Negueruela, I., et al. 2002, A&A, 393, 983, 983

Weisskopf, M. C., Cohen, G. G., Kestenbaum, H. L., et al. 1976, ApJL, 208, L125, L125

Weisskopf, M. C., Elsner, R. F., & O'Dell, S. L. 2010, in Society of Photo-Optical Instrumentation Engineers (SPIE) Conference Series, Vol. 7732, Society of Photo-Optical Instrumentation Engineers (SPIE) Conference Series

White, N. E., & Marshall, F. E. 1984, ApJ, 281, 354, 354

White, N. E., Nagase, F., & Parmar, A. N. 1995, X-ray Binaries, 1, 1

White, N. E., Swank, J. H., & Holt, S. S. 1983, ApJ, 270, 711, 711

Wilson, C. A., Finger, M. H., & Camero-Arranz, A. 2008, ApJ, 678, 1263, 1263

Wilson, C. A., Finger, M. H., Coe, M. J., & Negueruela, I. 2003, ApJ, 584, 996, 996

Wilson, C. A., Finger, M. H., Wilson, R. B., & Scott, D. M. 1998, IAU Circ., 7014, 2, 2

Yahel, R. Z. 1980, ApJ, 236, 911, 911

Zdziarski, A. A., & Gierliński, M. 2004, Progress of Theoretical Physics Supplement, 155, 99, 99

Zeldovich, Y. B., & Guseynov, O. H. 1966, ApJ, 144, 840, 840

Zel'dovich, Y. B., & Novikov, I. D. 1964, Soviet Physics Doklady, 9, 246, 246

Zhang, S. N., Cui, W., Harmon, B. A., & Paciesas, W. S. 1997, in American Institute of Physics Conference Series, Vol. 410, Proceedings of the Fourth Compton Symposium, ed. C. D. Dermer, M. S. Strickman, & J. D. Kurfess, 839–843

Zhang, W., Giles, A. B., Jahoda, K., et al. 1993, in Society of Photo-Optical Instrumentation Engineers (SPIE) Conference Series, Vol. 2006, Society of Photo-Optical Instrumentation Engineers (SPIE) Conference Series, ed. O. H. Siegmund, 324–333